UNIVERSITY OF CALIFORNIA,
IRVINE

Secondary Coordination Sphere Effects on the Properties of High Valent Iron and Manganese Complexes with Oxido and Hydroxido Ligands

DISSERTATION

submitted in partial satisfaction of the requirements
for the degree of

DOCTOR OF PHILOSOPHY

in Chemistry

by

Ethan A. Hill

Dissertation Committee:
Professor A.S. Borovik, Chair
Professor Alan F. Heyduk
Professor William J. Evans

2016

DEDICATION

To my mother who has been a constant source
of love, support, and inspiration.

TABLE OF CONTENTS

LIST OF FIGURES

LIST OF TABLES

LIST OF SCHEMES

ACKNOWLEDGMENTS

Throughout my academic career at UCI I have had the privilege of learning from and interacting with an incredible group of scientists. First I would like to thank my advisor Andy. The amount I have matured as a scientist is in no small part due to your guidance and direction. The freedom you provide graduate students to pursue their interests and ideas fosters a thoughtful, thorough, and scientific mind. This kind of freedom is uncommon in the academic setting and not something that I have taken for granted. I can only hope to be even partly as capable of inspiring and guiding others in their own path. And despite the times I've been frustrated, I'm grateful to have had the opportunity to work with you.

The Borovik group has changed a lot since I joined, and I've been fortunate to have learned from so many of the great people past and present. In particular I must thank Dr. David Lacy. You were the first to really show me the ropes in the lab and get me started on a project that would become both the majority of this thesis and the occasional subject of my nightmares. The times spent talking science over a pipe at the Tobacco Barn are something I'll think fondly on and I hope we'll be able to share more good times like that again. And I would be remise to leave out Dr. Taketo Taguchi. Your incredible work ethic and patience have influenced me more than you will know. I often miss the times where all I needed to do was lean back in my chair a little to ask you a question and know you'd be willing to stop what you're doing and talk through a problem I was having or even just chat about something completely random. I've also had the pleasure of sharing space and learning from some fantastic people who taught me things from the start and got me settled in; Yohei, Sonja, Nate, Dave, and Jon, I can't thank you all enough not only for teaching me, but for all the good times and laughs, I couldn't have asked for a better crew to start out with in the Borovik group. To the members who came after me, Nate, Jason, Sam, Victoria, Kelsey, Noam, Maisha, Justin, and Lisa it's been a pleasure to get to know you all. You all have contributed so much to the positive atmosphere and environment that makes the Borovik group what it is today. From the jokes in lab, the conversations over morning coffee, meals together, movies, games, and more, all these things have made the trials of graduate school just a little more bearable. I will really miss all of this more than I realize right now.

Where would I be without my corner buddy, Sarah. Right away I knew you were someone I could get along with. I relied on you many times over the years, even if just to get a second opinion when I was stuck on the next step in an experiment. Before long I had to rely on you as a source of encouragement as things in the lab stalled and I became frustrated. I've missed being able to just pop over to your box and chat or sit and drink scotch at the end of the day or offer you coffee in the morning knowing you would never take it. I'm privileged to not only be able to have called you a labmate, but now my friend. I look forward to seeing where life takes us both and I hope we will maintain our close friendship for years and years to come.

In addition to these great lab members, collaborators have played an important role in making me who I am today. The Hendrich lab in particular has been a constant source of knowledge. I must acknowledge Andrew for being extremely patient and helpful in teaching me about the techniques used in his lab. I also had the pleasure of getting to know you while at a Gordon Conference together and I hope we can stay in touch. The group at SSRL has also been incredible. It was amazing to see a group of scientists from all different fields and countries can come together with one goal in mind, and despite near constant frustration, maintain a positive attitude. It was an experience I will not forget.

Outside the lab, friends and family have been my support system and the people I've relied on to unwind. My old friends have been there for years, some since middle school and I'm so thankful for the lifelong friendships that I can always fall back on. I have made so many new friends here at UCI. We've had a lot fun whether it was out on an adventure or just drinks and a movie at someone's apartment, I've really enjoyed it. I look forward to seeing where everyone ends up as we part ways and I hope we can keep in touch. My family have always been there for me. My grandparents have always been just a phone call away should I want to chat and waiting with open arms whenever I make it back home to Colorado. My brother, Aaron, you were my first friend. Our relationship has matured a lot since those early days and I'm glad that we've remained close. I'm thankful that even if we don't talk on the phone much, we can make time to play some Xbox every now and then to keep in touch.

Finally to my mother, who has been an example of strength, love, and perseverance all my life. I know I would not be who I am or where I am today without everything you've done for both me and Aaron. Over the years you've been supportive of me pursuing my dreams and following my aspirations even when it took me all the way across the country. The love and appreciation I have for you is difficult to express in words but know that I love you and am so thankful to have you in my life.

Curriculum Vitae

Ethan Hill

Education

August 2016	*Department of Chemistry, University of California, Irvine* Ph.D., Chemistry Research Advisor: A.S. Borovik
May 2011	*Department of Chemistry, Colorado State University* B.S. Chemistry, ACS Certified

Publications

Hill, E. A., Weitz, A. C., Onderko, E., Romero-Rivera, A., Guo, Y., Swart, M., Bominaar, E. L., Green, M. T., Hendrich, M. P., Lacy, D. C., Borovik, A. S.
"Reactivity of an Fe^{IV}-Oxo Complex with Protons and Oxidants"
(Manuscript Submitted)

Kroll, T., Kern, J., Kubin, M., Ratner, D., Gul, S., Fuller, F. D., Löchel, H., Krzywinski, J., Lutman, A., Ding, Y., Dakovski, G. L., Moeller, S., Turner, J. J., Alonso-Mori, R., Nordlund, D. L., Rehanek, J., Weniger, C., Firsov, A., Brzhesinskaya, M., Chatterjee, R., Lassale-Kaiser, B., Sierra, R. G., Lakshmono, H., Hill, E. A., Borovik, A. S., Erko, A., Föhlisch, A., Mitzner, R., Yachandra, V. K., Yano, J., Wernet, P. Bergmann, U.
"X-ray Absorption Spectroscopy Using a Self-Seeded Soft X-ray Free-Electron Laser"
(Manuscript Accepted)

Cook, S. A., Hill, E. A., Borovik, A. S.
"Lessons from Nature: A Bio-Inspired Approach to Molecular Design"
Biochemistry, **2015**, *54*, 4167-4180

McDaniel, A. M., Tseng, H., Hill, E. A., Damrauer, N. H. Rappé, A. K., Shores, M. P.
"Synthesis and Photophysical Investigations of Cr(III) Hexadentate Iminopyridine Complexes and Their Tris(Bidentate) Analogues"
Inorg. Chem., **2013**, *52*, 1368-1378

Hoffert, W. A., Kabir, M. K., Hill, E. A., Mueller, S. M., Shores, M. P.
"Stepwise Acetylide Ligand Substitution for the Assembly of Ethynylbenzene-Linked Co(III) complexes"
Inorganica Chimica Acta, **2012**, *380*, 174-180

Posters and Presentations

Hill, E. A., Lacy, D. C., Weitz, A. C., Hendrich, M. P., Borovik, A. S.
"Generation and Characterization of a Putative, Mononuclear Fe(IV)-Hydroxide Complex"
Poster at the Bioinorganic Chemistry Gordon Research Seminar, Ventura, CA, 2016

Hill, E. A., Lacy, D. C., Weitz, A. C., Hendrich, M. P., Borovik, A. S.
"Generation and Characterization of a Putative, Mononuclear Fe(IV)-Hydroxide Complex"
Presentation at the Bioinorganic Chemistry Gordon Research Seminar, Ventura, CA, 2015

Hill, E. A., Lacy, D. C., Weitz, A. C., Hendrich, M. P., Borovik, A. S.
"Generation and Characterization of a Putative, Mononuclear Fe(IV)-Hydroxide Complex"
Poster at the Bioinorganic Chemistry Gordon Research Seminar, Ventura, CA, 2014

Hill, E. A., Lacy, D. C., Weitz, A. C., Hendrich, M. P., Borovik, A. S.
"Generation of a Putative, Mononuclear Fe(IV)-Hydroxide Complex"
248th A. C. S. National Meeting, San Fransisco, CA, 2014

Awards and Scholarships

Fall 2015	*Dissertation Fellowship Award, University of California, Irvine*
2011	*ACS Undergraduate Award in Inorganic Chemistry, Colorado State University*
2008-2011	*ACS-Hach Land Grant Scholarship, Colorado State University*

Affiliations

American Chemical Society

Abstract of the Dissertation

Secondary Coordination Sphere Effects on the Properties of High Valent Iron and Manganese Complexes with Oxido and Hydroxido Ligands

By
Ethan A. Hill
Doctor of Philosophy in Chemistry
University of California, Irvine, 2016
Professor A. S. Borovik, Chair

In nature, metalloproteins have evolved a precise control over the primary and secondary coordination sphere of their active sites to perform chemical transformations with high selectivity and efficiency. The approach developed in the Borovik lab to emulate these properties has been to synthesize molecular constructs that are capable of stabilizing reactive species through control of the primary coordination sphere of a metal ion with a rigid ligand platform and the secondary coordination sphere through hydrogen-bonding (H-bonding) interactions. This thesis describes how modifications of the secondary coordination sphere by incorporating both H-bond acceptors and donors affects the chemistry of metal complexes. Chapter 2 describes the protonation and oxidation of the previously reported $[Fe^{IV}H_3buea(O)]^-$ complex. Addition of either a proton or oxidant to the Fe^{IV}-oxido complex resulted in the formation of a new Fe^{IV} species, characterized as the protonated congener of $[Fe^{IV}H_3buea(O)]^-$. Density functional theory (DFT) calculations and X-ray absorption spectroscopy (XAS) provided insight into the structural properties of the complex and suggested that the $[H_3buea]^{3-}$ was the site of protonation, resulting in a tautomerization with the additional proton being H-bonded to the oxido ligand. These results demonstrated the difficulty in preparing high valent Fe^{IV}-hydroxido species. Chapter 3 explores the proton-coupled electron transfer (PCET) process for the oxidation of an Fe^{III}-hydroxido complex to generate the corresponding Fe^{IV}-oxido complex. It was shown that the choice of

solvent greatly affected the yield of the Fe^{IV}-oxido complex and that the decreased yield could be attributed to loss of the starting Fe^{III}-hydroxido complex by acting as a base in the reaction. Chapter 4 explores how modifications of the secondary coordination sphere of a metal complex via replacement of one H-bond donor with an acceptor affected the stability of high valent Fe complexes. The $[H_2bupa]^{3-}$ ligand incorporates an H-bond accepting group, an anionic amidate, within the secondary coordination sphere, which produced a unique "hybrid" Fe^{III}-oxido/hydroxido complex with a proton likely positioned between the amidate nitrogen and oxido ligand. When oxidized to the Fe^{IV} oxidation state, the complex is best characterized as an Fe^{IV}-oxido complex with the proton positioned on the ligand.

The last two chapters examine the effect of group 2 and 3 metal ions on high valent Mn-oxido complexes. Chapter 5 describes the alteration of the redox properties of a series of Mn-oxido complexes within the $[H_3buea]^{3-}$ ligand by the addition of Ca^{II}, Sr^{II}, or Sc^{III} ions. Addition of these Lewis acidic metal ions to a Mn^{V}-oxido complex resulted in spontaneous electron transfer to $[FeCp_2]$ to generate the analogous Mn^{IV}-oxido Lewis acid adduct. The Mn^{IV} adduct could be independently generated by the addition of Lewis acids to the Mn^{IV}-oxido complex. Of the metal ions examined, addition of Sc^{III} ions showed the greatest attenuation of the redox potential of the Mn-oxido complexes. Chapter 6 describes efforts to identify a putative Mn^{III}-peroxido species observed in parallel-mode electron paramagnetic resonance (EPR) spectroscopy that was generated by the addition of Ca^{II} ions and base to a Mn^{IV}-oxido complex within the $[H_2bupa]^{3-}$ ligand.

Chapter 1

Thesis Background and Introduction

In nature, metalloproteins perform a wide array of chemical transformations with impressive efficiency and selectivity.[1–4] These enzymes have evolved precise control over both the structural and electronic properties of metal complexes within their active site in order to facilitate function.[5,6] The structural and electronic properties of the active sites are governed by both the primary coordination sphere, ligands directly bound to the metal ions in the active site, and the secondary coordination sphere, non-covalent interactions surrounding the active site. The non-covalent interactions are mostly comprised of hydrogen-bonds (H-bonds), steric interactions, and electrostatic interactions that serve to bind and orient substrate, participate in proton and electron transfer, and stabilize reactive intermediates within the metalloprotein active site.[7–13]

While these primary and secondary sphere interactions are ubiquitous in metalloenzymes, one particular enzyme will be briefly discussed for its relevance to studies presented in this thesis. The oxygen evolving complex (OEC), a [$CaMn_4O_5$] cluster within photosystem II (PSII), demonstrates explicit control over the primary sphere of the metal cluster and the secondary sphere through H-bonds (Figure 1-1).[14–17] This system is capable of oxidizing two water molecules to a single dioxygen (O_2) molecule following the stepwise removal of four protons and four electrons that is instigated by the absorption of four photons by the light-harvesting chlorophyll-a component of the enzyme.[18–20] The OEC is oxidized four times prior to O_2 release, progressing from a $(Mn^{III})_3(Mn^{IV})$ state all the way to what is proposed to be a $(Mn^{IV})_3(Mn^{V})$ state in what are called the "S" states, S_0 through S_4, of the Kok cycle.[21–23] The OEC is anchored in place by several amino acid residues, of which all are anionic carboxylate donors

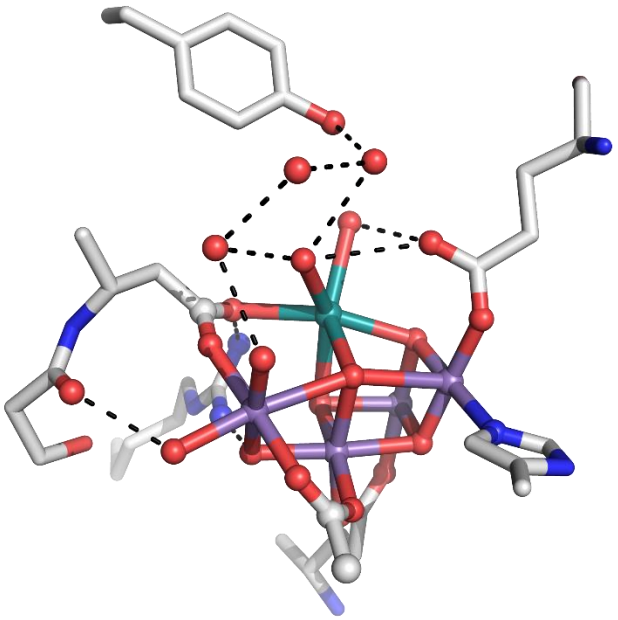

Figure 1-1. Depiction of the structure of the OEC determined by X-ray diffraction methods. Select H-bonding interactions are indicated by dashed lines. Key: Mn = purple, Ca = teal

except for a single histidine residue. The highly anionic primary sphere is likely to promote and stabilize the high oxidation states of Mn required for O_2 production.[19,24,25] Surrounding the cluster are a series of amino acid residues that serve to transfer protons and electrons and transport substrate water molecules. It has been clearly demonstrated that disruption of this delicate H-bonding environment hinders or halts O_2 production.[26–28] One such disruption involves a tyrosine labeled Y_z, that is vital for proton and electron transfer processes and its replacement by site-directed mutagenesis leads to deactivation of the enzyme. In fact, just altering neighboring residues to this tyrosine disrupts the H-bonding network enough to suppress function. Disruption of H-bonding networks by site-directed mutagenesis has proved invaluable in many enzymatic systems to tease out which of the dozens of amino acid residues surrounding various active sites are essential for function and to infer their function in the enzymatic cycle.[29,30]

Synthetic Model Compounds

Replicating the precise control of the primary and secondary coordination spheres demonstrated by metalloproteins in a synthetic metal complex is exceptionally difficult.[31–33] The primary coordination sphere has been the study of basic coordination chemistry for over a century beginning with the work of Werner.[34,35] However, extending this understanding and control beyond the primary sphere to weak, non-covalent interactions surrounding the metal complex has proved to be a great challenge for synthetic chemists. Several defining principles have been developed to provide control of the secondary coordination sphere; the use of H-bonds to interact with and stabilize reactive species, incorporation of pendant function groups for substrate binding or proton and electron transfer, and rigid ligand platforms to properly position these H-bonding and pendant functional groups.[36–39] Manipulation of the secondary coordination sphere by these principles has been shown in a multitude of examples to stabilize transient, reactive intermediate species in efforts to mimic and understand biological processes performed by metalloproteins.

One of the earliest examples of effective control of the primary and secondary sphere was reported by Collman in the 1970s.[40–43] Collman was interested in mimicking the chemistry of

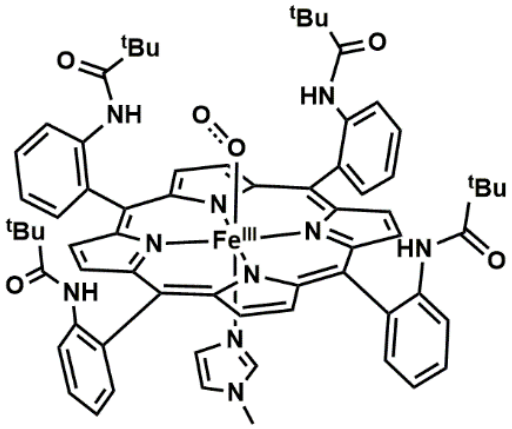

Figure 1-2. Depiction of the Fe–O_2 adduct stabilized by the picket fence porphyrin designed by Collman.

hemoglobin (Hb) and myoglobin (Mb), respiratory metalloproteins with active sites containing an Fe-heme bound to an imidazole from a proximal histidine residue within the protein. These proteins reversibly bind O_2 to the Fe center to generate an Fe-O_2 adduct stabilized by H-bonding interactions. Synthetic porphyrins had previously been used to generate Fe–O_2 adducts, however these required decreased temperatures as the thermodynamic end-point of Fe–O_2 species is the formation of Fe^{III}–O–Fe^{III} dimeric species. To prevent formation of these oxido-bridged dimers, Collman developed a synthetic porphyrin ligand, called a picket-fence porphyrin, with pendant pyvalamide functional groups to form a "fence" on one face of the porphyrin ligand (Figure 1-2). The other face was open to bind a methyl-imidazole to an Fe^{II} center to replicate the primary coordination sphere of Mb. Using the sterically hindered imidazole was vital as the methyl group pulled the Fe center slightly out of the plane of the four nitrogen donors of the porphyrin ligand preventing a second 2-methyl-imidazole from binding to the Fe center. Collman was able to show that the reversible binding of O_2 was possible and the Fe–O_2 adduct could be stabilized under ambient temperatures such that the structure from X-ray diffraction (XRD) could be determined. This work elegantly demonstrated that careful control of the primary coordination sphere and secondary sphere interactions could effectively reproduce the chemistry of metalloprotein systems.

Recently, advancements have been made to incorporate not only static H-bonding groups and steric interactions like those already discussed, but now incorporate functional groups with the potential to perform dynamic interactions with reactive species bound to the metal center. For example, the Mayer group has presented dramatic increases in the rate and selectivity of electrocatalytic O_2 reduction to water by Fe tetra-arylporphyrin complexes (Figure 1-3).[44–46] The porphyrin ligands were decorated with proton delivery functional groups, in this case carboxylic acids and pyridine, to promote reduction of O_2 to water rather than hydrogen peroxide. These

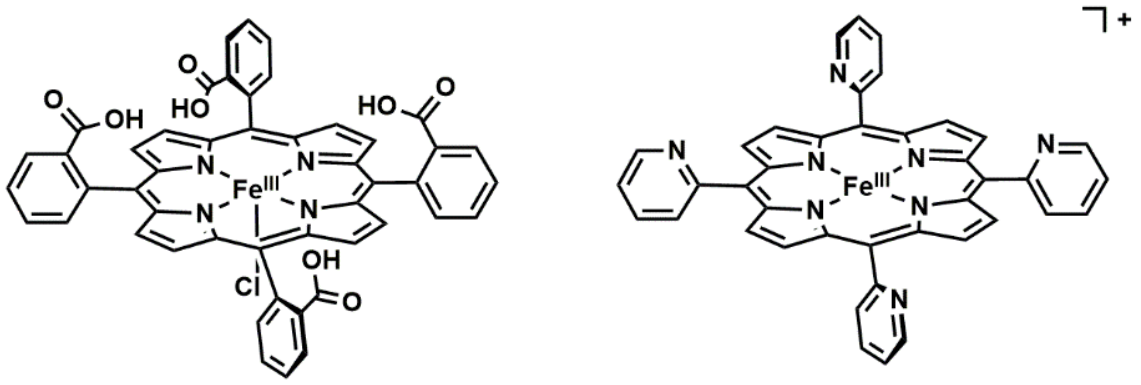

Figure 1-3. Two of the tetra-arylporphyrin Fe complexes used by Mayer to study the effect of proton relays on the electrocatalytic reduction of O_2 to water.

carboxylic acid and pyridine groups were most effective when oriented towards the Fe center by appending them in the ortho position of the aryl rings on the porphyrin. Therefore, the proposed function was to facilitate proton transfer to intermediate species generated during the reduction of O_2 such as peroxido, oxido, and hydroxido species.

Another excellent example of the incorporation of dynamic, pendant functional groups in the secondary coordination sphere of a metal complex comes from the DuBois group. Nickel complexes were synthesized containing a diphosphine ligand with pendant amines positioned in the secondary coordination sphere (Figure 1-4).[47–49] The role of the pendant amines was to serve

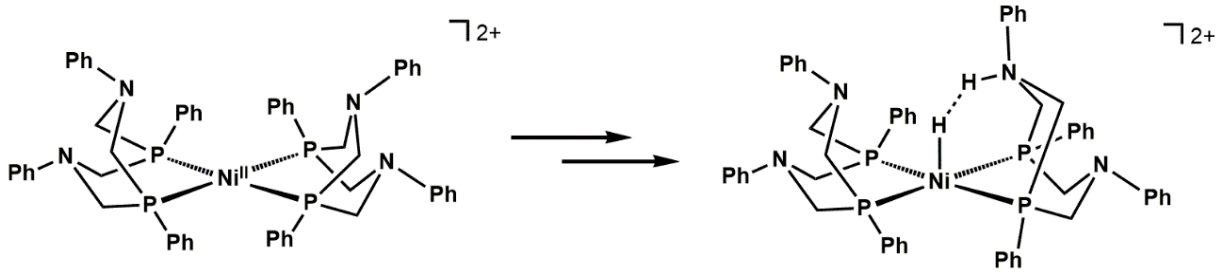

Figure 1-4. Catalyst for electrocatalytic H_2 production developed by Dubois. Pendant amine functional groups are proposed to shuttle protons to the metal center as depicted by the proposed intermediate to the right.

as proton relays to shuttle protons to and from the Ni center. This system has been shown to perform incredibly efficiently, with a greater than 100,000 s^{-1} turnover frequency for electrocatalytic H_2 production.

The Gilbertson group has recently reported the synthesis of a series of Fe complexes using an asymmetric pyridinediimine ligand (PDI) that allows for simple modifications to incorporate a variety of secondary sphere interactions. The ligand exerts both a passive, steric influence to

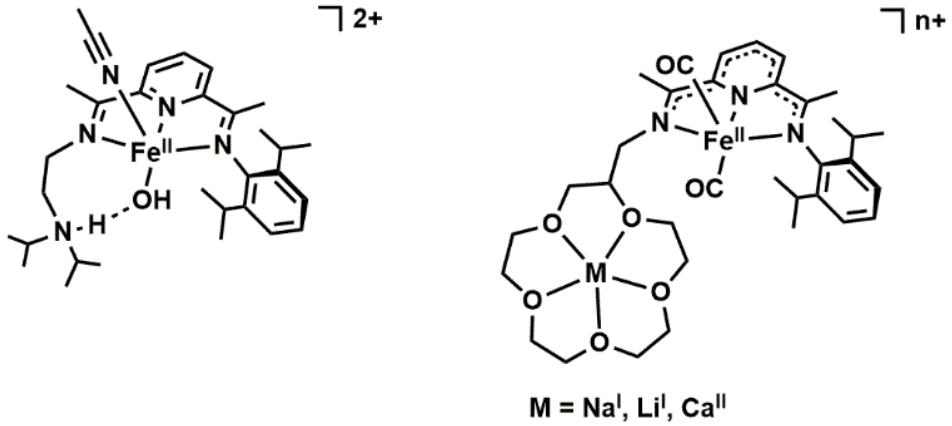

Figure 1-5. Synthetic PDI complexes developed by Gilbertson that contain pendant functional groups capable of dynamically interacting with the metal complex either by proton transfer, H-bonding, or sequestering Lewis acidic metal ions.

prevent dimerization by using a di-isopropylphenyl group on one of the imine arms, and an active functional group on the other imine arm. The pendant, interactive functional groups examined were either a tri-alkyl amine or a crown ether (Figure 1-5).[50–53] The amine has been shown to stabilize a terminal hydroxido ligand but could also be envisioned to serve the role of a proton relay to and from the metal center under the proper conditions. The latest addition to this series of PDI ligands used a 15-crown-5 ether appended to an imine arm to bind redox inactive metal ions, in particular Na^{I}, Li^{I}, or Ca^{II} ions. While this report is not the first example of a crown ether appended to the ligand of a metal complex, it is a promising result that may lead to informative chemistry relevant to biological water oxidation.

Previous Work in the Borovik Group

The focus of the Borovik group for over 15 years has been the manipulation and utilization of H-bonding to stabilize reactive species.[7,31,54] The ligands developed in the Borovik group use a tripodal, tetradentate nitrogen chelate with H-bonding functional groups that surround a single

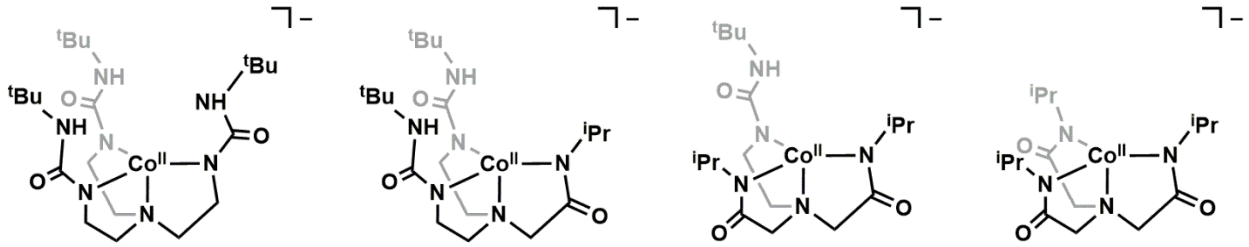

Figure 1-6. Synthetic Co complexes developed in the Borovik lab to examine the effect of varying the degree of H-bonding on the reactivity towards O_2.

open coordination site on the transition metal center. The secondary sphere interactions have been shown to greatly influence the chemistry of metal complexes in O_2 reduction reactions. One particular report directly explored the influence of varying the number of H-bond donors, from zero to three, in the O_2 reactivity of Co^{II} complexes and stability of the corresponding Co^{III}-hydroxido complexes (Figure 1-6).[7,31,55] The complexes containing three or two intramolecular H-bond donors reacted with half an equivalent of O_2 to generate terminal Co^{III}-hydroxido complexes. In contrast, the complex with a single intramolecular H-bond donor required an excess of O_2 and the complex with zero intramolecular H-bonds did not react with O_2 under any conditions examined. In addition, the stability of the generated Co^{III}-hydroxido complexes increased with increasing number of intramolecular H-bonds. The $[H_3buea]^{3-}$ ligand, in addition to producing the most stable Co^{III}-hydroxido complex in this study, has provided a multitude of stable M-oxido and M–hydroxido complexes. The ligand design principles exemplified by $[H_3buea]^{3-}$ provided the first examples of crystallographically characterized Mn^{III}-oxido and Fe^{III}-

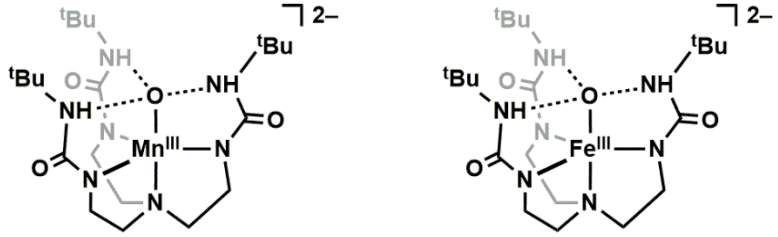

Figure 1-7. Isostructural Mn^{III}-oxido and Fe^{III}-oxido complexes isolated and characterized by the Borovik lab that demonstrate the stabilizing effect of multiple H-bonds.

oxido complexes (Figure 1-7).[56–58] The remarkable stability of these complexes was attributed to the steric protection from the *tert*-butyl groups and stabilization of the oxido ligand by the rigid, H-bonding cavity.

The incorporation of static H-bonds is extremely effective in stabilizing reactive species within transition metal complexes, but with increased stability often comes limited reactivity. Instead, use of a more dynamic secondary sphere by incorporating functional groups that can serve diverse functions such as a proton relay similar to what has been reported by Mayer and DuBois discussed above or secondary binding site for additional metal ions or substrates demonstrated by Gilbertson. To this end, a new ligand, $[H_2bupa]^{2-}$, was developed containing both intramolecular H-bond donating and accepting groups in the form of urea N–H groups and an anionic amidate group that can serve to shuttle protons in or out of the secondary sphere.[59,60] This ligand proved effective in the catalytic reduction of O_2 to water with modest turnover using

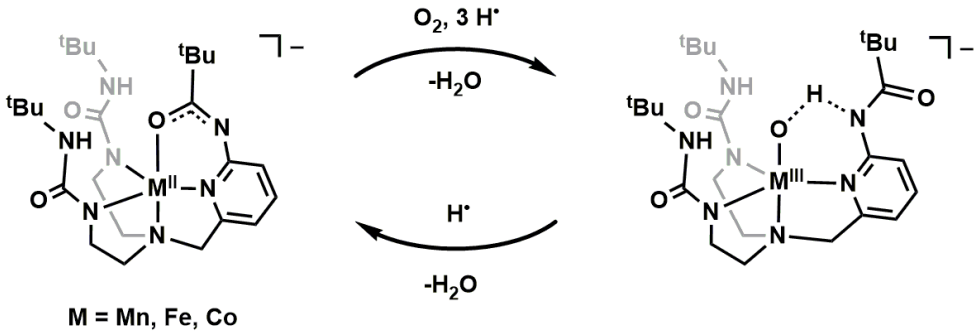

Figure 1-8. Catalytic reduction of O_2 by a $[M^{II}H_2bupa]^-$ complex developed in the Borovik lab that uses a pendant amidate functional group as a proton relay.

a sacrificial hydrogen-atom source (Figure 1-8). It was proposed that the amidate group was capable of not only facilitating proton transfer into and out of the complex, but can also rotate to position the carbonyl oxygen towards the metal ion and displace a bound ligand to drive the catalytic cycle back to the starting complex. This ligand system has provided the only example of catalysis reported by the Borovik lab to date and demonstrates the potential to convert a ligand

that stabilizes metal complexes to a catalytic system through straightforward alteration of the secondary coordination sphere.

Recent efforts in the Borovik lab have focused on changing the polarization of the H-bonding cavity by synthesizing new ligands with H-bond accepting groups rather than H-bond donating groups. The first of these ligands, $[MST]^{3-}$, contains the same tripodal, tetradentate platform with sulfonamide functional groups in place of urea or amide groups. This ligand showed reduced reactivity with O_2 in the absence of Lewis acidic counter cations.[61,62] However, the addition of the crown ether adducts of Lewis acidic metal ions such as Ca^{II}, Sr^{II}, and Ba^{II} ions dramatically accelerated the rate of O_2 reduction. The sulfonamide oxygens were shown to bind

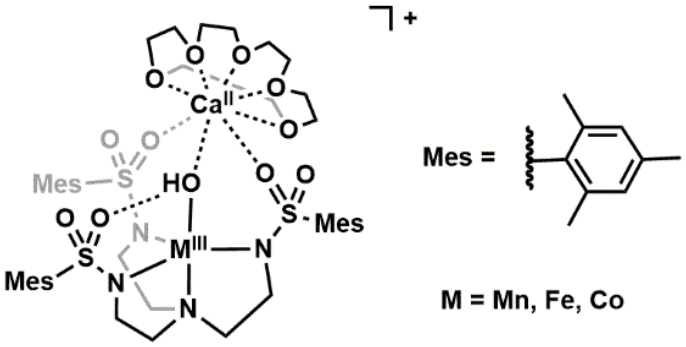

Figure 1-9. An example from the Borovik lab of a M^{III}-hydroxido complex generated by the reduction of O_2 by a M^{II} precursor with Ca^{II} bound in the secondary coordination sphere.

the secondary metal ions to generate heterobimetallic M^{III}-hydroxido complexes with a crown ether "capping" the complex (Figure 1-9). A limitation of this ligand system has been the higher reduction potentials of the metal complexes, prohibiting the generation of metal ions with oxidation states above the 3+.

Overview of the Remaining Chapters

The research described in this thesis focuses around the chemistry of high valent metal-oxido and –hydroxido complexes of Fe and Mn. The ligands $[H_3buea]^{3-}$ and $[H_2bupa]^{3-}$ are of primary interest and in some instances the reactivity of similar metal complexes of each ligand are often compared to one another.

Research in Chapter 2. The protonation and oxidation of the previously reported high valent Fe^{IV}-oxido complex, $[Fe^{IV}H_3buea(O)]^-$ was examined.[63,64] It was shown that a new Fe^{IV} species, assigned to $[Fe^{IV}H_3buea(O)(H)]$, was generated by either the addition of acid or oxidant to $[Fe^{IV}H_3buea(O)]^-$ at low temperatures (Figure 1-10). The protonation of $[Fe^{IV}H_3buea(O)]^-$ was found to be reversible, as the addition of base regenerated the starting complex. Characterization of the $[Fe^{IV}H_3buea(O)(H)]$ complex was conducted using standard spectroscopic techniques such as UV-vis and Mössbauer spectroscopies and was distinct from the $[Fe^{IV}H_3buea(O)]^-$ starting complex. In addition, the relatively new technique, nuclear resonance vibrational spectroscopy (NRVS) was used to probe the Fe-ligand bonds, in particular the vibration associated with the

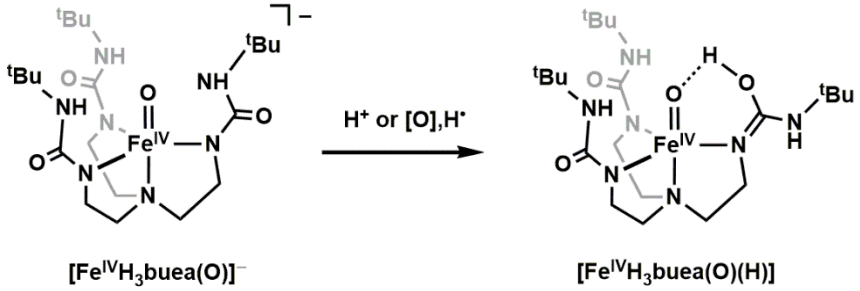

Figure 1-10. Generation of a protonated Fe^{IV}-oxido complex by addition of acid or oxidant to an Fe^{IV}-oxido precursor.

Fe–O bond. The Fe–O bond vibration was found to be identical within experimental error to the $[Fe^{IV}H_3buea(O)]^-$ complex, however the other Fe-ligand vibrations were dramatically changed. These data suggested a major change in the coordination environment of the protonated complex. Density functional theory (DFT) calculations determined that the lowest energy structure places the newly added proton onto a carbonyl of the $[H_3buea]^{3-}$ ligand, generating an isourea tautomer, which then rotates to hydrogen bond to the oxido ligand. The isourea can better explain the spectroscopic changes observed between $[Fe^{IV}H_3buea(O)(H)]$ and $[Fe^{IV}H_3buea(O)]^-$. Finally, the oxidation of $[Fe^{IV}H_3buea(O)]^-$ was carried out in the presence of substituted phenols to provide evidence for a transient [Fe^{V}-oxido] species. Oxidized phenolic products were detected in the final

reaction mixture along with spectroscopic characterization of the [$Fe^{IV}H_3$buea(O)(H)] complex. This chemistry is reminiscent of that observed in the cytochrome P450 enzymes where an Fe^{IV}-hydroxido complex is produced from what can be considered as the oxidizing equivalent of an Fe^{V}–oxido species.

Research in Chapter 3. A previous report described the synthesis of [$Fe^{IV}H_3$buea(O)]$^-$ from either the corresponding [$Fe^{III}H_3$buea(OH)]$^-$ or [$Fe^{III}H_3$buea(O)]$^{2-}$ complexes by the addition of $[FeCp_2]^+$ (Figure 1-11).[63] Despite the clean conversion in *N,N*-dimethylformamide (DMF), the isolated yield of K[$Fe^{IV}H_3$buea(O)] from addition of $[FeCp_2]^+$ to [$Fe^{III}H_3$buea(OH)]$^-$ in acetonitrile (MeCN) was substantially lower than the spectroscopic yield. In this chapter, the proton-coupled oxidation was examined further in order to understand the differences in yield between solvents

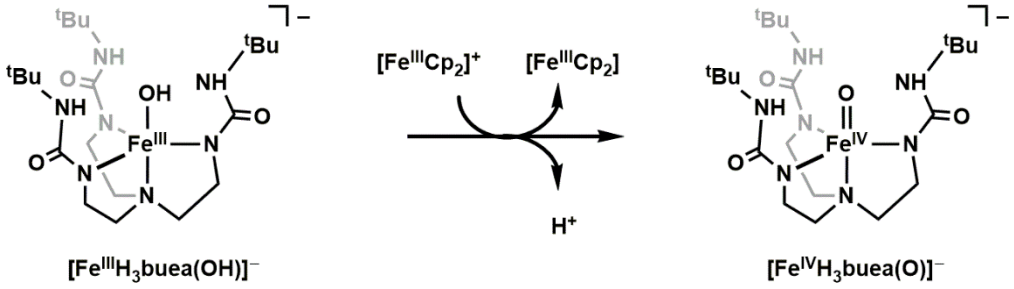

Figure 1-11. The oxidation of [$Fe^{III}H_3$buea(OH)]$^-$ by $[FeCp_2]^+$ to generate the corresponding [$Fe^{IV}H_3$buea(O)]$^-$ in a proton-coupled oxidation reaction.

and the species responsible for proton transfer during the reaction. A new spectroscopic signature could be observed when the oxidation of [$Fe^{III}H_3$buea(OH)]$^-$ by $[FeCp_2]^+$ in propionitrile (EtCN) at low temperatures. The same spectroscopic signature could be generated by the protonation of [$Fe^{III}H_3$buea(OH)]$^-$. Addition of [$Fe^{III}H_3$buea(OH)]$^-$ to a solution of [$Fe^{IV}H_3$buea(O)(H)] generated the same species along with a detectable amount of [$Fe^{IV}H_3$buea(O)]$^-$, demonstrating that under the reaction conditions used for bulk isolation of K[$Fe^{IV}H_3$buea(O)], the [$Fe^{III}H_3$buea(OH)]$^-$ complex is a sufficient base to accept the proton. This result helps to explain the low yield of

K[$Fe^{IV}H_3$buea(O)] reported because as the reaction progresses, the starting complex, [$Fe^{III}H_3$buea(OH)]$^-$, is consumed resulting in a maximum theoretical yield of ~50%. Finally, addition of a slight excess of a non-nucleophilic base during the oxidation of [$Fe^{III}H_3$buea(OH)]$^-$ by [$FeCp_2$]$^+$ in either MeCN or EtCN resulted in an approximate doubling of the yield of [$Fe^{IV}H_3$buea(O)]$^-$.

Research in Chapter 4. The DFT calculated structure of [$Fe^{IV}H_3$buea(O)(H)] suggested that the [H_3buea]$^{3-}$ ligand is capable of being protonated to generate a thermally unstable complex. Because of this, the premise that the incorporation of a basic site in the secondary coordination sphere would improve the stability of the analogous complex was tested. The [H_2bupa]$^{3-}$ ligand was chosen due to the basic amidate functional group positioned within the secondary coordination sphere and the changes in the primary coordination sphere best mimicking that determined by DFT for [$Fe^{IV}H_3$buea(O)(H)]. It was found that [$Fe^{III}H_2$bupa(O)(H)]$^-$ could be

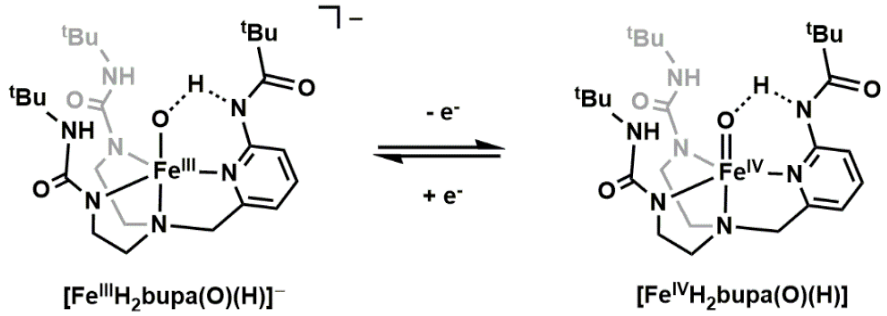

Figure 1-12. The reversible oxidation of an Fe^{III}-oxido/hydroxido hybrid complex. Reversibility is attributed to the basic site in the secondary coordination sphere.

generated by the addition of the oxygen-atom transfer agent, iodosylbenzene (PhIO), to the [$Fe^{II}H_2$bupa]$^-$ starting complex. Characterization of [$Fe^{III}H_2$bupa(O)(H)]$^-$ by NRVS showed that the Fe–O bond vibration is between those of the related [$Fe^{III}H_3$buea(O)]$^{2-}$ and [$Fe^{III}H_3$buea(OH)]$^-$ complexes, indicating that the complex is best described as an Fe^{III}-oxido/hydroxido "hybrid" just like the previously reported [$Mn^{III}H_2$bupa(O)(H)]$^-$ complex with the proton being delocalized between the oxygen ligand bound to Fe and the anionic amidate. Oxidation of

$[Fe^{III}H_2bupa(O)(H)]^-$ by the addition of $[FeCp_2]^+$ at decreased temperatures resulted in the formation of a new Fe^{IV} complex assigned to $[Fe^{IV}H_2bupa(O)(H)]$ (Figure 1-12). The spectroscopic and vibrational spectroscopic properties of $[Fe^{IV}H_2bupa(O)(H)]$ differed only slightly from $[Fe^{IV}H_3buea(O)(H)]$ as discussed in Chapter 2, indicating a similar coordination environment between the two complexes. In addition, the Fe^{III}/Fe^{IV} redox process was made chemically reversible by the incorporation of the basic site in the secondary coordination sphere.

Research in Chapter 5. A series of Mn–oxido complexes were examined for their reactivity towards the redox inactive Lewis acidic Ca^{II}, Sr^{II}, and Sc^{III} ions.[57,65–67] Treatment of $[Mn^{V}H_3buea(O)]$ with an excess of either Sc^{III} or Ca^{II} ions resulted in the generation of a Mn^{IV}

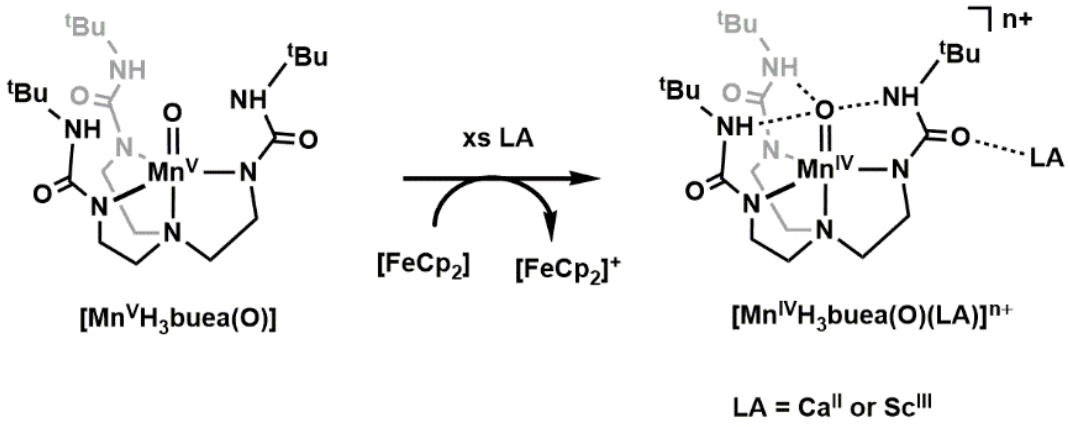

Figure 1-13. Electron transfer from ferrocene to $[Mn^{V}H_3buea(O)]$ induced by the addition of an excess of Lewis acids (LA).

complex, proposed to be $[Mn^{IV}H_3buea(O)(Sc)]^{2+}$ and $[Mn^{IV}H_3buea(O)(Ca)]^+$, by the transfer of an electron from $[FeCp_2]$ already in solution (Figure 1-13). Addition of a large excess of Sr^{II} ions, upwards of 400 equivalents, to $[Mn^{V}H_3buea(O)]$ failed to fully reduce the Mn^{V} complex. The same Mn^{IV} species could be independently generated by the addition of an excess of each Lewis acid to $[Mn^{IV}H_3buea(O)]^-$. Addition of Ca^{II}, Sr^{II}, or Sc^{III} ions to $[Mn^{III}H_3buea(O)]^{2-}$ generated what was assigned to the Lewis acid adducts of the Mn^{III}-oxido complex. Finally, the Mn^{III} and Mn^{IV} adducts of Ca^{II} and Sr^{II} could be interconverted by the addition of either oxidant or reductant; however

while $[Mn^{IV}H_3buea(O)(Sc)]^{2+}$ could be reduced to the corresponding Mn^{III} complex, the reverse of this reaction was not possible under the conditions examined.

Research in Chapter 6. The Mn complexes of the $[H_2bupa]^{3-}$ ligand were studied in an effort to provide evidence of O–O bond formation by a single Mn complex in the presence of Ca^{II} ions

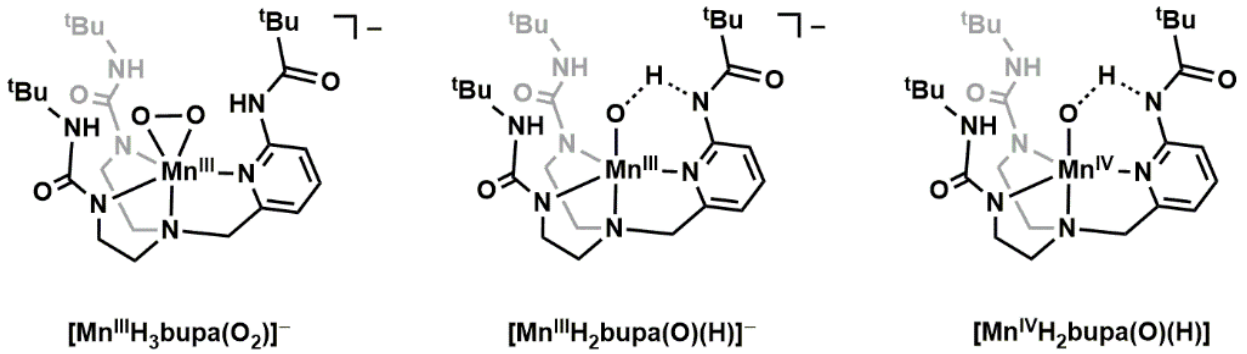

Figure 1-14. A series of Mn complexes used to study the effects of the addition of the Lewis acid, Ca^{II} in the presence of base towards O–O bond formation.

(Figure 1-14). Previously reported was the synthesis and characterization of $[Mn^{III}H_3bupa(O_2)]^-$; this complex was used as a spectroscopic handle for O–O bond formation for its unique parallel-mode electron paramagnetic resonance (EPR) signal.[59] The previously characterized $[Mn^{III}H_2bupa(O)(H)]^-$ complex was oxidized to $[Mn^{IV}H_2bupa(O)(H)]$, which was identified by EPR spectroscopy. The treatment of this complex with both Ca^{II} ions and DBU generated a distinct Mn^{IV} signal in perpendicular mode EPR spectroscopy and a Mn^{III} signal in parallel mode EPR spectroscopy. This new signal was only generated when both Ca^{II} ions and DBU were present. The Mn^{III} EPR signal is surprisingly similar to $[Mn^{III}H_3bupa(O_2)]^-$. The identity of the new Mn^{III} EPR signal is yet unknown and these studies represent only preliminary investigations for O–O bond formation.

References

(1) Poulos, T. L. *Chem. Rev.* **2014**, *114*, 3919–3962.
(2) Bassan, A.; Blomberg, M. R. A.; Borowski, T.; Siegbahn, P. E. M. *J. Inorg. Biochem.* **2006**, *100*, 727–743.

(3) Tommos, C.; Babcock, G. T. *Acc. Chem. Res.* **1998**, *31*, 18–25.
(4) Stone, K. L.; Borovik, A. S. *Curr. Opin. Chem. Biol.* **2009**, *13*, 114–118.
(5) Dawson, J. *Science* **1988**, *240*, 433–439.
(6) Capaldi, R. A. *Annu. Rev. Biochem.* **1990**, *59*, 569–596.
(7) Shook, R. L.; Borovik, A. S. *Inorg. Chem.* **2010**, *49*, 3646–3660.
(8) Shaw, W. J. *Catal. Rev.* **2012**, *54*, 489–550.
(9) Costas, M.; Mehn, M. P.; Jensen, M. P.; Que, L. *Chem. Rev.* **2004**, *104*, 939–986.
(10) Casadei, C. M.; Gumiero, A.; Metcalfe, C. L.; Murphy, E. J.; Basran, J.; Concilio, M. G.; Teixeira, S. C. M.; Schrader, T. E.; Fielding, A. J.; Ostermann, A.; Blakeley, M. P.; Raven, E. L.; Moody, P. C. E. *Science* **2014**, *345*, 193–197.
(11) Berggren, G.; Adamska, A.; Lambertz, C.; Simmons, T. R.; Esselborn, J.; Atta, M.; Gambarelli, S.; Mouesca, J.-M.; Reijerse, E.; Lubitz, W.; Happe, T.; Artero, V.; Fontecave, M. *Nature* **2013**, *499*, 66–69.
(12) Blasiak, L. C.; Vaillancourt, F. H.; Walsh, C. T.; Drennan, C. L. *Nature* **2006**, *440*, 368–371.
(13) Groves, J. T. *J. Inorg. Biochem.* **2006**, *100*, 434–447.
(14) Umena, Y.; Kawakami, K.; Shen, J.-R.; Kamiya, N. *Nature* **2011**, *473*, 55–60.
(15) Siegbahn, P. E. M. *Acc. Chem. Res.* **2009**, *42*, 1871–1880.
(16) Pantazis, D. A.; Ames, W.; Cox, N.; Lubitz, W.; Neese, F. *Angew. Chem. Int. Ed. Engl.* **2012**, *51*, 9935–9940.
(17) Suga, M.; Akita, F.; Hirata, K.; Ueno, G.; Murakami, H.; Nakajima, Y.; Shimizu, T.; Yamashita, K.; Yamamoto, M.; Ago, H.; Shen, J.-R. *Nature* **2014**, *517*, 99–103.
(18) Brudvig, G. W. *Philos. Trans. R. Soc. Lond. B. Biol. Sci.* **2008**, *363*, 1211–1218; discussion 1218–1219.
(19) Cox, N.; Pantazis, D. A.; Neese, F.; Lubitz, W. *Acc. Chem. Res.* **2013**, *46*, 1588–1596.
(20) Ferreira, K. N.; Iverson, T. M.; Maghlaoui, K.; Barber, J.; Iwata, S. *Science* **2004**, *303*, 1831–1838.
(21) Amin, M.; Vogt, L.; Szejgis, W.; Vassiliev, S.; Brudvig, G. W.; Bruce, D.; Gunner, M. R. *J. Phys. Chem. B* **2015**, *119*, 7366–7377.
(22) Yocum, C. *Coord. Chem. Rev.* **2008**, *252*, 296–305.
(23) Britt, R. D.; Suess, D. L. M.; Stich, T. A. *Proc. Natl. Acad. Sci.* **2015**, *112*, 201505223.
(24) Yano, J.; Walker, L. M.; Strickler, M. A.; Service, R. J.; Yachandra, V. K.; Debus, R. J. *J. Biol. Chem.* **2011**, *286*, 9257–9267.
(25) Stich, T. A.; Yeagle, G. J.; Service, R. J.; Debus, R. J.; Britt, R. D. *Biochemistry* **2011**, *50*, 7390–7404.
(26) Vogt, L.; Vinyard, D. J.; Khan, S.; Brudvig, G. W. *Curr. Opin. Chem. Biol.* **2015**, *25*, 152–158.
(27) Ono, T.; Rompel, A.; Mino, H.; Chiba, N. *Biophys. J.* **2001**, *81*, 1831–1840.
(28) Boussac, A.; Rappaport, F.; Carrier, P.; Verbavatz, J.-M.; Gobin, R.; Kirilovsky, D.; Rutherford, A. W.; Sugiura, M. *J. Biol. Chem.* **2004**, *279*, 22809–22819.
(29) Oyala, P. H.; Stich, T. A.; Debus, R. J.; Britt, R. D. *J. Am. Chem. Soc.* **2015**, 150617175123006.
(30) Pérez Navarro, M.; Ames, W. M.; Nilsson, H.; Lohmiller, T.; Pantazis, D. a; Rapatskiy, L.; Nowaczyk, M. M.; Neese, F.; Boussac, A.; Messinger, J.; Lubitz, W.; Cox, N. *Proc. Natl. Acad. Sci. U. S. A.* **2013**, *110*, 15561–15566.
(31) Lucas, R. L.; Zart, M. K.; Murkerjee, J.; Sorrell, T. N.; Powell, D. R.; Borovik, A. S. *J. Am. Chem. Soc.* **2006**, *128*, 15476–15489.
(32) Cook, S. A.; Borovik, A. S. *Acc. Chem. Res.* **2015**, *48*, 2407–2414.
(33) Borovik, A. S. *Acc. Chem. Res.* **2005**, *38*, 54–61.
(34) Werner, A. *Berichte der Dtsch. Chem. Gesellschaft* **1912**, *45*, 121–130.

(35) Werner, A. *Justus Liebig's Ann. der Chemie* **1912**, *386*, 1–272.
(36) Kamar, K. K.; Saha, A.; Goswami, S. *J. Chem. Sci.* **2002**, *114*, 339–346.
(37) Rakowski DuBois, M.; DuBois, D. L. *Chem. Soc. Rev.* **2009**, *38*, 62–72.
(38) MacBeth, C. E.; Gupta, R.; Mitchell-Koch, K. R.; Young, V. G.; Lushington, G. H.; Thompson, W. H.; Hendrich, M. P.; Borovik, A. S. *J. Am. Chem. Soc.* **2004**, *126*, 2556–2567.
(39) Blacquiere, J. M.; Pegis, M. L.; Raugei, S.; Kaminsky, W.; Forget, A.; Cook, S. A.; Taguchi, T.; Mayer, J. M. *Inorg. Chem.* **2014**, *53*, 9242–9253.
(40) Collman, J. P.; Gagne, R. R.; Halbert, T. R.; Marchon, J. C.; Reed, C. A. *J. Am. Chem. Soc.* **1973**, *95*, 7868–7870.
(41) Collman, J. P.; Brauman, J. I.; Doxsee, K. M.; Halbert, T. R.; Suslick, K. S. *Proc. Natl. Acad. Sci.* **1978**, *75*, 564–568.
(42) Collman, J. P.; Reed, C. A. *J. Am. Chem. Soc.* **1973**, *95*, 2048–2049.
(43) Collman, J. P.; Gagne, R. T.; Reed, C. A. *J. Am. Chem. Soc.* **1974**, *96*, 2629–2631.
(44) Rigsby, M. L.; Wasylenko, D. J.; Pegis, M. L.; Mayer, J. M. *J. Am. Chem. Soc.* **2015**, *137*, 4296–4299.
(45) Carver, C. T.; Matson, B. D.; Mayer, J. M. *J. Am. Chem. Soc.* **2012**, *134*, 5444–5447.
(46) Matson, B. D.; Carver, C. T.; Von Ruden, A.; Yang, J. Y.; Raugei, S.; Mayer, J. M. *Chem. Commun.* **2012**, *48*, 11100.
(47) Helm, M. L.; Stewart, M. P.; Bullock, R. M.; DuBois, M. R.; DuBois, D. L. *Science (80-.).* **2011**, *333*, 863–866.
(48) Ohagan, M.; Ho, M. H.; Yang, J. Y.; Appel, A. M.; Dubois, M. R.; Raugei, S.; Shaw, W. J.; Dubois, D. L.; Bullock, R. M. Proton delivery and removal in [Ni(PR2NR 22)2]2+ hydrogen production and oxidation catalysts. *Journal of the American Chemical Society*, 2012, *134*, 19409–19424.
(49) Wilson, A. D.; Newell, R. H.; McNevin, M. J.; Muckerman, J. T.; Rakowski DuBois, M.; DuBois, D. L. *J. Am. Chem. Soc.* **2006**, *128*, 358–366.
(50) Kendall, A. J.; Zakharov, L. N.; Gilbertson, J. D. *Inorg. Chem.* **2010**, *49*, 8656–8658.
(51) Delgado, M.; Ziegler, J. M.; Seda, T.; Zakharov, L. N.; Gilbertson, J. D. *Inorg. Chem.* **2016**, *55*, 555–557.
(52) Thammavongsy, Z.; LeDoux, M. E.; Breuhaus-Alvarez, A. G.; Seda, T.; Zakharov, L. N.; Gilbertson, J. D. *Eur. J. Inorg. Chem.* **2013**, *2013*, 4008–4015.
(53) Hartle, M. D.; Delgado, M.; Gilbertson, J. D.; Pluth, M. D. *Chem. Commun.* **2016**, *52*, 7680–7682.
(54) MacBeth, C. E.; Hammes, B. S.; Victor G. Young, J.; Borovik, A. S. *Inorg. Chem.* **2001**, *40*, 4733–4741.
(55) Lacy, D. C.; Mukherjee, J.; Lucas, R. L.; Day, V. W.; Borovik, A. S. *Polyhedron* **2013**, *52*, 261–267.
(56) Shirin, Z.; Hammes, B. S.; Young, V. G.; Borovik, A. S. *J. Am. Chem. Soc.* **2000**, *122*, 1836–1837.
(57) Gupta, R.; Borovik, A. S. *J. Am. Chem. Soc.* **2003**, *125*, 13234–13242.
(58) MacBeth, C. E.; Golombek, A. P.; Jr., V. G. Y.; Yang, C.; Kuczera, K.; Hendrich, M. P.; Borovik, A. S. *Science* **2000**, *289*, 938–941.
(59) Shook, R. L.; Gunderson, W. A.; Greaves, J.; Ziller, J. W.; Hendrich, M. P.; Borovik, A. S. *J. Am. Chem. Soc.* **2008**, *130*, 8888–8889.
(60) Shook, R. L.; Peterson, S. M.; Greaves, J.; Moore, C.; Rheingold, A. L.; Borovik, A. S. *J. Am. Chem. Soc.* **2011**, *133*, 5810–5817.
(61) Lacy, D.; Park, Y.; Ziller, J.; Yano, J.; Borovik, A. S. *J. Am. Chem. Soc.* **2012**, *134*,

17526−17535.
(62) Park, Y.; Cook, S.; Sickerman, N.; Sano, Y.; Ziller, J. W.; Borovik, A. S. *Chem. Sci.* **2013**, *4*, 717–726.
(63) Lacy, D. C.; Gupta, R.; Stone, K. L.; Greaves, J.; Ziller, J. W.; Hendrich, M. P.; Borovik, A. S. *J. Am. Chem. Soc.* **2010**, *132*, 12188–12190.
(64) Gupta, R.; Lacy, D. C.; Bominaar, E. L.; Borovik, A. S.; Hendrich, M. P. *J. Am. Chem. Soc.* **2012**, *134*, 9775–9784.
(65) Gupta, R.; Taguchi, T.; Lassalle-Kaiser, B.; Bominaar, E. L.; Yano, J.; Hendrich, M. P.; Borovik, A. S. *Proc. Natl. Acad. Sci. U. S. A.* **2015**, *112*, 5319–5324.
(66) Parsell, T. H.; Behan, R. K.; Green, M. T.; Hendrich, M. P.; Borovik, A. S. *J. Am. Chem. Soc.* **2006**, *128*, 8728–8729.
(67) Taguchi, T.; Stone, K. L.; Gupta, R.; Kaiser-Lassalle, B.; Yano, J.; Hendrich, M. P.; Borovik, A. S. *Chem. Sci.* **2014**, *5*, 3064.

Chapter 2

Generation and Characterization of a Protonated Monomeric, Non-Heme Fe^{IV}-Oxido Complex

Metal–oxido/hydroxido species are important classes of intermediates that are involved in a variety of oxidative transformations in biology.[1–3] The most well studied systems are produced from the activation of dioxygen or peroxide in heme enzymes. The paradigm systems are the cytochrome P450s (P450s), whose hydroxylase components have active sites that are composed of a single heme center and a hydrogen-bonding (H-bonding) network near the dioxygen binding site.[4] Many P450s promote the homolytic cleavage of unactivated C–H bonds, which is one of the most difficult chemical transformations due to the high bond strengths.[3,5] A common mechanistic proposal among P450s is that a high valent Fe–oxido intermediate is formed from the binding and subsequent activation of dioxygen, which then serves as the kinetically competent species in the oxidation of substrates.[5,6] Recent work by Green demonstrated the successful trapping of this transient intermediate in P450s (denoted Compound I) and has provided sufficient spectroscopic and kinetic evidence to definitively assign it as a high valent

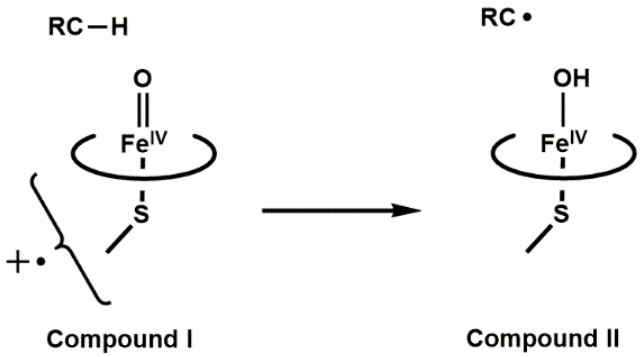

Scheme 2-1. The proposed mechanism for C–H bond cleavage by Compound I in P450s to generate Compound II. The ring denotes protoporphyrin IX.

Fe^{IV}–oxido(ligand radical) species.[7] The mechanism proposed for the reactivity of Compound I involves an initial C–H bond cleavage step leading to the generation of an Fe^{IV}–hydroxido species

and a carbon-based radical on the substrate (Scheme 2-1).[3] The Fe^{IV}–hydroxido species (Compound II) in P450s has taken on considerable importance with further work by Green who suggested that the axial coordination of a thiolate ligand both lowers the reduction potential and increases the Fe^{IV}–hydroxido pK_a value to ~12 in Compound II. The attenuation of the reduction potential of Compound I and pK_a of Compound II directs oxidation away from neighboring tyrosine and tryptophan residues that not only inhibits destruction of the protein but also facilitates C–H bond cleavage of the bound substrate and solidifies the importance of both Fe^{IV}-oxido and hydroxido complexes.[8]

Synthetic systems have been developed to further the understanding of these mechanistic connections; considerable progress has been made in preparing high valent Fe–oxido complexes with different coordination geometries and spin states that have been used to probe the reactivity with substrates containing C–H bonds.[9–12] In addition, a few examples of non-heme Fe^{V}–oxido complexes have been reported, but their reactivity and structural properties have yet to be fully developed.[13–15] Less is known about protonated Fe^{IV}–oxido species, but reports have suggested that their importance extends beyond P450s to non-heme Rieske-type monooxygenases and some synthetic systems.[16,17] However direct experimental evidence for protonation of non-heme, Fe^{IV}–oxido complexes is lacking and no complexes have been isolated in synthetic constructs.[18–20] While Que has reported the reversible protonation of a $[Fe^{IV}_2O_3]$ unit relevant to particulate

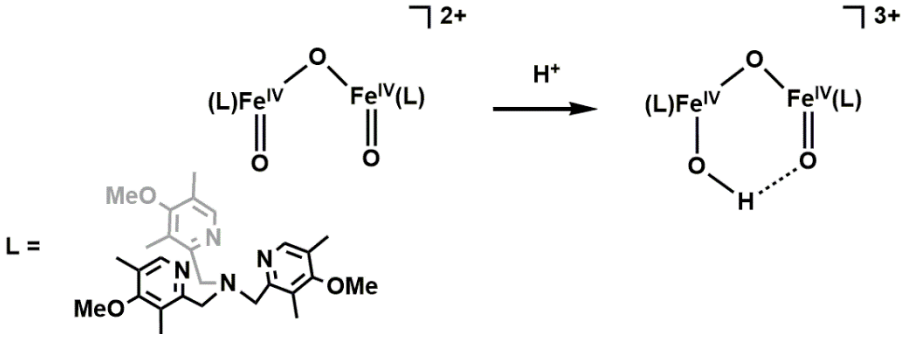

Figure 2-1. The proposed site of protonation upon addition of acid to a dinuclear, $[Fe^{IV}_2O_3]$ unit to generate the putative mixed Fe^{IV}-oxido/Fe^{IV}-hydroxido complex.

methane monooxygenase (pMMO) (Figure 2-1), evidence for the exact location of the proton was not presented and only postulated to be on an oxygen atom.[21] This represents one of the only examples of reversible protonation of a high valent Fe–oxido complex. One key structural difference between protein active sites and synthetic systems that contributes to the difficulty in preparing such a species is the absence of vital intramolecular H-bonding networks that assist in regulating the protonation state of Fe–oxido species.

The Borovik group has previously generated a series of synthetic high valent metal–oxido species supported by the $[H_3buea]^{3-}$ ligand (Scheme 2-2).[11,22–26] Included in this series is the high-spin, mononuclear Fe^{IV}–oxido complex, $[Fe^{IV}H_3buea(O)]^-$, which has local C_3 symmetry that is enforced by the strong nitrogen donors of the deprotonated urea groups.[11,27] In addition, the $[H_3buea]^{3-}$ ligand promotes the formation of intramolecular H-bonds and provides steric protection by the incorporation of bulky *tert*-butyl groups. These features combined regulate the secondary sphere around the iron center to generate one of the most stable, high-spin Fe^{IV}-oxido complexes reported. The remarkable stability of the $[Fe^{IV}H_3buea(O)]^-$ complex allows for further reactivity studies in an attempt to address the viability of generating a true Fe^{IV}-OH complex.

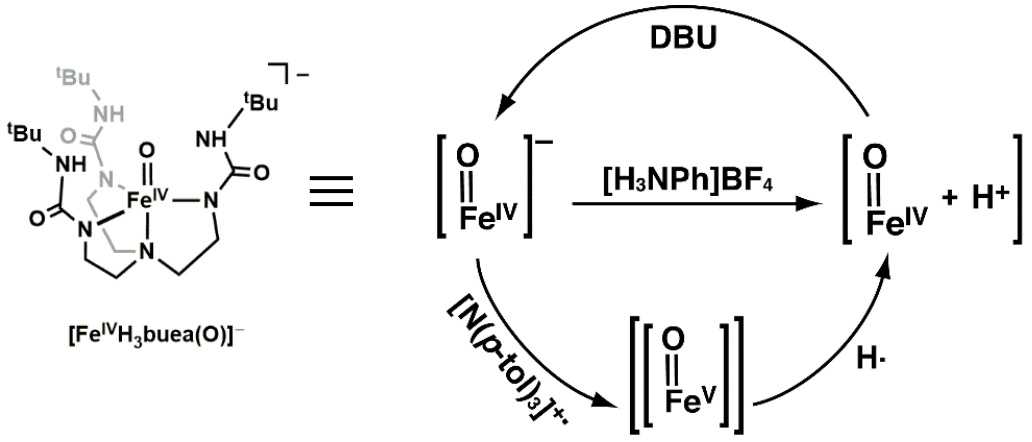

Scheme 2-2. Depiction of the structure of $[Fe^{IV}H_3buea(O)]^-$ and summary of reactions reported in this chapter.

Following the initial observation of the protonated congener of $[Fe^{IV}H_3buea(O)]^-$ by Dr. David Lacy,[28] the complex has now been generated by the addition of a single equivalent of acid and its physical properties have been characterized. Moreover, the same species is obtained via oxidation of **2**, implicating the formation of an Fe^{V}–oxido species that reacts by formal hydrogen-atom abstraction to generate a protonated Fe^{IV}–oxido complex in a manner similar to the conversion of Compound I to Compound II in P450s.

Results and Discussion

Protonation of $[Fe^{IV}H_3buea(O)]^-$ at Low Temperatures. The starting point of this study was $[Fe^{IV}H_3buea(O)]^-$, which has been previously prepared and reported.[11] Based on the thermodynamic properties of the family of Fe-oxido/hydroxido complexes generated using the $[H_3buea]^-$ ligand, it was calculated that the pK_a value of the conjugate acid of $[Fe^{IV}H_3buea(O)]^-$

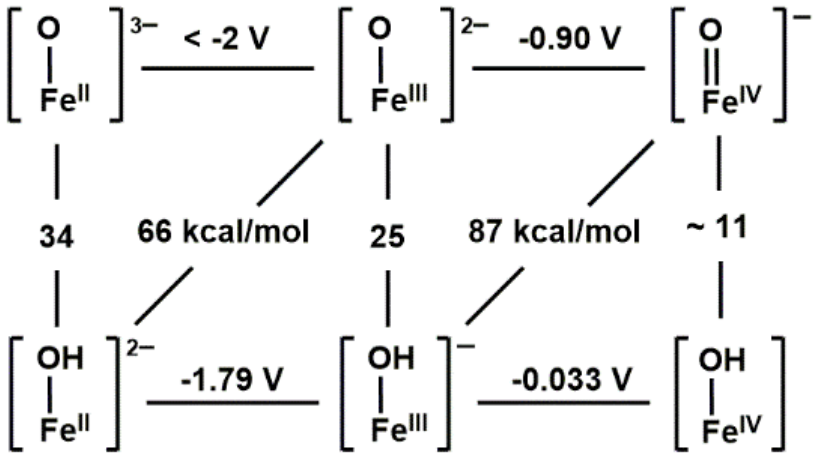

Figure 2-2. Thermodynamic square scheme of the Fe complexes of $[H_3buea]^{3-}$ where the horizontal direction represents reduction potentials vs $[FeCp_2]^{0/+}$, vertical direction represents pK_a of the hydroxido ligand, and diagonal represents the BDE_{OH}.

should be ~11 in DMSO (Figure 2-2).[29] Consistent with this prediction, treatment of $[Fe^{IV}H_3buea(O)]^-$ with one equivalent of $[H_3NPh]BF_4$ (pK_a = 5.2 in THF, rt)[30] at -80˚C in THF produced a new species that has been assigned as the protonated analog $[Fe^{IV}H_3buea(O)(H)]$ (Scheme 2-2). Spectrophotometric monitoring of the reaction showed loss of the characteristic

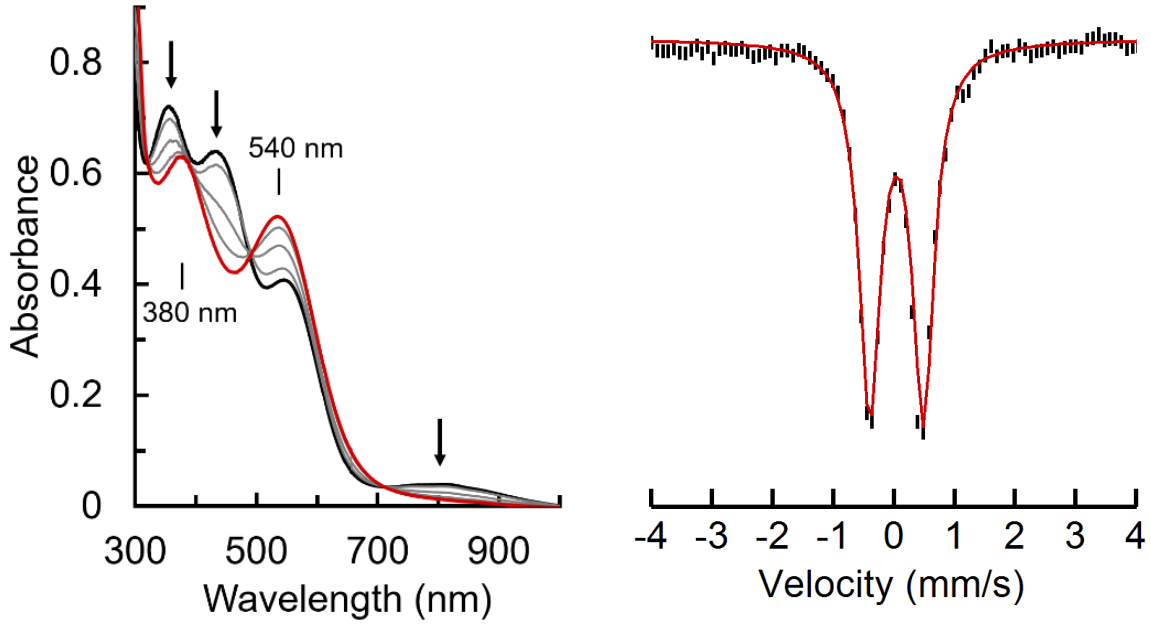

Figure 2-3. Electronic absorbance spectra (left) for the protonation of $[Fe^{IV}H_3buea(O)]^-$ (black) to $[Fe^{IV}H_3buea(O)(H)]$ (red) via sequential addition of 0.25, 0.50, 0.75, and 1.0 equiv of $[H_3NPh]^+$ at –80°C in THF. Mössbauer spectrum (right) of $[Fe^{IV}H_3buea(O)(H)]$ recorded at 4 K in THF. Red line is the least-square fit of the experimental data with linewidth of 0.37 mm/s.

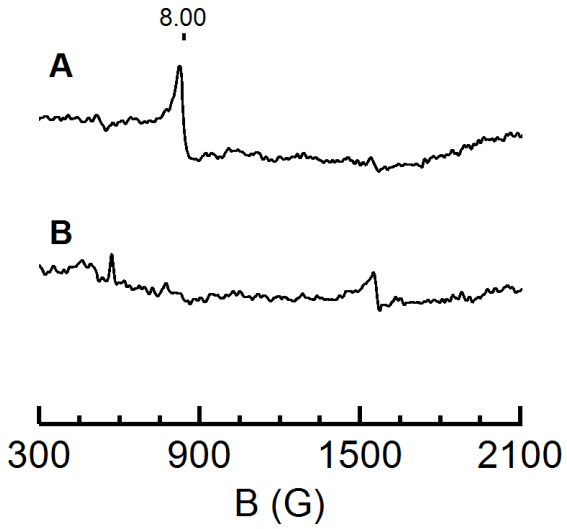

Figure 2-4. Parallel mode EPR spectra of (A) $[Fe^{IV}H_3buea(O)]^-$ and (B) $[Fe^{IV}H_3buea(O)]^-$ treated with one equivalent of $[H_3NPh]^+$. Spectra collected in frozen THF at 11K.

bands of $[Fe^{IV}H_3buea(O)]^-$ at λ_{max} = 350, 430, 530, and 810 nm with new peaks for $[Fe^{IV}H_3buea(O)(H)]$ at λ_{max} = 380 and 540 nm; this conversion exhibited isosbestic behavior upon incremental addition of the acid to a solution of $[Fe^{IV}H_3buea(O)]^-$ with isosbestic points observed at λ = 320, 490 and 710 nm (Figure 2-3). Monitoring this reaction using electron paramagnetic resonance (EPR) spectroscopy showed the loss of the signal from $[Fe^{IV}H_3buea(O)]^-$, however, there was no new signal that could be associated with $[Fe^{IV}H_3buea(O)(H)]$ (Figure 2-4). Addition of acid to $[Fe^{IV}H_3buea(O)]^-$ showed a commensurate change in the Mössbauer parameters from δ = 0.04 mm/s and ΔE_Q = 0.50 mm/s for $[Fe^{IV}H_3buea(O)]^-$ to δ = 0.04 mm/s and ΔE_Q = 0.87 mm/s for $[Fe^{IV}H_3buea(O)(H)]$ (Figure 2-3) consistent with an S = 2 spin ground state. This reaction can also be performed with other acids at -80˚C in THF: complete formation of $[Fe^{IV}H_3buea(O)(H)]$ was observed with 1.5 equiv of $[NH(CH_2CH_3)_3]BF_4$ (pK_a = 12.5 in THF, rt) but no reaction was found when $[Fe^{IV}H_3buea(O)]^-$ was treated with one equivalent of pyrrolidinium tetrafluoroborate (pK_a = 13.5 in THF, rt).[30] These observations suggest an approximate bracketing of the pK_a value for $[Fe^{IV}H_3buea(O)(H)]$ between 11-13, which is consistent with our previous thermodynamic predictions for the pK_a value in DSMO.

The vibrational properties of $[Fe^{IV}H_3buea(O)(H)]$ were evaluated using nuclear resonance vibrational spectroscopy (NRVS) in collaboration with the Hendrich lab (CMU). NRVS is a relatively new, synchrotron-based vibrational spectroscopy technique. Unlike other vibrational techniques such as Raman or IR spectroscopies, NRVS is selective for vibrations involving only a Mössbauer-active nucleus, such as ^{57}Fe, and therefore provides the complete set of vibrations that for the Fe atom. Analysis of a sample that contained 80% of $[^{57}Fe^{IV}H_3buea(^{16}O)(H)]$, determined by Mössbauer spectroscopy, displayed a NRVS spectrum with a prominent peak at 800 cm^{-1} that is assigned to the Fe–O vibration (Figure 2-5). This band shifts to 764 cm^{-1} in the (^{57}Fe-^{18}O) isotopomer which is expected based on an Fe–O diatomic harmonic oscillator model that predicts

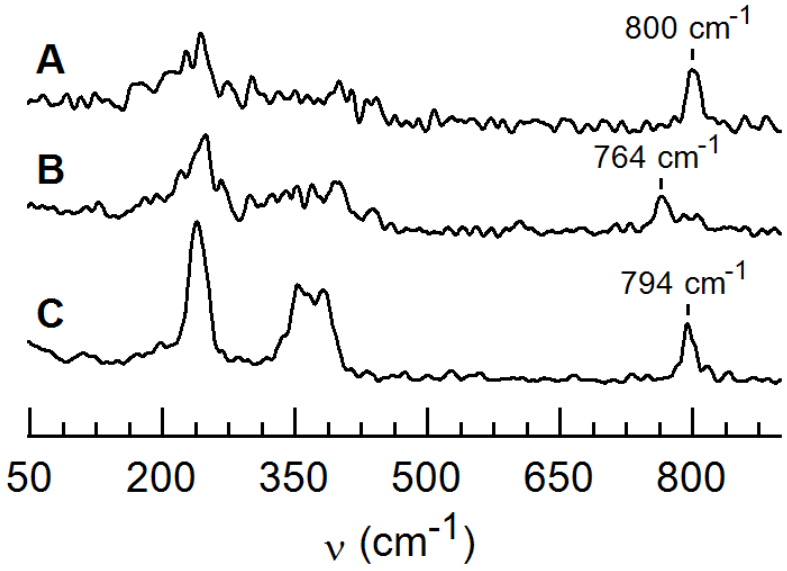

Figure 2-5. NRVS spectra for (A) the reaction of a solution of [$^{57}Fe^{IV}H_3buea(^{16}O)]^-$ with one equivalent of $[H_3NPh]^+$, (B) the reaction of a solution of [$^{57}Fe^{IV}H_3buea(^{18}O)]^-$ with one equivalent $[H_3NPh]^+$, and (C) a solution of [$^{57}Fe^{IV}H_3buea(^{16}O)]^-$. Solutions were 10 mM in THF. Labeled peak assigned to the Fe—O vibration.

a difference of 36 cm^{-1}. This vibrational feature does not originate from $[Fe^{IV}H_3buea(O)]^-$, which only represents ~10% of the sample as determined by Mössbauer spectroscopy. In addition, the NRVS spectrum of [$^{57}Fe^{IV}H_3buea(^{16}O)]^-$ measured independently and under identical conditions showed a peak assigned to an Fe^{IV}–oxido vibration at 794 cm^{-1}, matching well with previous vibrational measurements using FTIR spectroscopy. Furthermore, the lower energy features (450-200 cm^{-1}) for [$^{57}Fe^{IV}H_3buea(^{16}O)(H)$] and [$^{57}Fe^{IV}H_3buea(^{16}O)]^-$ that arise from Fe–N vibrations are significantly different, indicative of a structural change upon protonation.

Structural Properties of [$Fe^{IV}H_3buea(O)(H)$]. The thermal instability of $[Fe^{IV}H_3buea(O)(H)]$ prohibited the determination of its structure by X-ray diffraction (XRD) methods in collaboration with the Green lab. However, evaluation of the Fe-coordination environment was carried out using X-ray absorption spectroscopy (XAS). The XANES spectrum for $[Fe^{IV}H_3buea(O)(H)]$ has an energy edge at 7122.9 eV that is similar to the 7123.3 eV value found for $[Fe^{IV}H_3buea(O)]^-$ **(**Figure

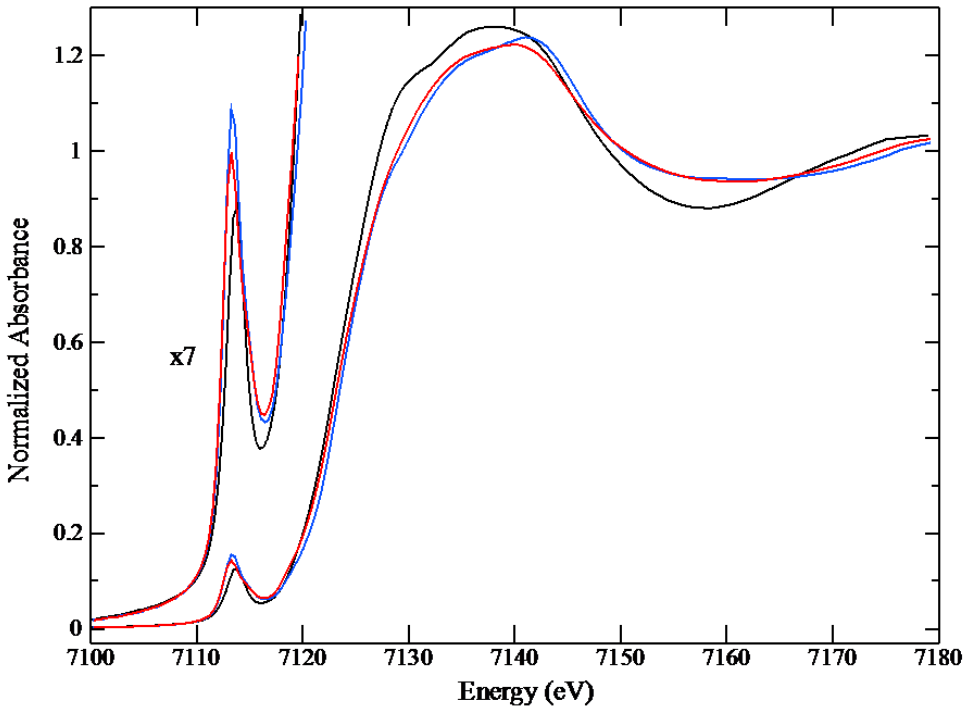

Figure 2-6. XANES spectrum comparing $[Fe^{III}H_3buea(OH)]^-$ (black), $[Fe^{IV}H_3buea(O)]^-$ (blue), and $[Fe^{IV}H_3buea(O)(H)]$ (red).

Metal Complex	Fe-O			Fe-N_{eq}			Fe-N_{ax}			E_0	Error
	N	R	σ^2	N	R	σ^2	N	R	σ^2		
$[Fe^{III}H_3buea(O)(H)]^-$	1	1.85	0.00070	3	2.02	0.00329	1	2.26	0.00266	1.4	0.299
$[Fe^{IV}H_3buea(O)]^-$	1	1.67	0.00273	4	2.00	0.00362	0	----	------	0.2	0.305
$[Fe^{IV}H_3buea(O)(H)]$	1	1.65	0.00331	3	1.96	0.00519	0	----	------	-4.7	0.330

Table 2-1. Best fits of the EXAFS data collected for $[Fe^{III}H_3buea(OH)]^-$, $[Fe^{IV}H_3buea(O)]^-$, and $[Fe^{IV}H_3buea(O)(H)]$.

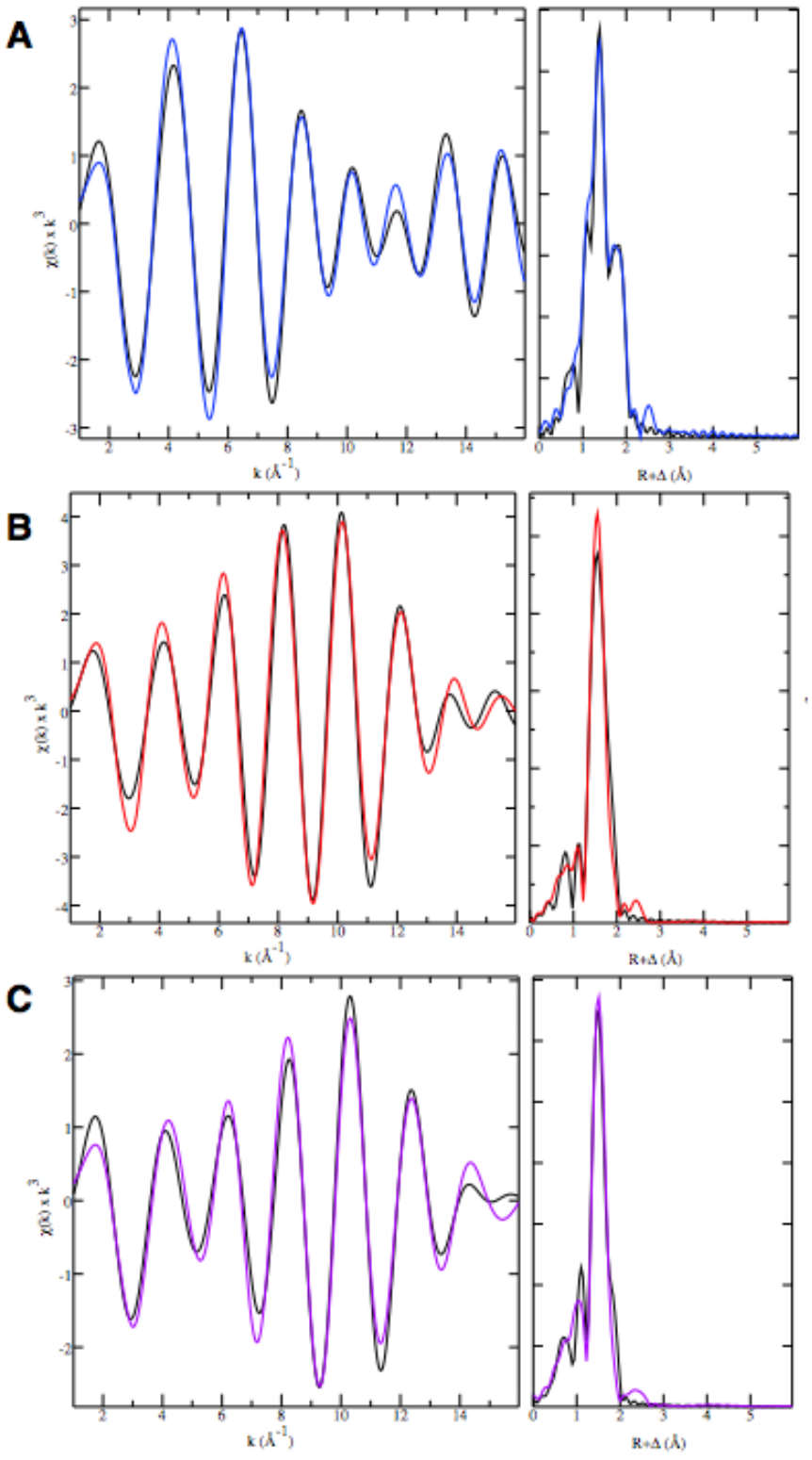

Figure 2-7. Experimental EXAFS data and best fits plotted for $[Fe^{III}H_3buea(OH)]^-$ (A), $[Fe^{IV}H_3buea(O)]^-$ (B), and $[Fe^{IV}H_3buea(O)(H)]$ (C).

2-6); both edge energies are higher than the $[Fe^{III}H_3buea(OH)]^-$ complex and consistent with an Fe^{IV} center.

EXAFS analysis found that the Fe–O bond lengths in $[Fe^{IV}H_3buea(O)(H)]$ (1.65 Å) and $[Fe^{IV}H_3buea(O)]^-$ (1.67 Å) are the same within experimental error (Table 2-1, Figure 2-7) with the distance in $[Fe^{IV}H_3buea(O)]^-$ matching that found by XRD on a crystalline sample.[12] However, the two complexes have statistically significant differences in the remaining components of the primary coordination. In particular, the EXAFS data for $[Fe^{IV}H_3buea(O)(H)]$ were best fit to three Fe–N bonds at a distance of 1.95 Å while for $[Fe^{IV}H_3buea(O)]^-$ the fit gave four Fe–N bonds at a distance of 2.00. The details of these metrical differences are not yet known but it clear that structural changes occur upon conversion of $[Fe^{IV}H_3buea(O)]^-$ to $[Fe^{IV}H_3buea(O)(H)]$.

Structural Properties by Density Functional Theory. Density functional theory (DFT) methods have also been used to further understand the structural properties of $[Fe^{IV}H_3buea(O)(H)]$.[31] The DFT analysis suggested the newly introduced proton is located between the oxido group and one of the $[H_3buea]^{3-}$ arms. Three low-energy optimized structures for $[Fe^{IV}H_3buea(O)(H)]$ were found that differ by no more than 5 kcal/mol using different functionals, and all predicted structure **A** to be lowest in energy. The two lowest energy tautomers have the proton localized

Property	A	B	C
Fe1—O1	1.703	1.696	1.812
Fe1—N1	2.056	2.074	2.098
Fe1—N2	2.062	2.118	1.919
Fe1—N4	1.962	1.956	1.938
Fe1—N6	1.963	1.962	2.025
O1…O2	2.495	–	–
O1…H1	1.450	1.549	0.989
O2…H1	1.056	–	–
O2—C10	1.319	1.238	1.243
N2—C10	1.329	1.322	1.384

Table 2-2. Selected bond metrics for the geometry optimized structures of $[Fe^{IV}H_3buea(O)(H)]$. Bond and contact distances given in Å.

on $[H_3buea]^{3-}$ (Figure 2-8). The structure of **A** has one urea group rotated such that one carbonyl group is positioned within the cavity with the proton on O2 (Figure 2-8). The rotated urea in **A** adopts an imidic acid tautomer (or isourea) with a O2-C10 bond distance of 1.319 Å and a relatively short N2–C10 bond length of 1.329 Å (Table 2-2).[32–34] The second tautomer **B** has the proton centered on one of the urea arms to form a quaternarized

nitrogen center. The third structure **C** has the proton on the oxido ligand to form what is a true hydroxido group. One urea arm in **C** has a pronounced twist, which is presumably to avoid steric clashing with the O–H bond.

The Fe–O1 bond distances of 1.696 and 1.703 Å in **A** and **B** are not significantly changed from the analogous bond distance of 1.680(1) Å in $[Fe^{IV}H_3buea(O)]^-$, which was previously

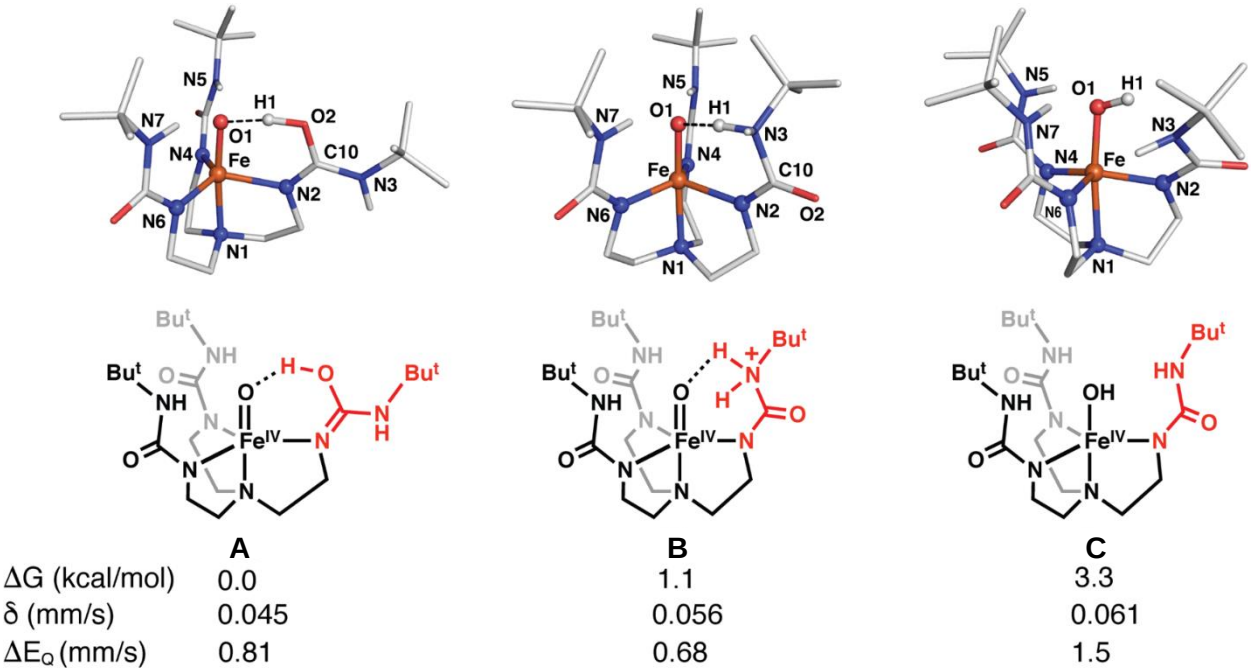

Figure 2-8. Geometry optimizations, relative free energies at RT, and computed Mössbauer parameters for **A-C** determined from DFT. The red segments represent structural changes in $[H_3buea]^{3-}$.

determined by XRD methods and computed to be 1.689 Å by DFT.[11,27] The long O1···H1 distances of 1.450 Å in **A** and 1.549 Å in **B** suggest that the apical ligand is better described as a H-bonded

oxido than a hydroxido. However, the O1···O2 distance in **A** (2.495 Å) and O1···N3 distance in **B** (2.614 Å) are shorter than in other characterized monomeric M–OH or M–oxido structures with $[H_3buea]^{3-}$, indicating that stronger H-bonds are formed because of the increased acidity of these new H-bond donors.[35] For **C**, the Fe–O1 bond length is increased to 1.812 Å that reflects the formation of the hydroxido ligand. Moreover, DFT finds that in each tautomer an asymmetry exists within the equatorial plane that is caused by one $Fe–N_{eq}$ bond length being substantially larger (greater than 2 Å) than the others (Table 2-2); these bond length differences could explain the changes in the Fe-N vibrations observed between $[Fe^{IV}H_3buea(O)(H)]$ and $[Fe^{IV}H_3buea(O)]^-$ by NRVS. Finally, DFT predicted that each tautomer has an $S = 2$ spin state with computed Mössbauer parameters comparable to our experimental findings.

Based on the results from spectroscopy and computations, the oxido ligand in $[Fe^{IV}H_3buea(O)(H)]$ is the less likely site of protonation. This claim is based on the similarities of the Fe–O vibrations for $[Fe^{IV}H_3buea(O)(H)]$ and $[Fe^{IV}H_3buea(O)]^-$ as determined by NRVS measurements and the small changes in the Fe–O/N bond lengths between the two Fe^{IV} complexes obtained from EXAFS analysis. These data suggest that the protonation occurs on one of the urea arms of the $[H_3buea]^{3-}$, as illustrated in the structures of **A** and **B**. Based on relative free energy considerations, **A** and **B** are nearly equivalent and their Mössbauer parameters match well with values obtained from experiments. Tautomer **C** contains an Fe^{IV}–OH unit but with structural parameters that do not match those found by EXAFS. In addition, a Badger's rule analysis predicts that an Fe–O bond length of 1.82 Å as computed for **C** should have a ν(Fe–O) ~ 560 cm^{-1}, which does not agree with experiment (Figure 2-5).[36]

Reactivity of $[Fe^{IV}H_3buea(O)(H)]$. Given that the properties of protonated Fe^{IV}-oxido complexes had not been fully explored, the reactivity of $[Fe^{IV}H_3buea(O)(H)]$ was examined further. Despite the inherent thermal instability of $[Fe^{IV}H_3buea(O)(H)]$, it was found to be

unreactive towards external C–H bonds like those in dihydroanthracene or cyclohexadiene under the reaction conditions. However, the [$Fe^{IV}H_3$buea(O)(H)] complex will react with diphenylhydrazine even at –80 °C in THF; the same reactivity can be observed for the parent [$Fe^{IV}H_3$buea(O)]$^-$ complex under identical conditions.

Rather than continue to test reactivity with external substrates, [$Fe^{IV}H_3$buea(O)(H)] was instead examined for its reactivity as a "hydroxido-like" complex. First, the deprotonation of [$Fe^{IV}H_3$buea(O)(H)] was studied at -80˚C in THF using the non-nucleophilic base, diazabicycloundecene (DBU, pK_a 16.8 in THF, rt):[30] both UV-vis and Mössbauer spectroscopies

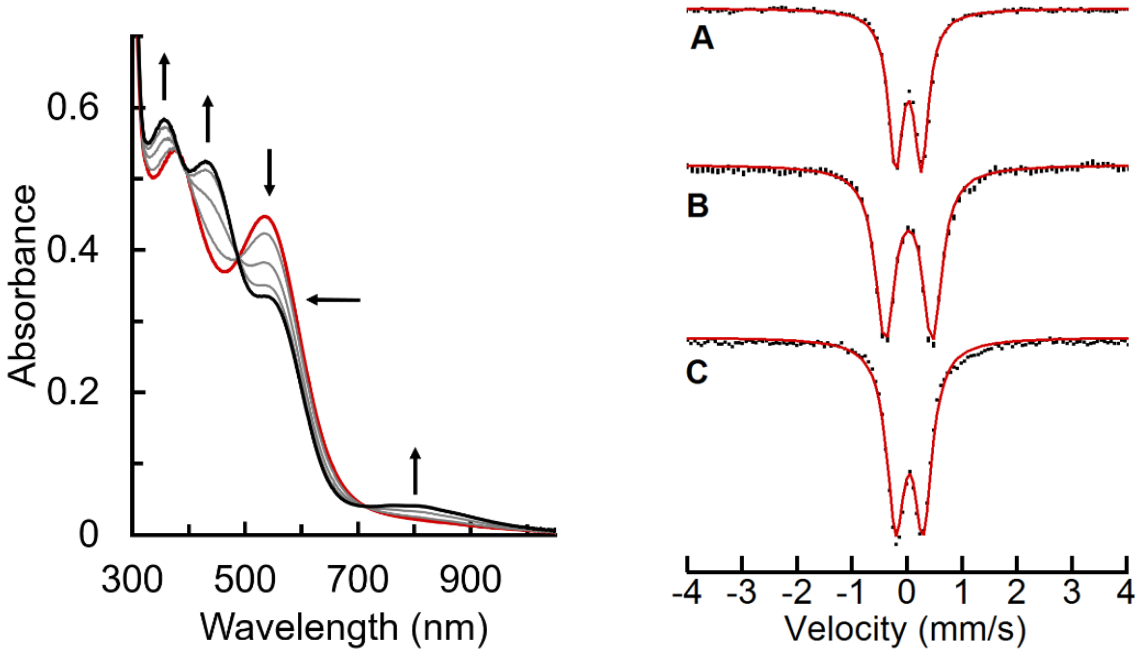

Figure 2-9. Electronic absorption spectra (left) recorded at –80 °C in THF for the deprotonation of [$Fe^{IV}H_3$buea(O)(H)] (red) with 0.25, 0.50, 0.75, and 1.0 equivalents of DBU to regenerate [$Fe^{IV}H_3$buea(O)]$^-$ (black) and Mössbauer spectra recorded at 4 K in THF for [$Fe^{IV}H_3$buea(O)]$^-$ (A), [$Fe^{IV}H_3$buea(O)(H)] (B), and [$Fe^{IV}H_3$buea(O)(H)] plus DBU (C) to regenerate [$Fe^{IV}H_3$buea(O)]$^-$. Red lines are least square fits of experimental data with linewidths: (A) 0.32 mm/s, (B) 0.37 mm/s, and (C) 0.39 mm/s.

showed that [$Fe^{IV}H_3$buea(O)(H)] can be cleanly converted to [$Fe^{IV}H_3$buea(O)]$^-$ (Scheme 2-1, Figure 2-9) in a yield of 90%. These results demonstrate the reversibility of the protonation/deprotonation process. Moreover, if [$Fe^{IV}H_3$buea(O)(H)] behaves as a "hydroxide-

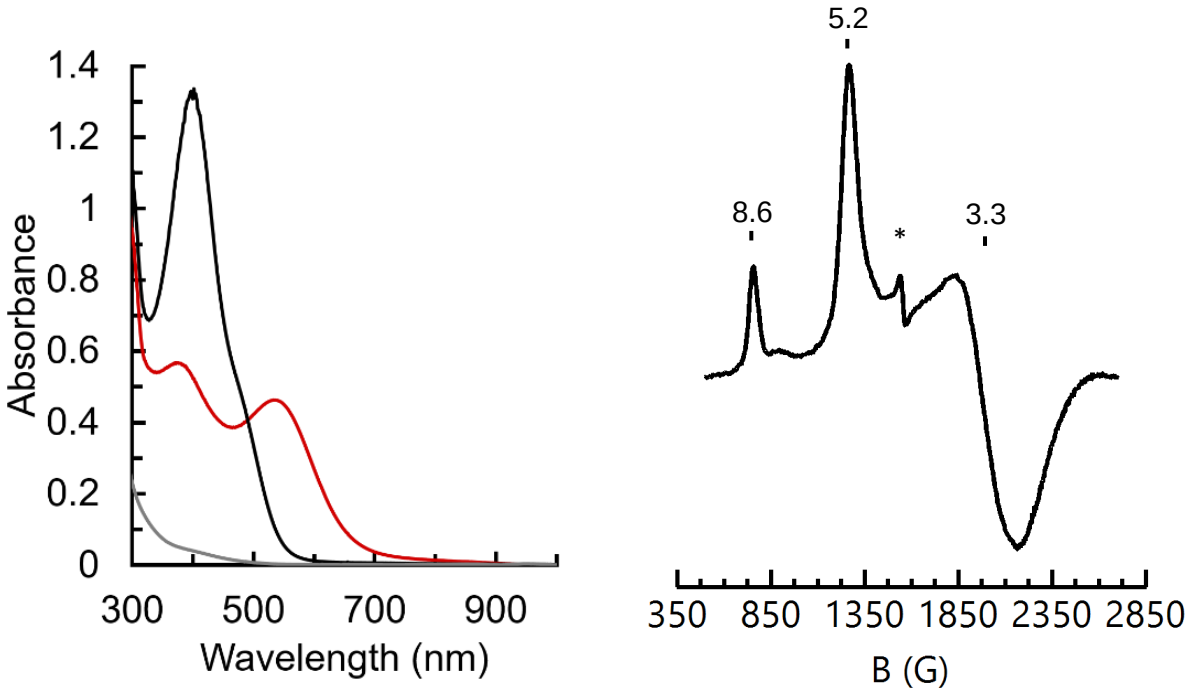

Figure 2-10. Electronic absorption spectra (left) recorded at –80 °C in THF for the comproportionation reaction of [$Fe^{IV}H_3buea(O)(H)$] (red) with one equivalent of [$Fe^{II}H_3buea(OH)]^{2-}$ (gray) to produce two equivalents of [$Fe^{III}H_3buea(OH)]^{-}$ (black) and the perpendicular mode EPR spectrum (right) recorded at 10 K. Asterisk indicates an adventitious ferric impurity.

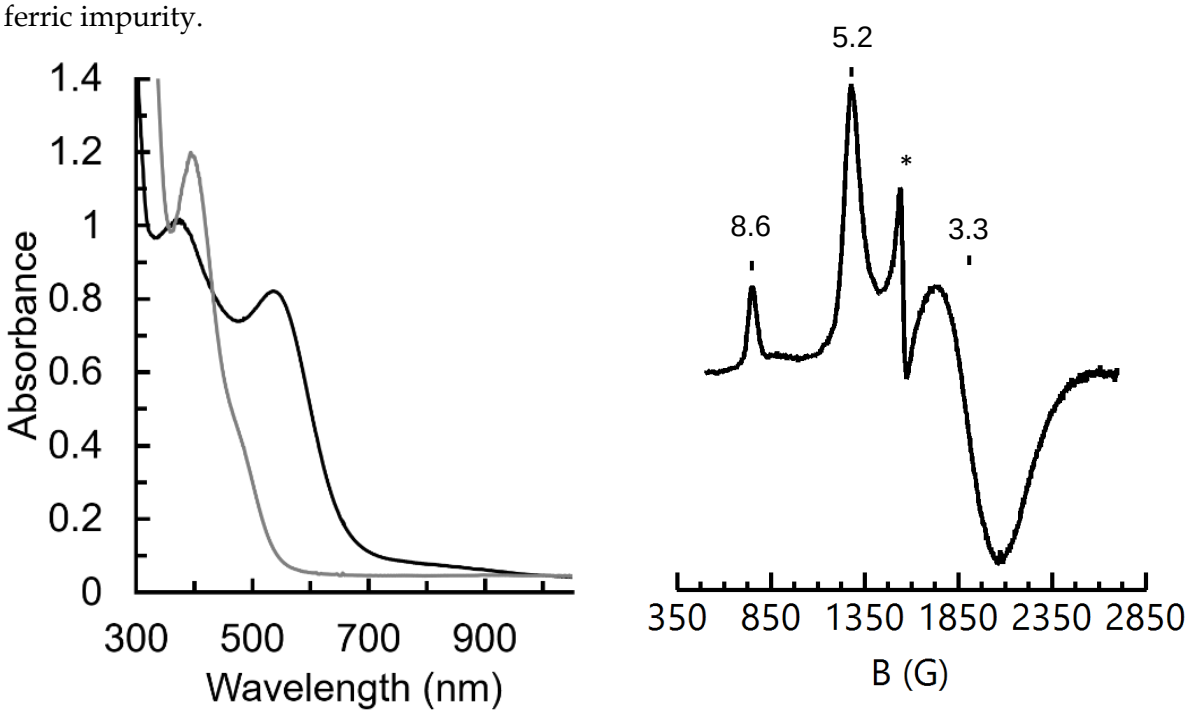

Figure 2-11. Electronic absorption spectra (left) recorded at –80 °C in THF for the reduction of [$Fe^{IV}H_3buea(O)(H)$] (black) with one equivalent of $CoCp_2$ to produce [$Fe^{III}H_3buea(OH)]^{-}$ (gray) and the perpendicular mode EPR spectrum (right) recorded at 10 K. Asterisk indicates an adventitious ferric impurity.

like" complex, a comproportionation reaction should occur between [$Fe^{IV}H_3$buea(O)(H)] and [$Fe^{II}H_3$buea(OH)]$^{2-}$ (eq 2-1) to form [$Fe^{III}H_3$buea(OH)]$^{-}$, two complexes that have been independently prepared and characterized. This premise was successfully affirmed by mixing

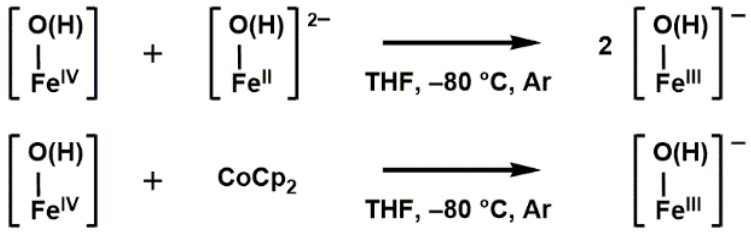

(2-1)

(2-2)

equimolar amounts of [$Fe^{IV}H_3$buea(O)(H)] and [$Fe^{II}H_3$buea(OH)]$^{2-}$ to afford [$Fe^{III}H_3$buea(OH)]$^{-}$ in a concentration that was twice that of the starting complexes (Eq 2-1). This reaction was followed using UV-vis and EPR spectroscopies, and the final product had identical spectra to those published for [$Fe^{III}H_3$buea(OH)]$^{-}$ (Figures 2-10). It was also found that [$Fe^{IV}H_3$buea(O)(H)] can be reduced to [$Fe^{III}H_3$buea(OH)]$^{-}$ in nearly quantitative yield using $CoCp_2$ as the reductant (Eq 2-2, Figure 2-11). These results indicate that the molecular structure of [$Fe^{IV}H_3$buea(O)]$^{-}$ is not irreversibly changed upon protonation to form [$Fe^{IV}H_3$buea(O)(H)].

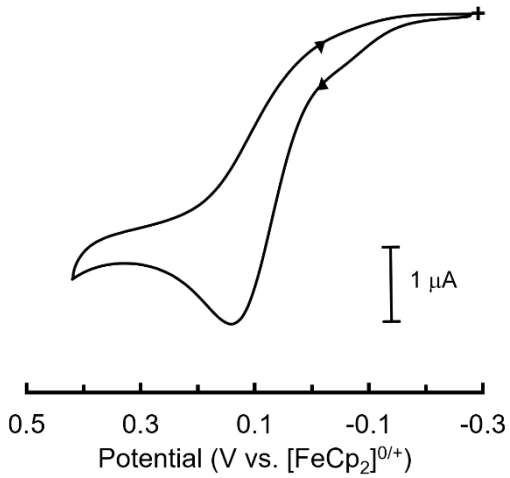

Figure 2-12. Cyclic voltammogram of [$Fe^{IV}H_3$buea(O)]$^{-}$ in THF. Collected in 0.1 M TBAP at 10 mV/s using the bis-pentamethylferrocene$^{0/+}$ couple as an internal standard then referenced to ferrocene$^{0/+}$.

Oxidation of [Fe^{IV}H$_3$buea(O)]$^-$ to generate [Fe^{IV}H$_3$buea(O)(H)]. An alternative pathway to generate the [Fe^{IV}H$_3$buea(O)(H)] complex was found via the oxidation of [Fe^{IV}H$_3$buea(O)]$^-$. Previously, it was reported that [Fe^{IV}H$_3$buea(O)]$^-$ exhibits an irreversible oxidation at 0.34 V vs. [FeCp$_2$]$^{0/+}$ in DMSO at room temperature.[11] The electrochemical properties of [Fe^{IV}H$_3$buea(O)]$^-$ have been reevaluated and found that the potential of the oxidative event shifts to 0.14 V vs. [FeCp$_2$]$^{0/+}$ in THF (Figure 2-12). To probe this oxidative event, the reaction between [Fe^{IV}H$_3$buea(O)]$^-$ and the radical amminium cation, N(*p*-tol)$_3^{+\bullet}$ (0.4 V vs. [FeCp$_2$]$^{0/+}$)[37] was monitored spectrophotometrically at -80˚C in THF. It was anticipated that a new Fe^V species would be produced by the single electron transfer, however, this reaction generated [Fe^{IV}H$_3$buea(O)(H)] as the major iron species in 60% yield. The formation of [Fe^{IV}H$_3$buea(O)(H)] was supported by spectrophotometric and Mössbauer experiments (Figure 2-13). This result was

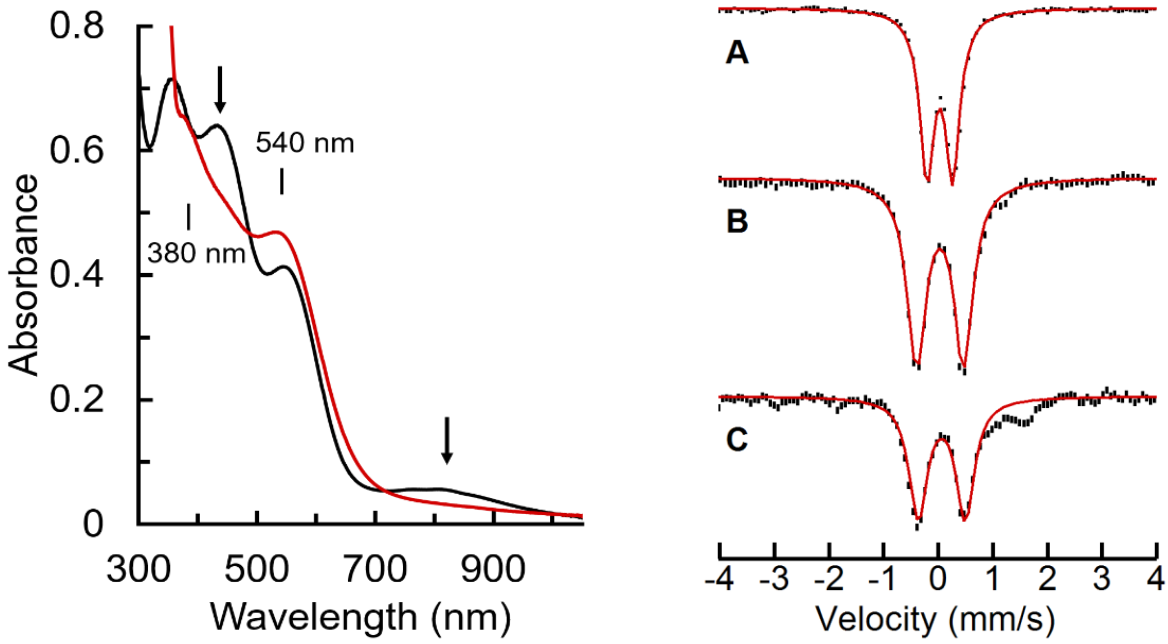

Figure 2-13. Electronic absorption spectra (left) recorded at –80 °C in THF for the oxidation of [Fe^{IV}H$_3$buea(O)]- (black) with one equivalent of [N(*p*-tolyl)$_3$]$^{+\bullet}$ to generate [Fe^{IV}H$_3$buea(O)(H)] (red) and Mössbauer spectra recorded at 4 K in THF for [Fe^{IV}H$_3$buea(O)]- (A), [Fe^{IV}H$_3$buea(O)(H)] from protonation (B), and [Fe^{IV}H$_3$buea(O)(H)] from oxidation (C). Red lines are least square fits of experimental data with linewidths: (A) 0.32 mm/s, (B) 0.37 mm/s, and (C) 0.39 mm/s. Note: Spectrum (C) also contains two minor ferric impurities.

ubiquitous under various reaction conditions including temperatures as low as –105˚C in THF or using solvents such as 2-MeTHF at –120˚C, dichloromethane (DCM) at –90 °C, propionitrile (EtCN) at –80 °C, benzonitrile at –10 °C, toluene at –95 °C, or d_8-THF at –105 °C. The above reactions were monitored by UV-vis spectroscopy and in some cases EPR spectroscopy, and while the stability of [$Fe^{IV}H_3$buea(O)(H)] under the conditions varied widely, it was the only identifiable reaction product from the oxidation of [$Fe^{IV}H_3$buea(O)]$^-$.

A mechanistic route that is consistent with these observations is the initial formation of an Fe^V–oxido intermediate that rapidly abstracts the equivalent of an H-atom, presumably from

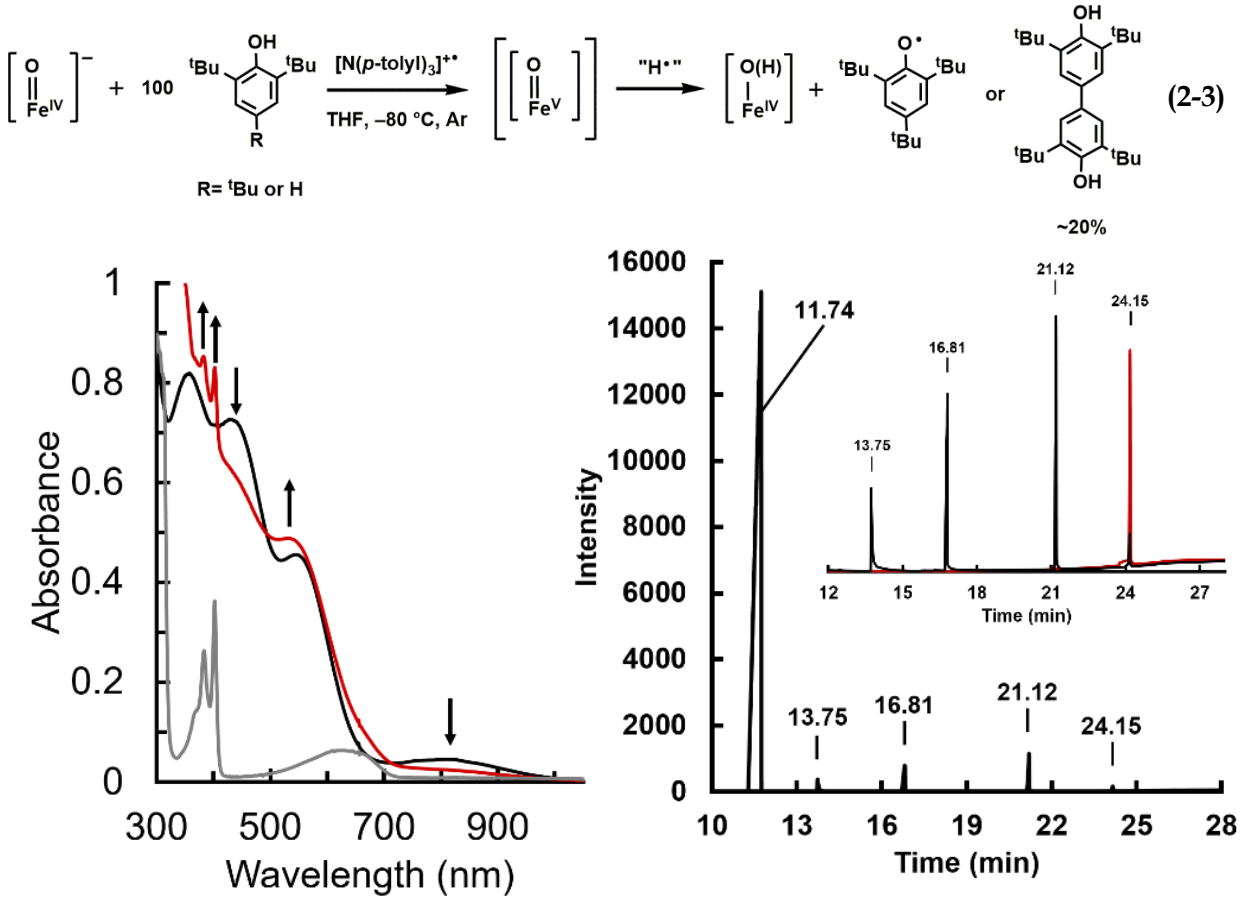

Figure 2-14. Electronic absorption spectra (left) recorded at –80 °C in THF for the oxidation of [$Fe^{IV}H_3$buea(O)]$^-$ (black) in the presence of 100 equivalents of TTBP with one equivalent of [N(*p*-tolyl)$_3$]$^{+\bullet}$ to generate [$Fe^{IV}H_3$buea(O)(H)] (red) and the corresponding phenoxy radical (gray). GC trace (right) of the reaction mixture, key: DTBP (11.74 min), excess DPH (13.75 min), 18-crown-6 ether (16.81 min), N(*p*-tolyl)$_3$ (21.12), and biphenol product (24.15 min). Inset: expanded region at longer retention times with authentic biphenol product overlaid in red.

solvent, to form [$Fe^{IV}H_3$buea(O)(H)] (Scheme 2-2). Due to difficulties detecting any oxidized products from solvent, the oxidation of [$Fe^{IV}H_3$buea(O)]$^-$ was instead examined in the presence of external substrates. When 100 equivalents of 2,4,6-tri-*tert*-butylphenol (TTBP) were present in the oxidation reaction, the formation of [$Fe^{IV}H_3$buea(O)(H)] and the corresponding phenoxy radical were observed, as evidenced by the appearance of its characteristic optical bands at λ_{max} = 382 and 402 nm (Eq 2-3, Figure 2-14). Furthermore, 2,2',6,6'-tetra-*tert*-butyl-4,4'-biphenol was produced in a 20(5)% yield when 2,6-di-*tert*-butylphenol (DTBP) was used, as determined by gas chromatography (GC) and gas chromatography-mass spectrometry (GC-MS) (Figure 2-14). These results provide additional evidence that an Fe^V–oxido species could initially be formed during the oxidative conversion of [$Fe^{IV}H_3$buea(O)]$^-$ to [$Fe^{IV}H_3$buea(O)(H)].

Summary and Conclusion

Protonated Fe^{IV}–oxido complexes are exceptionally difficult to prepare, yet such species are proposed to readily form within protein active site. Using the synthetic ligand [H_3buea]$^{3-}$, we have demonstrated that the well-characterized Fe^{IV}–oxido complex [$Fe^{IV}H_3$buea(O)]$^-$ reacts with acids to produce a new species that is assigned to the protonated species, [$Fe^{IV}H_3$buea(O)(H)]. The properties and reactivity of [$Fe^{IV}H_3$buea(O)(H)] are all consistent with this assignment, including its reversion back to [$Fe^{IV}H_3$buea(O)]$^-$ with the addition of the base DBU, its reaction with the [$Fe^{II}H_3$buea(OH)]$^{2-}$ complex to produce the [$Fe^{III}H_3$buea(OH)]$^-$ species, and its conversion to [$Fe^{III}H_3$buea(OH)]$^-$ by reduction with $CoCp_2$. While the reactivity of [$Fe^{IV}H_3$buea(O)(H)] hints at its identity being a true Fe^{IV}-hydroxido complex, insights into the structure of [$Fe^{IV}H_3$buea(O)(H)] from vibrational spectroscopy and DFT calculations suggest that the likely site of protonation is instead the [H_3buea]$^{3-}$ ligand. The results from NRVS spectroscopy indicated that the Fe–O unit in [$Fe^{IV}H_3$buea(O)(H)] remains intact and mostly unperturbed relative to the starting [$Fe^{IV}H_3$buea(O)]$^-$ complex, which is not in support of an assignment as a

Fe^{IV}-hydroxido complex. In addition, the lowest energy structures provided by DFT show that one tripodal arm is protonated, resulting in a new intramolecular H-bonding interaction with the Fe–O unit. The computational studies implicate the Fe–O···H–X (X = O, N) intramolecular H-bond as a key contributor to the stability of this structure.

Treatment of $[Fe^{IV}H_3buea(O)]^-$ with oxidant did not yield a detectable Fe^V species that would be comparable to Compound I; instead, $[Fe^{IV}H_3buea(O)(H)]$ was obtained in good yield. The detection of $[Fe^{IV}H_3buea(O)(H)]$ provided the opportunity to examine its formation from routes similar to those used to produce Compound II in P450s. In the presence of phenolic substrates, the expected oxidation products were found, which indicated that a putative Fe^V–oxido species may have been produced. Taken together, these findings offer experimental and computational evidence that a synthetic protonated Fe^{IV}–oxido complex has been prepared via a route that is similar to that proposed in P450s.[8]

To reiterate, experimental results showed that $[Fe^{IV}H_3buea(O)(H)]$ and $[Fe^{IV}H_3buea(O)]^-$ differ from one another by a single proton, but the combination of theory and spectroscopy suggest protonation of $[Fe^{IV}H_3buea(O)]^-$ most likely occurred on $[H_3buea]^{3-}$ rather than forming an Fe^{IV}–OH unit as might be expected. The structure of **A** illustrates how facile a proton transfer can be within the secondary coordination sphere of an Fe^{IV}–O unit. The argument this supports is that these types of interactions are unlikely to be limited to the synthetic system described in this chapter and may occur within the active site of a proteins or other synthetic complexes. For instance, mechanisms for non-heme iron enzymes and their synthetic models often invoke Fe^{IV}–OH and Fe^V–OH intermediates,[13,14,17,38] but evidence for the protonation of a monomeric Fe^{IV}–oxido unit has only been observed in heme-containing proteins such as Compound II of P450s and the chloroperoxidases.[8,39,40] Such reactivity has yet to be definitively observed in other metalloproteins that invoke high valent Fe–OH species such as the Rieske non-heme

oxygenases.[1,14] Our results question the feasibility of these high valent Fe–OH species in mechanisms other than P450s, particularly when the possibility of protonation at other sites within the complex (or active site) cannot be ruled out.

Experimental Section

General Procedures. All manipulations, unless otherwise stated, were performed under an argon atmosphere in a Vac-atmospheres dry box. All chemicals were purchased from commercial sources and used without further purification unless otherwise stated. $K[Fe^{IV}H_3buea(O)]$, $K[Fe^{III}H_3buea(OH)]$, $K_2[Fe^{II}H_3buea(OH)]$, and [N(*p*-tolyl)$_3$][OTf] were prepared according to previously published procedures.[11,37,41,42]

General Procedure for Synthesis of Acids. A modified procedure for the synthesis of the conjugate acid of an amine was followed for all acids.[43] A solution of amine in diethyl ether was cooled to 0 °C in an ice water bath. An excess of tetrafluoroboric acid diethyl ether adduct ($HBF_4 \bullet Et_2O$, 50-55% v/v) was added drop-wise to the cold amine. A white precipitate immediately formed. The reaction was allowed to stir for ~1 h at 0 °C. The white precipitate was collected on a fritted glass funnel and washed with room temperature ether (3 x 10 mL) to remove excess $HBF_4 \bullet Et_2O$. The acid salt was transferred to a Schlenk flask and dried under vacuum at room temperature overnight to yield the acid as a white to off-white solid in near quantitative yields. When necessary, additional purification was performed by recrystallization from THF/pentane at –35 °C under an argon atmosphere.

Physical Methods. Electronic absorption spectra were recorded in a 1 cm cuvette on an 8453 Agilent UV-Vis spectrometer equipped with an Unisoku Unispeks cryostat. X-band (9.28 GHz) EPR spectra were collected as frozen solutions using a Bruker EMX spectrometer equipped with an ER041XG microwave bridge. Mössbauer spectra were recorded with a Janis Research Super-

Varitemp dewar. Isomer shifts are reported relative to Fe metal at 298 K. Product(s) were detected by gas-chromatography mass spectrometry (GC-MS) in the Mass Spectrometry Facility at the University of California, Irvine. The GC-MS was a Trace MSplus from Thermo Fisher (San Jose, CA) using a 30m long x 0.25 mm i.d. DB-5 column from Agilent JW Scientific (Santa Clara, CA). The oven was held at 50°C for 1 minute then heated at a rate of 10°C min^{-1} to 290°C and held for an additional 35 minutes. The mass spectrometry used electron ionization (70 eV) scanning (1/sec) from m/z 50-650. Estimation of product yield was determined using an HP-6890 gas chromatograph with a flame ionization detector (FID) and a 30 m × 0.32 mm (5% phenyl)-methylpolysiloxane (0.25 ⌈m coating) capillary column (J&W Scientific DB-5) and helium carrier gas. The oven was held at 50°C for 1 minute then heated at a rate of 10°C min^{-1} to 290°C and held for an additional 5 minutes. Cyclic voltammetric experiments were conducted using a CHI600C electrochemical analyzer. A 2.0 mm glassy carbon electrode was used as the working electrode at scan velocities 0.01 $V{\cdot}s^{-1}$. A pentamethylferrocenium/pentamethylferrocene couple (-0.48 V vs. $[FeCp_2]^{+/0}$) was used as an internal reference to monitor the reference electrode (Ag^+/Ag).[37]

The ^{57}Fe nuclear resonance vibrational spectroscopy (NRVS) data were recorded using published procedures on multiple occasions at beamline 3-ID at the Advanced Photon Source (APS).[44,45] The incident flux provided by the beamline is ~2 x 10^9 photos/s in a 1 meV bandwidth centered at 14.4125 keV in a 1 mm (vertical) x 3 mm (horizontal) spot. The monochromators used in the experiment consisted of a water-cooled diamond (1,1,1) double crystal with 1.1 eV bandpass, followed by two separate Si(4,0,0) and Si(10,6,4) channel-cut crystals in a symmetric geometry. During the measurements, samples were maintained at low temperatures using a closed-cycle helium cryostat. The temperature for individual spectra were calculated using the ratio of anti-Stokes to Stokes intensity according to $S(-E) = S(E)\exp(-E/kT)$ and were generally in the range of 40 K to 80 K. Spectra were recorded between -40 meV and 120 meV in 0.25 meV steps.

Delayed nuclear fluorescence and iron K fluorescence (from internal conversion) were recorded with a single avalanche photodiode detector (APD) with 1 cm^2 detection area. Each scan required about 50 minutes, and all scans were added and normalized to the intensity of the incident beam. The ^{57}Fe partial vibrational density of state (PVDOS) was extracted from the raw NRVS data using the PHOENIX software package.[46]

XAS experiments were performed at the Stanford Synchrotron Radiation Laboratory (SSRL) on beam line 7-3 at 10 K. Fe K-edge data was collected using a Si(220) φ=0° double-crystal monochromator with a 9.0 keV cutoff for harmonic rejection. Soller slits were used in conjunction with an Mn filter. Data was collected in fluorescence mode with a Canberra 30-element Ge solid-state detector. To limit photoreduction of the samples, only first scans were averaged into the final data sets (exposure time ~35 minutes). Fe K-edge data for the both the $[Fe^{III}H_3buea(OH)]^-$ and $[Fe^{IV}H_3buea(O)]^-$ species was comprised of 11 first scans, while the data sets for the $[Fe^{IV}H_3buea(O)(H)]$ species contained 30 first scans. Energies were calibrated using an iron foil (7111.2 eV) and edge energies were obtained from the first derivative of the data with 1.0 eV smoothing and a third order polynomial in the program EXAFSPAK.

The Fe K-edge data sets were fit over the region k = 1-16 $Å^{-1}$ using EXAFSPAK[47] with *ab initio* phases and amplitudes generated with the program FEFF v8.40.[48] The Fe K-edge fits for the three iron species were comprised of the first and second shell atoms as well as one multiple scattering component. In all cases, the second shell atoms included the carbon atoms neighboring the equatorial and axial nitrogen atoms (N = 9, 6, and 4 for $[Fe^{III}H_3buea(OH)]$, $[Fe^{IV}H_3buea(O)]^-$, and $[Fe^{IV}H_3buea(O)(H)]$, respectively) and in the case of the $[Fe^{IV}H_3buea(O)(H)]$ species, the arm nitrogen atoms (N = 3) were included. The Fe-N-C-Fe multiple scattering pathway involving the surrounding nitrogen atoms and their nearest neighbor carbon atom was included for the $[Fe^{III}H_3buea(OH)]^-$ and $[Fe^{IV}H_3buea(O)]^-$ species (N = 12 and 18, respectively), however was

omitted from the [$Fe^{IV}H_3$buea(O)(H)] fit in favor of the second shell N_{arm} scattering which had a greater contribution to the scattering. All Debye-Waller factors were treated as free parameters. The scale factor, S_0, was set to 0.9. Monochromator glitches in the Fe K-edge data sets at approximately k = 14.5 $Å^{-1}$ were removed using a cubic polynomial fit to the data. No other modifications to the raw data were performed.

DFT Calculations. The DFT calculations were performed with the program suite Gaussian '09.[49] The geometry optimizations were performed using the functional/basis set combination bp86/tzvp. The free energy differences reported in the main text were evaluated using Gibbs free energies obtained with the frequency keyword at 298 K. ΔE_Q and η were calculated with bp86/tzvp, using Q = 0.17 barn. The ^{57}Fe isomer shift δ was evaluated for electron densities obtained with single point bp86/6-311g calculations at bp86/tzvp optimized structures.

Reactivity Studies of [$Fe^{IV}H_3$buea(O)]$^-$ at Low Temperature using UV-vis Spectroscopy. For a typical experiment, a stock solution of [$Fe^{IV}H_3$buea(O)]$^-$ at ~100-200 μM concentration (2 mg, 0.004 mmol) was prepared in THF (15 mL) with 1.5 equiv 18-crown-6 ether (2 mg, 0.01 mmol) and stored at −36 °C. The concentration of [$Fe^{IV}H_3$buea(O)]$^-$ was determined using the extinction coefficient at λ_{max} = 550 nm (ε = 3000 $M^{-1}cm^{-1}$). To a 1 cm cuvette was added 2 mL of metal complex solution. The cuvette was sealed with a rubber septum then transferred to the precooled UV-vis spectrometer and allowed to equilibrate for at least 20 minutes at –80 °C under a flow of argon gas. Stock solutions of reactants were prepared by dissolving 10 mg in 1 mL of the appropriate solvent generating solutions between 20-40 mM. Solutions of reagents were then injected via gas-tight syringe and the progress of the reaction monitored optically.

Oxidation of [$Fe^{IV}H_3$buea(O)]$^-$ in the Presence of a Phenol. A stock solution of [$Fe^{IV}H_3$buea(O)]$^-$ was prepared in THF as described above. Stock solutions of phenol, either 2,4,6-tri-*tert*-butylphenol (66 mg, 0.25 mmol) or 2,4-di-*tert*-butylphenol (56 mg, 0.25 mmol), were

prepared in THF (250 μL). A stock solution of [N(*p*-tolyl)$_3$][OTf] was prepared by dissolving the deep blue solid (10 mg, 0.023 mmol) in THF (1 mL). A stock solution of diphenylhydrazine (DPH) was prepared by dissolving the solid (10 mg, 0.054 mmol) in THF (5 mL). A 2 mL aliquot of the solution of [Fe^{IV}H$_3$buea(O)]$^-$ was transferred to a 1 cm quartz cuvette and sealed with a rubber septum before cooling to –80 °C in the cryostat of the UV-vis spectrometer. To this solution, 100 equiv of phenol was added via gas-tight syringe and the mixture was allowed to stir for 1 min before injection of 1 equiv of [N(*p*-tolyl)$_3$][OTf]. Reactions with 2,4,6-tri-*tert*-butylphenol were monitored optically for the generation of [Fe^{IV}H$_3$buea(O)(H)] and 2,4,6-tri-*tert*-butylphenoxy radical (λ_{max} = 380 and 400 nm).

In the case of 2,4-di-*tert*-butylphenol, the generation of [Fe^{IV}H$_3$buea(O)(H)] was monitored by the growth of the absorbance band at λ_{max} = 540 nm, requiring ~60 seconds, and then treated with 0.5 equiv of DPH to quench the reaction. The reaction was deemed complete after the complete loss of the optical band of [Fe^{IV}H$_3$buea(O)(H)] at λ_{max} = 540 nm. After completion, the solution was transferred at room temperature in air from the cuvette into a 1.8 mL vial for analysis using GC-MS. Product yield was calculated from GC using a calibration curve generated for pure 2,2',6,6'-tetra-*tert*-butyl-4,4'-biphenol. ESI$^+$ m/z *Anal* (calc): *410.45* ($C_{28}H_{42}O_2$ 410.32)

Control Reaction of [Fe^{IV}H$_3$buea(O)(H)] with Phenol. Stock solutions of [Fe^{IV}H$_3$buea(O)]$^-$, phenol, and DPH prepared as described above. A solution of [H$_3$NPh][BF$_4$] was prepared by dissolving the white solid (10 mg, 0.055 mmol) in THF (2 mL). To a solution of [Fe^{IV}H$_3$buea(O)]$^-$ precooled to –80 °C was added 1 equiv [H$_3$NPh][BF$_4$] and the reaction was monitored optically for the generation of [Fe^{IV}H$_3$buea(O)(H)]. Upon complete generation of [Fe^{IV}H$_3$buea(O)(H)], 100 equiv of phenol were added and in the case of 2,4,6-tri-*tert*-butylphenol were monitored optically for the decrease of [Fe^{IV}H$_3$buea(O)(H)] and generation of 2,4,6-tri-*tert*-butylphenoxy radical (λ_{max} = 380 and 400 nm). After 120 seconds, the typical reaction time for complimentary oxidation

reactions, 0.5 equiv of DPH were added and the decrease of the band at λ_{max} = 540 nm was monitored to observe quenching of the reaction. After reaction completion, in the case of 2,4-di-*tert*-butylphenol, the contents of the cuvette were transferred at room temperature in air to a 1.8 mL vial and subjected to analysis by GC-MS.

Control Reaction of [Fe^{IV}H$_3$buea(O)]$^-$ with Phenol. Stock solutions of [Fe^{IV}H$_3$buea(O)]$^-$ and phenol prepared as described above. To a solution of [Fe^{IV}H$_3$buea(O)]$^-$ precooled to –80 °C in a 1 cm cuvette was added 100 equiv of phenol. The reaction mixture was monitored optically for the generation of 2,4,6-tri-*tert*-butylphenoxy radical (λ_{max} = 380 and 400 nm) coupled with the decrease in absorbance bands associated with the [Fe^{IV}H$_3$buea(O)]$^-$ complex. After 120 seconds, the typical reaction time for complimentary oxidation reactions, 0.5 equiv of DPH were added and the decrease of the band at λ_{max} = 550 and 800 nm were monitored to determine quenching of the reaction. After reaction completion, in the case of 2,4-di-*tert*-butylphenol, the contents of the cuvette were transferred at room temperature in air to a 1.8 mL vial and subjected to analysis by GC-MS.

Control Reaction of [N(p-tolyl)$_3$][OTf] and Phenol. Stock solutions of [N(*p*-tolyl)$_3$][OTf] and 2,4,6-tri-*tert*-butylphenol prepared as described above. To a solution of [N(*p*-tolyl)$_3$][OTf] (2 mL, 100-200 μM) precooled to –80 °C was added 100 equiv of phenol. The mixture was monitored optically for 120 seconds for the decrease of the bands associated with [N(*p*-tolyl)$_3$][OTf] and the generation of 2,4,6-tri-*tert*-butylphenoxy radical.

Preparation of Mössbauer Samples of [Fe^{IV}H$_3$buea(O)(H)] with ^{57}Fe. A 3 mM solution of ~96% ^{57}Fe-enriched, [^{57}Fe^{IV}H$_3$buea(O)]$^-$ (3 mg, 0.005 mmol) was prepared in THF (1.7 mL) with 1.5 equiv 18-crown-6 ether (2 mg, 0.01 mmol). This solution is transferred to a 1 cm cuvette and placed inside the cryostat of a UV-vis spectrometer cooled to –100 °C. The rubber septum sealing the cuvette was quickly removed with the aid of a razor blade under a flow of argon gas. The

precooled solution was then treated with either oxidant or acid solution and monitored for the disappearance of the low energy band for $[Fe^{IV}H_3buea(O)]^-$ at λ_{max} = 800 nm (ε = 300 $M^{-1}cm^{-1}$). After ~30 seconds, the cuvette was removed from the cryostat and its contents were quickly poured into liquid nitrogen. The resulting frozen solution was then packed into pre-cooled Mössbauer cups for analysis.

Preparation of NRVS Samples for $[Fe^{IV}H_3buea(O)]^-$. Solution NRVS sample holders were prepared from Mössbauer sample holders by cutting a 2 x 6 mm slot out of the bottom and covering the hole with kapton tape. A 10 mM solution of 96% ^{57}Fe-enriched $[Fe^{IV}H_3buea(O)]^-$ (10 mg, 0.02 mmol) was prepared in THF (2 mL) with 18-crown-6 ether (6 mg, 0.02 mmol) added to increase solubility. The concentration of $[Fe^{IV}H_3buea(O)]^-$ was determined by UV-vis spectroscopy as described above for the preparation of Mössbauer samples by transferring a portion of the solution to a 1 mm path length cuvette. A NRVS sample holder was cooled in the cold well of a drybox to -196 °C. To the pre-cooled NRVS sample holder, a sample of $[Fe^{IV}H_3buea(O)]^-$ (500 μL of the 10 mM solution) was added via syringe and allowed to freeze completely. The sample was then transferred from the dry box and quickly placed in a storage container pre-cooled to 77 K. Samples were analyzed for purity using Mössbauer spectroscopy prior to, and after NRVS data collection.

Preparation of NRVS Samples for $[Fe^{IV}H_3buea(O)(H)]$. The same general procedure described above for the preparation of NRVS samples of $[Fe^{IV}H_3buea(O)]^-$ was used to prepare those of $[Fe^{IV}H_3buea(O)(H)]$ with the following modifications. A 10 mM solution of $[Fe^{IV}H_3buea(O)]^-$ in THF was transferred to a cuvette and placed inside a cryostat of a UV-vis spectrometer pre-cooled to –100 °C. The rubber septum sealing the cuvette was quickly removed with the aid of a razor blade under a flow of argon gas. The pre-cooled solution was then treated with a solution of $[H_3NPh][BF_4]$ (40 μL, 0.5 M in THF) added via gas-tight syringe and monitored for the

disappearance of the low energy band for $[Fe^{IV}H_3buea(O)]^-$ at λ_{max} = 800 nm (ε = 300 $M^{-1}cm^{-1}$). After ~30 s, the cuvette was removed from the cryostat and its contents were rapidly poured into liquid N_2. The resulting frozen solution was transferred into pre-cooled NRVS sample holder and packed by carefully thawing and refreezing the frozen solution under a stream of argon gas. Samples were analyzed for purity using Mössbauer spectroscopy prior to, and after NRVS data collection.

Preparation of Low-Temperature EPR Samples. A solution of $[Fe^{IV}H_3buea(O)]^-$ (~15 mM, 250 µL) was transferred to an EPR tube and sealed with a rubber septum. The tube was brought out of the dry box and placed in a −95 °C methanol/liquid nitrogen bath and allowed to equilibrate for five minutes. Stock solutions of reactant prepared as described above were added via a syringe. After mixing by careful shaking of the tube, the EPR tube was quickly removed from the cold bath, wiped clean of methanol, and frozen in liquid nitrogen before analysis.

Preparation of Low-Temperature Solution XAS Samples of $[Fe^{IV}H_3buea(O)]^-$. Solution XAS samples were prepared in a similar manner as solution NRVS samples described above with the following modifications: a 10 mM solution of $[Fe^{IV}H_3buea(O)]^-$ (10 mg, 0.02 mmol), of which 2 mM was prepared with 96% ^{57}Fe-enriched $[Fe^{IV}H_3buea(O)]^-$, was prepared in THF (2 mL) with 18-crown-6 ether (6 mg, 0.02 mmol) added for increase solubility. A XAS sample holder was cooled in a cold well of a drybox to -196 °C. To the pre-cooled XAS sample holder, a sample of $[Fe^{IV}H_3buea(O)]^-$ (500 µL of the 10 mM solution) was added via syringe and allowed to completely freeze. The sample was then transferred from the drybox and quickly placed in a container pre-cooled to 77 K. Samples were analyzed for purity using Mössbauer spectroscopy prior to XAS data collection. Solution XAS sample holders were prepared from Mössbauer sample holders by cutting off the bottom and covering the hole with kapton tape.

Preparation of Low-Temperature Solution XAS Samples of $[Fe^{III}H_3buea(OH)]^-$. Solution XAS

samples were prepared in a similar manner as solution NRVS samples described above with the following modifications: a 10 mM solution of $[Fe^{III}H_3buea(OH)]^-$ (10 mg, 0.02 mmol), of which 2 mM was prepared with 96% ^{57}Fe-enriched $[Fe^{III}H_3buea(OH)]^-$, was prepared in THF (2 mL) with 18-crown-6 ether (6 mg, 0.02 mmol) added for increase solubility. A XAS sample holder was cooled in a cold well of a drybox to -196 °C. To the pre-cooled XAS sample holder, a sample of $[Fe^{III}H_3buea(OH)]^-$ (500 μL of the 10 mM solution) was added via syringe and allowed to completely freeze. The sample was then transferred from the drybox and quickly placed in a container pre-cooled to 77 K. Samples were analyzed for purity using Mössbauer spectroscopy prior to XAS data collection. Solution XAS sample holders were prepared from Mössbauer sample holders by cutting off the bottom and covering the hole with kapton tape.

Preparation of Low-Temperature Solution XAS samples of $[Fe^{IV}H_3buea(O)(H)]$. The same general procedure described above for the preparation of XAS samples of $[Fe^{IV}H_3buea(O)]^-$ was used to prepare those of **1** with the following modifications: a 10 mM solution of $[Fe^{IV}H_3buea(O)]^-$, of which 2 mM was enriched with 96% ^{57}Fe-enriched $[Fe^{IV}H_3buea(O)]^-$, in THF was transferred to a cuvette and placed inside a cryostat of a UV-vis spectrometer pre-cooled to –100 °C. The rubber septum sealing the cuvette was quickly removed with the aid of a razor blade under a flow of argon. The pre-cooled solution was then treated with a solution of $[H_3NPh][BF_4]$ (40 μL, 0.5 M in THF) via gas-tight syringe and monitored for the disappearance of the low energy band for $[Fe^{IV}H_3buea(O)]^-$ at λ_{max} = 800 nm (ε = 300 $M^{-1}cm^{-1}$). After ~30 s, the cuvette was removed from the cryostat and its contents were rapidly poured into liquid N_2. The resulting frozen solution was transferred into a pre-cooled XAS sample holder and packed by carefully thawing and refreezing the frozen solution under a stream of argon. Samples were

analyzed for purity using Mössbauer spectroscopy prior to XAS data collection.

References

(1) Costas, M.; Mehn, M. P.; Jensen, M. P.; Que, L. *Chem. Rev.* **2004**, *104*, 939–986.
(2) Que, L.; Tolman, W. B. *Nature* **2008**, *455*, 333–340.
(3) Mas-Ballesté, R.; Que, L. *Science* **2006**, *312*, 1885–1886.
(4) Poulos, T. L. *Chem. Rev.* **2014**, *114*, 3919–3962.
(5) Krest, C. M.; Onderko, E. L.; Yosca, T. H.; Calixto, J. C.; Karp, R. F.; Livada, J.; Rittle, J.; Green, M. T. *J. Biol. Chem.* **2013**, *288*, 17074–17081.
(6) Denisov, I. G.; Makris, T. M.; Sligar, S. G.; Schlichting, I. *Chem. Rev.* **2005**, *105*, 2253–2277.
(7) Rittle, J.; Green, M. T. *Science* **2010**, *330*, 933–937.
(8) Yosca, T. H.; Rittle, J.; Krest, C. M.; Onderko, E. L.; Silakov, A.; Calixto, J. C.; Behan, R. K.; Green, M. T. *Science* **2013**, *342*, 825–829.
(9) McDonald, A. R.; Que, L. *Coord. Chem. Rev.* **2013**, *257*, 414–428.
(10) Puri, M.; Que, L. *Acc. Chem. Res.* **2015**, *48*, 2443–2452.
(11) Lacy, D. C.; Gupta, R.; Stone, K. L.; Greaves, J.; Ziller, J. W.; Hendrich, M. P.; Borovik, A. S. *J. Am. Chem. Soc.* **2010**, *132*, 12188–12190.
(12) Hohenberger, J.; Ray, K.; Meyer, K. *Nat. Commun.* **2012**, *3*, 1–13.
(13) Tiago de Oliveira, F.; Chanda, A.; Banerjee, D.; Shan, X.; Mondal, S.; Que, L.; Bominaar, E. L.; Münck, E.; Collins, T. J. *Science* **2007**, *315*, 835–838.
(14) Prat, I.; Mathieson, J. S.; Güell, M.; Ribas, X.; Luis, J. M.; Cronin, L.; Costas, M. *Nat. Chem.* **2011**, *3*, 788–793.
(15) Ghosh, M.; Singh, K. K.; Panda, C.; Weitz, A.; Hendrich, M. P.; Collins, T. J.; Dhar, B. B.; Sen Gupta, S. *J. Am. Chem. Soc.* **2014**, *136*, 9524–9527.
(16) Wackett, L. P. *Enzyme Microb. Technol.* **2002**, *31*, 577–587.
(17) Park, J.; Lee, Y.-M.; Nam, W.; Fukuzumi, S. *J. Am. Chem. Soc.* **2013**, *135*, 5052–5061.
(18) Yosca, T. H.; Behan, R. K.; Krest, C. M.; Onderko, E. L.; Langston, M. C.; Green, M. T. *J. Am. Chem. Soc.* **2014**, *136*, 9124–9131.
(19) Behan, R. K.; Green, M. T. *J. Inorg. Biochem.* **2006**, *100*, 448–459.
(20) Jensen, M. P.; Costas, M.; Ho, R. Y. N.; Kaizer, J.; Mairata i Payeras, A.; Münck, E.; Que, L.; Rohde, J.-U.; Stubna, A. *J. Am. Chem. Soc.* **2005**, *127*, 10512–10525.
(21) Stoian, S. A.; Xue, G.; Bominaar, E. L.; Que, L.; Münck, E. *J. Am. Chem. Soc.* **2014**, *136*, 1545–1558.
(22) MacBeth, C. E.; Golombek, A. P.; Jr., V. G. Y.; Yang, C.; Kuczera, K.; Hendrich, M. P.; Borovik, A. S. *Science* **2000**, *289*, 938–941.
(23) Borovik, A. S. *Acc. Chem. Res.* **2005**, *38*, 54–61.
(24) Gupta, R.; Taguchi, T.; Lassalle-Kaiser, B.; Bominaar, E. L.; Yano, J.; Hendrich, M. P.; Borovik, A. S. *Proc. Natl. Acad. Sci. U. S. A.* **2015**, *112*, 5319–5324.
(25) Cook, S. A.; Borovik, A. S. *Acc. Chem. Res.* **2015**, *48*, 2407–2414.
(26) Shook, R. L.; Borovik, A. S. *Inorg. Chem.* **2010**, *49*, 3646–3660.
(27) Gupta, R.; Lacy, D. C.; Bominaar, E. L.; Borovik, A. S.; Hendrich, M. P. *J. Am. Chem. Soc.* **2012**, *134*, 9775–9784.
(28) Lacy, D. C. Incorporation of Intramolecular Hydrogen Bonds in Synthetic Trigonal Bipyramidal Manganese, Iron and Cobalt Complexes with Hydroxo, Oxo, and Aquo Ligands, University of California, Irvine, 2012.
(29) Usharani, D.; Lacy, D. C.; Borovik, A. S.; Shaik, S. *J. Am. Chem. Soc.* **2013**, *135*, 17090–

17104.
(30) Kaljurand, I.; Kütt, A.; Sooväli, L.; Rodima, T.; Mäemets, V.; Leito, I.; Koppel, I. A. *J. Org. Chem.* **2005**, *70*, 1019–1028.
(31) Swart, M.; Solà, M.; Bickelhaupt, F. M. *J. Chem. Phys.* **2009**, *131*, 094103.
(32) Fairlie, D. P.; Woon, T. C.; Wickramasinghe, W. A.; Willis, A. C. *Inorg. Chem.* **1994**, *33*, 6425–6428.
(33) Fairlie, D. P.; Taube, H. *Inorg. Chem.* **1985**, *24*, 3199–3206.
(34) Fairlie, D. P.; Ilan, Y.; Taube, H. *Inorg. Chem.* **1997**, *36*, 1029–1037.
(35) MacBeth, C. E.; Gupta, R.; Mitchell-Koch, K. R.; Young, V. G.; Lushington, G. H.; Thompson, W. H.; Hendrich, M. P.; Borovik, A. S. *J. Am. Chem. Soc.* **2004**, *126*, 2556–2567.
(36) Green, M. T. *J. Am. Chem. Soc.* **2006**, *128*, 1902–1906.
(37) Connelly, N. G.; Geiger, W. E. *Chem. Rev.* **1996**, *96*, 877–910.
(38) Prat, I.; Company, A.; Postils, V.; Ribas, X.; Que, L.; Luis, J. M.; Costas, M. *Chemistry* **2013**, *19*, 6724–6738.
(39) Green, M. T.; Dawson, J. H.; Gray, H. B. *Science* **2004**, *304*, 1653–1656.
(40) Stone, K. L.; Behan, R. K.; Green, M. T. *Proc. Natl. Acad. Sci. U. S. A.* **2006**, *103*, 12307–12310.
(41) Shirin, Z.; Hammes, B. S.; Young, V. G.; Borovik, A. S. *J. Am. Chem. Soc.* **2000**, *122*, 1836–1837.
(42) MacBeth, C. E.; Hammes, B. S.; Victor G. Young, J.; Borovik, A. S. *Inorg. Chem.* **2001**, *40*, 4733–4741.
(43) Kanamura, K.; Yonezawa, S.; Kawai, Y.; Takehara, Z.-I. *J. Electroanal. Chem. Interfacial Electrochem.* **1991**, *301*, 291–295.
(44) Sturhahn, W. *J. Phys. Condens. Matter* **2004**, *16*, S497–S530.
(45) Toellner, T. S. *Hyperfine Interact.* **2000**, *125*, 3–28.
(46) Sturhahn, W. *Hyperfine Interact.* **2000**, *125*, 149–172.
(47) Gearge, G. N. EXAFSPAK, 2000.
(48) Ankudinov, A. L.; Ravel, B.; Rehr, J. J.; Conradson, S. D. *Phys. Rev. B* **1998**, *58*, 7565–7576.
(49) Frisch, M. J.; Trucks, G. W.; Schlegel, H. B.; Scuseria, G. E.; Robb, M. A.; Cheeseman, J. R.; Scalmani, G.; Barone, V.; Mennucci, B.; Petersson, G. A.; Nakatsuji, H.; Caricato, M.; Li, X.; Hratchian, H. P.; Izmaylov, A. F.; Bloino, J.; Zheng, G.; Sonnenberg, J. L.; Hada, M.; Ehara, M.; Toyota, K.; Fukuda, R.; Hasegawa, J.; Ishida, M.; Nakajima, T.; Honda, Y.; Kitao, O.; Nakai, H.; Vreven, T.; Montgomery Jr., J. A.; Peralta, J. E.; Ogliaro, F.; Bearpark, M.; Heyd, J. J.; Brothers, E.; Kudin, K. N.; Staroverov, V. N.; Keith, T.; Kobayashi, R.; Normand, J.; Raghavachari, K.; Rendell, A.; Burant, J. C.; Iyengar, S. S.; Tomasi, J.; Cossi, M.; Rega, N.; Millam, J. M.; Klene, M.; Knox, J. E.; Cross, J. B.; Bakken, V.; Adamo, C.; Jaramillo, J.; Gomperts, R.; Stratmann, R. E.; Yazyev, O.; Austin, A. J.; Cammi, R.; Pomelli, C.; Ochterski, J. W.; Martin, R. L.; Morokuma, K.; Zakrzewski, V. G.; Voth, G. A.; Salvador, P.; Dannenberg, J. J.; Dapprich, S.; Daniels, A. D.; Farkas, O.; Foresman, J. B.; Ortiz, J. V.; Cioslowski, J.; Fox, D. J. Gaussian 09, 2010.

Chapter 3

Proton Transfer in the Generation of a Non-Heme Fe^{IV}-Oxido Complex from a Related Fe^{III}-Hydroxido Complex

Proton and electron transfer processes are nearly ubiquitous in biological and synthetic systems, performing diverse chemical transformations ranging from C–H bond activation to water oxidation.[1–3] These chemical processes involve steps that require the transfer of both protons and electrons and fall under the broader category of proton-coupled electron transfer (PCET) reactions. PCET reactions can proceed via two major pathways: 1) the concerted transfer of a proton and electron to a single site, as is often the case for radical reactions in organic chemistry (Scheme 3-1A),[4–6] or 2) the concerted transfer of a proton and electron to two different locations, a process frequently observed in enzymatic systems (Scheme 3-1B).[7–10] The latter

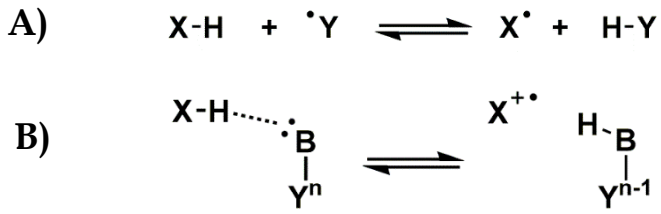

Scheme 3-1. Two different pathways for PCET: concerted pathway where both proton and electron are transferred to A) the same atom of a given molecule and B) two different locations.

pathway describes the type of reactivity often observed for high valent metal-oxido complexes. For example, in C–H bond activation, the metal center accepts the electron from the homolytic cleavage of the C–H bond and the oxido ligand accepts the proton.[11–14] The reverse of this mechanism with respect to the metal complex, the oxidation of the metal-hydroxido complex to yield a high valent metal-oxido complex, is also a PCET reaction. In order to understand these processes, several systems have been developed to examine the properties of proton and electron transfer in transition metal chemistry.[15–17]

The first use of the term PCET to describe a reaction pathway was by Meyer when examining aqueous Ru chemistry.[18,19] He found that a $[(bpy)_2(py)Ru^{II}(OH_2)]^{2+}$ complex (bpy =

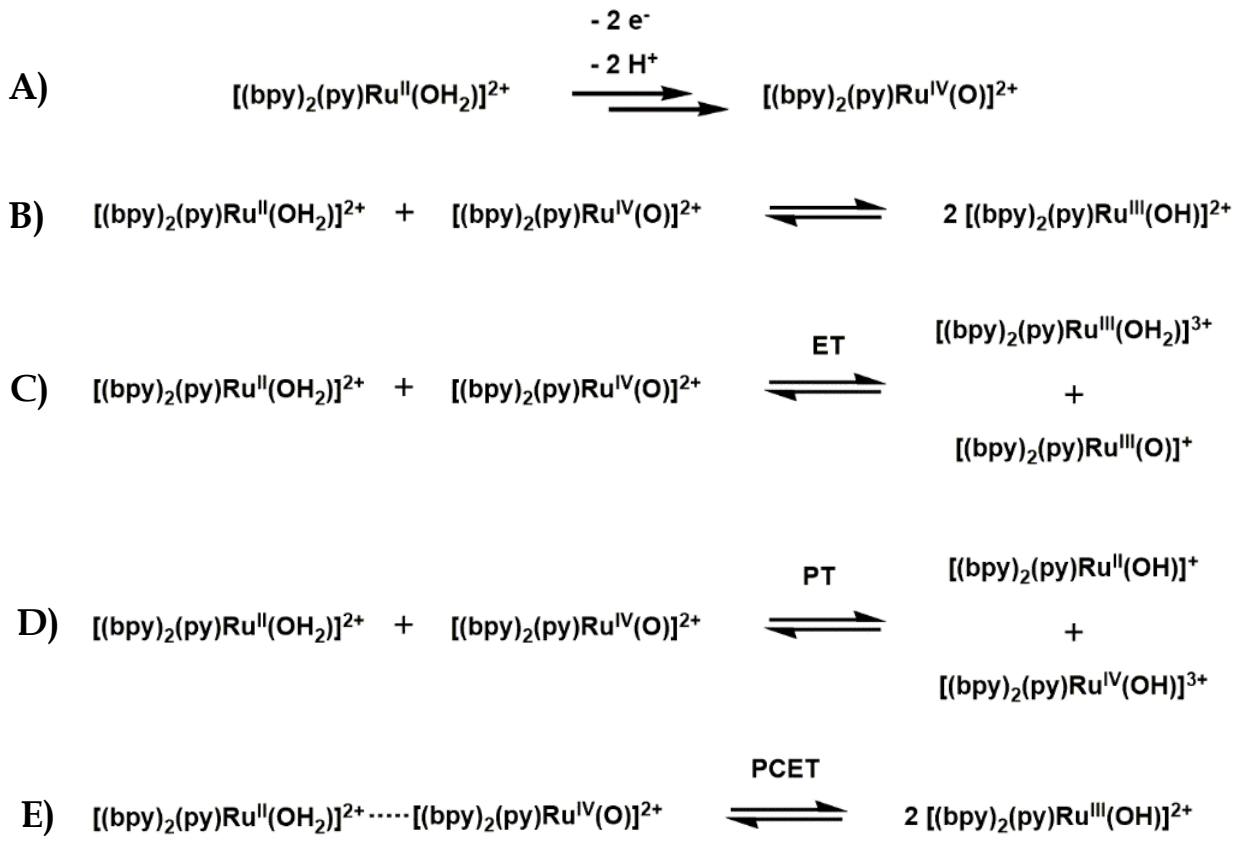

Scheme 3-2. The overall PCET reaction (A) for the oxidation of $[(bpy)_2(py)Ru^{II}(OH_2)]^{2+}$. The overall comproportionation reaction (B) between $[(bpy)_2(py)Ru^{II}(OH_2)]^{2+}$ and $[(bpy)_2(py)Ru^{IV}(O)]^{2+}$ to produce two equivalents of $[(bpy)_2(py)Ru^{III}(OH)]^{2+}$ broken down into three potential mechanisms: (C) first an electron transfer between the two reagents, (D) first a proton transfer between the two reagents, or (E) the pre-association of the two reagents, represented by the dotted line, to facilitate the PCET process.

2,2′-bipyridine and py = pyridine) could be oxidized to the corresponding $[(bpy)_2(py)Ru^{IV}(O)]^{2+}$ complex in two, one-electron steps with the loss of a proton at each step (Scheme 3-2A). Under neutral pH conditions, the conclusion was that the comproportionation reaction between $[(bpy)_2(py)Ru^{II}(OH_2)]^{2+}$ and $[(bpy)_2(py)Ru^{IV}(O)]^{2+}$ to produce two equivalents of $[(bpy)_2(py)Ru^{III}(OH)]^{2+}$ (Scheme 3-2B) was extremely unlikely to proceed via discrete proton and electron transfer steps due to the requirement of high energy intermediates:

$[(bpy)_2(py)Ru^{III}(OH_2)]^{3+}$, $[(bpy)_2(py)Ru^{III}(O)]^{+}$, or $[(bpy)_2(py)Ru^{IV}(OH)]^{3+}$ (Scheme 3-2C and D). Instead, the alternative hypothesis is a pre-association of the two reactants so that concerted proton and electron transfer occurs to avoid generation of any high energy intermediates (Scheme 3-2E).[20] The applications of PCET would come to extend beyond these seminal studies of Ru complexes to a multitude of biological and synthetic systems involving metal-oxido complexes.[9,21–24]

In non-heme Fe chemistry, there are fewer well studied examples of systems similar to the Ru chemistry just described. This may be due to the difficulty in preparing relevant species such as terminal aqua, hydroxido, and oxido complexes all within the same coordination environment suitable for detailed studies.[12,25,26] One of the limited examples comes from the Nam lab using the pentadentate poly-pyridyl ligand N4Py (N4Py = N,N-bis(2-pyridylmethyl)-N-bis-(2-pyridyl)methylamine).[27] With the N4Py ligand, they are able to oxidize an $[Fe^{II}(N4Py)(MeCN)]^{2+}$ precursor complex in the presence of a large excess of water to generate a

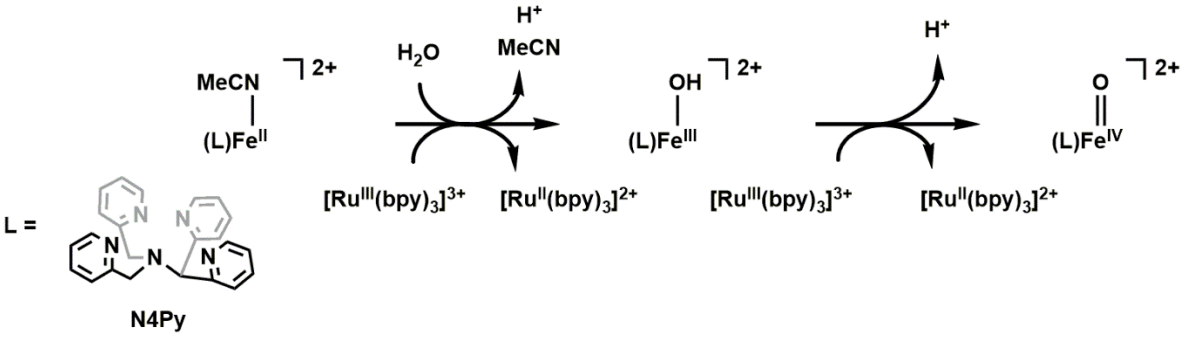

Scheme 3-3. Depiction of the stepwise oxidation of $[Fe^{II}(N4Py)(MeCN)]^{2+}$ in the presence of water to produce $[Fe^{IV}(N4Py)(O)]^{2+}$ via PCET processes.

species that was assigned as a putative $[Fe^{III}(N4Py)(OH)]^{2+}$ complex. The addition of a second equivalent of oxidant resulted in the conversion to the previously characterized $[Fe^{IV}(N4Py)(O)]^{2+}$ complex in what can be best described as a PCET process (Scheme 3-3).[28] Finally, if the oxidation from Fe^{III} to Fe^{IV} was carried out in the presence of weak bases such as OTf^-, TsO^-, or CF_3COO^-,

there was a dramatic increase in the rate of oxidation which was correlated with the strength of the bases. This chemistry is a rare example of detailed PCET in non-heme Fe chemistry.

This chapter focuses on the relationship between the $[Fe^{III}H_3buea(OH)]^-$, $[Fe^{IV}H_3buea(O)]^-$, and $[Fe^{IV}H_3buea(O)(H)]$ complexes with respect to PCET. Previously, the Borovik group reported that the oxidation of $[Fe^{III}H_3buea(OH)]^-$ generates $[Fe^{IV}H_3buea(O)]^-$, not the $[Fe^{IV}H_3buea(O)(H)]$ complex as might be expected, through what is likely a PCET process.[29]

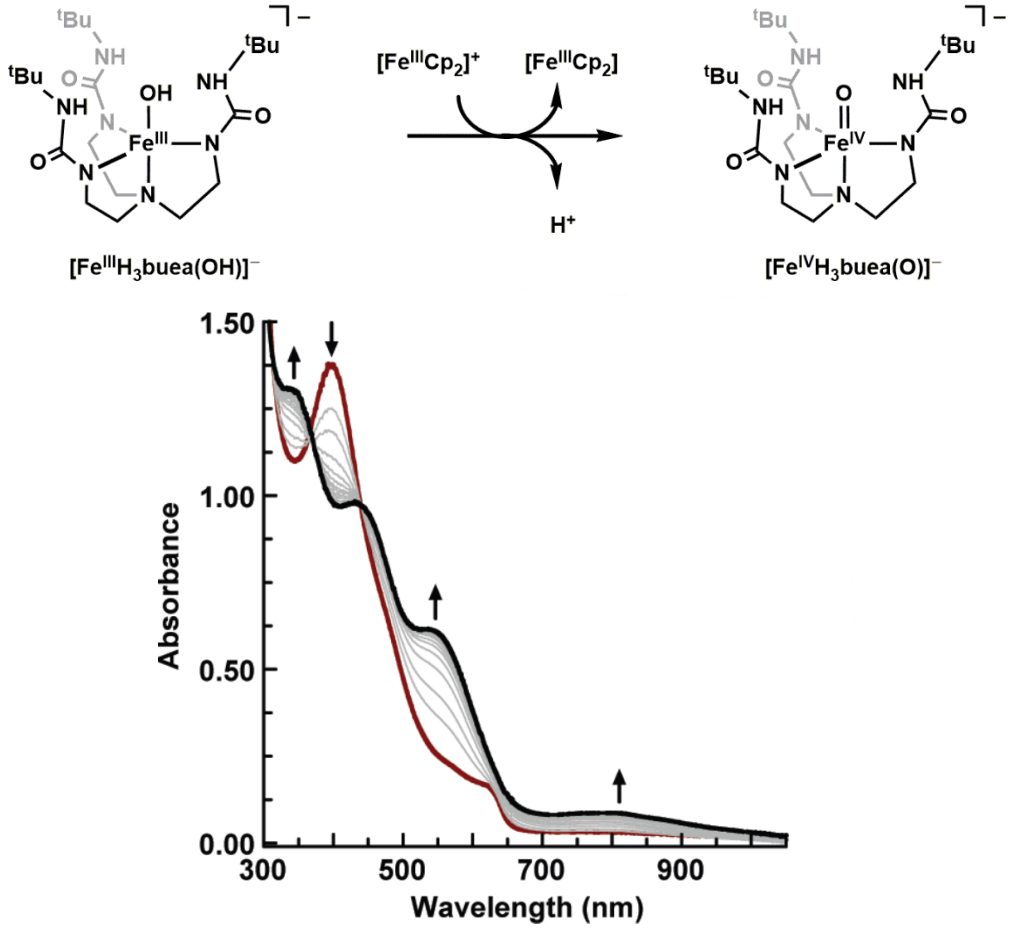

Figure 3-1. Reaction scheme and UV-vis spectral changes for the formation of $[Fe^{IV}H_3buea(O)]^-$ (black) from the oxidation of $[Fe^{III}H_3buea(OH)]^-$ (red) by the addition of $[FeCp_2]^+$. Figure adapted from reference 29.

Following the oxidation spectrophotometrically showed the oxidation of $[Fe^{III}H_3buea(OH)]^-$ proceeds cleanly to $[Fe^{IV}H_3buea(O)]^-$ in *N,N*-dimethylformamide (DMF) at –60 °C, with no observable intermediate (Figure 3-1). The isolation of $[Fe^{IV}H_3buea(O)]^-$ can be achieved by

oxidation of $[Fe^{III}H_3buea(OH)]^-$ with $[FeCp_2]^+$ in acetonitrile (MeCN), resulting in a maroon precipitate which can be collected as the potassium salt in only modest yields (~30 %). This yield is low considering the clean spectroscopic conversion in DMF. Understanding the dichotomous behavior of the oxidation reaction in different solvents became an area to explore given the characterization of the mono-protonated Fe^{IV}-oxido complex described in Chapter 2. The oxidation of $[Fe^{III}H_3buea(OH)]^-$ in less polar solvents was explored along with the reactivity of $[Fe^{IV}H_3buea(O)(H)]$ towards the transfer of a proton and/or an electron. Also discussed is the dramatic improvement of the isolated yield of $[Fe^{IV}H_3buea(O)]^-$ by the addition of the external base, diazabicycloundecene (DBU), to the reaction mixture prior to oxidation. The observed reactivity implicates the concomitant transfer of a proton during electron transfer, as described above for Ru chemistry. The experimental results support the premise put forward in Chapter 2 that protonated Fe^{IV}-oxido complexes are exceptionally challenging to prepare and also demonstrates the role of PCET in the generation of high valent metal-oxido complexes.

Results and Discussion

The Oxidation of $[Fe^{III}H_3buea(OH)]^-$ Under Various Conditions. As mentioned above, treatment of $[Fe^{III}H_3buea(OH)]^-$ with one equivalent of $[FeCp_2]^+$ in DMF at –60 °C resulted in the clean conversion to $[Fe^{IV}H_3buea(O)]^-$ through what may best be described as a PCET reaction. Despite this, performing the same oxidation in acetonitrile (MeCN) resulted in unexpectedly low yields of the isolated $K[Fe^{IV}H_3buea(O)]$. This behavior is not easily explained. For example, one might expect solvent C–H bond activation to be a likely culprit for loss of product, however, the C–H bond strength of MeCN ($C\mathbf{H}_3CN$, 95 kcal/mol) is stronger than that of DMF ($(CH_3)_2NCO\mathbf{H}$, 82 kcal/mol).[30] To examine if this behavior is temperature related, the oxidation reaction was followed spectrophotometrically in propionitrile (EtCN) at –80 °C (Figure 3-2) and showed a different final spectrum from what has previously been reported in DMF (Figure 3-1). The

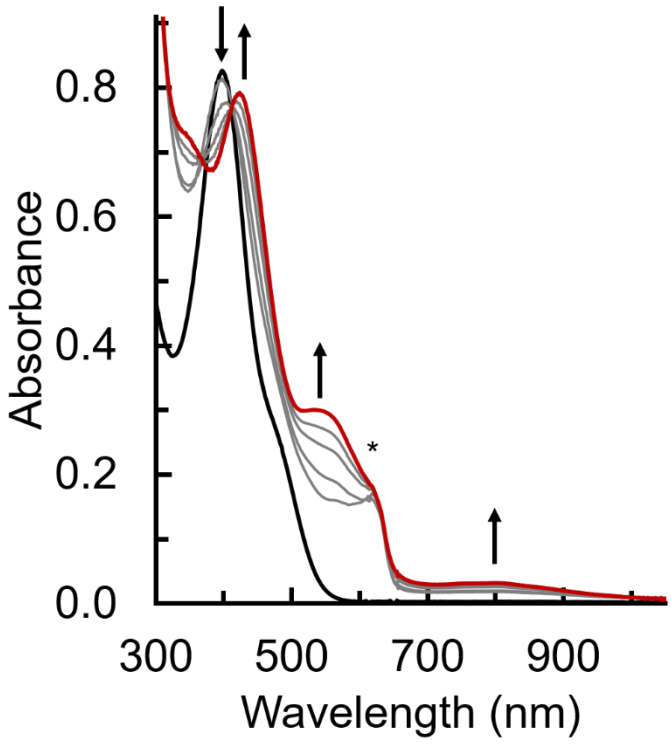

Figure 3-2. UV-vis spectral changes upon the addition of $[FeCp_2]^+$ to $[Fe^{III}H_3buea(OH)]^-$ (black) in EtCN at –80 °C to yield absorbance features consistent with $[Fe^{IV}H_3buea(O)]^-$ and an additional absorbance at 425 nm (red). The asterisk indicates unreacted $[FeCp_2]^+$. Gray lines represent spectra recorded at 30 second intervals.

spectrophotometric yield of $[Fe^{IV}H_3buea(O)]^-$ can be estimated using the extinction coefficient at λ_{max} = 550 nm (ε = 3000 $M^{-1}cm^{-1}$) and was found to be approximately 40%. In addition to bands associated with $[Fe^{IV}H_3buea(O)]^-$, a new and relatively intense band at λ_{max} = 425 nm was observed that was not present in the oxidation in DMF.

Reactivity of $[Fe^{IV}H_3buea(O)(H)]$ with ferrocene and $[Fe^{III}H_3buea(OH)]^-$. The recently characterized protonated Fe^{IV}-oxido complex, $[Fe^{IV}H_3buea(O)(H)]$, may be an intermediate during the oxidation of $[Fe^{III}H_3buea(OH)]^-$ with $[FeCp_2]^+$. With this in mind, the complex may be used as a probe to determine what species in solution could be acting as a base to accept the proton during the PCET reaction and give rise to the absorbance band at λ_{max} = 425 nm. Previously, it was postulated that the equivalent of $[FeCp_2]$ is responsible for accepting the proton. While the protonation of $[FeCp_2]$ has been reported, it has only been observed under

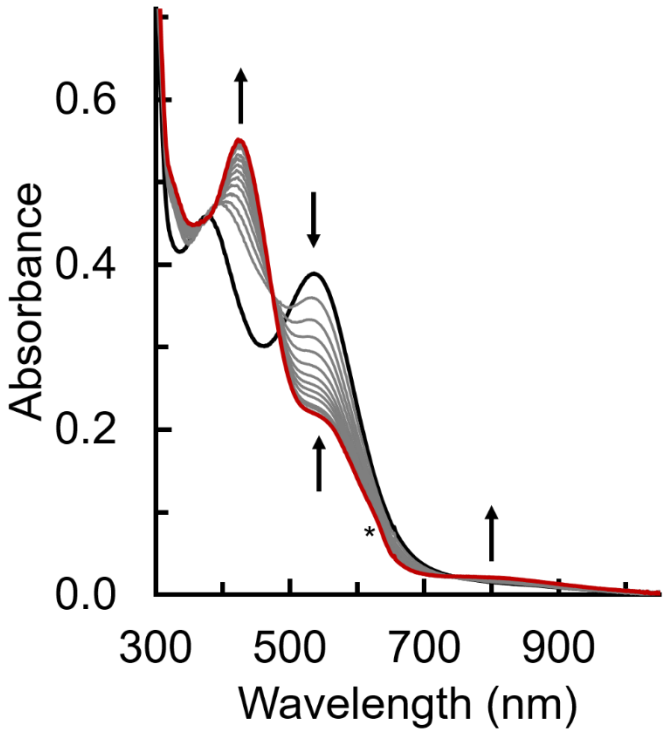

Figure 3-3. UV-vis spectral changes upon the addition of $[FeCp_2]$ to $[Fe^{IV}H_3buea(O)(H)]$ (black) in THF at –80 °C to yield absorbance features consistent with $[Fe^{IV}H_3buea(O)]^-$ and an additional absorbance at 425 nm (red). The asterisk marks the shoulder assigned to $[FeCp_2]^+$. Gray lines represent spectra recorded at 10 second intervals.

strongly acidic conditions and is therefore unlikely under the reaction conditions.[31] As expected, addition of H_3NPh^+, the same acid shown to protonate $[Fe^{IV}H_3buea(O)]^-$, to a solution of $[FeCp_2]$ results in no reaction at -80 °C or room temperature. In addition, no reaction was observed when $[Fe^{IV}H_3buea(O)(H)]$, generated by addition of H_3NPh^+ to a solution of $[Fe^{IV}H_3buea(O)]^-$ in THF at –80 °C, was treated with one equivalent of $[FeCp_2]$. If an excess of $[FeCp_2]$ (10 equivalents) was added under the same conditions, there was a reaction that produced ~40% $[Fe^{IV}H_3buea(O)]^-$, an intense band at λ_{max} = 425 nm, and a shoulder at λ_{max} = ~625 nm consistent with the production of $[FeCp_2]^+$ (Figure 3-3). The generation of $[FeCp_2]^+$ suggests that the addition of excess $[FeCp_2]$ results in partial reduction from $[Fe^{IV}H_3buea(O)(H)]$ to $[Fe^{III}H_3buea(OH)]^-$ (the Fe^{III}/Fe^{IV} oxidative wave of $[Fe^{III}H_3buea(OH)]^-$ is 0.03 V vs. $[FeCp_2]^{0/+}$)[29] implicating an Fe^{III} species giving rise to the signal at λ_{max} = 425 nm.

Protonation of [Fe^{III}H$_3$buea(OH)]$^-$. The premise that [FeCp$_2$] acts as a reductant when added in excess to [Fe^{IV}H$_3$buea(O)(H)], and knowing that [FeCp$_2$] itself does not act as a base under the reaction conditions, suggests the starting comlex, [Fe^{III}H$_3$buea(OH)]$^-$, acts as a base in the reaction.

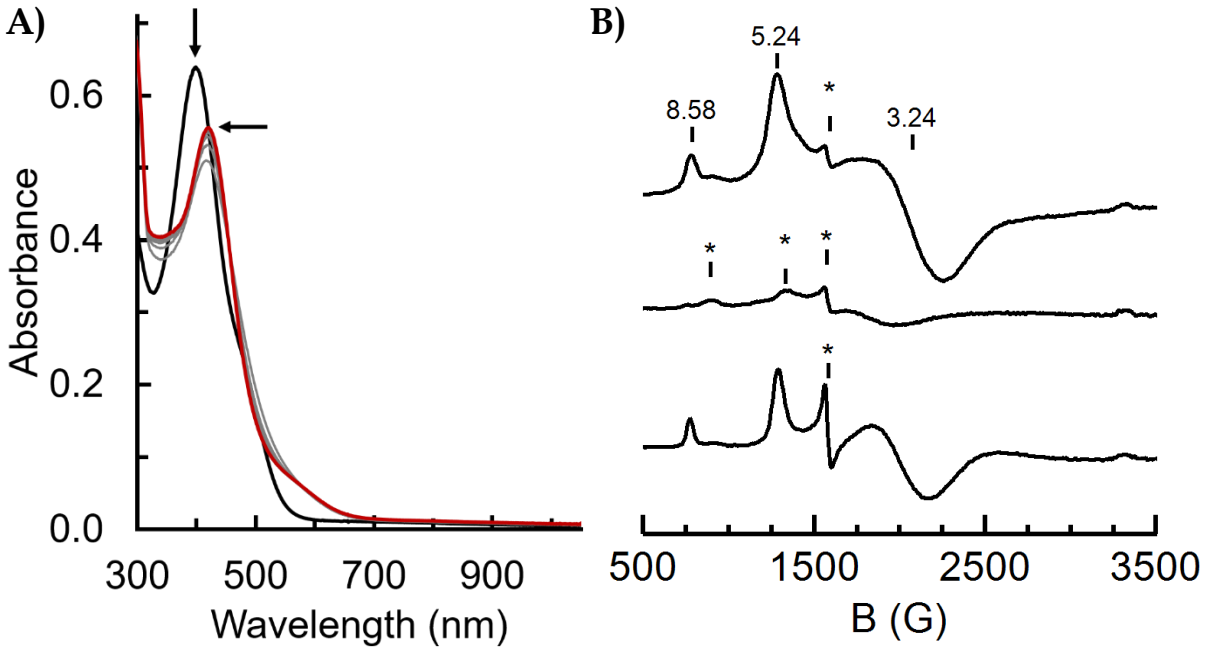

Figure 3-4. UV-vis spectral changes (A) upon the addition of H$_3$NPh$^+$ to [Fe^{III}H$_3$buea(OH)]$^-$ (black) in THF at –80 °C to yield an absorbance feature at 425 nm (red). Gray lines represent spectra recorded at 10 second intervals. Perpendicular mode EPR spectra (B) of [Fe^{III}H$_3$buea(OH)]$^-$ (top) and changes upon the addition of H$_3$NPh$^+$ (middle) followed by deprotonation with DBU (bottom). The asterisk indicates impurities present in the starting spectrum that carry through the reaction.

To first test whether [Fe^{III}H$_3$buea(OH)]$^-$ can be protonated, the complex was treated with one equivalent of [H$_3$NPh]$^+$ at –80 °C in THF resulting in the conversion to a new species with a λ_{max} = 425 nm (Figure 3-4A). This band was nearly identical to the band produced during the oxidation of [Fe^{III}H$_3$buea(OH)]$^-$ by [FeCp$_2$]$^+$ in EtCN (Figure 3-2). The protonated [Fe^{III}H$_3$buea(OH)]$^-$ is not room temperature stable and reacts further to give an optical spectrum which is featureless in the visible region. The protonated [Fe^{III}H$_3$buea(OH)]$^-$ was also treated with up to ten equivalents of [FeCp$_2$] and no reaction was observed at –80 °C in THF, again demonstrating that [FeCp$_2$] does not act as a base or reductant under these reaction conditions. Examining the protonation of

[$Fe^{III}H_3$buea(OH)]- by electron paramagnetic resonance (EPR) spectroscopy showed that the protonated species does not have a signal in either parallel or perpendicular modes, suggesting dimerization to generate a coupled system. Addition of one equivalent of diazabicycloundecene (DBU) resulted in the partial regeneration of [$Fe^{III}H_3$buea(OH)]- (Figure 3-4B). Finally, [$Fe^{III}H_3$buea(OH)]- was added to a solution of [$Fe^{IV}H_3$buea(O)(H)] at –80 °C resulting in a loss of the band at λ_{max} = 540 nm associated with [$Fe^{IV}H_3$buea(O)(H)] along with an increase in features for [$Fe^{IV}H_3$buea(O)]⁻ at λ_{max} = 550 and 800 nm and the growth of a band at λ_{max} = 425 nm consistent with the protonated [$Fe^{III}H_3$buea(OH)]- (Figure 3-5). Taken together, the preceding reactions demonstrate that [$Fe^{III}H_3$buea(OH)]- can act as a base to deprotonate [$Fe^{IV}H_3$buea(O)(H)] and account for the absorbance band at λ_{max} = 425 nm when protonated.

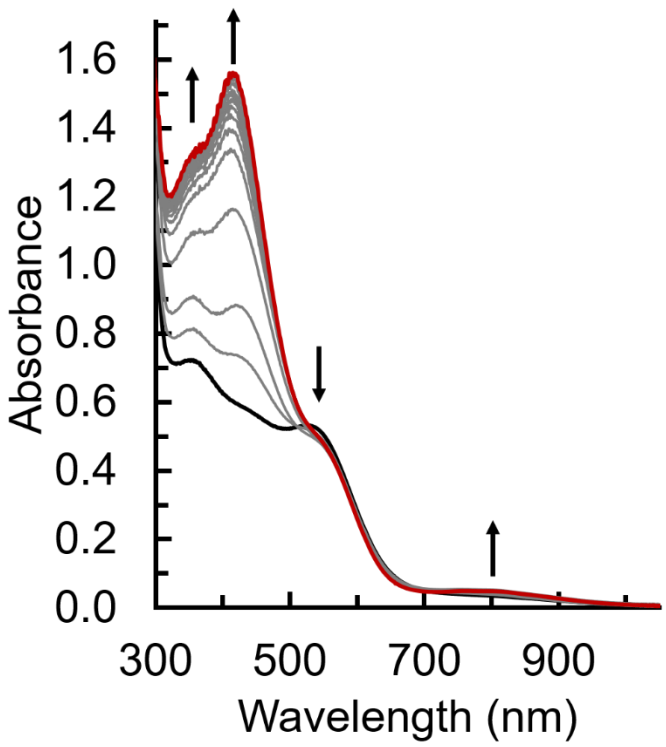

Figure 3-5. UV-vis spectral changes upon the addition of [$Fe^{III}H_3$buea(OH)]- to [$Fe^{IV}H_3$buea(O)(H)] (black) in THF at –80 °C to yield absorbance features for [$Fe^{IV}H_3$buea(O)]- and an absorbance feature at 425 nm (red). Gray lines represent spectra recorded at 5 second intervals.

Improving the Yield of [Fe^{IV}H$_3$buea(O)]$^-$. The ability of [Fe^{III}H$_3$buea(OH)]$^-$ to act as a base during the oxidation reaction to produce [Fe^{IV}H$_3$buea(O)]$^-$ provides an explanation for the low yield of [Fe^{IV}H$_3$buea(O)]$^-$ in solvents other than DMF. During the course of the oxidation reaction in solvents such as MeCN, EtCN, and THF, the starting complex, [Fe^{III}H$_3$buea(OH)]-, is lost due

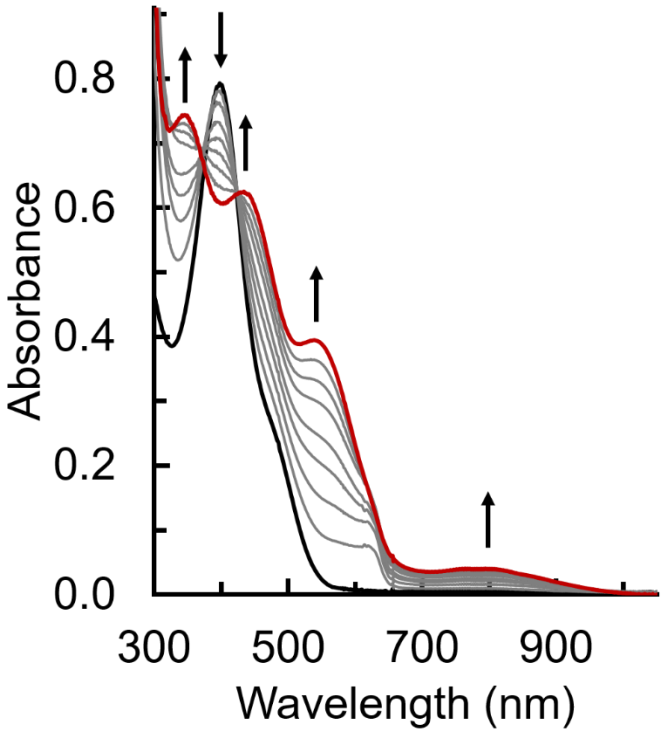

Figure 3-6. UV-vis spectral changes during the oxidation of [Fe^{III}H$_3$buea(OH)]$^-$ to (black) with [FeCp$_2$]$^+$ in EtCN at –80 °C in the presence of five equivalents of DBU to yield absorbance features for [Fe^{IV}H$_3$buea(O)]$^-$ (red). Gray lines represent spectra recorded at 10 second intervals.

to protonation; meaning the maximum yield of [Fe^{IV}H$_3$buea(O)]$^-$ under these conditions would be 50%. To mitigate the loss of starting Fe^{III}-hydroxido complex, the oxidation of [Fe^{III}H$_3$buea(OH)]$^-$ by [FeCp$_2$]$^+$ in EtCN at –80 °C was carried out in the presence of excess DBU resulting in the generation of [Fe^{IV}H$_3$buea(O)]$^-$ in ~70% spectroscopic yield (Figure 3-6). In addition, the λ_{max} = 425 nm band associated with the protonated [Fe^{III}H$_3$buea(OH)]$^-$ complex was not observed. The isolated yield of the potassium salt of [Fe^{IV}H$_3$buea(O)]$^-$ could also be dramatically improved by the addition of base. The treatment of a solution of [Fe^{III}H$_3$buea(OH)]$^-$

in MeCN at –35 °C with $[FeCp_2]^+$ in the presence of five equivalents of DBU resulted in the isolation of $K[Fe^{IV}H_3buea(O)]$ as a maroon solid in 65(5)% yield with physical properties identical to what has been previously reported.[29]

Summary and Conclusion

The oxidation of an Fe^{III}-hydroxido complex, $[Fe^{III}H_3buea(OH)]^-$, has been shown to result in isolation of an Fe^{IV}-oxido complex, $[Fe^{IV}H_3buea(O)]^-$, in what is formally a PCET reaction with no observable intermediate. This reaction proceeded cleanly in solvents like DMF, but was low yielding in less protophilic solvents like MeCN and THF. Oxidation of $[Fe^{III}H_3buea(OH)]^-$ in MeCN/EtCN produced a new band at λ_{max} = 425 nm in addition to bands associated with $[Fe^{IV}H_3buea(O)]^-$. The origin of the band at λ_{max} = 425 nm was independently shown to be the mono-protonated form of $[Fe^{III}H_3buea(OH)]^-$, likely a dimeric Fe^{III} species, which can be produced either by the direct protonation of $[Fe^{III}H_3buea(OH)]^-$. The same absorbance feature was also observed from the addition of either excess $[FeCp_2]$ or one equivalent of $[Fe^{III}H_3buea(OH)]^-$ to $[Fe^{IV}H_3buea(O)(H)]$. These results suggested that $[Fe^{III}H_3buea(OH)]^-$ can act as a base and that the maximum theoretical yield of $[Fe^{IV}H_3buea(O)]^-$ can be only up to 50% from the oxidation of $[Fe^{III}H_3buea(OH)]^-$. However, with the addition of five equivalents of DBU, the yield of $[Fe^{IV}H_3buea(O)]^-$ was nearly twice that produced in the absence of base as determined by both spectroscopic and isolated mass measurements.

The reactivity described is an example of how a high valent metal-oxido complex can be formed by PCET from a related metal-hydroxido complex. While the Nam group has described the effect of weak bases on a PCET processes of a series of mononuclear Fe complexes in MeCN, the chemistry discussed in this chapter illustrates not only the role of proton acceptors in solution, but the role of the solvent itself in affecting a PCET reaction. Similar solvent considerations may benefit those working with model systems attempting to generate enzymatic reaction

intermediates by accounting for changes in protonation states associated with PCET processes by high valent metal-oxido and –hydroxido complexes.

Experimental Section

General Procedures. All manipulations, unless otherwise stated, were performed under an argon atmosphere in a Vac-atmospheres dry box. All chemicals were purchased from commercial sources and used without further purification unless otherwise stated. Ferrocene was sublimed prior to use. $K[Fe^{IV}H_3buea(O)]$, $K[Fe^{III}H_3buea(OH)]$, $[FeCp_2][BF_4]$, and [N(*p*-tolyl)$_3$][OTf] were prepared according to previously published procedures.[29,32–34]

Physical Methods. Electronic absorption spectra were recorded in a 1 cm cuvette on an 8453 Agilent UV-Vis spectrometer equipped with an Unisoku Unispeks cryostat. X-band (9.28 GHz) EPR spectra were collected as frozen solutions using a Bruker EMX spectrometer equipped with an ER041XG microwave bridge.

Reactivity Studies of $[Fe^{III}H_3buea(OH)]^-$ at Low Temperature using UV-vis Spectroscopy. A stock solution of $[Fe^{III}H_3buea(OH)]^-$ at 20 mM concentration (11 mg, 0.020 mmol) was prepared in THF or EtCN (1 mL) with 1.5 equiv 18-crown-6 ether (8 mg, 0.05 mmol) and stored at −36 °C. In a typical experiment, to a 1 cm cuvette was transferred 20 μL of this solution and 2 mL of pure solvent to yield a 0.2 mM solution of $[Fe^{III}H_3buea(OH)]^-$. The cuvette was sealed with a rubber septum then transferred to the precooled UV-vis spectrometer and allowed to equilibrate for at least 20 minutes at –80 °C under a flow of argon gas. Stock solutions of reactants were prepared by dissolving 10 mg in 1 mL of the appropriate solvent generating solutions between 20-40 mM. Solutions of reagents were then injected via gas-tight syringe and the progress of the reaction was monitored spectrophotometrically.

Oxidation of $[Fe^{III}H_3buea(OH)]^-$ in the Absence and Presence of DBU. A stock solution of $[Fe^{III}H_3buea(OH)]^-$ was prepared in either EtCN or DMF as described above. A stock solution of

$[FeCp_2][BF_4]$ (10 mg, 0.036 mmol), was prepared in either EtCN or DMF (2 mL). If necessary, a stock solution of DBU (20 mg, 0.130 mmol) was prepared by dissolving in EtCN (1 mL). A 2 mL solution of 0.2 mM $[Fe^{III}H_3buea(OH)]^-$ was prepared in a 1 cm quartz cuvette as described above and sealed with a rubber septum before cooling to –80 °C in the cryostat of the UV-vis spectrometer. To this solution, either one equivalent of $[FeCp_2]^+$ was added via gas-tight syringe directly or the solution was first treated with five equivalents of DBU prior to oxidation. Reactions were monitored spectrophotometrically until no further changes were observed.

Reaction of $[Fe^{IV}H_3buea(O)(H)]$ with $[FeCp_2]$ or $[Fe^{III}H_3buea(OH)]$-. A stock solution of $[Fe^{III}H_3buea(OH)]$- was prepared as described above. For a typical experiment, a stock solution of $[Fe^{IV}H_3buea(O)]^-$ at ~100-200 μM concentration (2 mg, 0.004 mmol) was prepared in THF (15 mL) with 1.5 equiv 18-crown-6 ether (2 mg, 0.01 mmol) and stored at −36 °C. The concentration of $[Fe^{IV}H_3buea(O)]^-$ was determined using the extinction coefficient at λ_{max} = 550 nm (ε = 3000 $M^{-1}cm^{-1}$). To a 1 cm cuvette was added 2 mL of metal complex solution. The cuvette was sealed with a rubber septum then transferred to the precooled UV-vis spectrometer and allowed to equilibrate for at least 20 minutes at –80 °C under a flow of argon gas. A solution of $[H_3NPh][BF_4]$ was prepared by dissolving the white solid (10 mg, 0.055 mmol) in THF (2 mL). A stock solution of $[FeCp_2]$ (20 mg, 0.11 mmol) was prepared in THF (1 mL). To a solution of $[Fe^{IV}H_3buea(O)]^-$ precooled to –80 °C was added one equivalent of $[H_3NPh][BF_4]$ and the reaction was monitored spectrophotometrically for the generation of $[Fe^{IV}H_3buea(O)(H)]$ and disappearance of $[Fe^{IV}H_3buea(O)]^-$. Upon complete generation of $[Fe^{IV}H_3buea(O)(H)]$, the solution was treated either with 10 equivalents of $[FeCp_2]$ or one equivalent of $[Fe^{III}H_3buea(OH)]$- and monitored spectrophotometrically until no further changes were observed.

Preparation of Low-Temperature EPR Samples. A solution of 20 mM solution of $[Fe^{III}H_3buea(OH)]^-$ was transferred to an EPR tube and sealed with a rubber septum. The tube

was brought out of the dry box and placed in a −78 °C acetone/dry ice bath and allowed to equilibrate for five minutes. Stock solutions of reactant prepared as described above were added via a gas-tight syringe. After mixing by careful shaking of the tube, the EPR tube was quickly removed from the cold bath, wiped clean of methanol, and frozen in liquid nitrogen before analysis.

Bulk Preparation of K[Fe^{IV}H$_3$buea(O)]. In a 20 mL scintillation vial equipped with a stir bar, K[Fe^{III}H$_3$buea(OH)] (50 mg, 0.090 mmol) was dissolved in MeCN (7 mL). The solution was filtered using a fine fritted glass funnel and the insoluble material was washed with diethyl ether (Et_2O), dried briefly under vacuum, and the mass removed was used to adjust the mass of K[Fe^{III}H$_3$buea(OH)] in solution for future calculations. After correcting for mass lost, 1-5 mg in a typical experiment, five equivalents of DBU (68 mg, 0.45 mmol) were added and the solution was cooled to –35 °C. After 15 minutes, the solution was brought out of the freezer and placed into a pre-cooled aluminum block drilled to hold a scintillation vial to maintain the temperature near –35 °C. After adjusting for the mass lost, [$FeCp_2$][BF_4] (24 mg, 0.089 mmol) was added to the solution of [Fe^{III}H$_3$buea(OH)]$^-$ in several portions resulting in the immediate precipitation of a dark maroon solid. The solution was immediately filtered on a fine fritted glass funnel to collect the solid which was washed three times with 0.5 mL of MeCN until the filtrate was light pink, then with 5 mL of THF, 5 mL of Et_2O, and 5 mL of pentane before drying under vacuum for one hour yielding a dark red/brown or maroon solid in 65(5)% yield. The physical and spectroscopic properties of this solid were identical to those previously reported.[29]

References

(1) Cox, N.; Pantazis, D. A.; Neese, F.; Lubitz, W. *Acc. Chem. Res.* **2013**, *46*, 1588–1596.
(2) Groves, J. T. *Nat. Chem.* **2014**, *6*, 89–91.
(3) Shook, R. L.; Borovik, A. S. *Inorg. Chem.* **2010**, *49*, 3646–3660.
(4) Eberson, L. *Adv. Phys. Org. Chem.* **1982**, *18*, 79–185.
(5) Matyjaszewski, K.; Xia, J. *Chem. Rev.* **2001**, *101*, 2921–2990.

(6) Li, C.-J. *Chem. Rev.* **2005**, *105*, 3095–3166.
(7) Mayer, J. M. *Annu. Rev. Phys. Chem.* **2004**, *55*, 363–390.
(8) Weinberg, D. R.; Gagliardi, C. J.; Hull, J. F.; Murphy, C. F.; Kent, C. A.; Westlake, B. C.; Paul, A.; Ess, D. H.; McCafferty, D. G.; Meyer, T. J. *Chem. Rev.* **2012**, *112*, 4016–4093.
(9) Usharani, D.; Lacy, D. C.; Borovik, A. S.; Shaik, S. *J. Am. Chem. Soc.* **2013**, *135*, 17090–17104.
(10) Lai, W.; Li, C.; Chen, H.; Shaik, S. *Angew. Chem. Int. Ed. Engl.* **2012**, *51*, 5556–5578.
(11) Mayer, J. *Acc. Chem. Res.* **1998**, *31*, 441–450.
(12) Chen, Z.; Yin, G. *Chem. Soc. Rev.* **2015**, *44*, 1083–1100.
(13) Prat, I.; Company, A.; Postils, V.; Ribas, X.; Que, L.; Luis, J. M.; Costas, M. *Chemistry* **2013**, *19*, 6724–6738.
(14) Krest, C. M.; Onderko, E. L.; Yosca, T. H.; Calixto, J. C.; Karp, R. F.; Livada, J.; Rittle, J.; Green, M. T. *J. Biol. Chem.* **2013**, *288*, 17074–17081.
(15) Green, M. T. *Curr. Opin. Chem. Biol.* **2009**, *13*, 84–88.
(16) Godula, K.; Sames, D. *Science* **2006**, *312*, 67–72.
(17) Wasylenko, D. J.; Palmer, R. D.; Berlinguette, C. P. *Chem. Commun.* **2013**, *49*, 218–227.
(18) Moyer, B. A.; Meyer, T. J. *J. Am. Chem. Soc.* **1978**, *100*, 3601–3603.
(19) Binstead, R. A.; Moyer, B. A.; Samuels, G. J.; Meyer, T. J. *J. Am. Chem. Soc.* **1981**, *103*, 2897–2899.
(20) Moyer, B. A.; Meyer, T. J. *Inorg. Chem.* **1981**, *20*, 436–444.
(21) Cox, N.; Pantazis, D. A. DA; Neese, F.; Lubitz, W. *Acc. Chem. Res.* **2013**, *46*, 1588–1596.
(22) Gupta, R.; Taguchi, T.; Lassalle-Kaiser, B.; Bominaar, E. L.; Yano, J.; Hendrich, M. P.; Borovik, A. S. *Proc. Natl. Acad. Sci. U. S. A.* **2015**, *112*, 5319–5324.
(23) Fukuzumi, S.; Mandal, S.; Mase, K.; Ohkubo, K.; Park, H.; Benet-Buchholz, J.; Nam, W.; Llobet, A. *J. Am. Chem. Soc.* **2012**.
(24) Chang, C. J.; Chng, L. L.; Nocera, D. G. *J. Am. Chem. Soc.* **2003**, *125*, 1866–1876.
(25) Lee, Y.-M.; Dhuri, S. N.; Sawant, S. C.; Cho, J.; Kubo, M.; Ogura, T.; Fukuzumi, S.; Nam, W. *Angew. Chemie* **2009**, *121*, 1835–1838.
(26) Brines, L. M.; Coggins, M. K.; Poon, P. C. Y.; Toledo, S.; Kaminsky, W.; Kirk, M. L.; Kovacs, J. A. *J. Am. Chem. Soc.* **2015**, *137*, 2253–2264.
(27) Nishida, Y.; Morimoto, Y.; Lee, Y.-M.; Nam, W.; Fukuzumi, S. *Inorg. Chem.* **2013**, *52*, 3094–3101.
(28) Kaizer, J.; Klinker, E. J.; Oh, N. Y.; Rohde, J.-U.; Song, W. J.; Stubna, A.; Kim, J.; Münck, E.; Nam, W.; Que, L. *J. Am. Chem. Soc.* **2004**, *126*, 472–473.
(29) Lacy, D. C.; Gupta, R.; Stone, K. L.; Greaves, J.; Ziller, J. W.; Hendrich, M. P.; Borovik, A. S. *J. Am. Chem. Soc.* **2010**, *132*, 12188–12190.
(30) Luo, Y.-R. *Comprehensive Handbook of Chemical Bond Energies*; CRC Press, 2007.
(31) Curphey, T. J.; Santer, J. O.; Rosenblum, M.; Richards, J. H. *J. Am. Chem. Soc.* **1960**, *82*, 5249–5250.
(32) Shirin, Z.; Hammes, B. S.; Young, V. G.; Borovik, A. S. *J. Am. Chem. Soc.* **2000**, *122*, 1836–1837.
(33) MacBeth, C. E.; Hammes, B. S.; Victor G. Young, J.; Borovik, A. S. *Inorg. Chem.* **2001**, *40*, 4733–4741.
(34) Connelly, N. G.; Geiger, W. E. *Chem. Rev.* **1996**, *96*, 877–910.

Chapter 4

Modulation of the Secondary Coordination Sphere of a Series of High Valent Fe-Oxido Complexes

Introduction

The importance of the secondary coordination sphere in controlling and modulating the catalytic function of metalloproteins cannot be overstated.[1–3] Non-covalent interactions are used to facilitate the transfer of protons and electrons, as well as control the position of substrates within the active site. Secondary coordination sphere interactions can often be dynamic, in order to accommodate various species that bind to a metal center; this type of dynamic behavior is especially significant in metalloproteins.[4] One family of enzymes that demonstrates dynamic interactions within the secondary coordination sphere are the cytochrome c peroxidases (CCPs).[4-6] The active site contains several key structural and functional components: a heme-Fe with axial histidine (His) ligation, a distal His, and a nearby redox-active tryptophan (Trp) residue. CCPs belong to a family of heme enzymes that use H_2O_2 as an oxidant to oxidize cytochrome c.[7] In this process, there are several steps involving the movement of protons and electrons to and from the

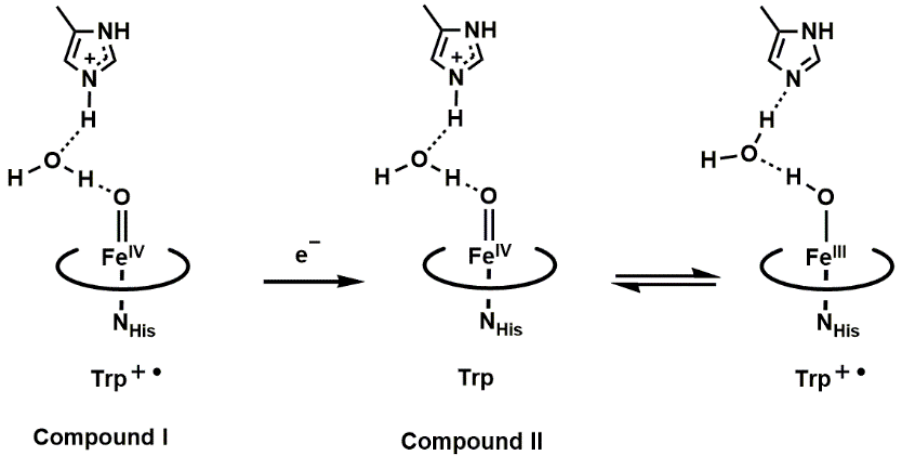

Scheme 4-1. The proposed mechanism for proton transfer in CCP as Compound I is reduced to Compound II. Dotted lines indicate H-bonding. Trp designates a nearby tryptophan residue which participates in electron transfer.

heme active site. After the O–O bond of H_2O_2 is cleaved, there is a proton transferred to the distal His coupled with the formation of Compound I (CCP-I). Rather than a porphyrin-based radical like in Compound I of P450s, CCP-I consists of an Fe^{IV}-oxido complex with a radical being delocalized onto the nearby Trp residue. CCP-I is then reduced by one electron to generate Compound II (CCP-II), which still contains an Fe^{IV}-oxido heme unit but with the Trp radical quenched.[8] Recently, Poulos was able to determine that the pK_a of the distal His increases upon generation of CCP-I so that a proton liberated from the reduction of H_2O_2 protonates this His rather than the Fe^{IV}–oxido unit (Scheme 4-1). As CCP-I is reduced, the pK_a of the distal His decreases and the proton transfers to the oxido unit via a H-bonded, structural water molecule and an electron transfer occurs to regenerate the $Trp^{+\bullet}$ and an Fe^{III}-hydroxido complex.[9] This type of dynamic proton transfer is a challenge to reproduce in a synthetic system, but it would be beneficial to incorporate similar architectures to serve as proton relays in a synthetic metal complex.

Chapter 2 discussed the generation of a protonated Fe^{IV}-oxido complex, [$Fe^{IV}H_3$buea(O)(H)] in which the proton is most likely located on the urea ligand. This demonstrates the potential for a ligand bound to a metal complex to facilitate proton transfer to and from the metal complex. However, a limitation of [$Fe^{IV}H_3$buea(O)(H)] was its thermal instability that may possibly be caused by inefficient proton transfer to the $[H_3buea]^{3-}$ ligand. While excellent at forming intramolecular H-bonds, $[H_3buea]^{3-}$ does not contain basic sites within the cavity to effectively transfer protons. An example of such a system, discussed in the introduction, was developed by Dubois using pendant amine functional groups to improve electrocatalytic hydrogen production.[10–12] A system was sought within a tripodal ligand scaffold that could install a basic site within the secondary coordination sphere that could accept or donate a proton to an oxido ligand. The ligand chosen, $[H_2bupa]^{3-}$, is a hybrid tripodal ligand which

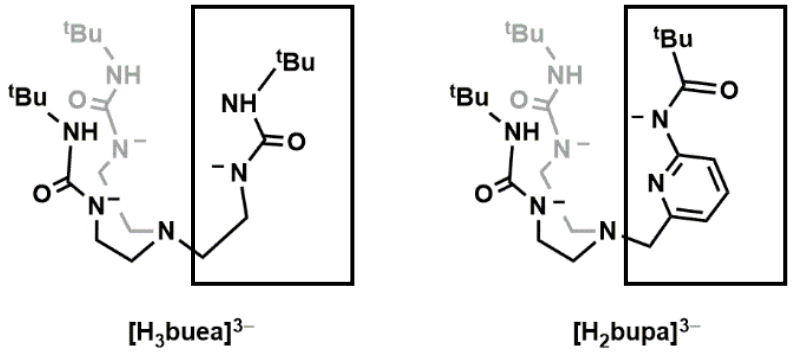

Figure 4-1. Comparison of the structures of the $[H_3buea]^{3-}$ and $[H_2bupa]^{3-}$ ligands. The boxes highlight changes in the primary and secondary coordination sphere upon formation of a metal complex.

contains two urea-based arms like those in $[H_3buea]^{3-}$, but the third arm is a pyridyl-amide moiety (Figure 4-1). The pyridyl-amide moiety has been used by several groups including Collman, Masuda, and Goldberg to stabilize various traditionally reactive species such as O_2 adducts and high valent oxido complexes.[13–17] Changing this arm affects a metal complex in two ways: 1) the primary sphere is changed from three anionic, ureate donors to two with the addition of a neutral pyridine which should result in slightly less electronic donation to the metal ion and 2) the secondary coordination sphere is now asymmetric because of the difference in the pK_a values of the amide (~21, DMSO, r.t.) compared to the urea (~26, DMSO, r.t.).[18] Because of this difference

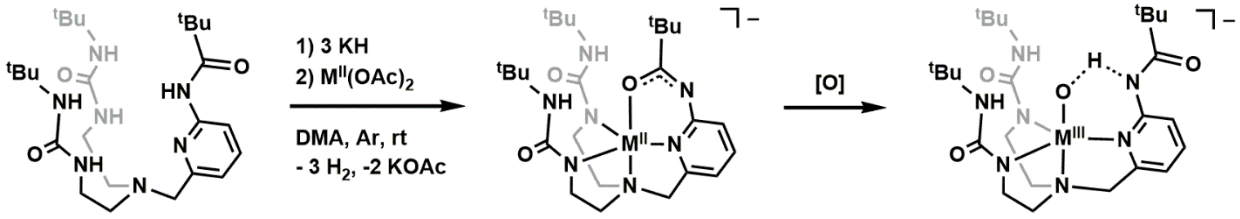

Scheme 4-2. Generic synthesis of a $[M^{II}H_2bupa]^-$ complex by the addition of three equivalents of potassium hydride followed by the $M^{II}(OAc)_2$ to H_5bupa in DMA. To the right is a depiction of the oxidation of $[M^{II}H_2bupa]^-$ with an oxygen-atom source under various conditions to generate a $[M^{III}H_2bupa(O)(H)]^-$ complex.

in pK_a values between amides and ureas, the addition of three equivalents of potassium hydride when synthesizing a metal complex results in the deprotonation of the amide prior to the urea arms to generate two ureate and one amidate groups. The binding of a metal ion results in the

ureates, pyridine, and amidate coordinating to the metal ion. Note that the amidate coordinates to the metal ion through the oxygen atom of the carbonyl group and can also serve as a basic site within the secondary coordination sphere (Figure 4-2). The initial reports on the Mn chemistry with this ligand demonstrated these structural concepts: in the absence of a suitable exogenous ligand, the amidate oxygen can rotate towards the metal ion and serve as a fifth ligand to a Mn^{II} ion (Scheme 4-2).[19] From the addition of dioxygen to the $[Mn^{II}H_2bupa]^-$ complex, a new species was isolated and shown to be a $[Mn^{III}H_2bupa(O)(H)]^-$ complex.[20] The structure of this complex as determined by X-ray diffraction (XRD) methods showed that the amidate has rotated so that there is a close contact between the amidate nitrogen and oxido ligand (less than 2.7 Å), suggesting the proton is positioned between the nitrogen and oxygen atoms. The uncertainty in the location of the proton produced a complex which cannot be easily assigned as either a Mn-hydroxido or Mn-oxido complex and was reported as a "hybrid" between these two possible states. These findings illustrated the changes in structure of metal complexes of the $[H_2bupa]^{3-}$ ligand that affects the properties within the secondary coordination sphere. Moreover, the structural changes are linked to the protonation states of the M–O unit that could be further exploited to facilitate proton transfer process.

This chapter describes a series of Fe complexes with the $[H_2bupa]^{3-}$ ligand that are generated and characterized by several spectroscopic methods including UV-vis, electron paramagnetic resonance (EPR), Mössbauer, nuclear resonance vibrational spectroscopies (NRVS), and cyclic voltammetry. The data showed that addition of dioxygen or O-atom transfer agents to the $[Fe^{II}H_2bupa]^-$ complex generated an Fe^{III} complex assigned to $[Fe^{III}H_2bupa(O)(H)]^-$. This new Fe^{III} complex behaves as a "hybrid" of an oxido or hydroxido complex (similar to $[Mn^{III}H_2bupa(O)(H)]^-$) based on vibrational, EPR, and voltammetry experiments. The $[Fe^{III}H_2bupa(O)(H)]^-$ complex can be further oxidized to give an Fe^{IV} species. In contrast to the

Fe^{III} complex, this complex appears to be a true Fe^{IV}-oxido complex with spectroscopic properties strikingly similar to $[Fe^{IV}H_3buea(O)(H)]$, suggesting very similar electronic and coordination properties. Unlike the $[H_3buea]^{3-}$ system, the $Fe^{III/IV}$ redox process was chemically reversible. The reversibility was attributed to the ability of the proton to shift between the oxido ligand and the amidate nitrogen as the complex is oxidized or reduced similar to the protonation state changes observed in CCPs. Throughout this chapter, the properties of the complexes with the $[H_2bupa]^{3-}$ ligand will be compared to those of $[H_3buea]^{3-}$ in an attempt to show how the location of the proton changes from the oxido ligand as the oxidation state is changed.

Results and Discussion

Synthesis and Characterization of $[Fe^{II}H_2bupa]^-$. Treatment of a solution of H_5bupa in DMA with three equivalents of potassium hydride generates the ligand $[H_2bupa]^{3-}$ and the addition of $Fe^{II}(OAc)_2$ results in the formation of $[Fe^{II}H_2bupa]^-$ which can be isolated as the potassium salt. This complex exhibits an intense, asymmetric absorbance feature at λ_{max} = 560 nm (ε = 1200 M-

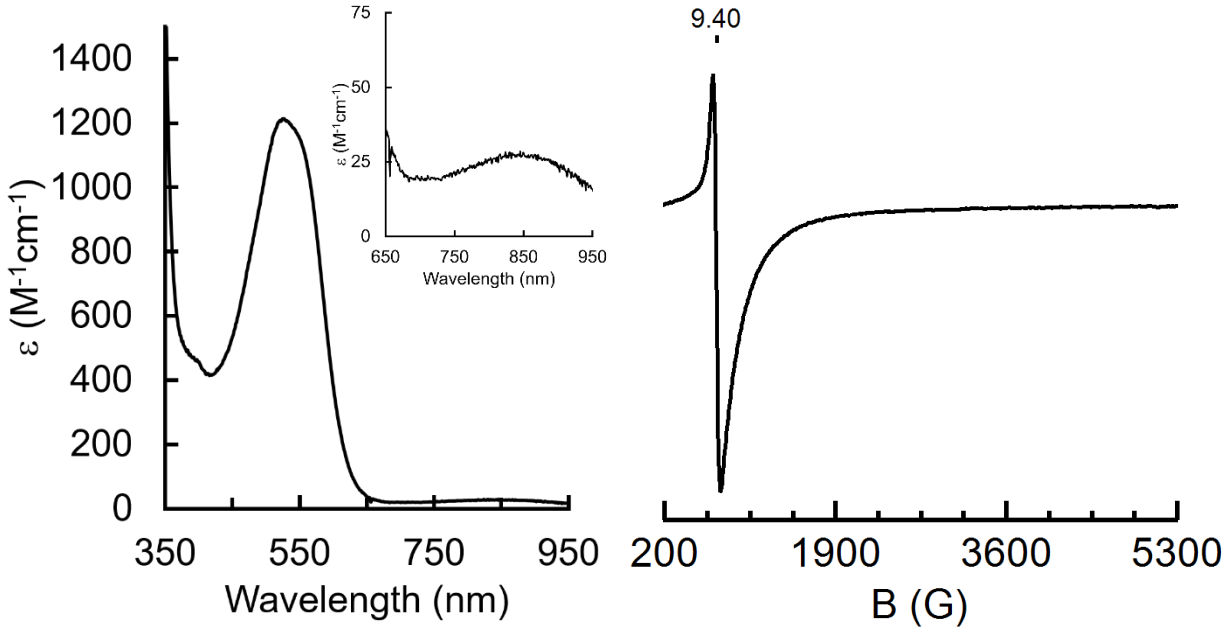

Figure 4-2. Optical absorbance spectrum (left) of a 0.2 mM solution of $[Fe^{II}H_2bupa]^-$ in EtCN at 10 °C and parallel mode EPR spectrum (right) of a 20 mM solution of $[Fe^{II}H_2bupa]^-$ in 1:1 DMF:THF collected at 10 K. Inset: Low energy region showing the low intensity absorption.

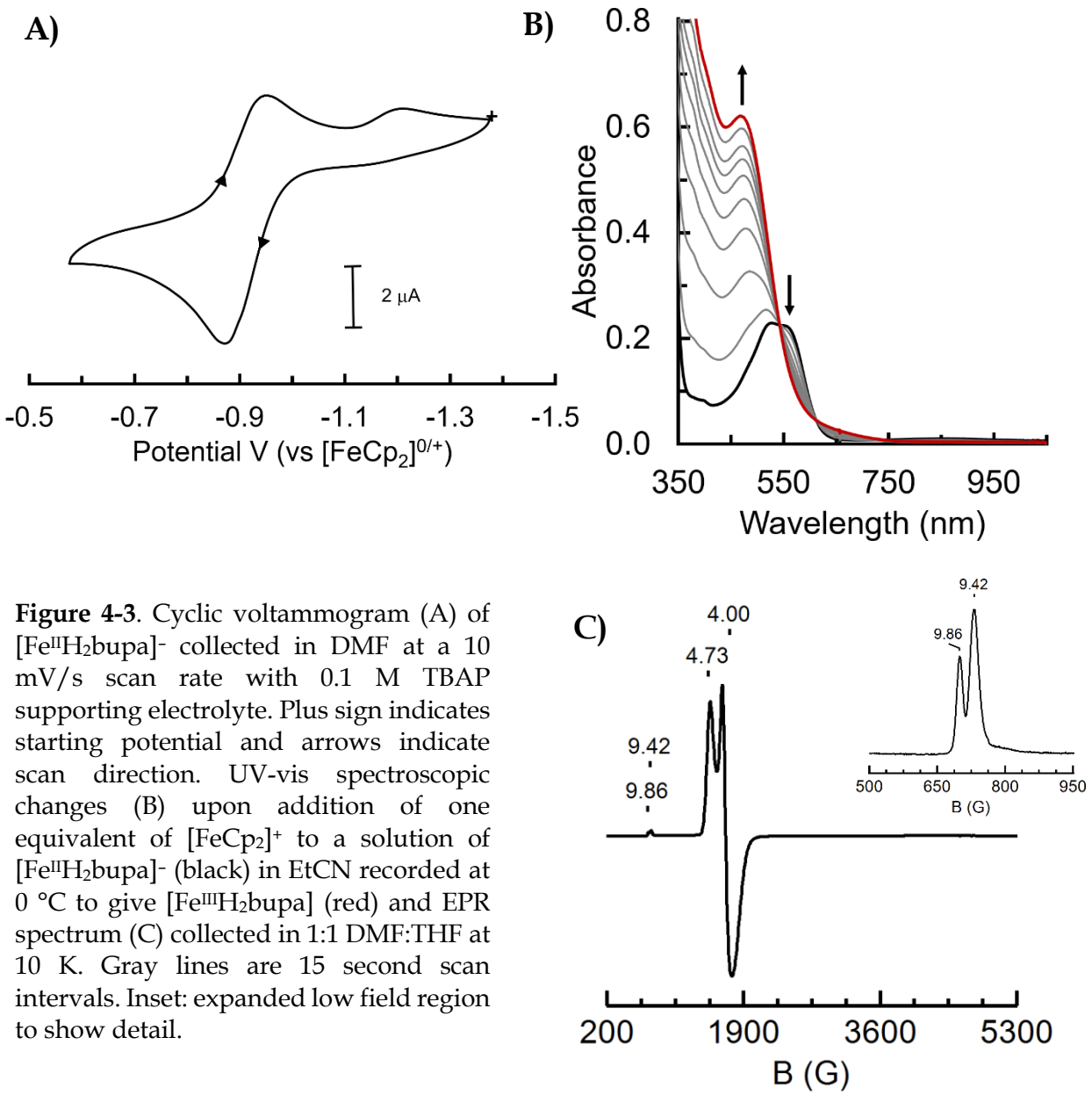

Figure 4-3. Cyclic voltammogram (A) of $[Fe^{II}H_2bupa]^-$ collected in DMF at a 10 mV/s scan rate with 0.1 M TBAP supporting electrolyte. Plus sign indicates starting potential and arrows indicate scan direction. UV-vis spectroscopic changes (B) upon addition of one equivalent of $[FeCp_2]^+$ to a solution of $[Fe^{II}H_2bupa]^-$ (black) in EtCN recorded at 0 °C to give $[Fe^{III}H_2bupa]$ (red) and EPR spectrum (C) collected in 1:1 DMF:THF at 10 K. Gray lines are 15 second scan intervals. Inset: expanded low field region to show detail.

$^1cm^{-1}$), due to a metal-to-ligand charge transfer between the Fe^{II} center and the coordinated pyridine, and a weak, broad absorbance at λ_{max} = 850 nm (ε = 25 $M^{-1}cm^{-1}$) consistent with a d-d transition. The parallel-mode EPR spectrum shows a sharp derivative signal at g = 9.4, consistent with a mononuclear, high spin Fe^{II} center with an S = 2 spin ground state (Figure 4-2). The molecular structure of $K[Fe^{II}H_2bupa]$ by X-ray diffraction (XRD) methods and other characterization data have previously been reported.[21]

The electrochemical properties of $[Fe^{II}H_2bupa]^-$ were evaluated in *N,N*-dimethylformamide (DMF) by cyclic voltammetry and revealed a single oxidative event at –0.91 V vs. $[FeCp_2]^{0/+}$ with $i_{p,c}/i_{p,a}$ = 0.61 (Figure 4-3A). There is also an additional, unidentified reductive event at –1.19 V vs. $[FeCp_2]^{0/+}$. The oxidation was examined chemically by the addition of $[FeCp_2]^+$ to a solution of $[Fe^{II}H_2bupa]^-$ in propionitrile (EtCN) at 0 °C which showed a loss of the characteristic absorbance bands of the starting Fe^{II} complex to give a broad absorbance band centered at λ_{max} = 470 nm. Examining the oxidation of $[Fe^{II}H_2bupa]^-$ with $[FeCp_2]^+$ by EPR spectroscopy gave a spectrum consistent with a mononuclear, high spin Fe^{III} center with g-values at 4.00, 4.73, 9.42, and 9.86. The identification and characterization of the proposed $[Fe^{III}H_2bupa]$ are important because they may be useful in future mechanistic examinations of either the reduction of dioxygen or the oxidation of water in the $[Fe^{II}H_2bupa]^-$ system.

Synthesis and Characterization of $[Fe^{III}H_2bupa(O)(H)]^-$. The $[Fe^{II}H_2bupa]^-$ can be oxidized using either dioxygen (O_2) or the oxygen-atom (O-atom) transfer agent, *N*-methylmorphyline *n*-

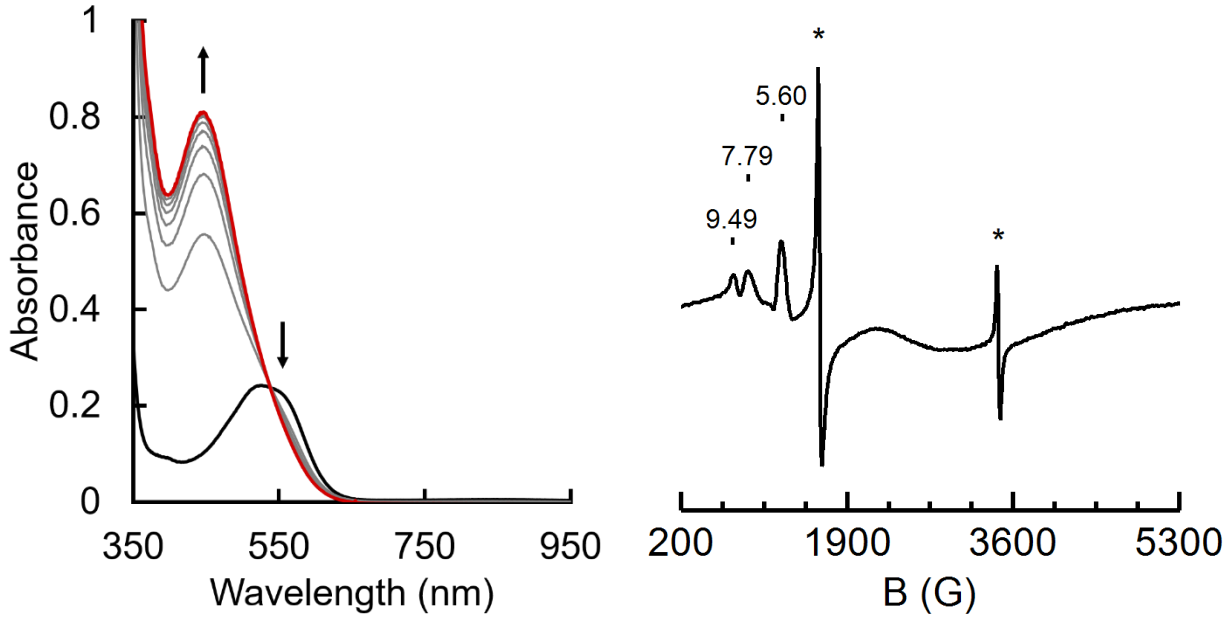

Figure 4-4. UV-vis (left) spectroscopic changes upon addition of one equivalent of NMO to a solution of $[Fe^{II}H_2bupa]^-$ (black) in EtCN recorded at 10 °C to give $[Fe^{III}H_2bupa(O)(H)]^-$ (red) and EPR spectrum collected in 1:1 DMF:THF at 10 K. Gray lines are 15 minute scan intervals. Asterisks indicate minor ferric and radical impurities at g = 4.3 and 2.0.

oxide (NMO), to give the same complex assigned as $[Fe^{III}H_2bupa(O)(H)]^-$. The reaction between $[Fe^{II}H_2bupa]^-$ with NMO was monitored spectrophotometrically in EtCN at room temperature and shows the disappearance of the visible absorbance bands of $[Fe^{II}H_2bupa]^-$ and the growth of a single visible band at λ_{max} = 430 nm (Figure 4-4). A perpendicular EPR spectrum of the reaction mixture collected at 10 K shows prominent peaks at g = 5.60, 7.79, and 9.49 consistent with a mononuclear, high spin Fe^{III} center (Figure 4-4).

To interrogate the Fe–O bond, a NRVS spectrum, in collaboration with the Hendrich lab (CMU), was collected on a frozen solution of $[Fe^{III}H_2bupa(O)(H)]^-$ and showed a peak at 593 cm^{-1} that was assigned to the Fe–O vibrational band. For comparison to this complex, two other Fe^{III} complexes were examined by NRVS as well, $[Fe^{III}H_3buea(OH)]^-$ and $[Fe^{III}H_3buea(O)]^{2-}$. The Fe–O vibrations for the $[Fe^{III}H_3buea(OH)]^-$ and $[Fe^{III}H_3buea(O)]^{2-}$ complexes were observed at 477 cm^{-1} and 663 cm^{-1}, respectively. This result demonstrates that, similar to the previously reported

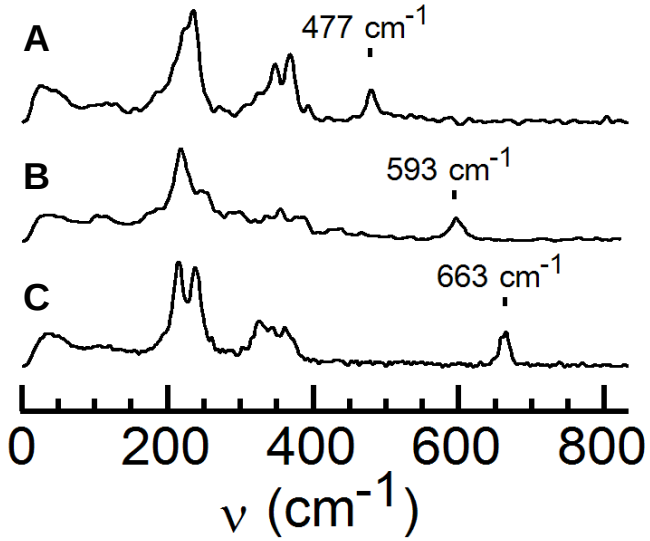

Figure 4-5. NRVS spectra for (A) a 20 mM solution of $[^{57}Fe^{III}H_3buea(^{16}OH)]^-$ in THF, (B) the reaction of a 30 mM solution of $[^{57}Fe^{II}H_2bupa]^-$ with one equivalent NMO in EtCN, and C) a 15 mM solution of $[^{57}Fe^{III}H_3buea(^{16}O)]^{2-}$ in THF. Labeled peaks assigned to the Fe—O vibrations.

$[Mn^{III}H_2bupa(O)(H)]^-$ complex, the $[Fe^{III}H_2bupa(O)(H)]^-$ complex can best be described as a "hybrid" between an Fe^{III}-oxido and Fe^{III}-hydroxido complex. This is likely a result of anionic

nitrogen from the amidate in the secondary coordination sphere serving to position the proton between the nitrogen and oxygen atoms. A solid state structure has not been determined for $[Fe^{III}H_2bupa(O)(H)]^-$ as the complex is not stable enough in solution for extended periods of time.

The electrochemical properties of $[Fe^{III}H_2bupa(O)(H)]^-$ were examined using cyclic voltammetry. The complex displays both a quasi-reversible oxidation and quasi-reversible reduction when collected at room temperature in DMF. The Fe^{III}/Fe^{IV} couple was assigned to a quasi-reversible oxidative event at –0.17 V vs. $[FeCp_2]^{0/+}$ with $i_{p,c}/i_{p,a}$ = 0.78. The irreversible reduction event at –1.76 V vs $[FeCp_2]^{0/+}$ was assigned to the Fe^{III}/Fe^{II} redox process (Figure 4-6). However, if successive scans are taken, the growth of an additional redox event can be observed which matches the Fe^{III}/Fe^{II} redox couple for $[Fe^{II}H_2bupa]^-$. This suggests that the one electron reduction of $[Fe^{III}H_2bupa(O)(H)]^-$ results in the expulsion of the hydroxido ligand to generate $[Fe^{II}H_2bupa]^-$. This may have mechanistic implications for the mechanism of the reduction of O_2 to water by complexes supported by the $[H_2bupa]^{3-}$ ligand.

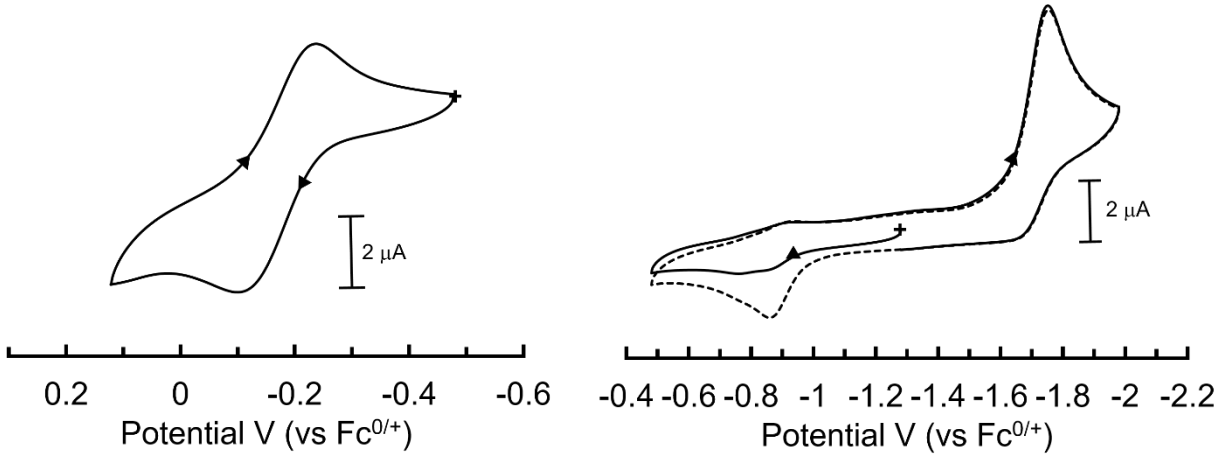

Figure 4-6. Cyclic voltammograms of a solution of $[Fe^{III}H_2bupa(O)(H)]^-$ generated from the addition of one equivalent of NMO to $[Fe^{II}H_2bupa]^-$ in DMF showing the Fe^{III}/Fe^{IV} couple (left) and the reductive portion (right) showing initial reduction from Fe^{III} to Fe^{II} with growth of an event assigned to $[Fe^{II}H_2bupa]^-$ on the second sweep (dashed line). Both voltammograms recorded in DMF at 10 mV/s scan rate with 0.1 M TBAP as the supporting electrolyte.

Oxidation of [Fe^{III}H$_2$bupa(O)(H)]$^-$ to generate an Fe^{IV}-oxido Complex. The oxidation of [Fe^{III}H$_2$bupa(O)(H)]$^-$ can be accomplished using [FeCp$_2$]$^+$. Monitoring this reaction in EtCN at –35 °C by UV-vis spectroscopy showed two prominent absorbance features at λ_{max} = 385 and 545 nm assigned to [Fe^{IV}H$_2$bupa(O)(H)] (Figure 4-7). The Fe^{IV} complex persists at room temperature for ~10 minutes before decaying to a featureless spectrum; this stability is several orders of

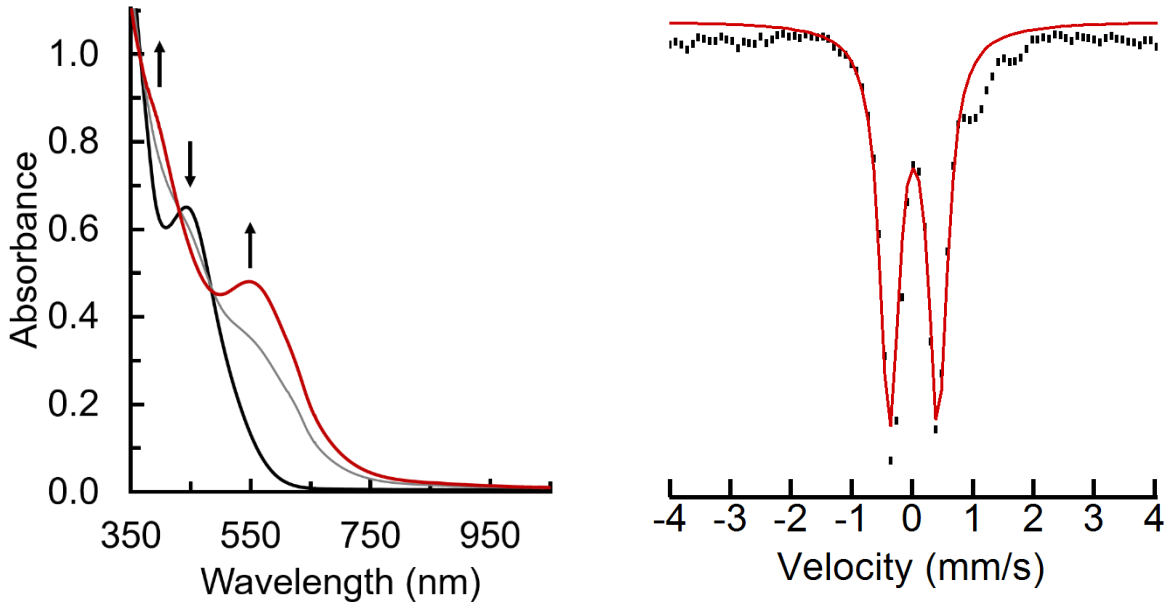

Figure 4-7. UV-vis (left) spectroscopic changes upon addition of one equivalent of [FeCp$_2$]$^+$ to a solution of [Fe^{III}H$_2$bupa(O)(H)]$^-$ (black) in EtCN recorded at –35 °C to give [Fe^{IV}H$_2$bupa(O)(H)] (red) and the corresponding Mössbauer spectrum collected in EtCN at 4 K. Gray line is a single 5 second scan interval between the first and last spectrum collected. Red line is the least-square fit of the experimental Mössbauer data with linewidth of 0.39 mm/s.

magnitude longer than [Fe^{IV}H$_3$buea(O)(H)], which reacts within seconds at room temperature. Following the same reaction by EPR spectroscopy showed the loss of the signal for [Fe^{III}H$_2$bupa(O)(H)]$^-$, however there was no new signal in either perpendicular- or parallel-mode that can be assigned to an Fe^{IV} species. The presence of an Fe^{IV} species was verified using Mössbauer spectroscopy which showed a prominent doublet with δ = 0.02 mm/s and ΔE_Q = 0.80 mm/s, features that are consistent with an Fe^{IV} species with an S = 2 spin ground state. Also

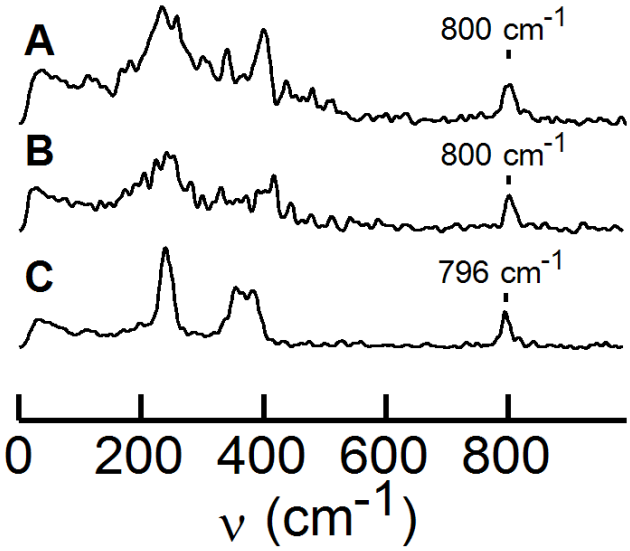

Figure 4-8. NRVS spectra for (A) a 10 mM solution of [$^{57}Fe^{IV}H_2bupa(^{16}O)(H)$] in EtCN, (B) a 10 mM solution of [$^{57}Fe^{IV}H_3buea(^{16}O)(H)$] in THF, and (C) a 10 mM solution of [$^{57}Fe^{IV}H_3buea(^{16}O)]^-$ in THF. Labeled peaks are assigned to the Fe–O vibrations.

present in the spectrum were features associated with some Fe^{III} species, including unreacted $[Fe^{III}H_2bupa(O)(H)]^-$, that accounted for ~35% of the total ^{57}Fe in the sample. Further evidence for the existence of an Fe^{IV}–oxido species came from NRVS data. The NRVS spectrum of the oxidized product showed a prominent peak at 801 cm^{-1}; this energy is nearly the same as the ν_{Fe-O} for the previously characterized $[Fe^{IV}H_3buea(O)]^-$ and its protonated congener discussed in Chapter 2 (Figure 4-8).[22] These data support the premise that a new Fe^{IV}-oxido complex, $[Fe^{IV}H_2bupa(O)(H)]$, has been synthesized.

Reactivity of $[Fe^{IV}H_2bupa(O)(H)]$. Consistent with the electrochemical data for $[Fe^{III}H_2bupa(O)(H)]^-$, the oxidation of $[Fe^{III}H_2bupa(O)(H)]^-$ to generate $[Fe^{IV}H_2bupa(O)(H)]$ was found to be chemically reversible. The addition of $[CoCp_2]$ to a solution of $[Fe^{IV}H_2bupa(O)(H)]$ at –35 °C in EtCN showed the clean conversion back to $[Fe^{III}H_2bupa(O)(H)]^-$ in ~90% yield based on the starting absorbance λ_{max} = 440 nm (Figure 4-9). The reversibility of this redox process supports

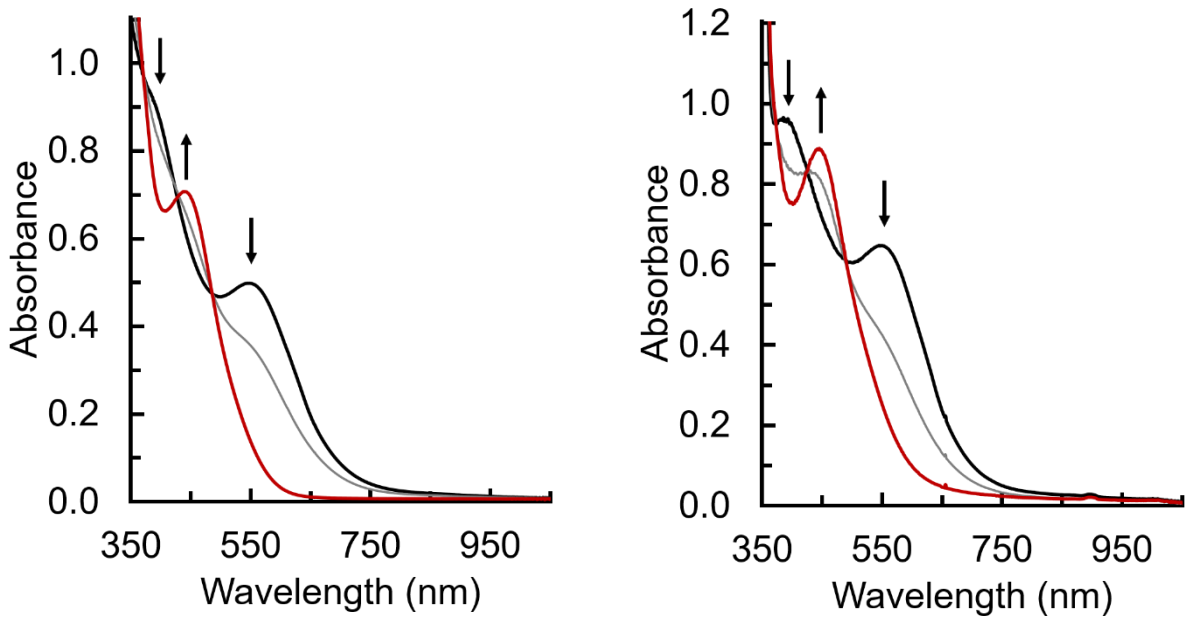

Figure 4-9. UV-vis spectral changes upon addition of one equivalent of $[CoCp_2]$ (left) to a solution of $[Fe^{IV}H_2bupa(O)(H)]$ (black) in EtCN recorded at 0 °C to give $[Fe^{III}H_2bupa(O)(H)]^-$ (red) and addition one equivalent of KO^tBu (right) to a solution of $[Fe^{IV}H_2bupa(O)(H)]$ (black) in EtCN at –80 °C to give $[Fe^{III}H_2bupa(O)(H)]^-$ (red). Gray lines in both represent a single intermediate scan at a 10 second interval.

the initial premise that altering the secondary coordination sphere to provide a site for a single, intramolecular H-bond acceptor could stabilize an Fe^{IV}-(O)(H) complex.

The reactivity of $[Fe^{IV}H_2bupa(O)(H)]$ with acid and base were also examined. Treatment of $[Fe^{IV}H_2bupa(O)(H)]$ with one to three equivalents of $[H_3NPh]^+$ at –80 °C or –35 °C in EtCN resulted in the slight decrease of the absorbance features of $[Fe^{IV}H_2bupa(O)(H)]$, however no new absorbance features were observed. Addition of one to three equivalents of DBU to a solution of $[Fe^{IV}H_2bupa(O)(H)]$ in EtCN at –80 °C or –35 °C resulted in no reaction. If the stronger base, potassium *tert*-butoxide (KO^tBu), was used, the absorbance features of $[Fe^{IV}H_2bupa(O)(H)]$ decrease as a single new band at λ_{max} = 445 nm grows in intensity, suggesting the generation of $[Fe^{III}H_2bupa(O)(H)]^-$ (Figure 4-8). The growth of $[Fe^{III}H_2bupa(O)(H)]^-$ can best be explained by initial deprotonation of $[Fe^{IV}H_2bupa(O)(H)]$ by $^tBuO^-$ to generate a more exposed Fe^{IV}-oxido complex which can then abstract an H-atom, likely from solvent, in order to give

[$Fe^{III}H_2$bupa(O)(H)]$^-$. Alternatively, KO^{t}Bu has been shown to interact with both nitriles and pyridines, under different conditions, to form various electron donors, which could in turn reduce [$Fe^{IV}H_2$bupa(O)(H)] back to [$Fe^{III}H_2$bupa(O)(H)]$^-$ by a simple outer-sphere electron transfer process.[23,24]

The [$Fe^{IV}H_2$bupa(O)(H)] complex was also tested for reactivity towards X–H bond activation and oxygen-atom (O-atom) transfer using various substrates. Treatment of [$Fe^{IV}H_2$bupa(O)(H)] at –35 °C in EtCN with phosphines resulted in no evidence for O-atom

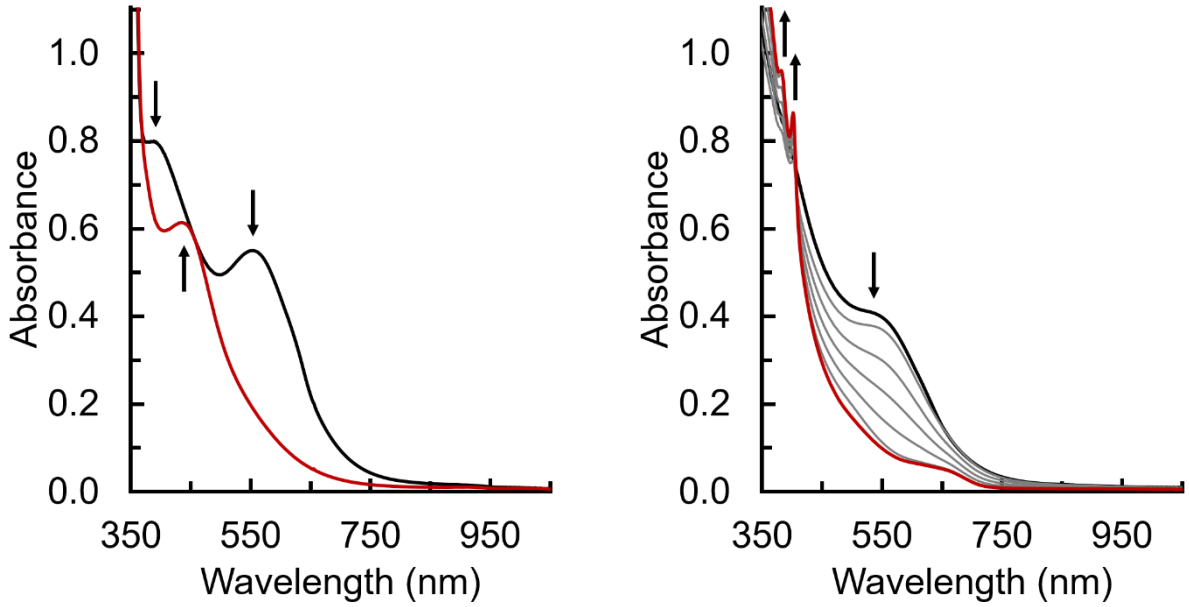

Figure 4-10. UV-vis spectroscopic changes upon addition of half an equivalent of DPH (left) to a solution of [$Fe^{IV}H_2$bupa(O)(H)] (black) in EtCN recorded at –35 °C to give an intense absorbance feature at 435 nm (red) after 5 seconds and addition 100 equivalents of TTBP (right) to a solution of [$Fe^{IV}H_2$bupa(O)(H)] (black) in EtCN at 0 °C to give TTBP radical (red). Gray lines represent 3 minute scan intervals.

transfer either spectrophotometrically or by GC analysis of the reaction mixtures. Additionally, C–H bond activation was not observed under identical conditions using 1,4-cyclohexadiene (CHD), 9,10-dihydroanthracene (DHA), or cumene. Treatment of [$Fe^{IV}H_2$bupa(O)(H)] with diphenylhydrazine (DPH) at –35 °C in EtCN resulted in immediate loss, within 5 seconds, of absorbance features for [$Fe^{IV}H_2$bupa(O)(H)] and growth of a single absorbance feature at λ_{max} =

440 nm which is likely due, in part, to the absorbance of azobenzene and some unidentified Fe species. Finally, reactivity with a substituted phenol was also examined. Addition of a large excess of tri-*tert*-butylphenol (TTBP) to a solution of [$Fe^{IV}H_2$bupa(O)(H)] at 0 °C in EtCN resulted in a slow decrease in absorbance features of [$Fe^{IV}H_2$bupa(O)(H)] and growth of absorbance features associated with TTBP radical at λ_{max} = 380, 400, and 635 nm (Figure 4-10).

Summary and Conclusion

In Chapter 3, the proton coupled electron transfer (PCET) properties observed during the oxidation of [$Fe^{III}H_3$buea(OH)]$^-$ to give [$Fe^{IV}H_3$buea(O)]$^-$ were examined.[22] During this redox process, there is a spontaneous proton transfer which can be taken up by either solvent or a suitable base in solution. This process precludes the reversibility of one electron oxidation of [$Fe^{III}H_3$buea(OH)]$^-$ under the reaction conditions, which may have implications related to PCET in the formation of high valent oxido complexes from related hydroxido complexes. In order to better control the properties of such a redox process, the ligand [H_2bupa]$^{3-}$ was used because of the anionic, basic amidate functional group positioned within the secondary coordination sphere upon metalation. Incorporation of this H–bond accepting site within the secondary coordination sphere gave a reversible redox reaction between [$Fe^{III}H_2$bupa(O)(H)]$^-$ and [$Fe^{IV}H_2$bupa(O)(H)]. These results show that with proper manipulation of both the primary and secondary coordination sphere, proton and electron transfer can be more precisely controlled.

The newly formed Fe^{IV}-oxido, [$Fe^{IV}H_2$bupa(O)(H)], exhibits several spectroscopic features which bear striking resemblance with the protonated Fe^{IV}-oxido complex, [$Fe^{IV}H_3$buea(O)(H)], described in Chapter 2. The absorbance spectra of both complexes contain two prominent visible transitions between 380-385 nm and 540-545 nm, suggesting very similar electronic properties. Mössbauer spectroscopy also shows that the electronic properties of both of these complexes are similar, with nearly identical isomer shifts and quadrupole splitting parameters. In addition,

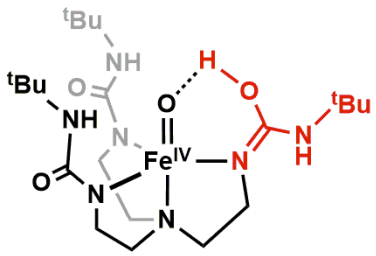

[$Fe^{IV}H_3$buea(O)(H)]

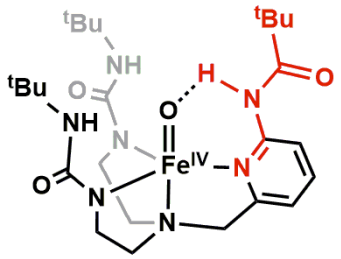

[$Fe^{IV}H_2$bupa(O)(H)]

Figure 4-11. Depiction of the suggested structures of [$Fe^{IV}H_3$buea(O)(H)] (left) and [$Fe^{IV}H_2$bupa(O)(H)] (right) with portions highlighted in red that show similarities in the primary and secondary coordination sphere of both complexes which may give rise to the similarities in spectroscopic features.

analysis of the NRVS spectrum of both complexes showed the energies for the Fe–O vibrations were identical within experimental error. The similarities in the spectroscopic properties of [$Fe^{IV}H_3$buea(O)(H)] and [$Fe^{IV}H_2$bupa(O)(H)] suggest a similar coordination environment for both complexes (Figure 4-11). This conclusion supports the assignment of the structure of [$Fe^{IV}H_3$buea(O)(H)] where one arm of the ligand is protonated, resulting in a tautomerization to give an iso-urea functional group and an imine-like nitrogen binding to the Fe^{IV} center. Because of this, both the [$Fe^{IV}H_3$buea(O)(H)] and [$Fe^{IV}H_2$bupa(O)(H)] complexes exhibit asymmetry in the trigonal plane because of the single arm having a neutral nitrogen donor with two anionic ureate donors which likely gives rise to the similar spectroscopic properties. The difference between the two complexes is in the secondary coordination sphere where the amidate functional group of [$Fe^{IV}H_2$bupa(O)(H)] is able to hold the acidic proton in place within the secondary coordination sphere, but in the [$Fe^{IV}H_3$buea(O)(H)] complex a urea functional group must drastically rearrange to accommodate the acidic proton, likely leading to the decreased thermal stability. This is an example of how a synthetic system, with a single modification, can be made to perform intramolecular proton transfer in response to changes in the pK_a value of the coordinated ligand.

This dynamic, responsive secondary coordination sphere is similar to the proposed pK_a changes of the proximal His in CCPs.[7,9]

Experimental Section

General Procedures. All manipulations, unless otherwise stated, were performed under an argon atmosphere in a Vac-atmospheres dry box. All chemicals were purchased from commercial sources and used without further purification unless otherwise stated. Ferrocene was sublimed prior to use. Potassium hydride as a 40 % w/w suspension in mineral oil was collected on a fine fritted glass funnel under an argon atmosphere and washed 5 x with 15 mL of anhydrous pentane before drying under vacuum to yield a gray solid which was used without further purification. $[FeCp_2][BF_4]$ and H_5bupa were prepared according to previously published procedures.[19,25]

Physical Methods. Electronic absorption spectra were recorded in a 1 cm cuvette on an 8453 Agilent UV-Vis spectrometer equipped with an Unisoku Unispeks cryostat. X-band (9.28 GHz) EPR spectra were collected as frozen solutions using a Bruker EMX spectrometer equipped with an ER041XG microwave bridge. Mössbauer spectra were recorded with a Janis Research Super-Varitemp dewar. Cyclic voltammetric experiments were conducted using a CHI600C electrochemical analyzer. A 2.0 mm glassy carbon electrode was used as the working electrode at scan velocities 0.01 $V{\cdot}s^{-1}$. A pentamethylferrocenium/pentamethylferrocene couple (-0.48 V vs. $[FeCp_2]^{+/0}$) was used as an internal reference to monitor the reference electrode (Ag^+/Ag).[25] The ^{57}Fe nuclear resonance vibrational spectroscopy (NRVS) data were recorded using published procedures on multiple occasions at beamline 3-ID at the Advanced Photon Source (APS).[26,27] The incident flux provided by the beamline is ~2 x 10^9 photos/s in a 1 meV bandwidth centered at 14.4125 keV in a 1 mm (vertical) x 3 mm (horizontal) spot. The monochromators used in the experiment consisted of a water-cooled diamond (1,1,1) double crystal with 1.1 eV bandpass,

followed by two separate Si(4,0,0) and Si(10,6,4) channel-cut crystals in a symmetric geometry. During the measurements, samples were maintained at low temperatures using a closed-cycle helium cryostat. The temperature for individual spectra were calculated using the ratio of anti-Stokes to Stokes intensity according to $S(-E) = S(E) \exp(-E/kT)$ and were generally in the range of 40 K to 80 K. Spectra were recorded between -40 meV and 120 meV in 0.25 meV steps. Delayed nuclear fluorescence and iron K fluorescence (from internal conversion) were recorded with a single avalanche photodiode detector (APD) with 1 cm^2 detection area. Each scan required about 50 minutes, and all scans were added and normalized to the intensity of the incident beam. The ^{57}Fe partial vibrational density of state (PVDOS) was extracted from the raw NRVS data using the PHOENIX software package.[28]

Synthesis of K[Fe^{II}H$_2$bupa]. A previously published procedure for the synthesis of K[Mn^{II}H$_2$bupa] was modified to synthesize the analogous Fe complex.[19] To a solution of H_5bupa (400 mg, 0.815 mmol) in anhydrous *N,N*-dimethylacetamide (DMA) (10 mL) was added potassium hydride (KH) (98 mg, 2.4 mmol) and the reaction allowed to proceed until gas evolution ceased and all solids were dissolved. To the yellow solution was added Fe^{II}(OAc)$_2$ (177 mg, 0.815 mmol) resulting in a dramatic color change to dark purple. The solution was stirred for one hour and then filtered through a medium fritted glass funnel to remove KOAc (170 mg, 2.1 equiv). Dark red crystals (390 mg, 82%) are afforded by vapor diffusion of diethyl ether (Et_2O) into the filtered, purple solution. The physical properties of the crystalline material matches those previously reported.[21]

Bulk Preparation of [Fe^{III}H$_2$bupa(O)(H)]$^-$ for Spectroscopy. A 20 mM solution of [Fe^{II}H$_2$bupa]$^-$ (12 mg, 0.020 mmol) was prepared in 1 mL of a given solvent or solvent mixture (THF, EtCN, MeCN, or 1:1 DMF:THF) with the addition of 18-crown-6 ether (8 mg, 0.04 mmol) for solubility and consistency between solvents. To this light purple solution was added *N*-methylmorphyline,

N-oxide (NMO) (2 mg, 0.02 mmol) resulting in a gradual color change to dark red over the course of 30 minutes at room temperature. After this time, the solution was stored at –35 °C for up to 24 hours. Purity and concentration of $[Fe^{III}H_2bupa(O)(H)]^-$ was typically determined using UV-vis spectroscopy monitoring the band at λ_{max} = 445 nm.

UV-vis Experiments using $[Fe^{II}H_2bupa]^-$ and $[Fe^{III}H_2bupa(O)(H)]^-$. A stock solution of either $[Fe^{II}H_2bupa]^-$ or $[Fe^{III}H_2bupa(O)(H)]^-$ was prepared as described above. An aliquot of the 20 mM stock solution (40 μL) was added to a 1 cm quartz cuvette containing 2 mL of the desired solvent to give a final concentration of 0.2 mM in metal complex. The cuvette was then transferred to the cryostat of a UV-vis spectrophotometer and cooled to the desired temperature. Stock solutions of reactants and substrates were prepared to between 20-40 mM by dissolving 10 mg of the reagent in 1 mL of solvent. Solutions of reagents were injected into the cuvette via a gas-tight syringe while monitoring the reaction optically.

EPR Experiments using $[Fe^{II}H_2bupa]^-$ and $[Fe^{III}H_2bupa(O)(H)]^-$. A stock solution of either $[Fe^{II}H_2bupa]^-$ or $[Fe^{III}H_2bupa(O)(H)]^-$ was prepared as described above. An aliquot of the 20 mM stock solution (200 μL) was added to an EPR tube. The tube was then sealed with a rubber septum, removed from the dry box, and either frozen in liquid nitrogen or an appropriate temperature bath. Solutions of substrate were injected via gas-tight syringe through the rubber septum and carefully shaken to mix before freezing in liquid nitrogen.

Preparation of Mössbauer Samples of $[Fe^{III}H_2bupa(O)(H)]^-$ and $[Fe^{IV}H_2bupa(O)(H)]$ with ^{57}Fe. A solution of ~96% ^{57}Fe-enriched, $[^{57}Fe^{II}H_2bupa]^-$ (3 mg, 0.005 mmol) was prepared in EtCN (1.5 mL) with 1.5 equiv 18-crown-6 ether (2 mg, 0.01 mmol). This solution is transferred to a 1 cm cuvette and placed inside the cryostat of a UV-vis spectrometer at room temperature. A solution of NMO (10 mg, 0.083 mmol) was prepared in EtCN (250 μL). A solution of $[FeCp_2][BF_4]$ (10 mg, 0.034 mmol) was prepared in EtCN (250 μL). One equivalent of NMO was added via gas-tight

syringe and the reaction was monitored for completion by loss of the absorbance features for $[Fe^{III}H_2bupa]^-$. To prepare $[Fe^{IV}H_2bupa(O)(H)]$, the cuvette containing a solution of $[Fe^{III}H_2bupa(O)(H)]^-$ was cooled to –80 °C, one equivalent of $[FeCp_2][BF_4]$ was added via gas-tight syringe, and the reaction stirred for five minutes. After reaction completion, the rubber septum sealing the cuvette was quickly removed with the aid of a razor blade under a flow of argon gas and the cuvette was removed from the cryostat and its contents were quickly poured into liquid nitrogen. The resulting frozen solution was then packed into pre-cooled Mössbauer cups for analysis.

Preparation of NRVS Samples of $[Fe^{III}H_2bupa(O)(H)]^-$ and $[Fe^{IV}H_2bupa(O)(H)]$ with ^{57}Fe. Solution NRVS sample holders were prepared from Mössbauer sample holders by cutting a 2 x 6 mm slot out of the bottom and covering the hole with kapton tape. Solutions of NMO and $[FeCp_2][BF_4]$ prepared as described above. A 30 mM solution of 96% ^{57}Fe-enriched $[Fe^{III}H_2bupa]^-$ (27 mg, 0.046 mmol) was prepared in EtCN (1.5 mL) with 18-crown-6 ether (15 mg, 0.057 mmol) added to increase solubility. This solution was transferred to a 1 cm cuvette, sealed with a rubber septum, and transferred to the cryostat of a UV-vis spectrophotometer One equivalent of NMO was added via gas-tight syringe and the reaction was monitored for completion by loss of the absorbance features for $[Fe^{III}H_2bupa]^-$. In the case of $[Fe^{IV}H_2bupa(O)(H)]$ and following formation of $[Fe^{III}H_2bupa(O)(H)]^-$, the cuvette was cooled to –80 °C and one equivalent of $[FeCp_2][BF_4]$ was added via gas-tight syringe and stirred for five minutes. After reaction completion, the rubber septum sealing the cuvette was quickly removed with the aid of a razor blade under a flow of argon gas and the cuvette was removed from the cryostat and its contents were quickly poured into liquid nitrogen. The resulting frozen solution was transferred into pre-cooled NRVS sample holder and packed by carefully thawing and refreezing the frozen solution under a stream of

argon gas. Samples were analyzed for purity using Mössbauer spectroscopy prior to, and after NRVS data collection.

References

(1) Shook, R. L.; Borovik, A. S. *Inorg. Chem.* **2010**, *49*, 3646–3660.
(2) Borovik, A. S. *Acc. Chem. Res.* **2005**, *38*, 54–61.
(3) Cook, S. A.; Borovik, A. S. *Acc. Chem. Res.* **2015**, *48*, 2407–2414.
(4) Dawson, J. *Science* **1988**, *240*, 433–439.
(5) Bollinger, J. M.; Krebs, C. *J. Inorg. Biochem.* **2006**, *100*, 586–605.
(6) Rutter, R.; Hager, L. P.; Dhonau, H.; Hendrich, M.; Valentine, M.; Debrunner, P. *Biochemistry* **1984**, *23*, 6809–6816.
(7) Casadei, C. M.; Gumiero, A.; Metcalfe, C. L.; Murphy, E. J.; Basran, J.; Concilio, M. G.; Teixeira, S. C. M.; Schrader, T. E.; Fielding, A. J.; Ostermann, A.; Blakeley, M. P.; Raven, E. L.; Moody, P. C. E. *Science* **2014**, *345*, 193–197.
(8) Poulos, T. L. *Chem. Rev.* **2014**, *114*, 3919–3962.
(9) Chreifi, G.; Baxter, E. L.; Doukov, T.; Cohen, A. E.; McPhillips, S. E.; Song, J.; Meharenna, Y. T.; Soltis, S. M.; Poulos, T. L. *Proc. Natl. Acad. Sci. U. S. A.* **2016**, *113*, 1226–1231.
(10) Kilgore, U. J.; Roberts, J. A. S.; Pool, D. H.; Appel, A. M.; Stewart, M. P.; Dubois, M. R.; Dougherty, W. G.; Kassel, W. S.; Bullock, R. M.; Dubois, D. L. *J. Am. Chem. Soc.* **2011**, *133*, 5861–5872.
(11) Ohagan, M.; Ho, M. H.; Yang, J. Y.; Appel, A. M.; Dubois, M. R.; Raugei, S.; Shaw, W. J.; Dubois, D. L.; Bullock, R. M. Proton delivery and removal in [Ni(PR2NR 22)2]2+ hydrogen production and oxidation catalysts. *Journal of the American Chemical Society*, 2012, *134*, 19409–19424.
(12) Helm, M. L.; Stewart, M. P.; Bullock, R. M.; DuBois, M. R.; DuBois, D. L. *Science (80-.).* **2011**, *333*, 863–866.
(13) Collman, J. P.; Gagne, R. T.; Reed, C. A. *J. Am. Chem. Soc.* **1974**, *96*, 2629–2631.
(14) Collman, J. P.; Brauman, J. I.; Doxsee, K. M.; Halbert, T. R.; Suslick, K. S. *Proc. Natl. Acad. Sci.* **1978**, *75*, 564–568.
(15) Ogo, S.; Wada, S.; Watanabe, Y.; Iwase, M.; Wada, A.; Harata, M.; Jitsukawa, K.; Masuda, H.; Einaga, H. *Angew. Chemie Int. Ed.* **1998**, *37*, 2102–2104.
(16) Wada, A.; Ogo, S.; Nagatomo, S.; Kitagawa, T.; Watanabe, Y.; Jitsukawa, K.; Masuda, H. *Inorg. Chem.* **2002**, *41*, 616–618.
(17) Widger, L. R.; Davies, C. G.; Yang, T.; Siegler, M. A.; Troeppner, O.; Jameson, G. N. L.; Ivanović-Burmazović, I.; Goldberg, D. P. *J. Am. Chem. Soc.* **2014**, *136*, 2699–2702.
(18) Kaljurand, I.; Kütt, A.; Sooväli, L.; Rodima, T.; Mäemets, V.; Leito, I.; Koppel, I. A. *J. Org. Chem.* **2005**, *70*, 1019–1028.
(19) Shook, R. L.; Gunderson, W. A.; Greaves, J.; Ziller, J. W.; Hendrich, M. P.; Borovik, A. S. *J. Am. Chem. Soc.* **2008**, *130*, 8888–8889.
(20) Shook, R. L.; Peterson, S. M.; Greaves, J.; Moore, C.; Rheingold, A. L.; Borovik, A. S. *J. Am. Chem. Soc.* **2011**, *133*, 5810–5817.
(21) Shook, R. L. Employing Hydrogen Bonds to Stabilize Reactive Intermediates in the Activation of Dioxygen, University of California, Irvine, 2009.
(22) Lacy, D. C.; Gupta, R.; Stone, K. L.; Greaves, J.; Ziller, J. W.; Hendrich, M. P.; Borovik, A. S. *J. Am. Chem. Soc.* **2010**, *132*, 12188–12190.

(23) Sustac Roman, D.; Takahashi, Y.; Charette, A. B. *Org. Lett.* **2011**, *13*, 3242–3245.
(24) Zhou, S.; Anderson, G. M.; Mondal, B.; Doni, E.; Ironmonger, V.; Kranz, M.; Tuttle, T.; Murphy, J. A. *Chem. Sci.* **2013**, *5*, 476–482.
(25) Connelly, N. G.; Geiger, W. E. *Chem. Rev.* **1996**, *96*, 877–910.
(26) Sturhahn, W. *J. Phys. Condens. Matter* **2004**, *16*, S497–S530.
(27) Toellner, T. S. *Hyperfine Interact.* **2000**, *125*, 3–28.
(28) Sturhahn, W. *Hyperfine Interact.* **2000**, *125*, 149–172.

Chapter 5

Reactivity of a Series of High Valent Mn-Oxido Complexes with Lewis Acids

Biological water oxidation occurs at the oxygen evolving complex (OEC) of Photosystem II (PSII). The OEC consists of a unique, multi-metallic [$CaMn_4O_5$] cluster where two equivalents of water are converted to dioxygen (Figure 5-1).[1–3] While the exact mechanism of O_2 formation is not yet fully understood, it has been proposed that an electrophilic Mn^V-oxido complex is

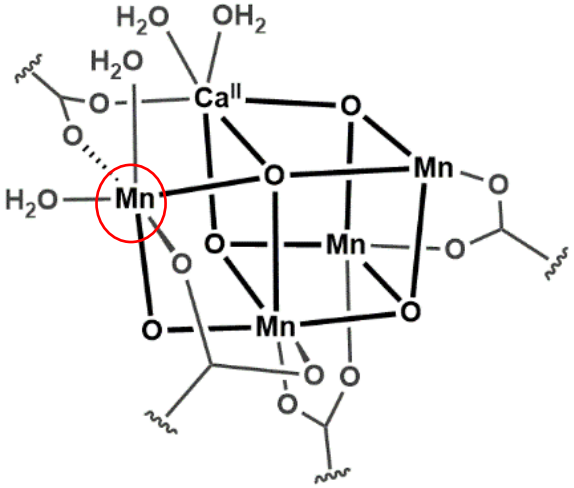

Figure 5-1. Depiction of the molecular structure of the oxygen evolving complex of photosystem II. Encircled is the Mn site where a Mn^V-oxido species is proposed to form.

generated and is susceptible to attack by a hydroxido ligand bound nearby on the cluster to form an O–O bond. In this mechanism the role of the Ca^{II} ion is unknown, but it may serve to activate a coordinated aqua or hydroxido ligands towards nucleophilic attack, or it may serve to attenuate the reduction potential of the OEC to drive O–O bond formation.[4–6] The presence of the Ca^{II} ion is essential and substitution of the Ca^{II} ion with other metal ions except the Sr^{II} ion impedes function.[7,8] To gain a better understanding of the role of the Ca^{II} ion in biological water oxidation, synthetic model compounds have been developed that are capable of probing the relationship between high valent metal-oxido complexes and Ca^{II} ions or other Lewis acids.[9–12]

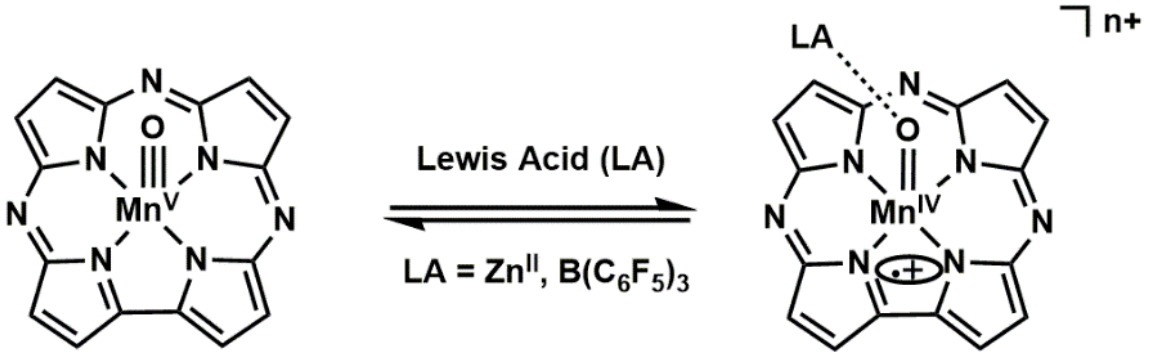

Figure 5-2. Depiction of the reaction of a Mn^{V}-oxido corrolazine complex towards Lewis acids to generate the valence tautomer Mn^{IV}-oxido corrolazine radical complex.

Several groups have begun to examine the effect of Lewis acids on high valent metal-oxido complexes including Nam, Que, Ray, and Goldberg.[13–19] In particular, the Goldberg lab synthesized a high valent Mn^{V}-oxido complex bound to a planer corrolazine ligand (Figure 5-2). They showed that addition of Zn^{2+} ions or $B(C_6F_5)_3$ to their Mn^{V}-oxido complex resulted in formation of the Mn^{IV}-oxido and a corrolazine-based radical (Figure 5-2).[17,18] These experiments suggest that the interaction of the Lewis acids with the metal-oxido modulates the reduction potential to elicit electron transfer from the corrolazine ligand to the Mn^{V}-oxido unit. Goldberg referred to this process as valence tautomerism.

One of the pioneering synthetic model compounds was developed by the Agapie group and featured a tri-Mn cluster with an open coordination site available to bind a fourth metal ion to the cluster (Figure 5-3).[20–22] They found that by binding a series of metal ions with differing Lewis acidities into the open site such as Ca^{II}, Sr^{II}, Zn^{II}, Y^{III}, Sc^{III}, and Mn^{III}, the redox potential could be varied by over 1 V.[21,23,24] The changes in redox potential were also found to be correlated with the Lewis acidity of each metal ion. One particular result relevant to the OEC was the finding that despite the difference in Lewis acidity between Ca^{II} and Sr^{II} ions, the redox potential for the cluster with a Ca^{II} ion bound was identical within experimental error to that containing a Sr^{II} ion. These data help to explain how a Sr^{II} ion is the only metal ion that is able to replace the Ca^{II} ion

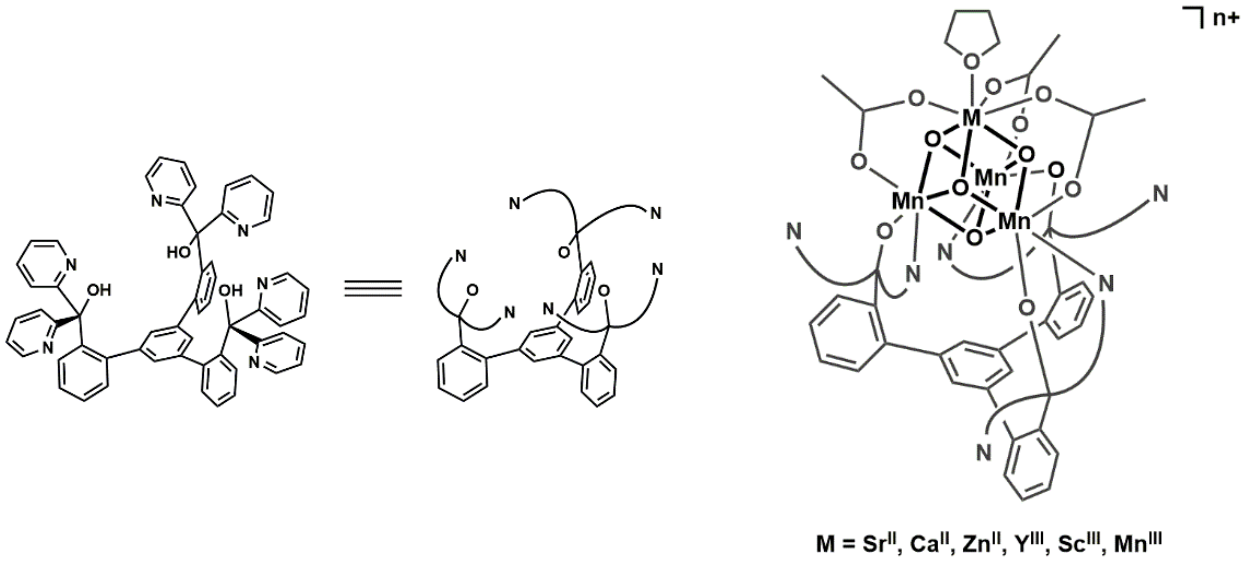

Figure 5-3. Chemical structure of the complexes synthesized by the Agapie group to study the effect of various metal ions on the electronic and reactivity properties of Mn-oxido cubane clusters.

in the OEC while maintaining partial function and also suggests that the role of Ca^{II} in the OEC is to regulate the redox potential of the cluster.

The Borovik lab has previously reported the synthesis and characterization of a series of Mn-oxido complexes using the $[H_3buea]^{3-}$ ligand where the Mn ion is in the 3+, 4+, and 5+ oxidation states (Scheme 5-1).[25–29] Each complex is high spin, with the Mn^{V}-oxido complex being

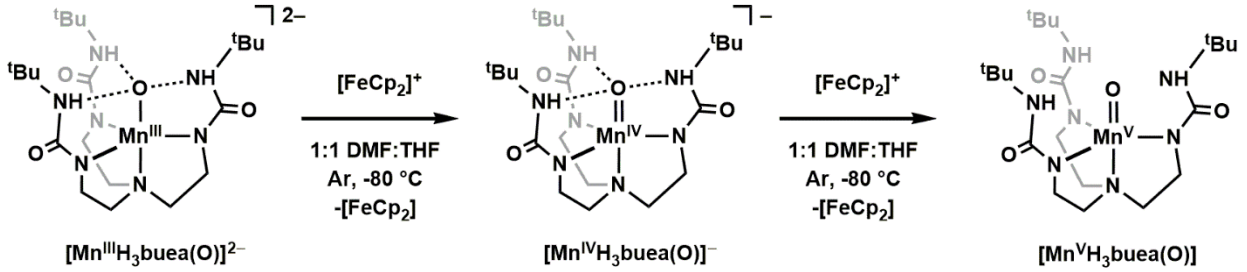

Scheme 5-1. A series of Mn-oxido complexes previously synthesized and characterized by the Borovik group all supported by the $[H_3buea]^{3-}$ ligand.

the only example to date of a Mn^{V}-oxido complex with an S = 1 spin ground state. Isolation and characterization of this series of complexes paved the way for the work presented here on the reactivity of a Mn-oxido complexes in differing oxidation states with Ca^{II}, Sr^{II}, and Sc^{III} ions.

Addition of excess Ca^{II} or Sc^{III} ions to the $[Mn^{V}H_3buea(O)]$ complex resulted in reduction of the complex to a new Mn^{IV} species that is assigned to the Group 2 and 3 metal ion adducts of $[Mn^{IV}H_3buea(O)]^-$ based on characterization by UV-vis and EPR spectroscopies. The $[Mn^{IV}H_3buea(O)(Ca)]^+$ and $[Mn^{IV}H_3buea(O)(Sc)]^{2+}$ species could also be independently generated by the addition of Ca^{II} or Sc^{III} ions to $[Mn^{IV}H_3buea(O)]^-$. In addition, both of these Mn^{IV} complexes could be further reduced by the addition of $[CoCp_2]$ to yield what is proposed to be the analogous Mn^{III} adducts. The absorbance spectra of these reduced complexes matched well with those generated by the addition of Ca^{II} and Sc^{III} ions to $[Mn^{III}H_3buea(O)]^{2-}$. The reactivity of Sr^{II} ions with $[Mn^{V}H_3buea(O)]$ was shown to be significantly lower than both Ca^{II} and Sc^{III} ions, and in fact, the $[Mn^{V}H_3buea(O)]$ required a prohibitively large amount of Sr^{II} ions to invoke reduction. Despite this, the absorbance spectra produced by Ca^{II} and Sr^{II} adducts of $[Mn^{IV}H_3buea(O)]^-$ or $[Mn^{III}H_3buea(O)]^{2-}$ were more similar to one another than the corresponding Sc^{III} adducts. This result suggested that despite the differences in Lewis acidity and general reactivity towards the Mn–oxido complexes, binding of these two metal ions produced species with similar electronic properties. These experiments corroborate those discussed above to suggest that the redox inactive metal ion in the OEC serves to modulate the electrochemical properties of the cluster.

Results and Discussion

Reactivity of Ca^{II} ions with $[Mn^{V}H_3buea(O)]$. The previously reported high spin Mn^{V}-oxido complex, $[Mn^{V}H_3buea(O)]$, was used as a synthon to investigate the effect of redox inactive metal ions on the properties and reactivity of high valent metal-oxido complexes that are similar to species proposed to be formed in the OEC. Addition of a 200 equivalents of Ca^{II} ions to a solution of $[Mn^{V}H_3buea(O)]$ in 1:1 *N,N*-dimethylformamide:tetrahydrofuran (DMF:THF) at –80 °C resulted in the rapid loss of absorbance features for $[Mn^{V}H_3buea(O)]$ and appearance of new absorbance features at λ_{max} = 455 and 770 nm (Figure 5-4). In addition, an absorbance band at λ_{max}

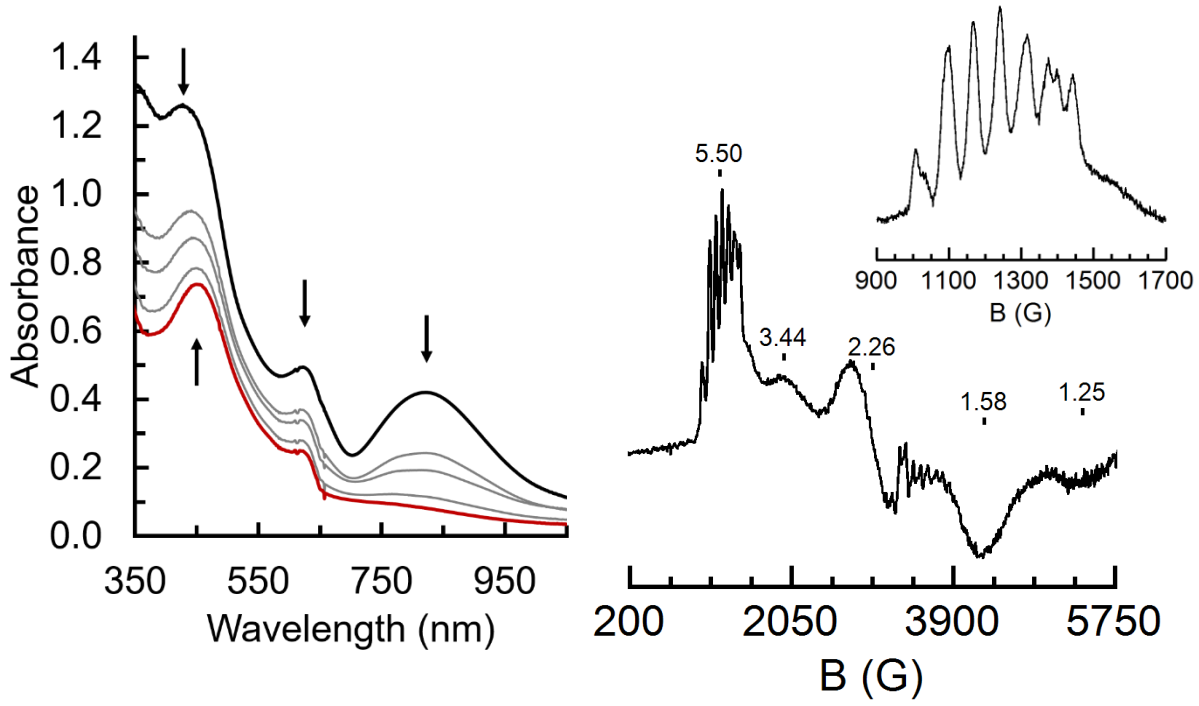

Figure 5-4. UV-vis spectral changes (left) upon the addition of 200 equivalents of Ca^{II} ions to $[Mn^{V}H_3buea(O)]$ (black) in 1:1 DMF:THF at –80 °C to generate a new Mn^{IV} species (red). Gray traces represent 30 s scans. Perpendicular mode EPR spectrum (right) of the same reaction recorded at 10 K in a 1:1 DMF:THF glass. Inset: expanded low field region showing hyperfine interactions.

= 620 nm appeared that is consistent with production of $[FeCp_2]^+$: note that $[FeCp_2]$ was already in solution from synthesis of $[Mn^{V}H_3buea(O)]$ (Figure 5-4, Scheme 5-1). These absorbances at λ_{max} = 455 and 770 nm were reminiscent of features found in the absorbance spectra of other Mn^{IV} complexes using $[H_3buea]^{3-}$, and the initial premise was that a new $[Mn^{IV}H_3buea(O)(Ca)]^+$ species may have been generated. Monitoring the same reaction by EPR spectroscopy showed a new signal with g = 5.50, 3.44, 2.26, 1.58, and 1.25 with nuclear hyperfine coupling of A = 68 G at g = 5.27 and A = 79 G at g = 5.57 consistent with the formation of a high spin mononuclear Mn^{IV} ion (Figure 5-4). The two sets of hyperfine features are likely due to transitions within the $m_s = \pm 1/2$ and $\pm 3/2$ doublets. In addition to the Mn^{IV} species, the absorbance feature for $[FeCp_2]^+$ was

observed, indicating electron transfer occurs from [$FeCp_2$] to the Ca^{II} adduct of [$Mn^{V}H_3buea(O)$] to generate the putative [$Mn^{IV}H_3buea(O)(Ca)]^+$ complex.

Reactivity of Ca^{II} ions with [$Mn^{IV}H_3buea(O)]^-$. In an attempt to generate the [$Mn^{IV}H_3buea(O)(Ca)]^+$ complex directly, the reactivity of [$Mn^{IV}H_3buea(O)]^-$ with Ca^{II} ions was examined. In an analogous experiment to the [$Mn^{V}H_3buea(O)$] experiment, addition of excess Ca^{II} ions to a solution of [$Mn^{IV}H_3buea(O)]^-$ in 1:1 DMF:THF at –80 °C generated a nearly identical absorbance spectrum with a prominent bands at λ_{max} = 455 and 770 nm (Figure 5-5). Following this reaction by EPR spectroscopy showed that the same Mn^{IV} species is generated by the addition of excess Ca^{II} ions to either [$Mn^{IV}H_3buea(O)]^-$ or [$Mn^{V}H_3buea(O)$] (Figure 5-5). This reactivity is similar to chemistry reported by Goldberg for a Mn^{V}-oxido corrolazine complex that exhibited

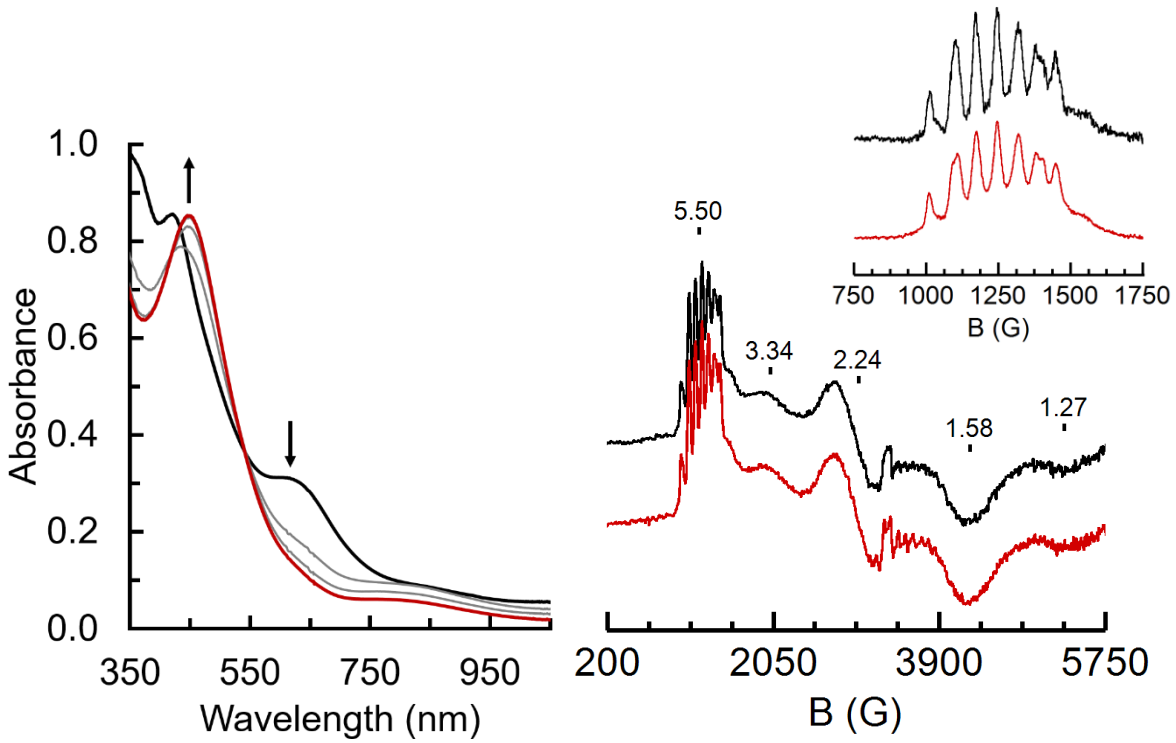

Figure 5-5. UV-vis spectral changes (left) upon the addition of 100 equivalents of Ca^{II} ions to [$Mn^{IV}H_3buea(O)]^-$ (black) in 1:1 DMF:THF at –80 °C to generate a new Mn^{IV} species (red). Gray traces represent 30 s scans. Perpendicular-mode EPR spectra (right) of the same reaction (black) compared to the reaction of [$Mn^{V}H_3buea(O)$] with 200 equivalents of Ca^{II} ions (red), both recorded at 10 K in a 1:1 DMF:THF glass. Inset: expanded low field region showing hyperfine interactions.

intramolecular electron transfer when treated with Lewis acids except in the $[H_3buea]^{3-}$ system, the ligand cannot serve as an electron source and so the $[FeCp_2]$ in solution transfers an electron to the Mn-oxido complex.

Reactivity of Ca^{II} ions with $[Mn^{III}H_3buea(O)]^{2-}$. A solution of $[Mn^{III}H_3buea(O)]^{2-}$ was treated with a slight excess of Ca^{II} ions in a 1:1 DMF:THF mixture at –80 °C which produced new absorbance bands at λ_{max} = 425 and 680 nm that are consistent with a new Mn^{III} species (Figure 5-6A). A parallel mode EPR spectrum collected of this reaction mixture showed a new signal at g = 8.10 and A = 96 G consistent with a high spin Mn^{III} species assigned to $[Mn^{III}H_3buea(O)(Ca)]$ (Figure 5-6B). The same species could also be generated by the addition of one equivalent of $[CoCp_2]$ to the $[Mn^{IV}H_3buea(O)(Ca)]^{+}$ complex in 1:1 DMF:THF at –80 °C (Figure 5-6C). The reverse redox process was also possible, with the addition of one equivalent of $[FeCp_2]^{+}$ to $[Mn^{III}H_3buea(O)(Ca)]$ under the same reaction conditions generating bands at λ_{max} = 455 and 770 nm that are consistent with $[Mn^{IV}H_3buea(O)(Ca)]^{+}$ (Figure 5-6D). Both $[Mn^{III}H_3buea(O)(Ca)]$ and $[Mn^{IV}H_3buea(O)(Ca)]^{+}$ were thermally unstable and decayed within 1-2 hours at temperatures above –35 °C, precluding additional potentiometric or crystallographic characterization.

Reactivity of Sr^{II} ions with $[Mn^{V}H_3buea(O)]$. In the OEC, the only redox inactive metal ion that can replace the Ca^{II} ion and maintain function is a Sr^{II} ion. Because of this relationship, Sr^{II} ions were added to $[Mn^{V}H_3buea(O)]$ to test whether the electron transfer from $[FeCp_2]$ to the $[Mn^{V}H_3buea(O)]$ complex that was observed for addition of Ca^{II} would be possible. Treatment of a solution of $[Mn^{V}H_3buea(O)]$ in 1:1 DMF:THF at –80 °C with a large excess of Sr^{II} resulted in almost negligible changes in the absorbance spectrum. Addition of up to 400 equivalents of Sr^{II} ions reduced the amount of $[Mn^{V}H_3buea(O)]$ in solution by only ~30% (Figure 5-7).

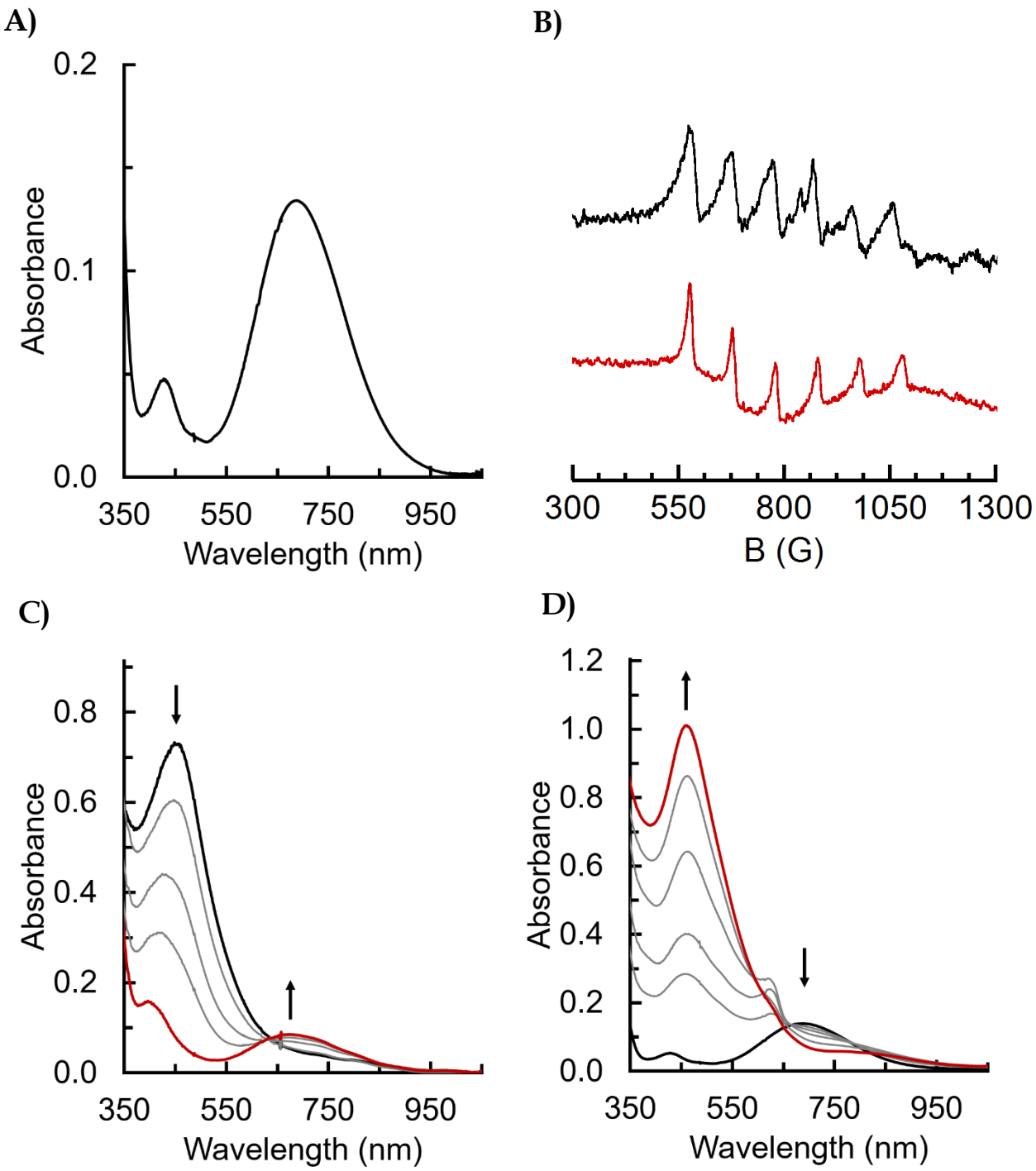

Figure 5-6. Final absorbance spectrum (A) from the reaction of $[Mn^{III}H_3buea(O)]^{2-}$ with 20 equivalents of Ca^{II} ions. Parallel-mode EPR spectra (B) of the same reaction (black) compared to $[Mn^{III}H_3buea(O)]^{2-}$ (red) collected at 10 K in a 1:1 DMF:THF glass. UV-vis spectral changes (C) upon the addition of $[CoCp_2]$ to $[Mn^{IV}H_3buea(O)(Ca)]^{+}$ (black) to generate a new $[Mn^{III}H_3buea(O)(Ca)]$ species (red). Gray traces represent 15 s scans. UV-vis spectral changes (D) upon the addition of $[FeCp_2]^{+}$ to $[Mn^{III}H_3buea(O)(Ca)]$ (black) to generate the $[Mn^{IV}H_3buea(O)(Ca)]^{+}$ species (red). Gray traces represent 30 s scans. UV-vis spectra collected in 1:1 DMF:THF at –80 °C.

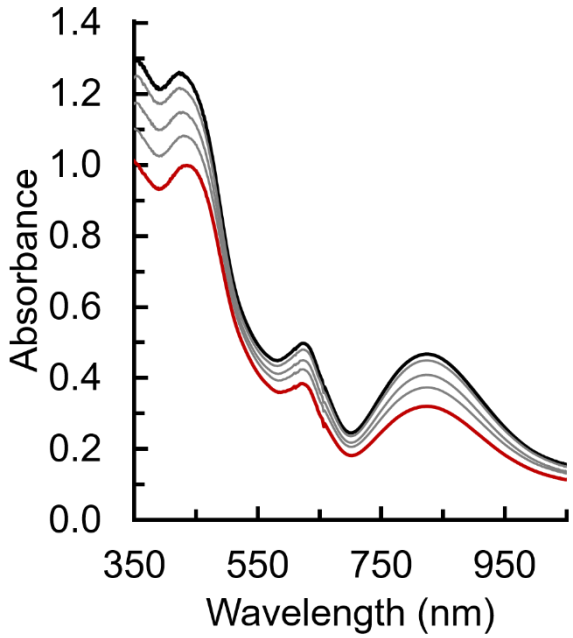

Figure 5-7. UV-vis spectral changes upon the addition of 400 equivalents of Sr^{II} ions to $[Mn^{V}H_3buea(O)]$ (black) in 1:1 DMF:THF at –80 °C resulting in the partial decrease in all absorbance features (red). Gray traces are sequential additions of 100 equivalents of Sr^{II} ions.

Reactivity of Sr^{II} ions with $[Mn^{IV}H_3buea(O)]^-$. The reactivity of Sr^{II} ions with $[Mn^{IV}H_3buea(O)]^-$ was found to be significantly lower than with Ca^{II}, similar to the reaction of Sr^{II} ions with $[Mn^{V}H_3buea(O)]$. However, with $[Mn^{IV}H_3buea(O)]^-$ complete reaction was observed upon addition of 200 equivalents of Sr^{II} ions in 1:1 DMF:THF at –80 °C to produce two absorbance bands at λ_{max} = 445 and 770 nm (Figure 5-8). The bands formed within 30 seconds, but the conversion was non-isosbestic. A perpendicular-mode EPR spectrum of this reaction in a 1:1 DMF:THF glass at 10 K showed features consistent with a high spin Mn^{IV} signal with features similar, but not identical to the starting $[Mn^{IV}H_3buea(O)]^-$ complex at g = 5.14, 3.49, 2.34, 1.61, and 1.26 with nuclear hyperfine coupling of A = 78 G at g = 5.60 and A = 68 G at g = 5.25 consistent with a high spin mononuclear Mn^{IV} ion (Figure 5-8).

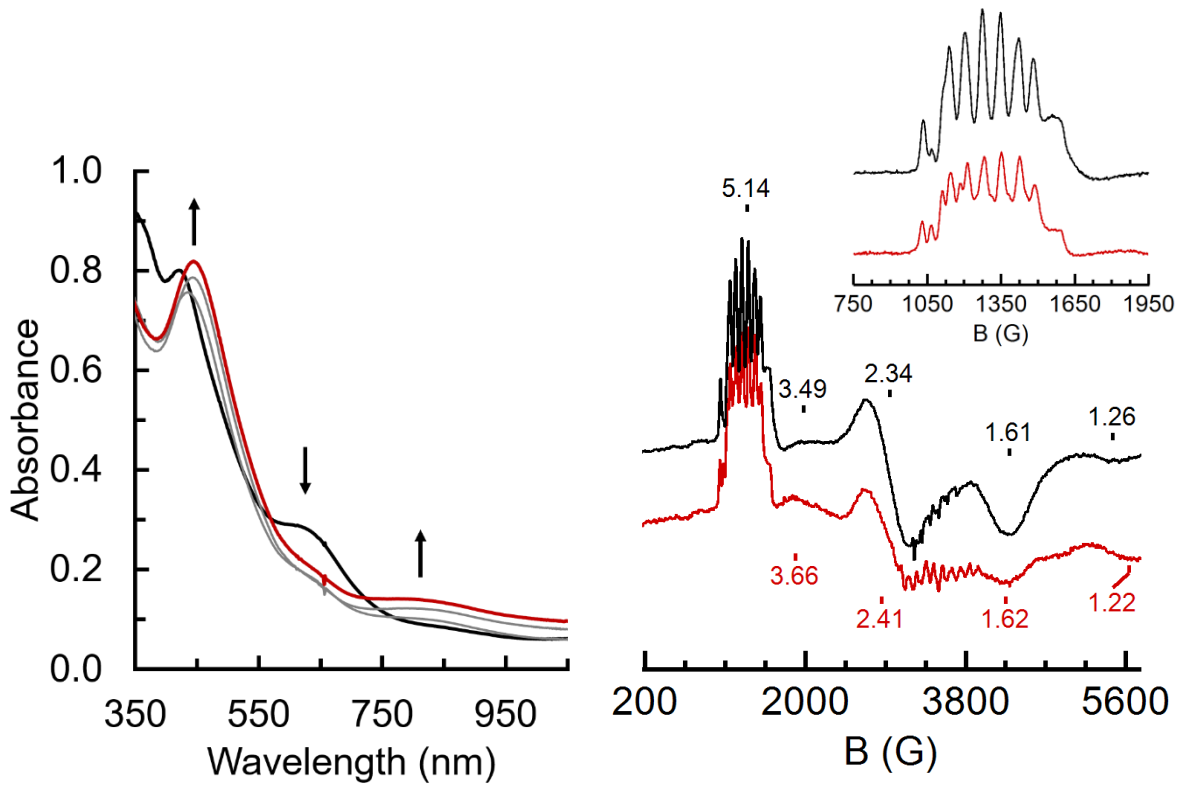

Figure 5-8. UV-vis spectral changes (left) upon the addition of 200 equivalents of Sr^{II} ions to $[Mn^{IV}H_3buea(O)]^-$ (black) in 1:1 DMF:THF at –80 °C to generate a new Mn^{IV} species (red). Gray traces represent 30 s scans. Perpendicular-mode EPR spectra (right) of the same reaction (black) compared to $[Mn^{IV}H_3buea(O)]^-$ (red) recorded at 10 K in a 1:1 DMF:THF glass. Inset: expanded low field region showing hyperfine interactions.

Reactivity of Sr^{II} ions with $[Mn^{III}H_3buea(O)]^{2-}$. A solution of $[Mn^{III}H_3buea(O)]^{2-}$ was treated with 20 equivalents of Sr^{II} ions in 1:1 DMF:THF at –80 °C to produce new absorbance features at λ_{max} = 430 and 685 nm consistent with a new Mn^{III} species (Figure 5-9A). The parallel-mode EPR spectrum of this reaction remained mostly unchanged from the starting $[Mn^{III}H_3buea(O)]^{2-}$ complex and showed a high spin Mn^{III} signal with g = 8.00 and A = 100 G (Figure 5-9B). A nearly identical absorbance spectrum for the Mn^{III} species could also be generated by the addition of one equivalent of $[CoCp_2]$ to the Sr^{II} adduct of $[Mn^{IV}H_3buea(O)]^-$ in 1:1 DMF:THF at –80 °C, although this species reacted further to produce an absorbance spectrum where the high energy band shifted from 430 nm to 400 nm (Figure 5-9C). The Mn^{III}/Mn^{IV} redox process was chemically

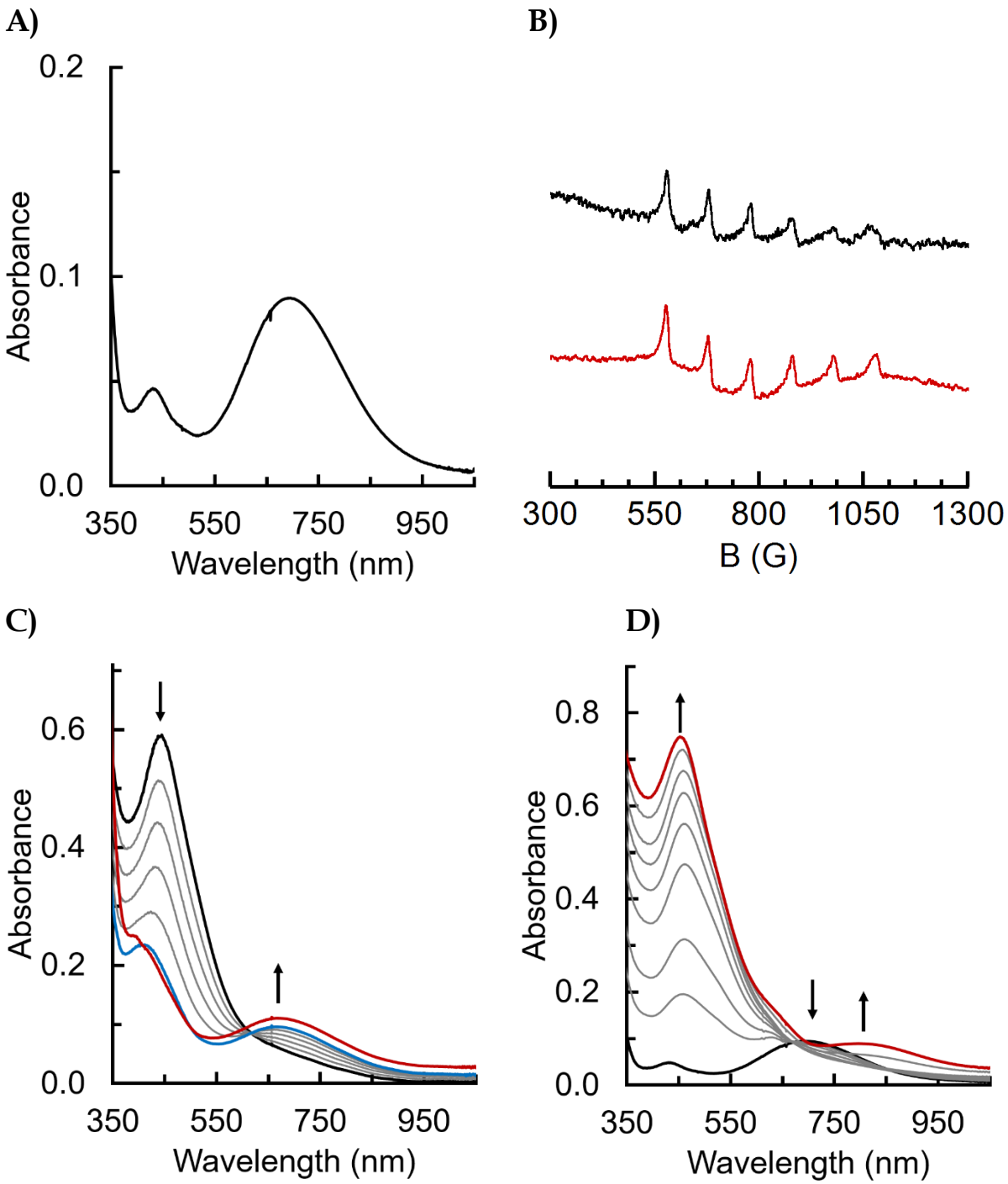

Figure 5-9. Final absorbance spectrum (A) from the reaction of $[Mn^{III}H_3buea(O)]^{2-}$ with 20 equivalents of Sr^{II} ions. Parallel-mode EPR spectra (B) of the same reaction (black) compared to $[Mn^{III}H_3buea(O)]^{2-}$ (red) collected at 10 K in a 1:1 DMF:THF glass. UV-vis spectral changes (C) upon the addition of $[CoCp_2]$ to $[Mn^{IV}H_3buea(O)(Sr)]^{+}$ (black) to generate a new $[Mn^{III}H_3buea(O)(Sr)]$ species (blue) which reacts further to produce the red trace. Gray traces represent 15 s scans. UV-vis spectral changes (D) upon the addition of $[FeCp_2]^{+}$ to $[Mn^{III}H_3buea(O)(Sr)]$ (black) to generate the $[Mn^{IV}H_3buea(O)(Sr)]^{+}$ species (red). Gray traces represent 30 s scans. UV-vis spectra collected in 1:1 DMF:THF at –80 °C.

reversible by the addition of one equivalent of $[FeCp_2]^+$ to the proposed $[Mn^{III}H_3buea(O)(Sr)]$ complex in 1:1 DMF:THF at –80 °C (Figure 5-9D). Both $[Mn^{III}H_3buea(O)(Sr)]$ and $[Mn^{IV}H_3buea(O)(Sr)]^+$ were thermally unstable and decayed within 1-2 hours at temperatures above –35 °C, precluding additional potentiometric or crystallographic characterization. The similarities in the absorbance spectra of $[Mn^{IV}H_3buea(O)(Ca)]^+$ and $[Mn^{III}H_3buea(O)(Ca)]$ with $[Mn^{IV}H_3buea(O)(Sr)]^+$ and $[Mn^{III}H_3buea(O)(Sr)]$ suggest that while differing amounts of the Lewis acid are required for complete reaction, the electronic properties of the complexes appear to be similar.

Reactivity of Sc^{III} ions with $[Mn^{V}H_3buea(O)]$. In addition to synthesizing clusters with dicationic metal ions, the Agapie group also reported a dramatic increase in the reduction

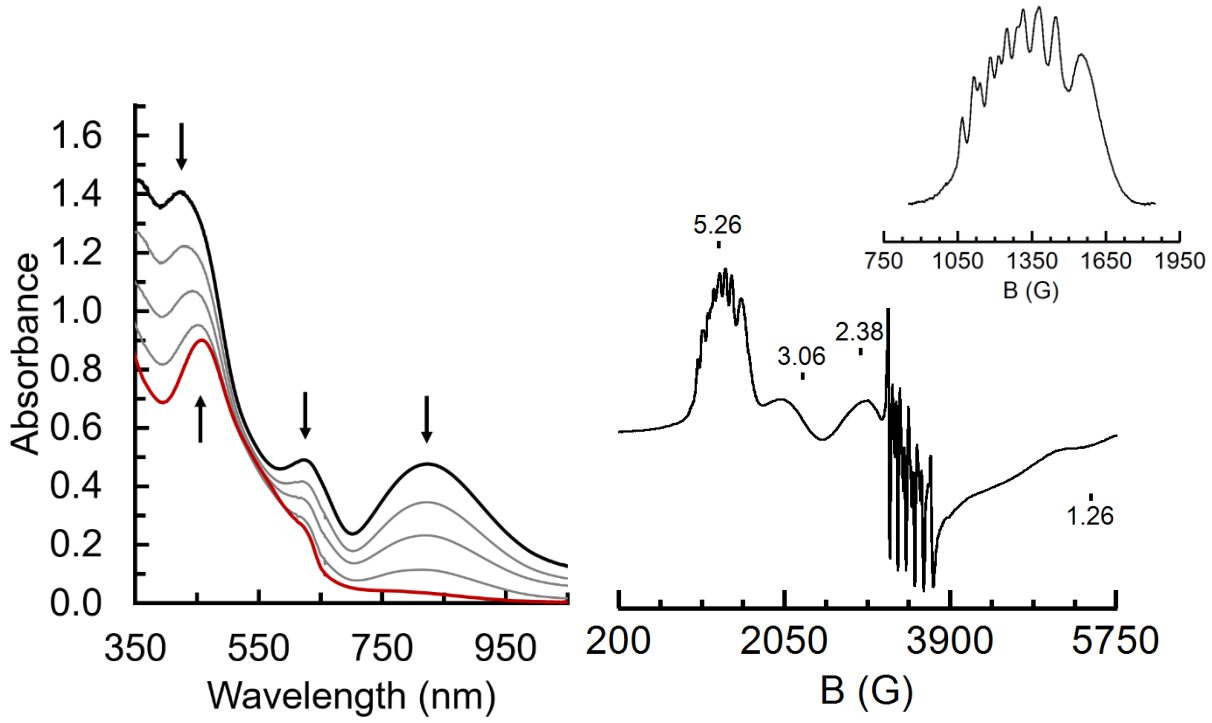

Figure 5-10. UV-vis spectral changes (left) upon the addition of 10 equivalents of Sc^{III} ions to $[Mn^{V}H_3buea(O)]$ (black) in 1:1 DMF:THF at –80 °C to generate a new Mn^{IV} species (red). Gray traces represent 30 s scans. Perpendicular-mode EPR spectrum (right) of the same reaction recorded at 10 K in a 1:1 DMF:THF glass. Inset: expanded low field region showing hyperfine interactions.

potentials of their clusters synthesized with stronger Lewis acids such as Sc^{III} and Y^{III} ions. To examine if a similar effect could be observed with the $[H_3buea]^{3-}$ system, the addition of 10 equivalents of Sc^{III} ions to a solution of $[Mn^{V}H_3buea(O)]$ in 1:1 DMF:THF at –80 °C was monitored spectrophotometrically. The reaction showed the reduction of $[Mn^{V}H_3buea(O)]$ to produce a new species with an absorbance band at λ_{max} = 455 nm in addition to a shoulder at λ_{max} = ~620 nm from the production of $[FeCp_2]^+$ that occurred because $[FeCp_2]$ was present in solution from the synthesis of $[Mn^{V}H_3buea(O)]$ (Figure 5-10, Scheme 5-1). Tthe perpendicular-mode EPR spectrum of this reaction showed a new high spin Mn^{IV} species at g = 5.26, 3.06, and 2.38 with nuclear hyperfine coupling of A = 73 G at g = 5.48 and A = 67 G at g = 5.38 consistent with the formation of a high spin mononuclear Mn^{IV} ion (Figure 5-10).

Reactivity of Sc^{III} ions with $[Mn^{IV}H_3buea(O)]^-$. Addition of two equivalents of Sc^{III} ions to a solution of $[Mn^{IV}H_3buea(O)]^-$ in 1:1 DMF:THF at –80 °C showed a clean conversion to a new spectrum with a single absorbance band at λ_{max} = 455 nm (Figure 5-11A), similar to the band produced by addition of Sc^{III} ions to $[Mn^{V}H_3buea(O)]$. The perpendicular-mode EPR spectrum of this reaction showed the same Mn^{IV} signal that was observed in the addition of Sc^{III} to $[Mn^{V}H_3buea(O)]$ but broadened slightly (Figure 5-11B). This result is consistent with the chemistry observed with Ca^{II} and Sr^{II} ions, although the signals observed are distinct from the previous experiments.

In addition to the Mn^{IV} signal observed by perpendicular mode EPR spectroscopy, the parallel mode spectrum showed a new Mn^{III} signals at g = 8.14 with A = 40 G (Figure 5-11C). The new Mn^{III} species may result from an increased reduction potential of the Sc^{III} adduct of the Mn^{IV}-oxido complex that causes reduction by $[FeCp_2]$ already in solution, or it may be from other unknown reactivity. To test whether $[FeCp_2]$ is responsible for the Mn^{III} signal, a solution of

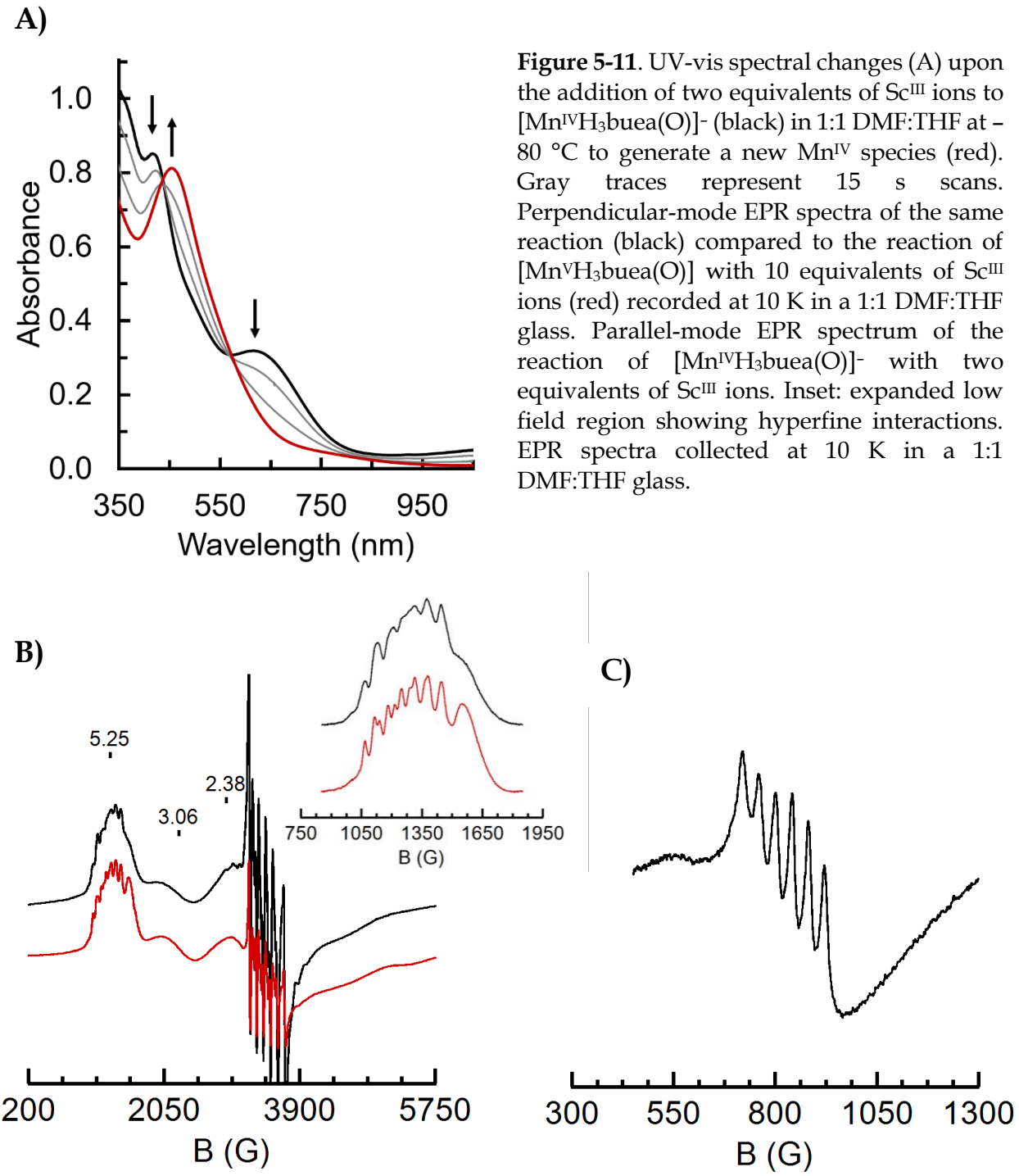

Figure 5-11. UV-vis spectral changes (A) upon the addition of two equivalents of Sc^{III} ions to $[Mn^{IV}H_3buea(O)]^-$ (black) in 1:1 DMF:THF at –80 °C to generate a new Mn^{IV} species (red). Gray traces represent 15 s scans. Perpendicular-mode EPR spectra of the same reaction (black) compared to the reaction of $[Mn^{V}H_3buea(O)]$ with 10 equivalents of Sc^{III} ions (red) recorded at 10 K in a 1:1 DMF:THF glass. Parallel-mode EPR spectrum of the reaction of $[Mn^{IV}H_3buea(O)]^-$ with two equivalents of Sc^{III} ions. Inset: expanded low field region showing hyperfine interactions. EPR spectra collected at 10 K in a 1:1 DMF:THF glass.

$[Mn^{IV}H_3buea(O)]^-$ in 1:1 DMF:THF at –80 °C was treated with Sc^{III} ions in the presence of excess $[FeCp_2]$. This resulted in the same band at λ_{max} = 455 nm with no discernable increase in the amount of $[FeCp_2]^+$ produced, suggesting the new Mn^{III} species is unlikely to be from direct reduction by $[FeCp_2]$.

Reactivity of Sc^{III} ions with $[Mn^{III}H_3buea(O)]^{2-}$. Addition of three equivalents of Sc^{III} ions to a solution of $[Mn^{III}H_3buea(O)]^{2-}$ in 1:1 DMF:THF at –80 °C generated a new Mn^{III} species with absorbance features at λ_{max} = 405 and 640 nm (Figure 5-12A). A parallel mode EPR spectrum of this reaction mixture showed a signal consistent with a high spin, S = 2 Mn^{III} center at g = 8.14 and A = 40 G (Figure 5-12B), the same signal that was observed in the parallel-mode EPR spectrum of the reaction of $[Mn^{IV}H_3buea(O)]^{-}$ with Sc^{III} ions. According to collaborators in the Hendrich lab (CMU), the dramatic narrowing of the hyperfine coupling is indicative of a change in the primary coordination sphere of the complex, for example a six-coordinate complex may have formed. As before with Ca^{II} and Sr^{II} ions, the same Mn^{III} absorbance spectrum was produced from the addition of one equivalent of $[CoCp_2]$ to $[Mn^{IV}H_3buea(O)(Sc)]^{2+}$ in 1:1 DMF:THF at –80 °C, but the bands decayed to a featureless spectrum (Figure 5-12C). Additionally, the Sc^{III} adduct of $[Mn^{III}H_3buea(O)]^{2-}$ did not react with $[FeCp_2]^{+}$ under the same solvent and temperature conditions, which may be due to the increase in reduction potential as the overall charge of the complex increased with the binding of a Sc^{III} ion (Figure 5-12D). Both $[Mn^{III}H_3buea(O)(Sc)]^{+}$ and $[Mn^{IV}H_3buea(O)(Sc)]^{2+}$ were thermally unstable and decayed within 1-2 hours at temperatures above –35 °C, precluding additional potentiometric or crystallographic characterization.

Additional Reactivity of $[Mn^{V}H_3buea(O)]$ and $[Mn^{IV}H_3buea(O)]^{-}$ with Sc^{III} Ions. To test whether the activation of water from the solvent was responsible for the observed reactivity and new absorbance bands, the $[Mn^{IV}H_3buea(O)(Sc)]^{2+}$ species was generated in 1:1 DMF:THF at –80 °C and treated with 300 equivalents of water, resulting in two new absorbance bands at λ_{max} = 440 and 530 nm (Figure 5-13A). These bands were also generated by the addition of two equivalents of $[H_3NPh]^{+}$ to the $[Mn^{IV}H_3buea(O)(Sc)]^{2+}$ species under the same conditions (Figure

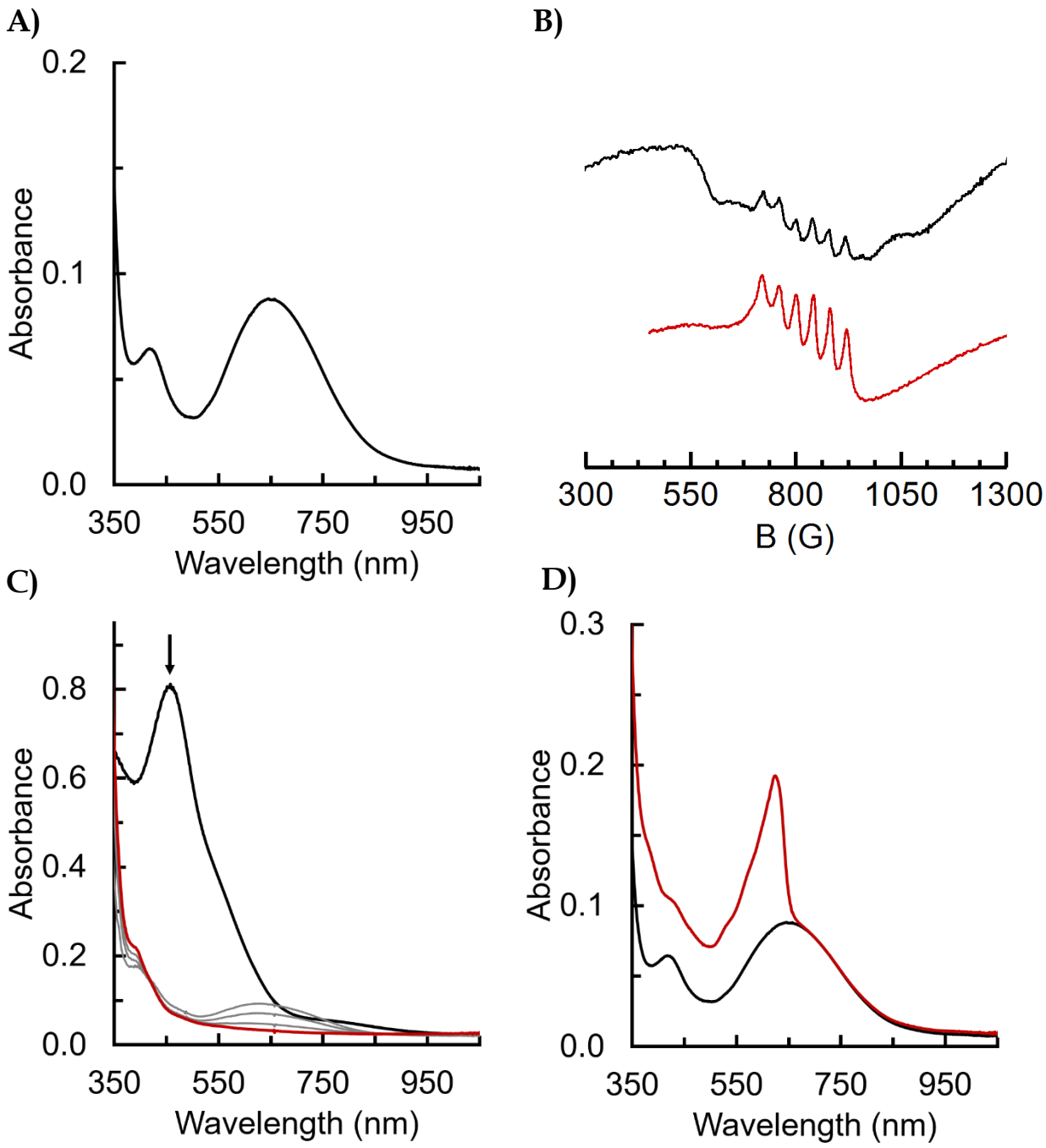

Figure 5-12. Final absorbance spectrum (A) from the reaction of $[Mn^{III}H_3buea(O)]^{2-}$ with 2 equivalents of Sc^{III} ions. Parallel-mode EPR spectrum of the same reaction (black) compared to the reaction of $[Mn^{IV}H_3buea(O)]^{-}$ with 2 equivalents of Sc^{III} ions (red) collected at 10 K in a 1:1 DMF:THF glass. UV-vis spectral changes (C) upon the addition of $[CoCp_2]$ to $[Mn^{IV}H_3buea(O)(Sc)]^{2+}$ (black) to generate a new $[Mn^{III}H_3buea(O)(Sc)]^{+}$ species which reacts further to produce a featureless spectrum (red). Gray traces represent 15 s scans. UV-vis spectra (D) of the addition of $[FeCp_2]^{+}$ to $[Mn^{III}H_3buea(O)(Sc)]^{+}$ (black) showing increase in absorbance features for unreacted $[FeCp_2]^{+}$ (red). UV-vis spectra collected in 1:1 DMF:THF at –80 °C.

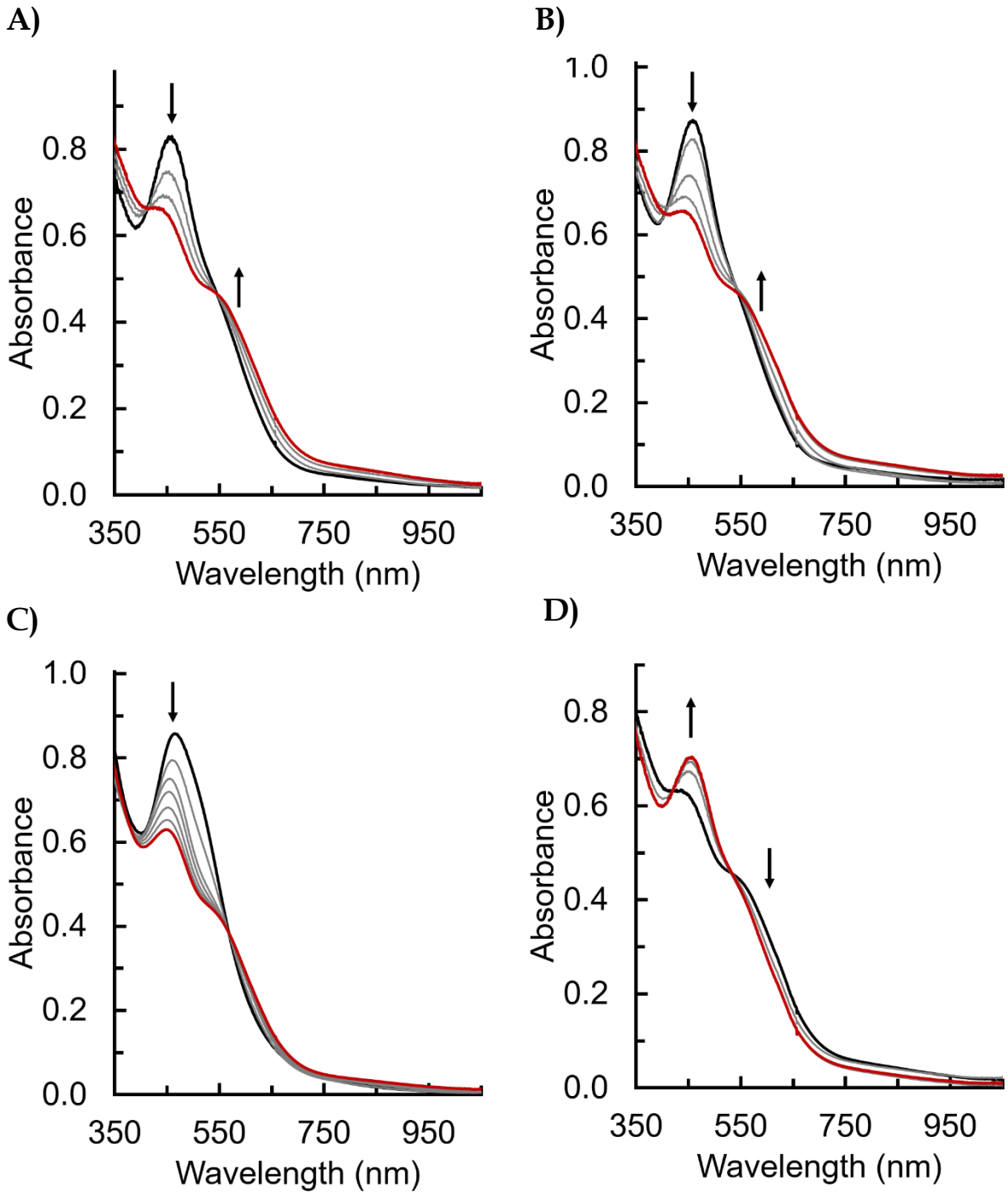

Figure 5-13. UV-vis spectral changes upon addition of 300 equivalents of water (A), two equivalents of $[H_3NPh]^+$ to $[Mn^{IV}H_3buea(O)(Sc)]^{2+}$ (black) (B), or 10 equivalents of Sc^{III} ions to $[Mn^{IV}H_3buea(OH)]$ (black) (C) to produce nearly identical final spectra (red). UV-vis spectral changes (D) upon the addition of 10 equivalents of DBU to $[Mn^{IV}H_3buea(O)(Sc)]^{2+}$ treated with two equivalents of $[H_3NPh]^+$ (black) to regenerate $[Mn^{IV}H_3buea(O)(Sc)]^{2+}$ (red). Gray traces represent 60 s scans. UV-vis spectra collected in 1:1 DMF:THF at –80 °C.

5-13B). In addition, treatment of [$Mn^{IV}H_3buea(OH)$] with ten equivalents of Sc^{III} produced nearly identical bands at λ_{max} = 445 and 530 nm (Figure 5-13C). Finally, addition of 10 equivalents of diazabicycloundecene (DBU) to the protonated [$Mn^{IV}H_3buea(O)(Sc)]^{2+}$ species regenerated ~80% of [$Mn^{IV}H_3buea(O)(Sc)]^{2+}$ (Figure 5-13D). These data suggest that protonation of [$Mn^{IV}H_3buea(O)(Sc)]^{2+}$, either by the addition of a large excess of water or slight excess of [$H_3NPh]^+$, produced the same Sc^{III} adduct of [$Mn^{IV}H_3buea(OH)$] (Scheme 5-2).

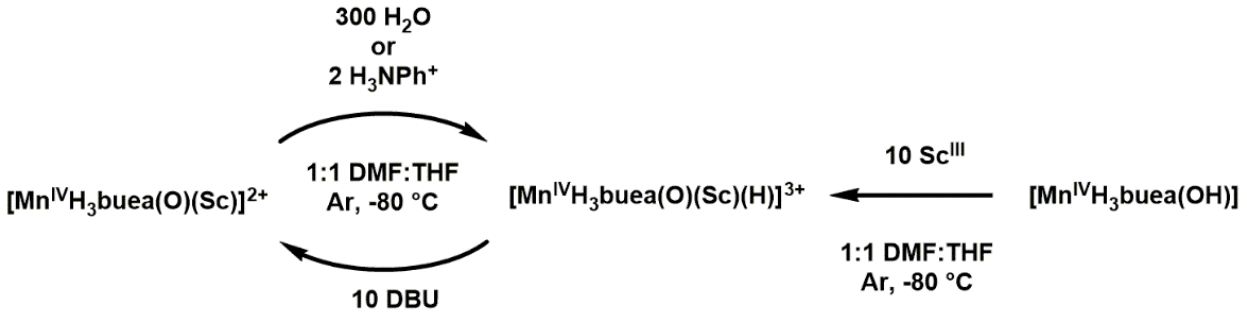

Scheme 5-2. Summary of reactions to produce the putative protonated congener of the [$Mn^{IV}H_3buea(O)(Sc)]^{2+}$ species.

Summary and Conclusions

The effect of redox inactive metal ions on a series of related high valent Mn–oxido complexes was examined. Treating [$Mn^{V}H_3buea(O)$] with an excess of Ca^{II} or Sc^{III} ions resulted in electron transfer from [$FeCp_2$] to generate what are proposed to be the Lewis acid adducts of [$Mn^{IV}H_3buea(O)]^-$; while treating [$Mn^{V}H_3buea(O)$] with up to 400 equivalents of Sr^{II} ions did not fully reduce the complex. The putative Lewis acid adducts of [$Mn^{IV}H_3buea(O)]^-$ could be independently generated by addition of either Ca^{II}, Sr^{II}, or Sc^{III} ions to [$Mn^{IV}H_3buea(O)]^-$. The three Lewis acid adducts of [$Mn^{IV}H_3buea(O)]^-$ could be further reduced by addition of [$CoCp_2$] to give the corresponding Mn^{III}-Lewis acid adducts. The redox process was reversible in the case of the Ca^{II} and Sr^{II} ions, but the [$Mn^{III}H_3buea(O)(Sc)]^+$ species did not react with [$FeCp_2]^+$ suggesting a substantial increase in the oxidation potential.

Despite differences in reactivity, the Ca^{II} and Sr^{II} adducts of $[Mn^{IV}H_3buea(O)]^-$ and $[Mn^{III}H_3buea(O)]^{2-}$ displayed similar spectroscopic properties, while the Sc^{III} adducts gave distinct properties attributed to the large increase in Lewis acidity of Sc^{III} ions. This result matched well with previous reports that synthetic Mn-oxido clusters with either Ca^{II} or Sr^{II} ions displayed nearly identical redox properties but the Sc^{III} adduct showed a dramatic increase in redox potential of the Mn-oxido cluster. The similarities in the properties between the Ca^{II} and Sr^{II} adducts of these metal complexes supports the reports that these two metal ions are the only two examined that can be utilized within the OEC and maintain function.

Experimental Details

General Procedures. All manipulations, unless otherwise stated, were performed under an argon atmosphere in a Vac-atmospheres dry box. All chemicals were purchased from commercial sources and used without further purification unless otherwise stated. $K_2[Mn^{III}H_3buea(O)]$, $[Mn^{IV}H_3buea(O)]^-$, $[Mn^{V}H_3buea(O)]$, $Sr(OTf)_2$, and $[FeCp_2][BF_4]$ were prepared according to previously published procedures.[25,27–30] $[H_3NPh][BF_4]$ was synthesized according to the general procedure for the synthesis of a protonated amine as described in Chapter 2.[31]

Physical Methods. Electronic absorption spectra were recorded in a 1 cm cuvette on an 8453 Agilent UV-Vis spectrometer equipped with an Unisoku Unispeks cryostat. X-band (9.28 GHz) EPR spectra were collected as frozen solutions using a Bruker EMX spectrometer equipped with an ER041XG microwave bridge.

Reactivity of $[Mn^{V}H_3buea(O)]$, $[Mn^{IV}H_3buea(O)]^-$, and $[Mn^{III}H_3buea(O)]^{2-}$ with Ca^{II}, Sr^{II}, and Sc^{III} by Low Temperature UV-vis Spectroscopy. A stock solution of $K_2[Mn^{III}H_3buea(O)]$ was prepared by dissolving (12 mg, 0.020 mmol) in 1 mL DMF:THF and stored at –35 °C. A stock solution of $[FeCp_2][BF_4]$ (11 mg, 0.04 mmol) was prepared in 1 mL of DMF:THF. A stock solution of $Ca(OTf)_2$ (80 mg, 0.24 mmol) was prepared in 500 μL of 1:1 DMF:THF. A stock solution of $Sc(OTf)_3$ (89 mg,

0.18 mmol) was prepared in 500 μL of 1:1 DMF:THF. A stock solution of $Sr(OTf)_2$ (95 mg, 0.25 mmol) was prepared in 500 μL of 1:1 DMF:THF. A stock solution of DBU (19 mg, 0.12 mmol) was prepared in 500 μL of 1:1 DMF:THF. A stock solution of $[H_3NPh][BF_4]$ was prepared by dissolving the white solid (10 mg, 0.055 mmol) in 2 mL of THF. A stock solution of $[CoCp_2]$ (13 mg, 0.069 mmol) was prepared in 500 μL of 1:1 DMF:THF and stored at –35 °C. To a 1 cm cuvette was added 2 mL of 1:1 DMF:THF. The cuvette was sealed with a rubber septum, transferred to the cryostat of a UV-vis spectrophotometer, and allowed to equilibrate for 15 minutes. For these studies, reagents must be added to the blank cuvette prior to $[Mn^{III}H_3buea(O)]^{2-}$ as dilution of $[Mn^{III}H_3buea(O)]^{2-}$ results in protonation from adventitious water to produce $[Mn^{III}H_3buea(OH)]^-$. Aliquots of reagents were added via gas-tight syringe and the reactions monitored spectrophotometrically.

Preparation of $[Mn^{V}H_3buea(O)]$, $[Mn^{IV}H_3buea(O)]^-$, and $[Mn^{III}H_3buea(O)]^{2-}$ with Ca^{II}, Sr^{II}, and Sc^{III} for EPR Spectroscopy. Stock solutions of $[Mn^{III}H_3buea(O)]^{2-}$, $[FeCp_2][BF_4]$, $Ca(OTf)_2$, $Sr(OTf)_2$, and $Sc(OTf)_3$ were prepared as described above. To an EPR tube was added 200 μL of $[Mn^{III}H_3buea(O)]^{2-}$ solution and then sealed with a rubber septum. The EPR tube was cooled in either a –78 °C or –35 °C acetone/dry ice bath and allowed to equilibrate for five minutes. Aliquots of reagents were added via gas-tight syringe and the tube was carefully and quickly shaken to mix. Reaction mixtures were maintained at low temperature for 5 minutes between each addition and prior to freezing in liquid nitrogen.

References

(1) Umena, Y.; Kawakami, K.; Shen, J.-R.; Kamiya, N. *Nature* **2011**, *473*, 55–60.
(2) Vogt, L.; Vinyard, D. J.; Khan, S.; Brudvig, G. W. *Curr. Opin. Chem. Biol.* **2015**, *25*, 152–158.
(3) Cox, N.; Pantazis, D. A.; Neese, F.; Lubitz, W. *Acc. Chem. Res.* **2013**, *46*, 1588–1596.
(4) Yocum, C. *Coord. Chem. Rev.* **2008**, *252*, 296–305.
(5) Boussac, A.; Rutherford, A. W. *Biochemistry* **1988**, *27*, 3476–3483.
(6) Brudvig, G. W. *Philos. Trans. R. Soc. Lond. B. Biol. Sci.* **2008**, *363*, 1211–1218; discussion 1218–1219.

(7) Vrettos, J. S.; Stone, D. A.; Brudvig, G. W. *Biochemistry* **2001**, *40*, 7937–7945.
(8) Boussac, A.; Rappaport, F.; Carrier, P.; Verbavatz, J.-M.; Gobin, R.; Kirilovsky, D.; Rutherford, A. W.; Sugiura, M. *J. Biol. Chem.* **2004**, *279*, 22809–22819.
(9) Mishra, A.; Wernsdorfer, W.; Abboud, K. A.; Christou, G. *Chem. Commun.* **2005**, 54–56.
(10) Zhang, C.; Chen, C.; Dong, H.; Shen, J.-R.; Dau, H.; Zhao, J. *Science* **2015**, *348*, 690–693.
(11) Kotzabasaki, V.; Siczek, M.; Lis, T.; Milios, C. J. *Inorg. Chem. Commun.* **2011**, *14*, 213–216.
(12) Mishra, A.; Yano, J.; Pushkar, Y.; Yachandra, V. K.; Abboud, K. A.; Christou, G. *Chem. Commun.* **2007**, 1538–1540.
(13) Codolà, Z.; Gómez, L.; Kleespies, S. T.; Que Jr, L.; Costas, M.; Lloret-Fillol, J. *Nat. Commun.* **2015**, *6*, 5865.
(14) Hong, S.; Pfaff, F. F.; Kwon, E.; Wang, Y.; Seo, M.-S.; Bill, E.; Ray, K.; Nam, W. *Angew. Chemie Int. Ed.* **2014**, n/a – n/a.
(15) Hong, S.; Lee, Y.-M.; Sankaralingam, M.; Vardhaman, A. K.; Park, Y. J.; Cho, K.-B.; Ogura, T.; Sarangi, R.; Fukuzumi, S.; Nam, W. *J. Am. Chem. Soc.* **2016**, *138*, 8523–8532.
(16) Prokop, K. A.; Goldberg, D. P. *J. Am. Chem. Soc.* **2012**, *134*, 8014–8017.
(17) Baglia, R. A.; Dürr, M.; Ivanović-Burmazović, I.; Goldberg, D. P. *Inorg. Chem.* **2014**, *53*, 5893–5895.
(18) Leeladee, P.; Baglia, R. A.; Prokop, K. A.; Latifi, R.; de Visser Sam, P.; Goldberg, D. P. *J. Am. Chem. Soc.* **2012**, *134*, 10397–10400.
(19) Zaragoza, J. P. T.; Baglia, R. A.; Siegler, M. A.; Goldberg, D. P. *J. Am. Chem. Soc.* **2015**, *137*, 6531–6540.
(20) Kanady, J. S.; Tsui, E. Y.; Day, M. W.; Agapie, T. *Science* **2011**, *333*, 733–736.
(21) Tsui, E. Y.; Agapie, T. *Proc. Natl. Acad. Sci. U. S. A.* **2013**, *110*, 10084–10088.
(22) Kanady, J. S.; Mendoza-Cortes, J. L.; Tsui, E. Y.; Nielsen, R. J.; Goddard, W. A.; Agapie, T. *J. Am. Chem. Soc.* **2013**, *135*, 1073–1082.
(23) Tsui, E. Y.; Kanady, J. S.; Agapie, T. *Inorg. Chem.* **2013**, *52*, 13833–13848.
(24) Tsui, E. Y.; Tran, R.; Yano, J.; Agapie, T. *Nat. Chem.* **2013**, *5*, 293–299.
(25) Shirin, Z.; Hammes, B. S.; Young, V. G.; Borovik, A. S. *J. Am. Chem. Soc.* **2000**, *122*, 1836–1837.
(26) Gupta, R.; Borovik, A. S. *J. Am. Chem. Soc.* **2003**, *125*, 13234–13242.
(27) Gupta, R.; Taguchi, T.; Lassalle-Kaiser, B.; Bominaar, E. L.; Yano, J.; Hendrich, M. P.; Borovik, A. S. *Proc. Natl. Acad. Sci. U. S. A.* **2015**, *112*, 5319–5324.
(28) Taguchi, T.; Gupta, R.; Lassalle-Kaiser, B.; Boyce, D. W.; Yachandra, V. K.; Tolman, W. B.; Yano, J.; Hendrich, M. P.; Borovik, A. S. *J. Am. Chem. Soc.* **2012**, *134*, 1996–1999.
(29) Parsell, T. H.; Behan, R. K.; Green, M. T.; Hendrich, M. P.; Borovik, A. S. *J. Am. Chem. Soc.* **2006**, *128*, 8728–8729.
(30) Connelly, N. G.; Geiger, W. E. *Chem. Rev.* **1996**, *96*, 877–910.
(31) Kanamura, K.; Yonezawa, S.; Kawai, Y.; Takehara, Z.-I. *J. Electroanal. Chem. Interfacial Electrochem.* **1991**, *301*, 291–295.

Chapter 6

Towards Reversible O–O Bond Formation by a Discrete Mn Oxygen Reduction Catalyst: Effect of Ca^{II} Ions

Reversible O–O bond formation is an important chemical process in both biological and synthetic systems.[1–6] The formation of O–O bonds, a crucial mechanistic step in water oxidation, occurs in only one known biological system, photosystem II (PSII).[7,8] In PSII, oxidation of water occurs at a [$CaMn_4O_5$] cluster known as the oxygen evolving complex (OEC).[2,9–12] A substantial amount of experimental data suggest that the cluster is oxidized to a state with three Mn^{IV} ions and one Mn^{V} ion prior to O–O bond formation.[13] The role of the Ca^{II} ion is not yet fully understood but it is known that substitution with other metal ions other than Sr^{II} inhibits O_2 formation.[14–16] Understanding the role of a redox inactive metal ion in O–O bond formation may require the development of synthetic systems that are capable of generating well-characterized peroxido or hydroperoxido complexes as these are important intermediates in O_2 production.[17–21]

Though there are a limited number of well-characterized metal peroxido or hydroperoxido complexes, examples exist purporting the interconversion between a metal

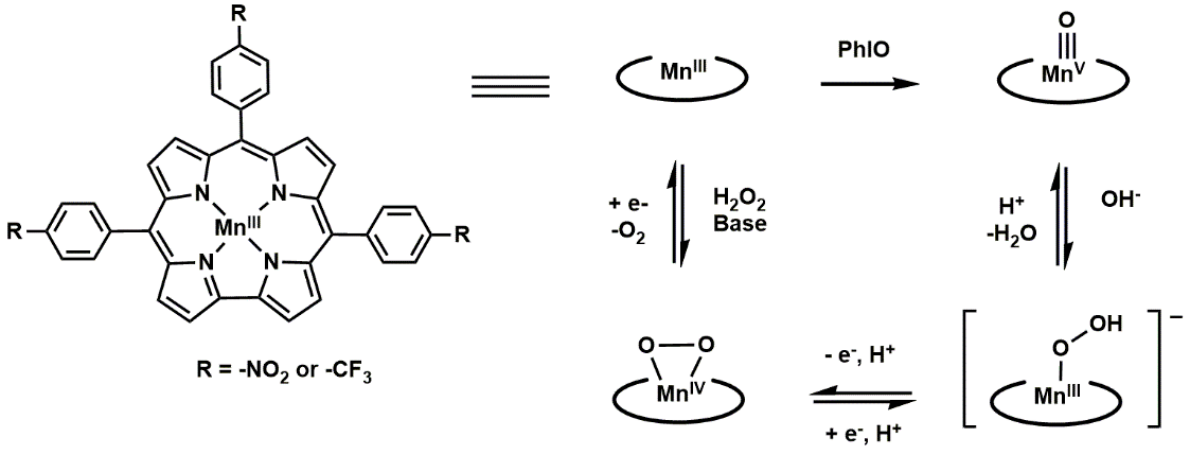

Scheme 6-1. The proposed mechanism for O–O bond making and breaking by Mn-corrole complexes.

peroxido and a high valent metal oxido species (Scheme 6-1).[22–26] Both of these systems use a Mn^{III}-corrole as a starting complex, with slight modifications at the ligand by incorporation of either nitro or trifluoromethyl functional groups.[22,27] Upon addition of the oxygen-atom (O-atom) transfer agent, iodosylbenzene (PhIO), a Mn^{V}-oxido complex was generated and characterized by standard methods such as UV-vis spectroscopy, resonance Raman (rR) spectroscopy, and mass spectrometry (MS). Addition of hydroxide anion to the Mn^{V}-oxido complex resulted in the formation of a putative Mn^{IV}-peroxido complex characterized by UV-vis and MS. While MS alone cannot confirm the presence of an intact O–O unit, the data, including labelling studies with ^{18}O, were consistent with the incorporation of two oxygen atoms into the starting complex. The Åkermark lab first reported the system and described the generation of O_2 from the addition of an oxidant to the Mn^{IV}-peroxido complex to regenerate the Mn^{III}-corrole starting complex where the cycle can be repeated.[27] The Nam lab reports that upon addition of acid to the Mn^{IV}-peroxido complex, the Mn^{V}-oxido complex can be regenerated.[22] Both authors report an example of conversion between a metal-peroxido and –oxido complex, but did not examine the effect of redox inactive metal ions on such a transformation.

The Borovik lab that has previously reported the generation of a Mn^{III}peroxido complex from the addition of O_2 to a Mn^{II} starting complex, $[Mn^{II}H_2bupa]^-$.[24] Addition of the hydrogen-atom (H-atom) source, diphenylhydrazine (DPH), resulted in the formation of

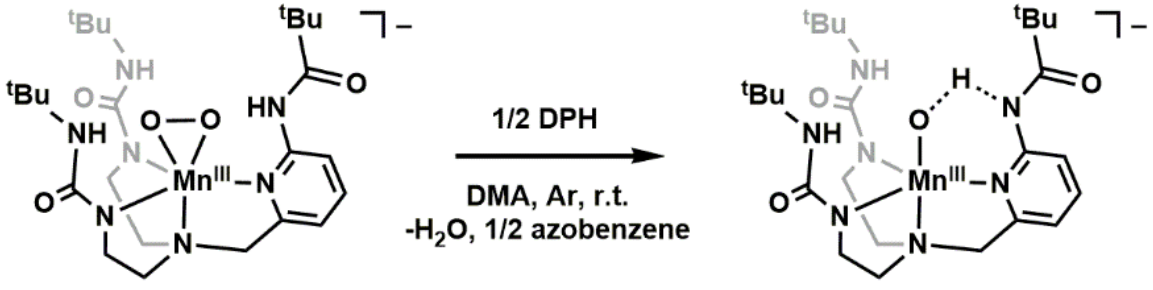

Scheme 6-2. The reaction of the conversion of $[Mn^{III}H_3bupa(O_2)]^-$ to yield $[Mn^{III}H_2bupa(O)(H)]^-$ by the addition of half an equivalent of DPH.

$[Mn^{III}H_2bupa(O)(H)]^-$, best described as a hybrid oxido/hydroxido complex. Further addition of DPH regenerates the $[Mn^{II}H_2bupa]^-$ starting complex where the cycle can be repeated for a modest number of turnovers (Scheme 6-2).[28] Chapter 5 described the interaction of high valent Mn-oxido complexes using the $[H_3buea]^{3-}$ ligand with various redox inactive metal ions. Those experiments demonstrated how the introduction of ions such as Ca^{II}, Sr^{II}, and Sc^{III} resulted in the attenuation of the reduction potentials of the Mn-oxido complexes resulting in electron transfer from ferrocene. In contrast to the chemistry of the $[H_3buea]^{3-}$ ligand system reported in Chapter 5, the $[H_2bupa]^{3-}$ ligand system provides an opportunity to examine the effect of redox inactive metal ions in O–O bond making and breaking using a discrete, well-characterized Mn^{III}-peroxido complex as a spectroscopic handle for O–O bond formation.

The potassium salt of $[Mn^{III}H_2bupa(O)(H)]^-$ can be isolated from the addition of PhIO in comparable yield to the reported synthesis from O_2.[29] From $[Mn^{III}H_2bupa(O)(H)]^-$, a high valent Mn^{IV} complex can be generated by the addition of $[FeCp_2]^+$ and was assigned to the $[Mn^{IV}H_2bupa(O)(H)]$ complex, likely to be a Mn^{IV}-oxido species. Treatment of a solution of $[Mn^{IV}H_2bupa(O)(H)]$ at low temperatures with a slight excess of Ca^{II} ions and base resulted in the partial generation of a Mn^{III} species identified by parallel mode electron paramagnetic resonance (EPR) spectroscopy which is similar to the previously reported $[Mn^{III}H_3bupa(O_2)]^-$ complex. Addition of one equivalent of acid to this solution regenerated a portion of $[Mn^{IV}H_2bupa(O)(H)]$, similar to the conversion reported by Nam and Åkermark discussed above. The new Mn^{III} species has not yet been fully characterized, but is preliminary evidence for the formation of an O–O bond. To date, such a Mn^{III} signal in parallel mode EPR spectroscopy has only been observed for $[Mn^{III}H_3bupa(O_2)]^-$ and no other Mn^{III} species generated using the $[H_2bupa]^{3-}$ ligand. The role of Ca^{II} in this system may be to attenuate either the basicity or reduction potential of the $[Mn^{IV}H_2bupa(O)(H)]$ complex as addition of Ca^{II} ions to independently generated

$[Mn^{III}H_3bupa(O_2)]^-$ did not produce a significant change by EPR spectroscopy. The experiments in this chapter serve as a starting point for further investigation into the identity of the Mn^{III} signal observed in the parallel-mode EPR spectrum and to gain a greater understanding of the potential role of Ca^{II} ions in the making and breaking of O–O bonds.

Results and Discussion

Synthesis and Characterization of $[Mn^{IV}H_2bupa(O)(H)]$. The generation of $[Mn^{III}H_2bupa(O)(H)]^-$ was accomplished by the addition of PhIO to a solution of $[Mn^{II}H_2bupa]^-$ and monitored for the loss of all insoluble PhIO. The solution of $[Mn^{III}H_2bupa(O)(H)]^-$ was then either stored at –35 °C for immediate use in spectroscopic experiments, or set up for recrystallization to obtain $K[Mn^{III}H_2bupa(O)(H)]$ for later use. The oxidation of $[Mn^{III}H_2bupa(O)(H)]^-$ by $[FeCp_2]^+$ at –35 °C in a 1:1 DMF:THF mixture was monitored

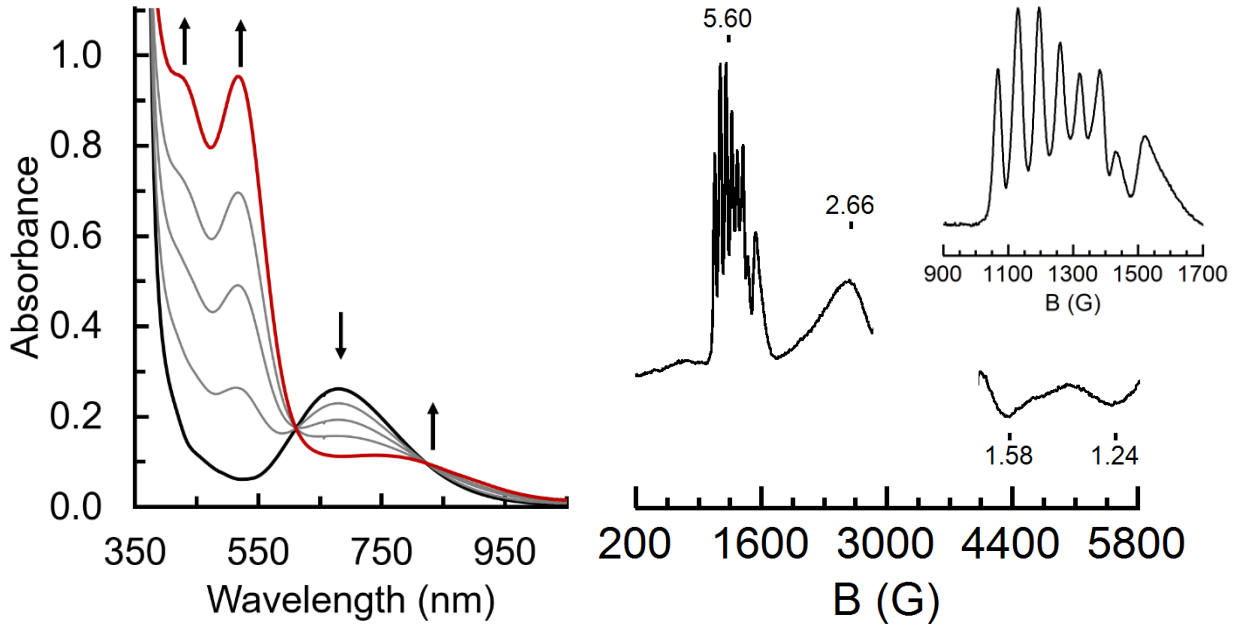

Figure 6-1. UV-vis (left) and EPR (right) spectral changes upon addition of one equivalent of $[FeCp_2]^+$ to $[Mn^{III}H_2bupa(O)(H)]^-$ (black) to generate $[Mn^{IV}H_2bupa(O)(H)]$ (red) at –35 °C in 1:1 DMF:THF. Gray lines indicate sequential 1/4 equivalent additions of $[FeCp_2]^+$. EPR spectrum collected at 10 K in a 1:1 DMF:THF glass. A portion of the spectrum centered at g = 2 is removed due to the presence of a large multiline signal. Inset: Expanded low field region showing hyperfine interaction from the ^{55}Mn nucleus with the $m_s \pm 1/2$ and $\pm 3/2$ doublets.

spectrophotometrically and showed the loss of the band for $[Mn^{III}H_2bupa(O)(H)]^-$ at λ_{max} = 685 nm with the growth of a new bands at λ_{max} = 425, 520, and 750 nm (Figure 6-1). A perpendicular mode EPR spectrum of the same reaction collected at 10 K in a 1:1 DMF:THF mixture revealed signals at g = 5.60, 2.66, 1.58, and 1.24 with nuclear hyperfine coupling of A = 62 G at g = 5.62 and A = 84 G at g = 5.27 consistent with the formation of a high spin mononuclear Mn^{IV} ion (Figure 6-1). The two sets of hyperfine features are due to transitions within the $m_s = \pm 1/2$ and $\pm 3/2$ doublets. The oxidized species was unstable at room temperature but persisted at –35 °C for several hours before reacting further to give a featureless spectrum in the visible region. While structural information on the identity of this species has yet to be obtained, a negative-mode mass spectrum of this reaction mixture revealed a molecular ion peak with a mass-to-charge ratio (m/z) of 647.14 that is consistent with $[Mn^{IV}H_2bupa(O)(H)(BF_4)]^-$ (calc: $C_{25}H_{44}O_4N_7BF_4Mn$ 647.28). This oxidative process was also shown to be reversible; monitoring spectrophotometrically the addition of one equivalent of $[CoCp_2]$ to the Mn^{IV} species at –35 °C in 1:1 DMF:THF resulted in

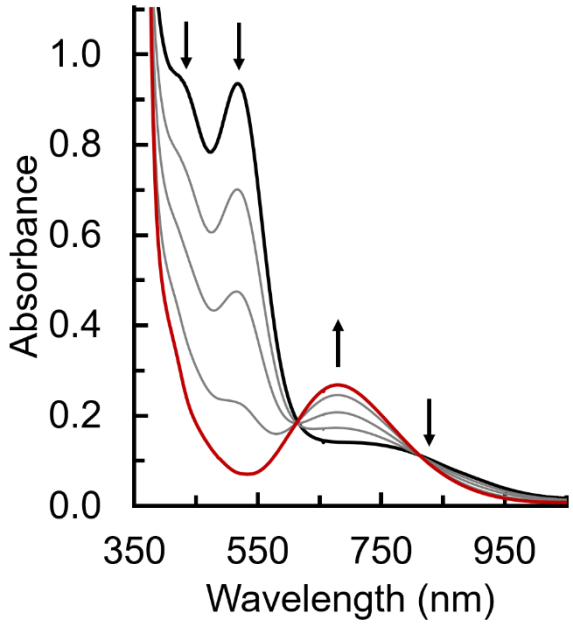

Figure 6-2. UV-vis spectral changes upon addition of one equivalent of $[CoCp_2]$ to $[Mn^{IV}H_2bupa(O)(H)]$ (black) to generate $[Mn^{III}H_2bupa(O)(H)]^-$ (red) at –35 °C in 1:1 DMF:THF. Gray lines indicate sequential 1/4 equivalent additions of $[CoCp_2]$.

regeneration of [$Mn^{III}H_2$bupa(O)(H)]$^-$, suggesting that the complex remains intact when oxidized (Figure 6-2). The [$Mn^{IV}H_2$bupa(O)(H)] complex does not react with weak X–H bonds; for example, treatment of [$Mn^{IV}H_2$bupa(O)(H)] with up to 3 equivalents of diphenylhydrazine (DPH) at –35 °C in 1:1 DMF:THF showed no reaction.

Reactivity of [$Mn^{IV}H_2$bupa(O)(H)] towards O–O bond formation. Because of the proposals which invoke high valent Mn^{IV}- and Mn^{V}-oxido or hydroxido complexes in biological and synthetic O–O bond formation, the [$Mn^{IV}H_2$bupa(O)(H)] complex was examined for any reactivity suggestive of O–O bond formation. Following the experiments discussed in Chapter 5 examining the reaction of Mn-oxido complexes with Lewis acids, [$Mn^{IV}H_2$bupa(O)(H)] was also treated with Ca^{II} ions. Addition of up to 10 equivalents of Ca^{II} ion to a solution of

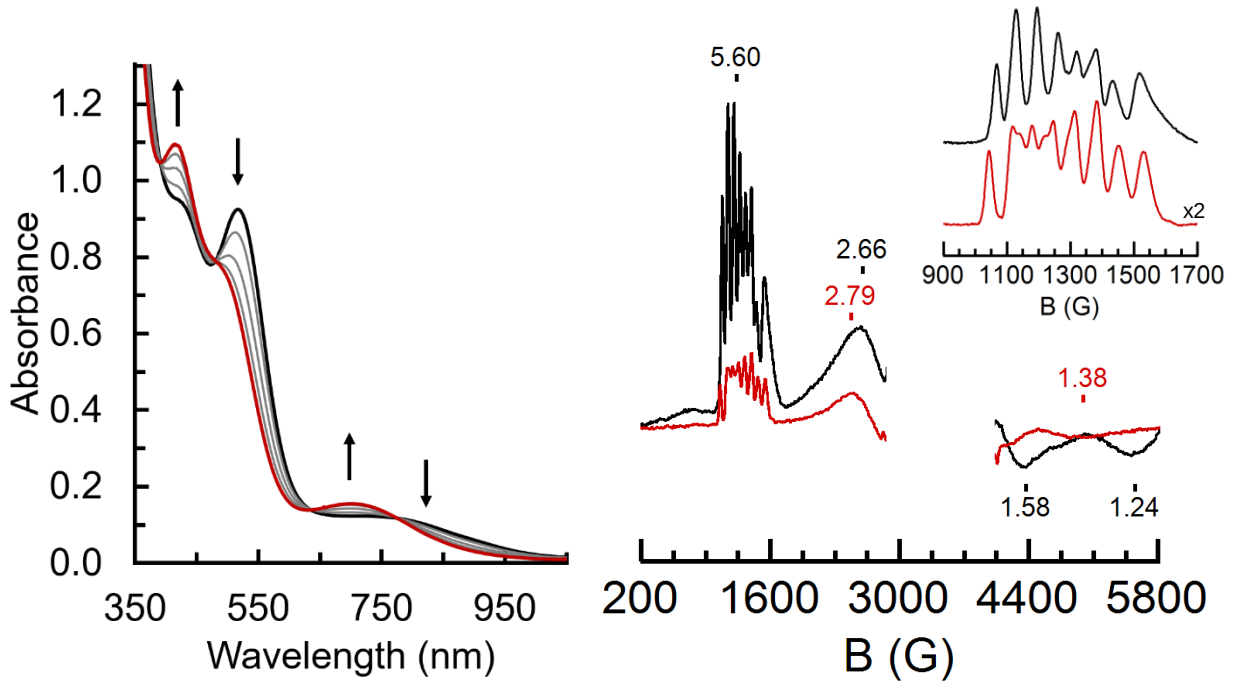

Figure 6-3. UV-vis (left) and EPR (right) spectral changes upon addition of two equivalents of DBU in the presence of three equivalents of Ca^{2+} ion to [$Mn^{IV}H_2$bupa(O)(H)] (black) to generate [$Mn^{IV}H_2$bupa(O)(Ca)]$^+$ (red) at –35 °C in 1:1 DMF:THF. Gray lines indicate five second scan intervals. EPR spectrum collected at 10 K in a 1:1 DMF:THF glass. A portion of the spectrum centered at g = 2 is removed due to the presence of a large multiline signal. Inset: Expanded low field region showing hyperfine interaction from the ^{55}Mn nucleus with the $m_s = \pm 1/2$ and $\pm 3/2$ doublets.

[$Mn^{IV}H_2$bupa(O)(H)] at –35 °C in 1:1 DMF:THF resulted in no observable changes in the spectroscopic properties of the complex. However, in the presence of two equivalents of diazabicycloundecene (DBU), addition of three equivalents of Ca^{II} ion again at –35 °C in 1:1 DMF:THF resulted in an immediate reaction to produce a new spectrum with bands at λ_{max} = 420 and 710 nm with a shoulder at 485 nm (Figure 6-3). When this reaction was examined by EPR spectroscopy two new species were produced. The majority of the Mn observed was a high spin, S = 3/2 Mn^{IV} species distinct from [$Mn^{IV}H_2$bupa(O)(H)] with g = 5.60, 2.79, and 1.38 with A = 68 G at g = 5.67 and A = 78 G at g = 5.16.

Addition of either Ca^{II} ions or DBU alone to [$Mn^{IV}H_2$bupa(O)(H)] at –35 °C in 1:1 DMF:THF did not produce a reaction and only in the presence of both was a new Mn^{IV} species observed. The requirement of both Ca^{II} ions and DBU suggests that while the addition of Ca^{II} ions does not produce an observable reaction, the Lewis acid may serve to modulate the pK_a of [$Mn^{IV}H_2$bupa(O)(H)] so that DBU can deprotonate it, generating what is tentatively assigned to [$Mn^{IV}H_2$bupa(O)(Ca)]$^+$ (Scheme 6-3). To test this hypothesis, the addition of two equivalents of [H_3NPh]$^+$ to the solution of [$Mn^{IV}H_2$bupa(O)(Ca)]$^+$ at –35 °C in 1:1 DMF:THF partially regenerated [$Mn^{IV}H_2$bupa(O)(H)] in ~60% spectroscopic yield based on the initial and final absorbance at λ_{max} = 420 nm (Figure 6-4). These results show that a proton must bind more strongly to

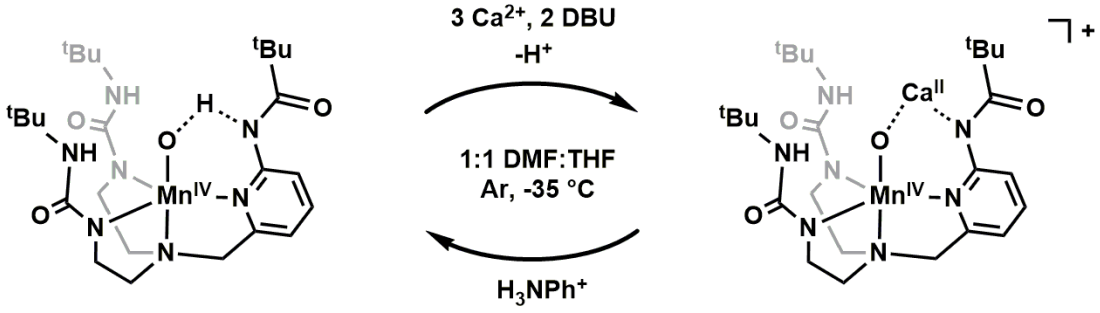

Scheme 6-3. Proposed reaction of [$Mn^{IV}H_2$bupa(O)(H)]$^-$ with Ca^{2+} in the presence of DBU to yield a putative [$Mn^{IV}H_2$bupa(O)(Ca)]$^+$ complex.

[$Mn^{IV}H_2$bupa(O)(H)] than a Ca^{2+} ion, and only upon removal of a proton is there a reaction to generate the new Mn^{IV} species identified by EPR spectroscopy.

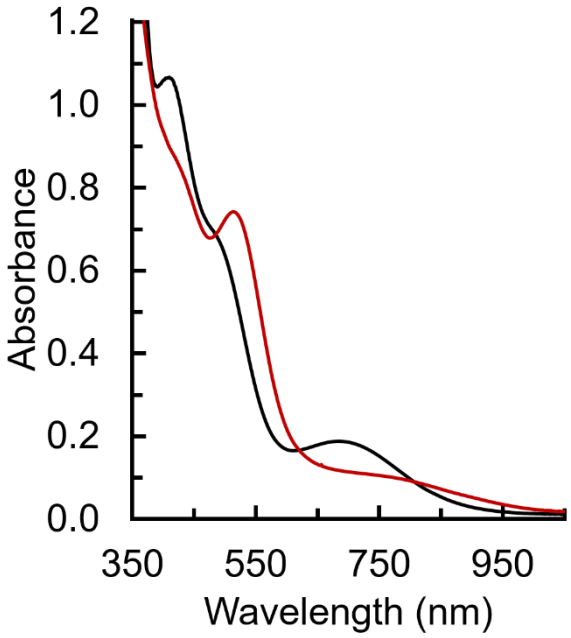

Figure 6-4. UV-vis spectroscopic changes upon addition of two equivalents of $[H_3NPh]^+$ to $[Mn^{IV}H_2$bupa(O)(Ca)$]^+$ (black) to regenerate ~60% [$Mn^{IV}H_2$bupa(O)(H)] (red) at –35 °C in 1:1 DMF:THF.

Control Reactions to Determine the Identity of the New Mn^{III} Species. In addition to the new Mn^{IV} species observed by UV-vis and perpendicular-mode EPR spectroscopies from the addition of a slight excess of Ca^{II} ions and DBU to a solution of [$Mn^{IV}H_2$bupa(O)(H)] in 1:1 DMF:THF at –35 °C, a minor species was observed in parallel-mode consistent with a high spin mononuclear Mn^{III} center at g = 8.35 with A = 53 G (Figure 6-5). The new Mn^{III} signal is of particular interest due to the similarity to the parallel-mode EPR signal associated with $[Mn^{III}H_3bupa(O_2)]^-$ generated from dioxygen (Figure 6-5). This EPR signal for $[Mn^{III}H_3bupa(O_2)]^-$ is the only parallel-mode signal observed in the Mn chemistry with the $[H_2bupa]^{3-}$ ligand, suggesting that the signal observed from the addition of Ca^{II} ions and DBU to [$Mn^{IV}H_2$bupa(O)(H)] may arise from O–O bond formation to generate a Mn^{III}-peroxido species via an unknown mechanism (Scheme 6-4).

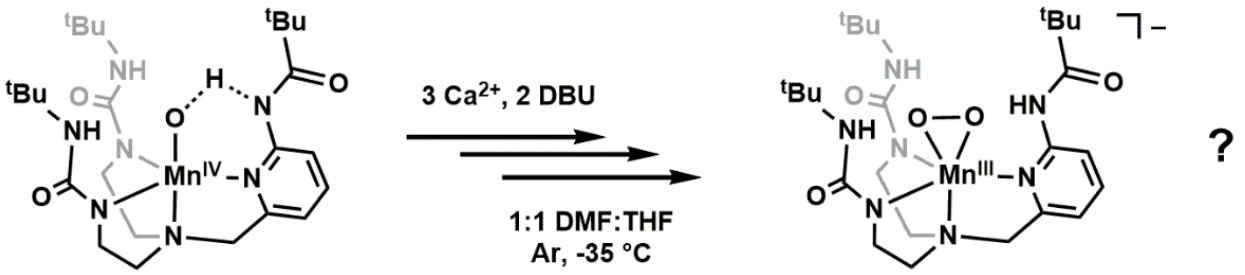

Scheme 6-4. The reaction of $[Mn^{IV}H_2bupa(O)(H)]^-$ with Ca^{2+} in the presence of DBU to yield the proposed Mn^{III}-peroxido complex via O–O bond formation.

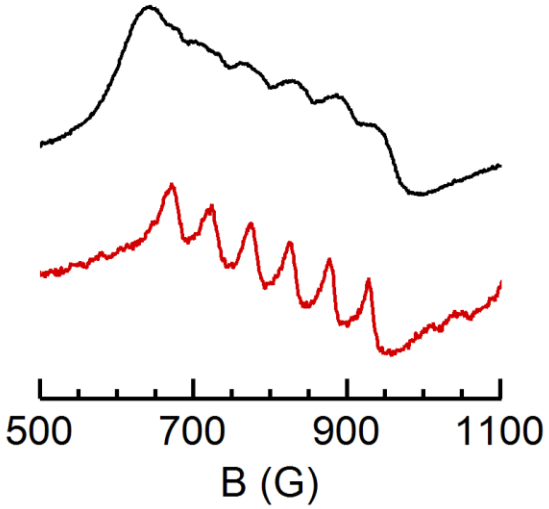

Figure 6-5. Parallel mode EPR spectra of $[Mn^{III}H_3bupa(O_2)]^-$ (black) and the reaction of $[Mn^{IV}H_2bupa(O)(H)]$ with three equivalents of Ca^{II} ion and two equivalents of DBU (red). Spectra recorded at 10K in a 1:1 DMF:THF glass.

While additional experiments are needed to confirm this premise, namely resonance Raman spectroscopy, some control experiments have been conducted to rule out other possible species that could produce this Mn^{III} EPR signal. For example, the signal could be from $[Mn^{III}H_2bupa]$, $[Mn^{III}H_2bupa(O)(Ca)]$, or a calcium bound peroxido complex, $[Mn^{III}H_2bupa(O_2)(Ca)]$.

To test this premise, the independent preparation and characterization of $[Mn^{III}H_2bupa]$ was first investigated: addition of $[FeCp_2]^+$ to $[Mn^{II}H_2bupa]^-$ at –35 °C in 1:1 DMF:THF was monitored by UV-vis and EPR spectroscopies. UV-vis spectral measurements showed the increase of a single band at λ_{max} = ~510 nm (Figure 6-6). The EPR signal for $[Mn^{II}H_2bupa]^-$

disappeared but there were no new signals associated with a Mn^{III} center in the parallel-mode EPR spectra.

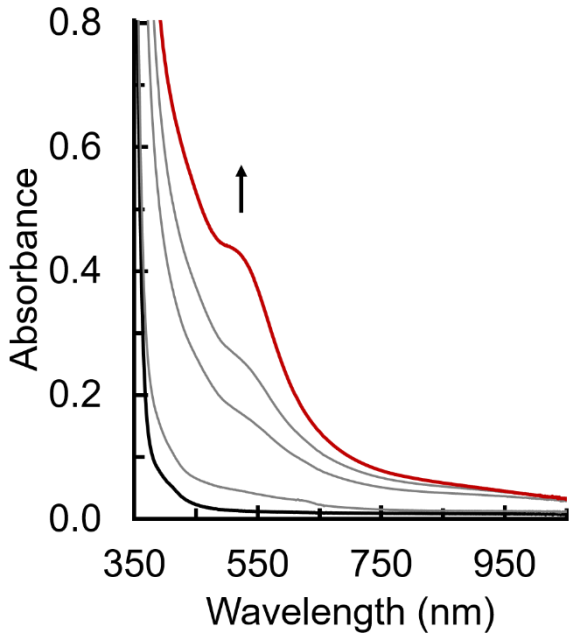

Figure 6-6. UV-vis spectroscopic changes upon addition of one equivalent of $[FeCp_2]^+$ to $[Mn^{II}H_2bupa]^-$ (black) to generate the putative $[Mn^{III}H_2bupa]$ complex (red) at –35 °C in 1:1 DMF:THF. Gray lines represent 20 sec scan intervals.

The chemistry of the Mn complexes with $[H_3buea]^{3-}$ described in Chapter 5 demonstrated that addition of Lewis acids to high valent Mn-oxido complexes often resulted in an electron transfer to reduce the metal complex. To examine whether the same reaction was giving rise to the Mn^{III} signal, the $[Mn^{IV}H_2bupa(O)(Ca)]^+$ complex was treated with $[CoCp_2]$ at –35 °C in 1:1 DMF:THF. A new species was generated with absorbance features at λ_{max} = ~415 and 660 nm. The same spectroscopic features could also be generated by the addition of one equivalent of Ca^{II} ion, in the absence or presence of DBU, to a solution of $[Mn^{III}H_2bupa(O)(H)]^-$ at –35 °C in 1:1 DMF:THF (Figure 6-7). These data suggest a new $[Mn^{III}H_2bupa(O)(H)(Ca)]^+$ can be generated by either method described above. Following the same reaction by EPR spectroscopy showed no new signals in either perpendicular- or parallel-modes. These results suggest that the Mn^{III} signal observed previously (Figure 6-5) was not from the putative $[Mn^{III}H_2bupa(O)(H)(Ca)]^+$.

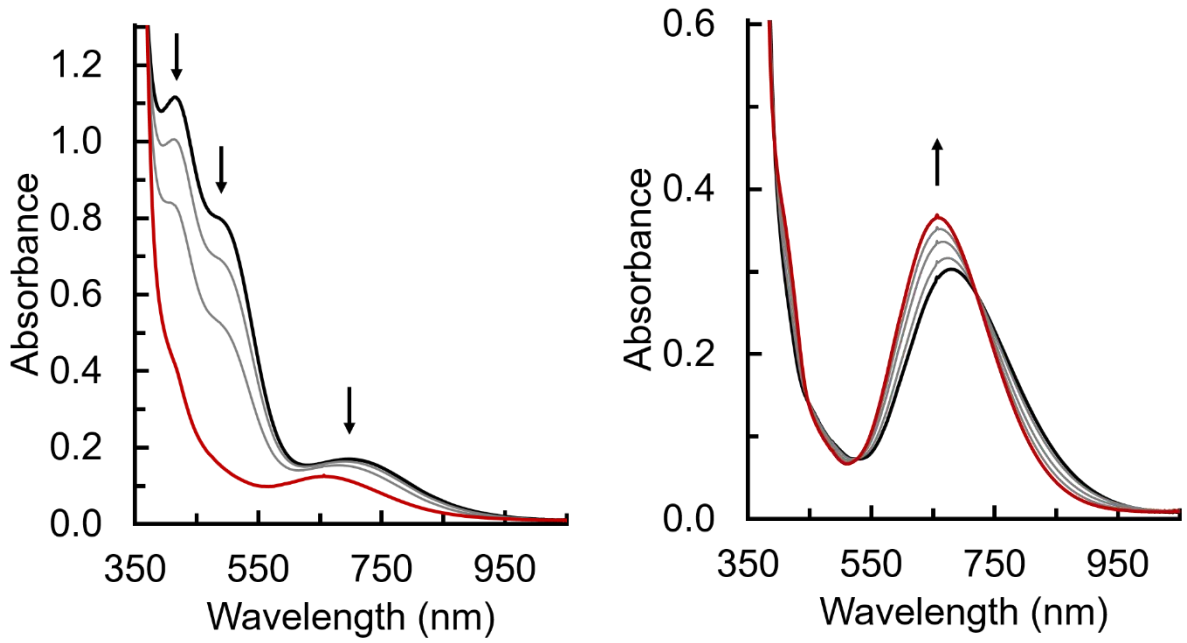

Figure 6-7. UV-vis spectral changes upon addition of (left) one equivalent of $[CoCp_2]$ to $[Mn^{IV}H_2bupa(O)(Ca)]^+$ (black) to generate a $[Mn^{III}H_2bupa(O)(H)(Ca)]^+$ complex (red) at –35 °C in 1:1 DMF:THF. Gray lines represent 1/4 equivalent additions of $[CoCp_2]$. UV-vis spectral changes upon addition of (right) three equivalents of Ca^{II} ion to $[Mn^{III}H_2bupa(O)(H)]^-$ (black) to generate a $[Mn^{III}H_2bupa(O)(H)(Ca)]^+$ complex (red) at –35 °C in 1:1 DMF:THF. Gray lines represent one second scan intervals.

To examine the reversibility of the reduction of $[Mn^{IV}H_2bupa(O)(Ca)]^+$, $[FeCp_2]^+$ was added to the solution of $[Mn^{III}H_2bupa(O)(H)(Ca)]^+$ which regenerated the $[Mn^{IV}H_2bupa(O)(H)]$ complex and not $[Mn^{IV}H_2bupa(O)(Ca)]^+$ (Figure 6-8A). However, if two equivalents of DBU were added prior to oxidation, the putative $[Mn^{IV}H_2bupa(O)(Ca)]^+$ complex could be generated (Figure 6-8B). As expected, when the $[Mn^{III}H_2bupa(O)(Ca)]^+$ complex was oxidized to generate $[Mn^{IV}H_2bupa(O)(H)]$ and solvated Ca^{II} ions, addition of two equivalents of DBU generated the $[Mn^{IV}H_2bupa(O)(Ca)]^+$ species (Figure 6-8C).

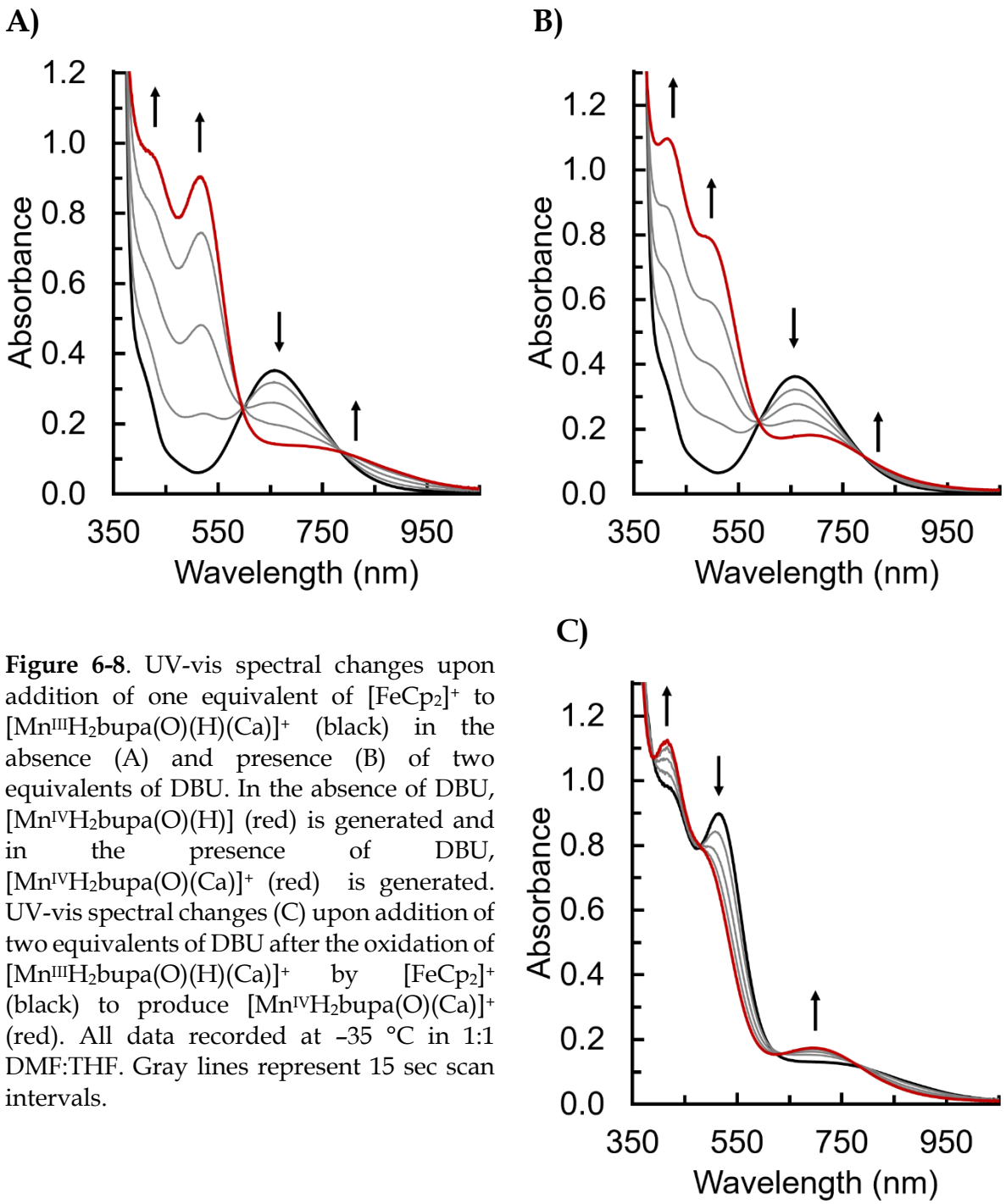

Figure 6-8. UV-vis spectral changes upon addition of one equivalent of $[FeCp_2]^+$ to $[Mn^{III}H_2bupa(O)(H)(Ca)]^+$ (black) in the absence (A) and presence (B) of two equivalents of DBU. In the absence of DBU, $[Mn^{IV}H_2bupa(O)(H)]$ (red) is generated and in the presence of DBU, $[Mn^{IV}H_2bupa(O)(Ca)]^+$ (red) is generated. UV-vis spectral changes (C) upon addition of two equivalents of DBU after the oxidation of $[Mn^{III}H_2bupa(O)(H)(Ca)]^+$ by $[FeCp_2]^+$ (black) to produce $[Mn^{IV}H_2bupa(O)(Ca)]^+$ (red). All data recorded at –35 °C in 1:1 DMF:THF. Gray lines represent 15 sec scan intervals.

Finally, the $[Mn^{III}H_3bupa(O_2)]^-$ was generated as previously described by the addition of O_2 to a solution of $[Mn^{II}H_2bupa]^-$ at room temperature in a 1:1 DMF:THF solution. This solution was then cooled to –35 °C and treated with Ca^{II} ions and an absorbance band at λ_{max} = 660 nm was generated, but was at a lower intensity compared to the addition of Ca^{II} ions to

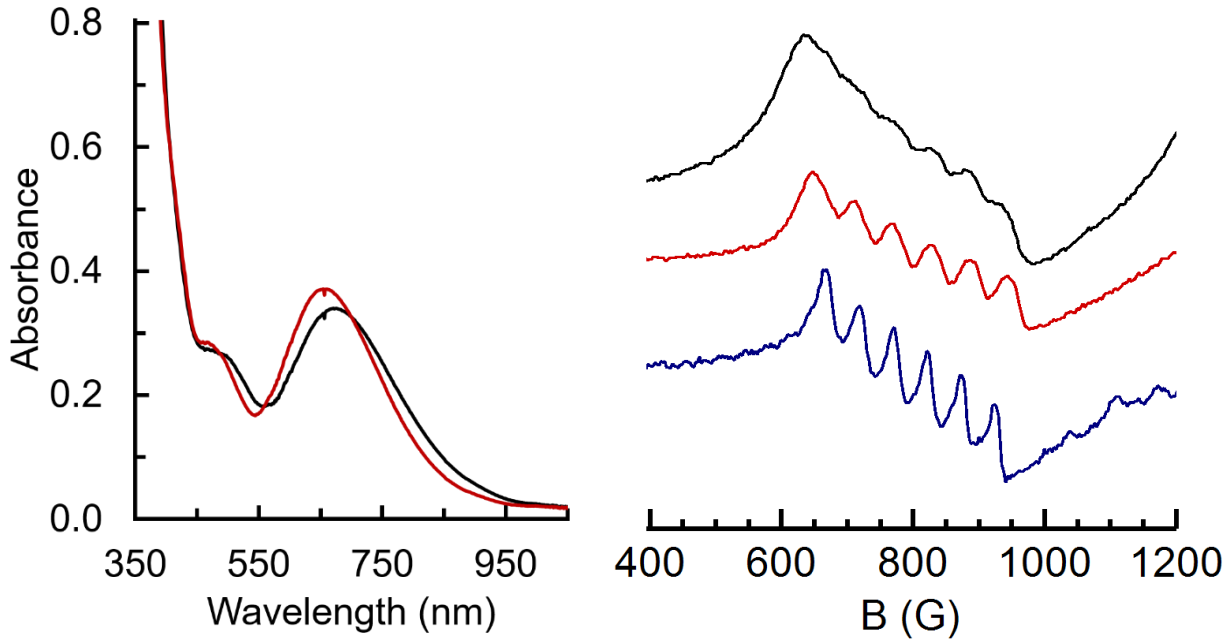

Figure 6-9. UV-vis (left) spectroscopic changes upon addition of three equivalents of Ca^{2+} ion to $[Mn^{III}H_3bupa(O_2)]^-$ (black) to yield a new spectrum (red) similar to $[Mn^{III}H_2bupa(O)(H)(Ca)]^+$ at –35 °C in 1:1 DMF:THF. Parallel mode EPR spectrum (right) comparing $[Mn^{III}H_3bupa(O_2)]^-$ (black), the reaction of $[Mn^{III}H_3bupa(O_2)]^-$ with three equivalents of Ca^{2+} ion (red), and the reaction of $[Mn^{IV}H_2bupa(O)(H)]$ with two equivalents of DBU in the presence of three equivalents of Ca^{2+} (blue) collected at 10 K in a 1:1 DMF:THF glass.

$[Mn^{III}H_2bupa(O)(H)]^-$ (Figure 6-9). While the absorbance band at λ_{max} = 660 nm is similar to the spectrum produced by the reaction of Ca^{II} ions with $[Mn^{III}H_2bupa(O)(H)]^-$, it was previously shown that $[Mn^{III}H_3bupa(O_2)]^-$ will slowly react to give $[Mn^{III}H_2bupa(O)(H)]^-$ which in turn may react with Ca^{II} in solution to produce the λ_{max} = 660 nm band. Preparing two, identical EPR samples of $[Mn^{III}H_3bupa(O_2)]^-$ and treating one with Ca^{II} ions gave nearly identical parallel mode spectra. Both the samples treated with and without Ca^{II} ions gave signals at g = 8.4 with A = 58 G; but the sample treated with Ca^{II} ions gave more well-defined hyperfine splitting (Figure 6-9). These results show that Ca^{II} ions do not degrade the $[Mn^{III}H_3bupa(O_2)]^-$ complex at –35 °C. Moreover, while these results suggest that a new Mn^{III}-peroxido species could be generated, more experiments are needed to confirm that this species is responsible for the new Mn^{III} parallel-mode signal generated by addition of Ca^{II} and DBU to $[Mn^{IV}H_2bupa(O)(H)]$.

Summary and Conclusion

Reversible O–O bond formation is a vital chemical reaction in biology and energy science. Systems have been developed that are capable of making and breaking O–O bonds, however the mechanistic steps that lead to these processes have not been fully explored. Moreover, the potential role(s) of redox inactive metal ions in these transformations, like the Ca^{II} ion within the OEC, are still uncertain. The $[H_2bupa]^{3-}$ ligand provides the opportunity for using a previously characterized Mn-peroxido complex, $[Mn^{III}H_3bupa(O_2)]^-$, as a potential spectroscopic reference to detect O–O bond formation from a high valent Mn-oxido complex. The addition of a slight excess of both Ca^{II} ions and DBU to the $[Mn^{IV}H_2bupa(O)(H)]$ complex resulted in the generation of two, detectable species: a new Mn^{IV} complex and a Mn^{III} species identified by EPR spectroscopy. The new Mn^{III} signal observed is similar to the previously characterized $[Mn^{III}H_3bupa(O_2)]^-$, suggesting O–O bond formation. However, additional data is needed to corroborate this assignment (e.g. vibrational measurements).Another complication is that while this species as been generated independently several times, the EPR signal could not always be reliably reproduced. Addition of Ca^{II} to independently generated $[Mn^{III}H_3bupa(O_2)]^-$ resulted in a sharpening of the ^{55}Mn hyperfine, indicating the Mn^{III}-peroxido complex does not decompose in the presence of Ca^{II}.

The new Mn^{IV} complex observed from the addition of Ca^{II} ions and DBU has been assigned to the putative $[Mn^{IV}H_2bupa(O)(Ca)]^+$. The same species can also be generated by the addition of $[FeCp_2]^+$ to $[Mn^{III}H_2bupa(O)(H)]^-$ in the presence of Ca^{II} ions and DBU. The requirement of both Ca^{II} ions and DBU to generate the $[Mn^{IV}H_2bupa(O)(Ca)]^+$ complex suggests the binding of a Ca^{II} ion at the Mn^{IV} oxidation state is not possible with a proton strongly associated with the oxido ligand (Scheme 6-3). However, the $[Mn^{III}H_2bupa(O)(H)]^-$ complex reacted with Ca^{II} ions and addition of DBU did not alter the final absorbance spectrum.

Experimental

General Procedures. All manipulations, unless otherwise stated, were performed under an argon atmosphere in a Vac-atmospheres dry box. All chemicals were purchased from commercial sources and used without further purification unless otherwise stated. K[$Mn^{II}H_2$bupa], solutions of [$Mn^{III}H_3$bupa(O_2)]$^-$, [$FeCp_2$][BF_4], and PhIO were prepared according to previously published procedures.[24,28,30]

Physical Methods. Electronic absorption spectra were recorded in a 1 cm cuvette on an 8453 Agilent UV-Vis spectrometer equipped with an Unisoku Unispeks cryostat. X-band (9.28 GHz) EPR spectra were collected as frozen solutions using a Bruker EMX spectrometer equipped with an ER041XG microwave bridge. The mass spectrometry (MS) was collected in the Mass Spectrometry Facility at the University of California, Irvine using a Trace MSplus from Thermo Fisher (San Jose, CA) by electron ionization (70 eV) scanning (1/sec) from m/z 200-1000.

Modified Synthesis of K[$Mn^{III}H_2$bupa(O)(H)]. The previously published procedure for the synthesis of K[$Mn^{III}H_2$bupa(O)(H)] was followed with slight modification. A solution of K[$Mn^{II}H_2$bupa] (100 mg, 0.172 mmol) in 3 mL of anhydrous *N,N*-dimethylacetamide (DMA) was treated with 1.05 equivalents of PhIO (38 mg, 0.17 mmol) at room temperature and allowed to stir for ~30 minutes until all solids dissolved. Dark green crystals (24 mg, 23%) were isolated by diffusion of diethyl ether (Et_2O) into the DMA solution at room temperature. The physical properties of the green crystals matched those previously reported.

Preparation of [$Mn^{IV}H_2$bupa(O)(H)] for Low Temperature UV-vis Experiments. A stock solution of [$Mn^{III}H_2$bupa(O)(H)]$^-$ was prepared either by dissolving crystalline K[$Mn^{III}H_2$bupa(O)(H)] (12 mg, 0.020 mmol) in 1 mL of 1:1 DMF:THF with 18-crown-6 ether (10 mg, 0.037 mmol) added for solubility or by in situ oxidation of [$Mn^{II}H_2$bupa]$^-$ by addition of PhIO (5 mg, 0.02 mmol) to a solution of K[$Mn^{II}H_2$bupa] (12 mg, 0.020 mmol) in 1 mL of 1:1 DMF:THF with 18-crown-6 ether

(10 mg, 0.037 mmol) added for solubility. The reaction was stirred for ~30 minutes until all solids dissolved and then stored at –35 °C. To a 1 cm cuvette was added 2 mL of 1:1 DMF:THF and an aliquot of the $[Mn^{III}H_2bupa(O)(H)]^-$ solution to yield a 0.2 mM final concentration. The cuvette was sealed with a rubber septum, transferred to the cryostat of a UV-vis spectrophotometer, and allowed to equilibrate for 15 minutes. A stock solution of $[FeCp_2][BF_4]$ (11 mg, 0.04 mmol) was prepared in 1 mL of DMF:THF and an aliquot of this solution was added via gas-tight syringe to the pre-cooled solution of $[Mn^{III}H_2bupa(O)(H)]^-$ to generate $[Mn^{IV}H_2bupa(O)(H)]$. ESI- m/z *Anal* (calc): *647.14* ($C_{25}H_{44}O_4N_7BF_4Mn$ 647.28).

Preparation of $[Mn^{IV}H_2bupa(O)(H)]$ for EPR Experiments. Stock solutions of $[Mn^{III}H_2bupa(O)(H)]^-$ and $[FeCp_2][BF_4]$ were prepared as described above. To an EPR tube was added 200 μL of this solution and then sealed with a rubber septum. The EPR tube was cooled in a –35 °C acetone/dry ice bath and allowed to equilibrate for five minutes. An aliquot of $[FeCp_2][BF_4]$ was added via gas-tight syringe and the tube was carefully and quickly shaken to mix. The mixture was maintained at –35 °C for five minutes before freezing in liquid nitrogen.

Reactivity of $[Mn^{III}H_2bupa(O)(H)]^-$ and $[Mn^{IV}H_2bupa(O)(H)]$ by Low Temperature UV-vis Spectroscopy. Stock solutions of $[Mn^{III}H_2bupa(O)(H)]^-$ and $[FeCp_2][BF_4]$ were prepared as described above. A stock solution of $Ca(OTf)_2$ (80 mg, 0.24 mmol) was prepared in 500 μL of 1:1 DMF:THF. A stock solution of DBU (19 mg, 0.12 mmol) was prepared in 500 μL of 1:1 DMF:THF. A stock solution of $[CoCp_2]$ (13 mg, 0.069 mmol) was prepared in 500 μL of 1:1 DMF:THF and stored at –35 °C. To a 1 cm cuvette was added 2 mL of 1:1 DMF:THF and an aliquot of the $[Mn^{III}H_2bupa(O)(H)]^-$ solution to yield a 0.2 mM final concentration. The cuvette was sealed with a rubber septum, transferred to the cryostat of a UV-vis spectrophotometer, and allowed to equilibrate for 15 minutes. For reactivity studies of $[Mn^{IV}H_2bupa(O)(H)]$, an aliquot of $[FeCp_2][BF_4]$ was added via gas-tight syringe to the pre-cooled solution of $[Mn^{III}H_2bupa(O)(H)]^-$

to generate [$Mn^{IV}H_2$bupa(O)(H)]. Aliquots of reagents were added via gas-tight syringe and the reaction monitored spectrophotometrically.

Reactivity of [$Mn^{III}H_2$bupa(O)(H)]$^-$ and [$Mn^{IV}H_2$bupa(O)(H)] by EPR Spectroscopy. Stock solutions of [$Mn^{III}H_2$bupa(O)(H)]$^-$, [$FeCp_2$][BF_4], $Ca(OTf)_2$, DBU, and [$CoCp_2$] were prepared as described above. To an EPR tube was added 200 μL of [$Mn^{III}H_2$bupa(O)(H)]$^-$ solution and then sealed with a rubber septum. The EPR tube was cooled in a –35 °C acetone/dry ice bath and allowed to equilibrate for five minutes. Aliquots of reagents were added via gas-tight syringe and the tube was carefully and quickly shaken to mix. Reaction mixtures were maintained at –35 °C for 5 minutes between each addition and prior to freezing in liquid nitrogen.

Generation and Reactivity of [$Mn^{III}H_3$bupa(O_2)]$^-$ with Ca^{II} by UV-vis and EPR Spectroscopy. [$Mn^{III}H_3$bupa(O_2)]$^-$ was prepared as previously described with minor modifications. A stock solution of K[$Mn^{II}H_2$bupa] (12 mg, 0.020 mmol) was prepared in 1 mL of 1:1 DMF:THF with 18-crown-6 ether (10 mg, 0.037 mmol) added for solubility. For UV-vis experiments, a 1 cm cuvette was charged with 2 mL of 1:1 DMF:THF and an aliquot of the [$Mn^{II}H_2$bupa]$^-$ solution was added to yield a 0.2 mM final concentration. The cuvette was sealed with a rubber septum, transferred to the cryostat of a UV-vis spectrophotometer maintained at 20 °C. To this solution was added 1 mL of dry O_2 via gas-tight syringe and the reaction was monitored for completion. An aliquot of $Ca(OTf)_2$ was added via gas-tight syringe and the reaction monitored spectroscopically.

For EPR experiments, an EPR tube was charged with 200 μL of [$Mn^{II}H_2$bupa]$^-$ solution and then sealed with a rubber septum. To this EPR tube was added 250 μL (1.2 equivalents) of dry O_2 via gas-tight syringe and tube carefully shaken to mix. The reaction was maintained at room temperature for 1.5 hours before cooling in a –35 °C acetone/dry ice bath and allowed to equilibrate for five minutes. After cooling, an aliquot of $Ca(OTf)_2$ was added via gas-tight syringe,

shaken carefully to mix, and the reaction maintained at –35 °C for five minutes prior to freezing in liquid nitrogen.

References

(1) Kanady, J. S.; Tsui, E. Y.; Day, M. W.; Agapie, T. *Science* **2011**, *333*, 733–736.
(2) Vogt, L.; Vinyard, D. J.; Khan, S.; Brudvig, G. W. *Curr. Opin. Chem. Biol.* **2015**, *25*, 152–158.
(3) Tsui, E. Y.; Kanady, J. S.; Agapie, T. *Inorg. Chem.* **2013**, *52*, 13833–13848.
(4) Kanady, J. S.; Tran, R.; Stull, J. A.; Lu, L.; Stich, T. A.; Day, M. W.; Yano, J.; Britt, R. D.; Agapie, T. *Chem. Sci.* **2013**, *4*, 3986–3996.
(5) Wang, D.; Que, L. *Chem. Commun. (Camb).* **2013**, *49*, 10682–10684.
(6) Kodera, M.; Kawahara, Y.; Hitomi, Y.; Nomura, T.; Ogura, T.; Kobayashi, Y. *J. Am. Chem. Soc.* **2012**, *134*, 13236–13239.
(7) Cox, N.; Pantazis, D. A.; Neese, F.; Lubitz, W. *Acc. Chem. Res.* **2013**, *46*, 1588–1596.
(8) Brudvig, G. W. *Philos. Trans. R. Soc. Lond. B. Biol. Sci.* **2008**, *363*, 1211–1218; discussion 1218–1219.
(9) Hewitt, I. J.; Tang, J.-K.; Madhu, N. T.; Clérac, R.; Buth, G.; Anson, C. E.; Powell, A. K. *Chem. Commun.* **2006**, 2650–2652.
(10) Siegbahn, P. E. M. *Acc. Chem. Res.* **2009**, *42*, 1871–1880.
(11) Amin, M.; Vogt, L.; Szejgis, W.; Vassiliev, S.; Brudvig, G. W.; Bruce, D.; Gunner, M. R. *J. Phys. Chem. B* **2015**, *119*, 7366–7377.
(12) Ferreira, K. N.; Iverson, T. M.; Maghlaoui, K.; Barber, J.; Iwata, S. *Science* **2004**, *303*, 1831–1838.
(13) Pérez-Navarro, M.; Neese, F.; Lubitz, W.; Pantazis, D. A.; Cox, N. *Curr. Opin. Chem. Biol.* **2016**, *31*, 113–119.
(14) Vrettos, J. S.; Stone, D. A.; Brudvig, G. W. *Biochemistry* **2001**, *40*, 7937–7945.
(15) Yocum, C. *Coord. Chem. Rev.* **2008**, *252*, 296–305.
(16) Boussac, A.; Rappaport, F.; Carrier, P.; Verbavatz, J.-M.; Gobin, R.; Kirilovsky, D.; Rutherford, A. W.; Sugiura, M. *J. Biol. Chem.* **2004**, *279*, 22809–22819.
(17) Kärkäs, M. D.; Verho, O.; Johnston, E. V.; Åkermark, B. *Chem. Rev.* **2014**, *114*, 11863–12001.
(18) Wasylenko, D. J.; Palmer, R. D.; Berlinguette, C. P. *Chem. Commun.* **2013**, *49*, 218–227.
(19) Mishra, A.; Wernsdorfer, W.; Abboud, K. A.; Christou, G. *Chem. Commun.* **2005**, 54–56.
(20) Liao, R.-Z.; Kärkäs, M. D.; Lee, B.-L.; Åkermark, B.; Siegbahn, P. E. M. *Inorg. Chem.* **2015**, *54*, 342–351.
(21) Lohmiller, T.; Shelby, M. L.; Long, X.; Yachandra, V. K.; Yano, J. *J. Phys. Chem. B* **2015**, *119*, 13742–13754.
(22) Kim, S. H.; Park, H.; Seo, M. S.; Kubo, M.; Ogura, T.; Klajn, J.; Gryko, D. T.; Valentine, J. S.; Nam, W. *J. Am. Chem. Soc.* **2010**, *132*, 14030–14032.
(23) Colmer, H. E.; Howcroft, A. W.; Jackson, T. A. *Inorg. Chem.* **2016**, *55*, 2055–2069.
(24) Shook, R. L.; Gunderson, W. A.; Greaves, J.; Ziller, J. W.; Hendrich, M. P.; Borovik, A. S. *J. Am. Chem. Soc.* **2008**, *130*, 8888–8889.
(25) Kovacs, J. A. *Acc. Chem. Res.* **2015**, *48*, 2744–2753.
(26) Nam, W. *Acc. Chem. Res.* **2015**, *48*, 2415–2423.
(27) Gao, Y.; Åkermark, T.; Liu, J.; Sun, L.; Åkermark, B. *J. Am. Chem. Soc.* **2009**, *131*, 8726–8727.
(28) Shook, R. L.; Peterson, S. M.; Greaves, J.; Moore, C.; Rheingold, A. L.; Borovik, A. S. *J. Am. Chem. Soc.* **2011**, *133*, 5810–5817.

(29) Shook, R. L.; Gunderson, W. A.; Greaves, J.; Ziller, J. W.; Hendrich, M. P.; Borovik, A. S. *J. Am. Chem. Soc.* **2008**, *130*, 8888–8889.
(30) Connelly, N. G.; Geiger, W. E. *Chem. Rev.* **1996**, *96*, 877–910.

Appendix A

High Valent Fe Species in the $[POAT]^{3-}$ Ligand

The chemistry in Chapters 2 and 4 discussed attempts to synthesize high valent, Fe^{IV}-hydroxido complexes. In both, the high valent Fe complexes could best be described as Fe^{IV}-oxido species with a protonated functional group in the secondary coordination sphere. In an attempt to synthesize new high valent Fe^{IV}-hydroxido species, a different ligand developed by Dr Sickerman, $[H_3POAT]^{3-}$, was examined (Figure A-1). Data here is meant as a preliminary study of Fe species synthesized or identified for future experiments.

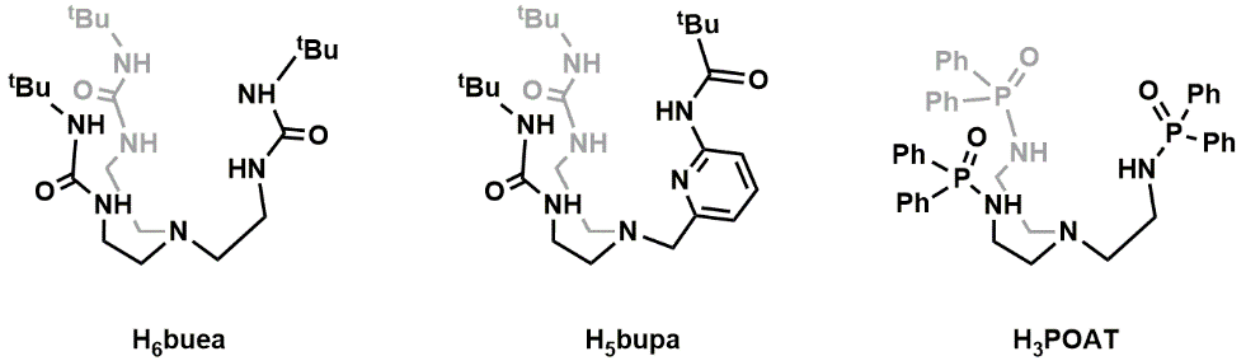

Figure A-1. Depiction of the ligands, H_6buea and H_5bupa, used in Chapters 2 and 4 to generate high valent Fe^{IV}-oxido complexes compared to the new ligand, H_3POAT.

Synthesis of Metal Complexes

Synthesis of K[Fe^{II}POAT]. A solution of H_3POAT was treated with three equivalents of potassium hydride in anhydrous tetrahydrofuran (THF). Once H_2 evolution had ceased, $Fe^{II}(OAc)_2$ was added. A Mössbauer spectrum of the reaction mixture showed a prominent doublet with δ = 1.08 mm/s and ΔE_Q = 2.92 mm/s, consistent with a high spin Fe^{II} center (Figure A-2). In addition, the parallel-mode electron paramagnetic resonance (EPR) spectrum gave a sharp valley at g = 9, again consistent with a high spin Fe^{II} center (Figure A-2). Single crystals of the metal salt were obtained by diffusion of diethyl ether (Et_2O) into the THF solution. The

molecular structure of K[Fe^{II}POAT] showed a mononuclear, Fe^{II} center in trigonal monopyramidal geometry with an open coordination site on the metal center and a potassium counterion bound to the phosphine-oxygen atoms (Figure A-3, Table A-1).

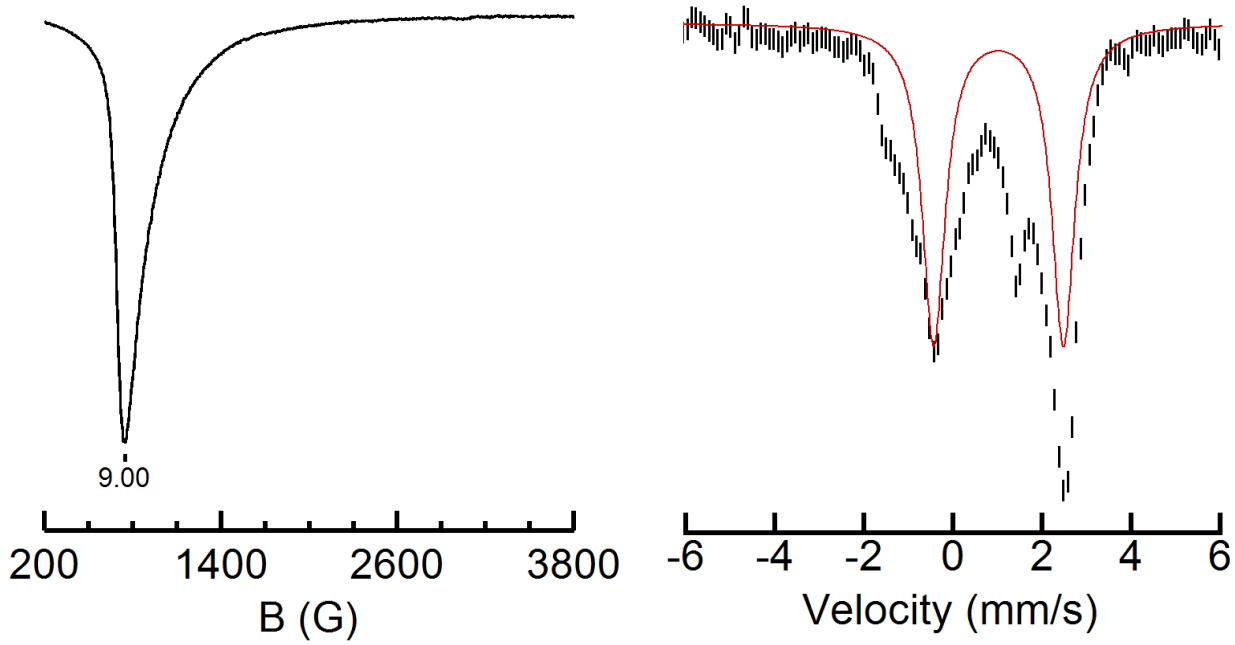

Figure A-2. Parallel-mode EPR (left) and Mössbauer (right) spectra for THF solutions of [Fe^{II}POAT]$^-$. EPR spectrum collected at 10K. Mössbauer spectrum collected at 4K, Red line is the least-square fit of the experimental Mössbauer data with linewidth of 0.62 mm/s. Not modelled is a ferric impurity.

Table A-1. Key metrical parameters for (K[Fe^{II}POAT])$_2$•3THF

	Bond Distances (Å)
Fe1-N1	2.138(7)
Fe1-N2	1.987(5)
	Bond Angles (°)
N1-Fe1-N2	83.54(14)
N2-Fe1-N2′	118.75(6)

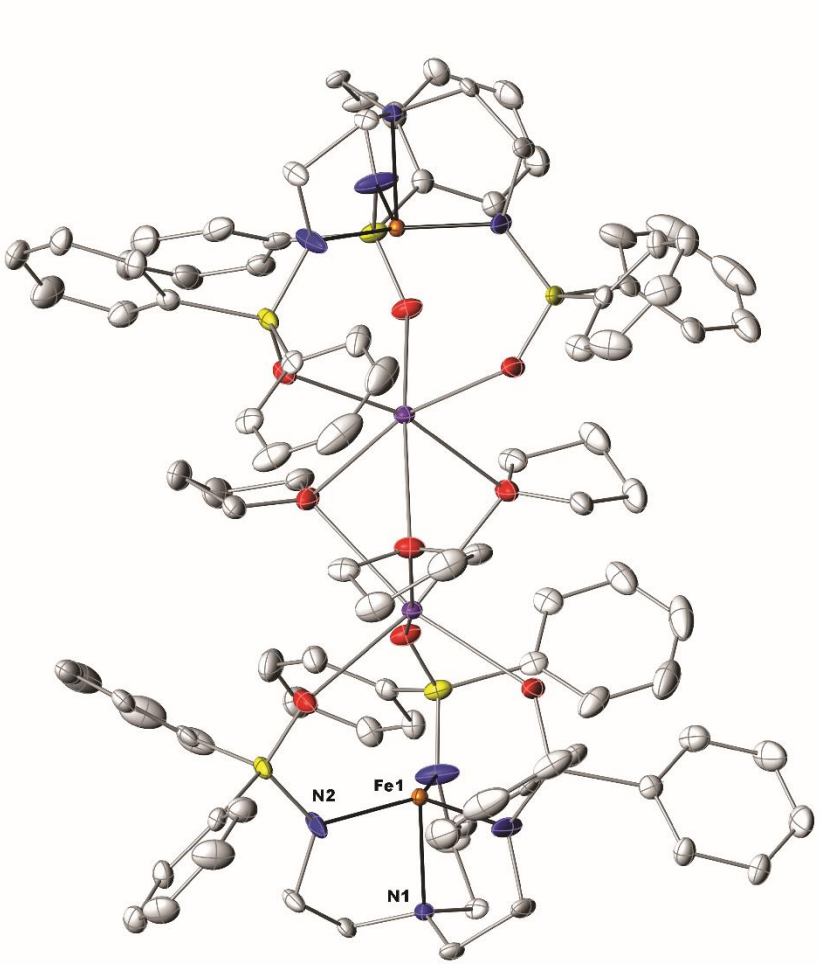

Figure A-3. Molecular structure of $(K[Fe^{II}POAT])_2 \bullet 3THF$ determined by XRD methods. Thermal ellipsoids are drawn at the 50% probability level.

Synthesis of $[Fe^{III}POAT]_2 \bullet KBF_4$. The direct oxidation of $K[Fe^{II}POAT]$ by addition of $[FeCp_2][BF_4]$ to a solution of $K[Fe^{II}POAT]$ in acetonitrile (MeCN). This produced a species with absorbance features at λ_{max} = 385 and 335 nm (Figure A-3). The perpendicular-mode EPR spectrum showed a high spin Fe^{III} center with features at g = 7.01, 5.52, and 3.27 (Figure A-4). Single crystals of the metal salt for XRD structural studies were obtained by diffusion of Et_2O into an MeCN solution. The molecular structure showed that two $[Fe^{III}POAT]$ species were held together by a single potassium ion bound to the phosphine-oxygen atoms from both metal complexes with an outer sphere $[BF_4]^-$ for charge balance (Figure A-4). The Fe-center in each is

best described as six-coordinate, with a single phosphine-oxygen atom binding to the metal center to produce a distorted tetragonal geometry (Figure A-5, Table A-2).

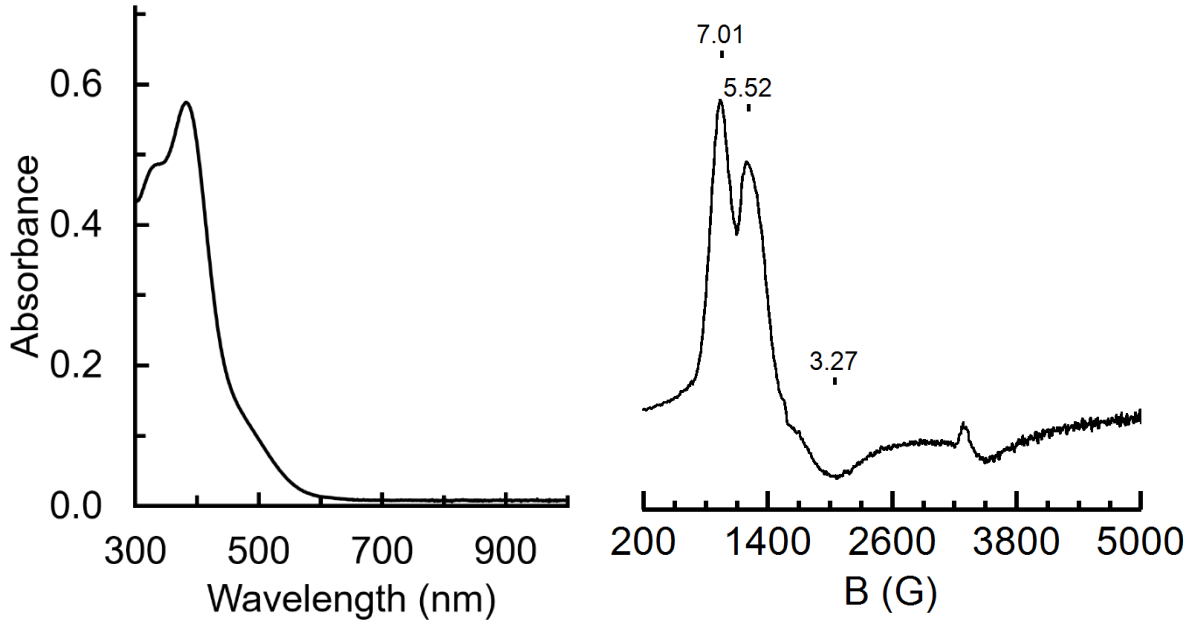

Figure A-4. UV-vis (left) and perpendicular-mode EPR (right) spectra for MeCN solutions of $[Fe^{II}POAT]^-$ treated with one equivalent of $[FeCp_2]^+$. EPR spectrum collected at 77K.

Table A-2. Key metrical parameters for $[Fe^{III}POAT]_2 \bullet KBF_4$

	Bond Distances (Å)
Fe1-N1	2.336(5)
Fe1-N2	1.972(5)
Fe1-N3	1.999(5)
Fe1-N4	2.004(5)
Fe1-O2	2.235(5)
Fe1-O3	2.336(5)
	Bond Angles (°)
N1-Fe1-N2	78.0(2)
N1-Fe1-N3	75.2(2)
N1-Fe1-N4	75.1(2)
N2-Fe1-N3	110.1(2)
N3-Fe1-N4	113.6(2)
N2-Fe1-N4	129.9(2)
N1-Fe1-O2	139.95(16)
N1-Fe1-O3	113.57(17)

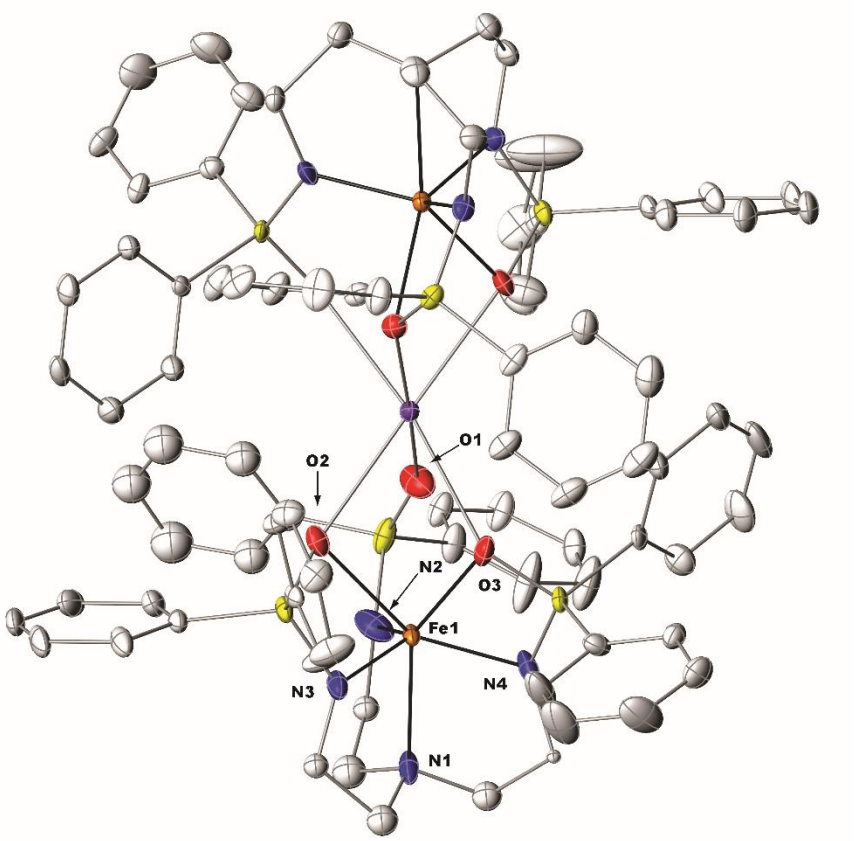

Figure A-5. Molecular structure of $[Fe^{III}POAT]_2 \bullet KBF_4$ determined by XRD methods. The BF_4^- counter ion is omitted for clarity. Thermal elipsoids are drawn at the 50% probability level.

Treatment of K[Fe^{II}POAT] with Oxygen-Atom Sources. The treatment of K[Fe^{II}POAT] with *N*-methylmorphyline, *N*-oxide (NMO) was monitored spectrophotometrically and showed absorbance features at λ_{max} = 340, 400, and 845 nm (Figure A-6A). The low energy absorbance band at λ_{max} = 845 nm is suggestive of a high valent Fe^{IV}-oxido complexes. Perpendicular-mode EPR spectroscopy showed a high spin Fe^{III} species with features at g = 8.72, 5.16, and 3.37, which could be reproduced using O_2 as the oxidizing agent (Figure A-6B). Finally the Mössbauer spectrum of the reaction mixture showed at least three species: [Fe^{II}POAT]$^-$ starting complex (δ = 1.08 mm/s, ΔE_Q = 2.92 mm/s), an Fe^{III} species (δ = 0.68 mm/s, ΔE_Q = 2.36 mm/s), and an Fe^{IV} species (δ = 0.09 mm/s, ΔE_Q = 0.42 mm/s) (Figure A-6C).

Single crystals were obtained from the reaction mixture of K[Fe^{II}POAT] and O_2 by diffusion of Et_2O into a THF solution. The molecular structure showed two, crystallographically identical Fe^{III}-hydroxido complexes bridged by two potassium counter ions. The potassium ions are bound to two of the phosphine-oxygen atoms and the hydroxide ligand (Figure A-7, Table A-3).

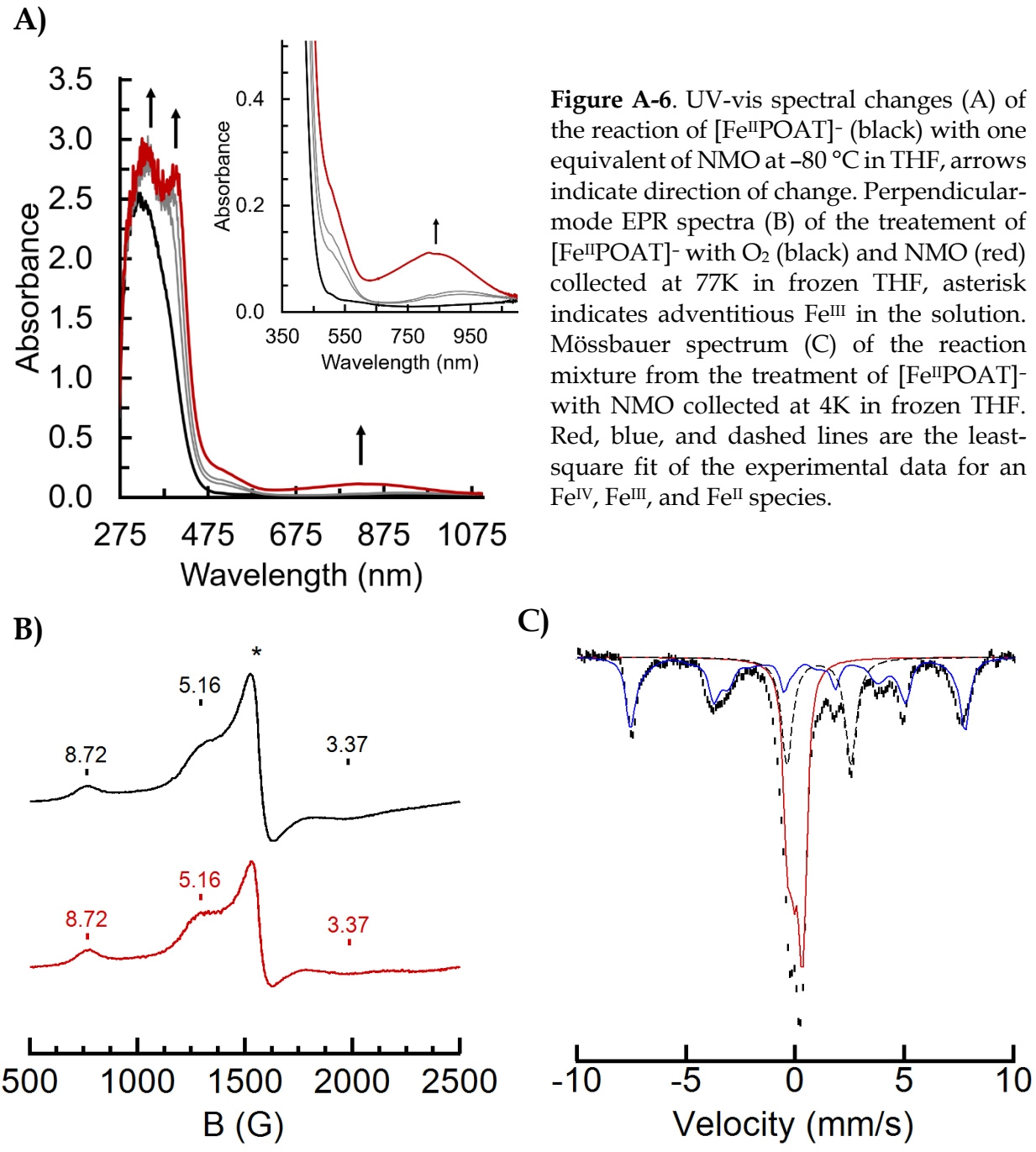

Figure A-6. UV-vis spectral changes (A) of the reaction of [Fe^{II}POAT]$^-$ (black) with one equivalent of NMO at –80 °C in THF, arrows indicate direction of change. Perpendicular-mode EPR spectra (B) of the treatement of [Fe^{II}POAT]$^-$ with O_2 (black) and NMO (red) collected at 77K in frozen THF, asterisk indicates adventitious Fe^{III} in the solution. Mössbauer spectrum (C) of the reaction mixture from the treatment of [Fe^{II}POAT]$^-$ with NMO collected at 4K in frozen THF. Red, blue, and dashed lines are the least-square fit of the experimental data for an Fe^{IV}, Fe^{III}, and Fe^{II} species.

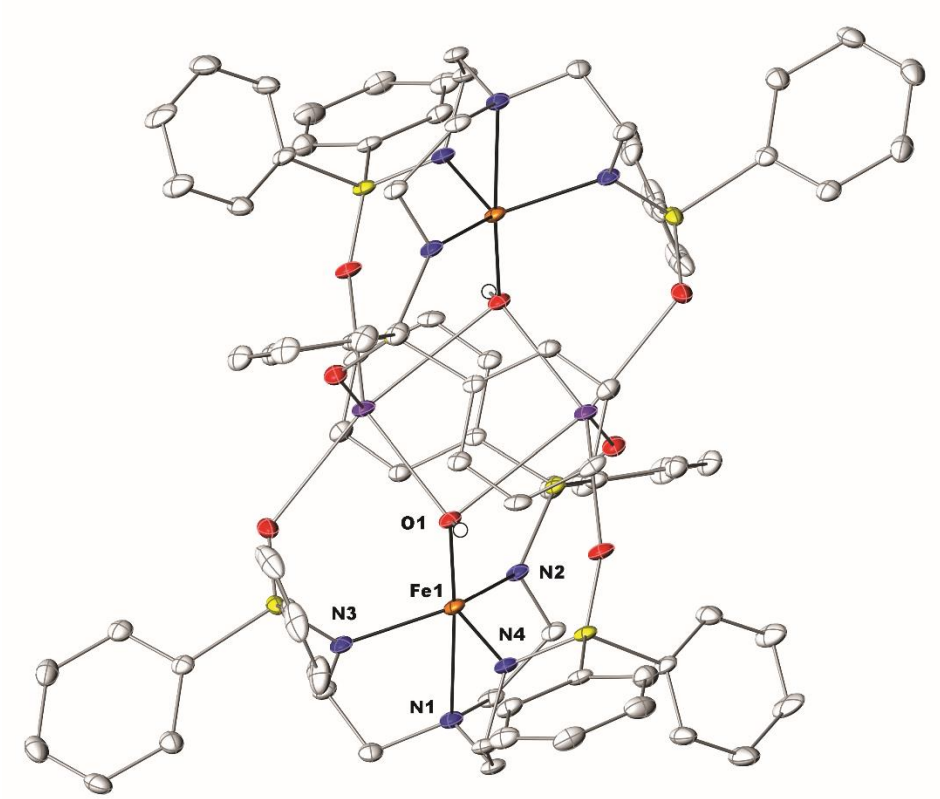

Figure A-7. Molecular structure of $(K[Fe^{III}POAT(OH)])_2$ determined by XRD methods. Thermal elipsoids are drawn at the 50% probability level.

Table A-3. Key metrical parameters for $(K[Fe^{III}POAT(OH)])_2$

	Bond Distances (Å)
Fe1-N1	2.3665(19)
Fe1-N2	2.0023(18)
Fe1-N3	2.022(2)
Fe1-N4	2.0072(19)
Fe1-O1	1.9004(16)
	Bond Angles (°)
N1-Fe1-N2	78.32(7)
N1-Fe1-N3	77.15(7)
N1-Fe1-N4	78.31(7)
N2-Fe1-N3	118.95(8)
N3-Fe1-N4	114.59(8)
N2-Fe1-N4	113.66(8)
N1-Fe1-O1	175.83(7)

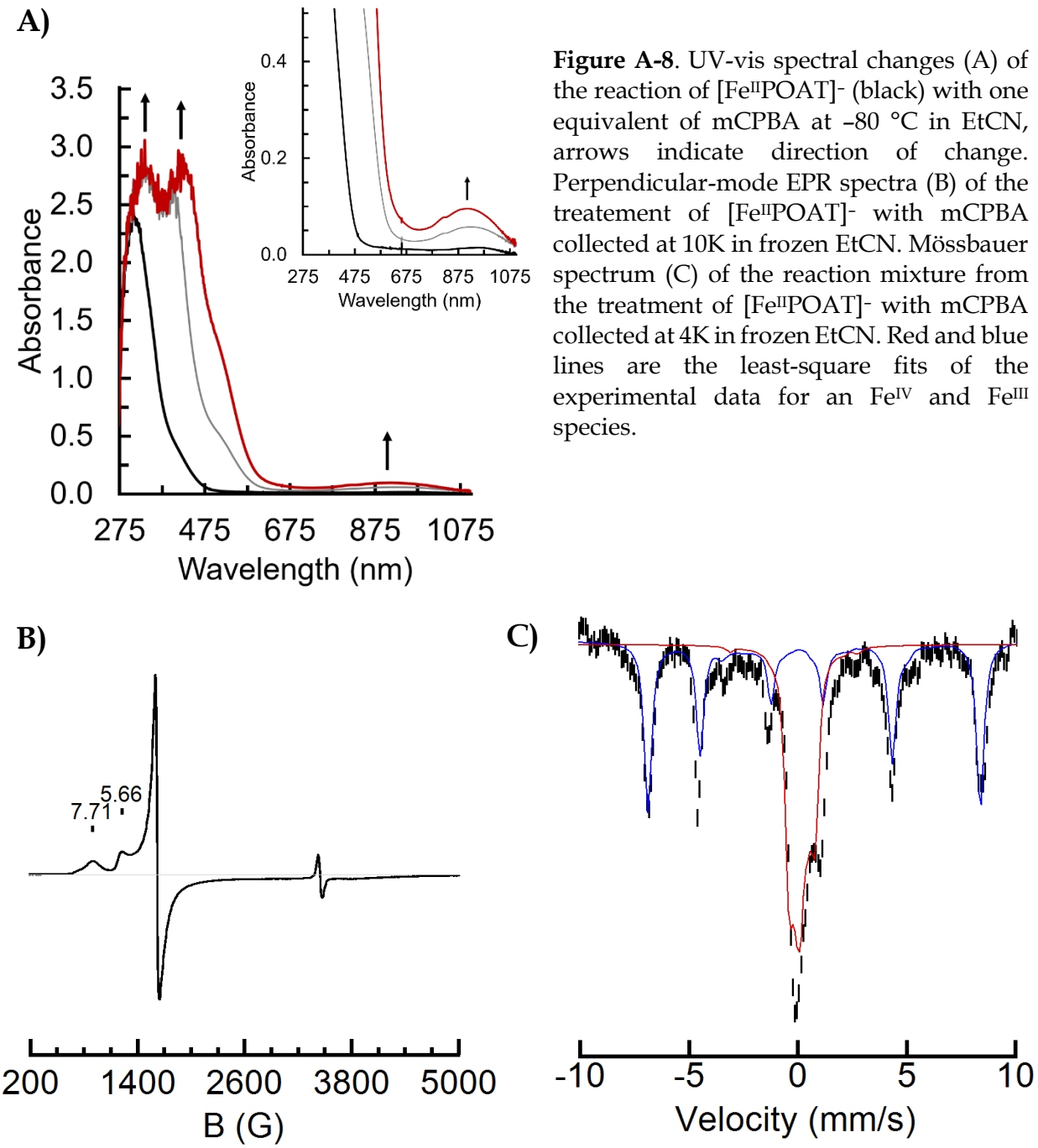

Figure A-8. UV-vis spectral changes (A) of the reaction of [Fe^{II}POAT]$^-$ (black) with one equivalent of mCPBA at –80 °C in EtCN, arrows indicate direction of change. Perpendicular-mode EPR spectra (B) of the treatement of [Fe^{II}POAT]$^-$ with mCPBA collected at 10K in frozen EtCN. Mössbauer spectrum (C) of the reaction mixture from the treatment of [Fe^{II}POAT]$^-$ with mCPBA collected at 4K in frozen EtCN. Red and blue lines are the least-square fits of the experimental data for an Fe^{IV} and Fe^{III} species.

The treatment of K[Fe^{II}POAT] with *meta*-chloroperbenzoic acid (mCPBA) was monitored spectrophotometrically and showed absorbance features at λ_{max} = 340, 430, and 920 nm (Figure A-8A). The low energy absorbance band suggested an Fe^{IV}-oxido species was produced during the reaction. The perpendicular-mode EPR spectrum showed a high spin Fe^{III} species with features at g = 7.71 and 5.62 (Figure A-8B). The Mössbauer spectrum of the reaction mixture

showed two species: an Fe^{III} species (δ = 0.07 mm/s, ΔE_Q = 2.38 mm/s) and an Fe^{IV} species (δ = 0.03 mm/s, ΔE_Q = 1.03 mm/s) (Figure A-8C).

Experimental Details

General Procedures. All manipulations, unless otherwise stated, were performed under an argon atmosphere in a Vac-atmospheres dry box. All chemicals were purchased from commercial sources and used without further purification unless otherwise stated. Ferrocene was sublimed prior to use. Potassium hydride as a 40 % w/w suspension in mineral oil was collected on a fine fritted glass funnel under an argon atmosphere and washed 5 x with 15 mL of anhydrous pentane before drying under vacuum to yield a gray solid which was used without further purification. $[FeCp_2][BF_4]$ and H_3POAT were prepared according to previously published procedures.[1,2]

Physical Methods. Electronic absorption spectra were recorded in a 1 cm cuvette on an 8453 Agilent UV-Vis spectrometer equipped with an Unisoku Unispeks cryostat. X-band (9.28 GHz) EPR spectra were collected as frozen solutions using a Bruker EMX spectrometer equipped with an ER041XG microwave bridge. Mössbauer spectra were recorded with a Janis Research Super-Varitemp dewar.

X-ray Crystallographic Methods. A Bruker SMART APEX II diffractometer was used to collect all data. The APEX2[3] program package was used to determine the unit-cell parameters and for data collections. The raw frame data was processed using SAINT[4] and SADABS[5] to yield the reflection data files. Subsequent calculations were carried out using the SHELXTL[6] program. The structures were solved by direct methods and refined on F^2 by full-matrix least-squares techniques. The analytical scattering factors[7] for neutral atoms were used throughout the analysis.

Table A-4. Crystallographic data and structure refinement parameters for the molecular structures presented in Appendix A.

Complex	$(K[Fe^{II}POAT])_2 \bullet 3THF$	$[Fe^{III}POAT]_2 \bullet 0.5KBF_4$	$(K[Fe^{III}POAT(OH)])_2$
Formula	$C_{111}H_{144}Fe_2K_2N_8O_9P_6$	$C_{84}H_{84}BF_4Fe_2KN_8O_6P_6$	$C_{84}H_{86}Fe_2K_2N_8O_8P_6$
Formula weight	2110.05	1725.02	1711.32
Crystal system	Trigonal	Triclinic	Monoclinic
Space group	*R c*	*P*	$P2_{1/c}$
a (Å)	14.8890(7)	14.409(2)	15.8033(11)
b (Å)	14.8890(7)	16.274(2)	14.5354(10)
c (Å)	85.781(4)	18.382(3)	19.8205(14)
α (°)	90	93.3944(19)	90
β (°)	90	90.1241(18)	110.8236(9)
χ (°)	120	95.9266(17)	90
Volume ($Å^3$)	16468.5(17)	4279.9(11)	4255.5(5)
Z	6	2	2
δ_{calc} (Mg/m_3)	1.277	1.339	1.336
Goodness-of-fit	1.087	1.018	1.031
R1	0.1179	0.1076	0.0363
wR2	0.2526	0.2882	0.0818

Hydrogen atoms for $(K[Fe^{II}POAT])_2 \bullet 3THF$ were included using a riding model. There was one molecule of pentane present in the formula unit. The $N(CH_2CH_2)NR$ groups were disordered.

Hydrogen atoms for $[Fe^{III}POAT]_2 \bullet 0.5KBF_4$ were included using a riding model. Several atoms were disordered and included using multiple components with partial site-occupancy-factors. There were several high residuals present in the final difference-Fourier map. It was not possible to determine the nature of the residuals although it was probable that acetonitrile solvent was present. The SQUEEZE[8] routine in the PLATON[9] program package was used to account for the electrons in the solvent accessible voids.

Hydrogen atom H1 for $(K[Fe^{III}POAT(OH)])_2$ was located from a difference-Fourier map and the remaining hydrogen atoms were included using a riding model. There were several high residuals present in the final difference-Fourier map. It was not possible to determine the nature of the residuals, although it is probable that tetrahydrofuran or diethyl ether solvent was present.

The SQUEEZE routine in the PLATON[6] program package was used to account for the electrons in the solvent accessible voids.

Synthesis of K[Fe^{II}POAT]. To a solution of H_3POAT (200 mg, 0.269 mmol) in anhydrous THF (6 mL) was added potassium hydride (KH) (33 mg, 0.81 mmol) and the reaction allowed to proceed until gas evolution ceased and all solids were dissolved. To the light yellow solution was added $Fe^{II}(OAc)_2$ (47 mg, 0.26 mmol). The solution was stirred for one hour and then filtered through a medium fritted glass funnel to remove insoluble material. Light yellow crystals (208 mg, 93%) are afforded by vapor diffusion of diethyl ether (Et_2O) into the solution of THF.

Synthesis of K[Fe^{III}POAT(OH)]. An initial procedure identical to the preparation of K[Fe^{II}POAT] was followed with the addition of anhydrous O_2 (3.2 mL, 0.13 mmol) via gas-tight syringe and stirred for one hour. The volatiles were then removed from the reaction mixture under vacuum. The resulting residue was redissolved in THF (3 mL) and layered under Et_2O. A few single crystals were isolated from this solution that were suitable for XRD studies.

Synthesis of K[Fe^{III}POAT]•0.5KBF$_4$. A solution of K[Fe^{II}POAT] (115 mg, 0.137 mmol) in THF (3 mL) was treated with $[FeCp_2][BF_4]$ (36 mg, 0.13 mmol) and stirred for two hours. The solution was filtered to remove orange solids. The orange solid was redissolved in MeCN and latered under Et_2O to yield a small amount of orange crystals suitable for XRD studies.

Solution studies using K[Fe^{II}POAT]. In a typical experiment, a 2 mM solution of K[Fe^{II}POAT] (17 mg, 0.020 mmol) was prepared in the desired solvent (10 mL). Stock solutions of other reagents prepared to between 20 and 50 mM in the same solvent and added via gas-tight syringe to an aliquote of [Fe^{II}POAT]$^-$. Reactions were monitored spectrophotometrically either by UV-vis or EPR spectroscopies. Mössbauer samples were prepared in an analogous manner using 95% ^{57}Fe-enriched K[Fe^{II}POAT].

References

(1) Connelly, N. G.; Geiger, W. E. *Chem. Rev.* **1996**, *96*, 877–910.
(2) Sickerman, N. Investigating the Effects of Non-covalent Interactions in Metal Complexes with Versatile Ligand Scaffolds, University of California, Irvine, 2014.
(3) APEX2, 2014.
(4) SAINT, 2013.
(5) Sheldrick, G. M. SADABS, 2014.
(6) Sheldrick, G. M. SHELXTL, 2014.
(7) Wilson, A. J. C.; Geist, V. *Cryst. Res. Technol.* **1993**, *28*, 110–110.
(8) Spek, A. L. *Acta Crystallogr. Sect. C Struct. Chem.* **2015**, *71*, 9–18.
(9) Spek, A. L. *Acta Crystallogr. Sect. D Biol. Crystallogr.* **2009**, *65*, 148–155.

Appendix B

Supplementary Information

Materials for Chapter 2

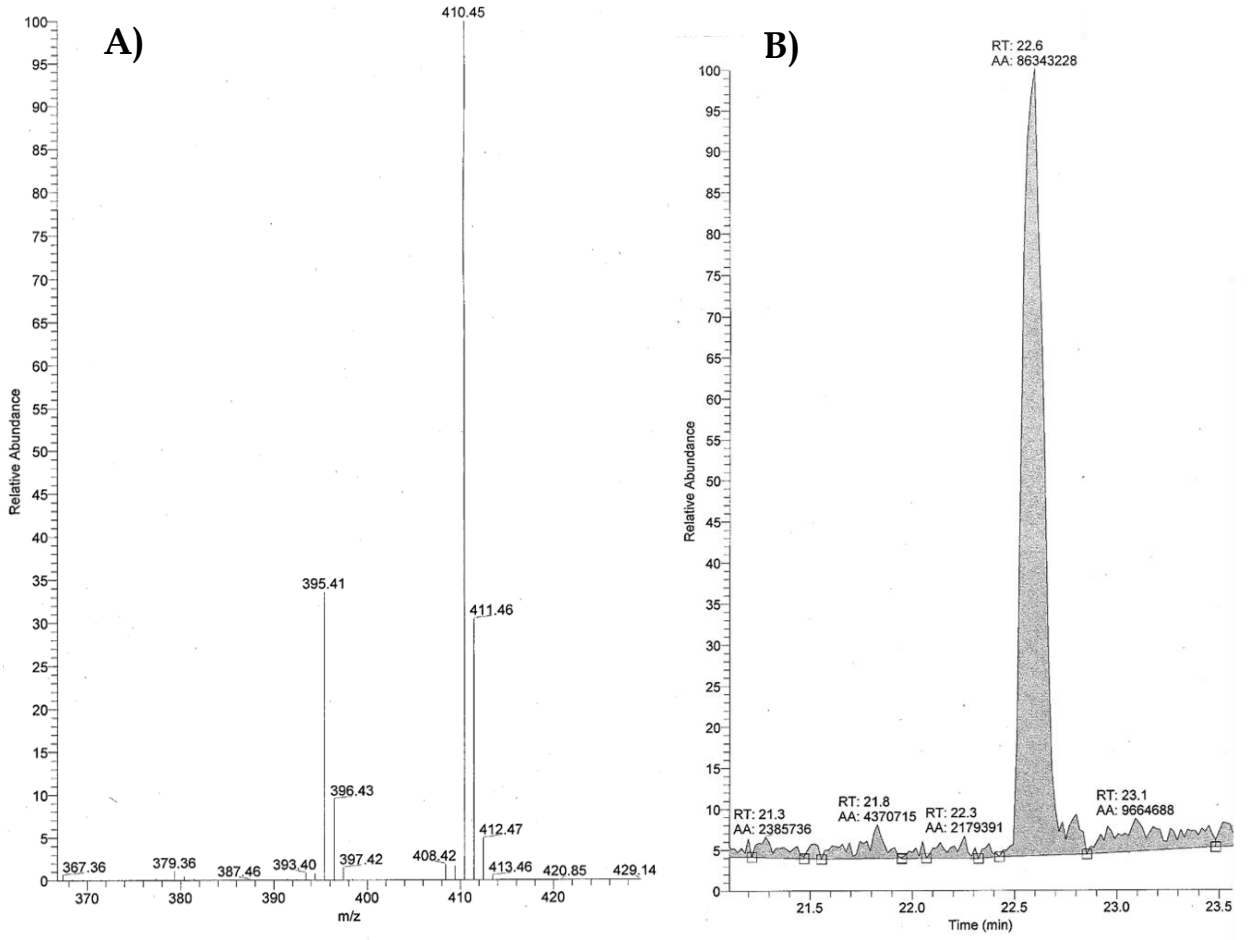

Figure B-1. The GC trace (A) and matching MS trace (B) for the oxidation of $[Fe^{IV}H_3buea]^-$ in the presence of 100 equiv 2,6-di-*tert*-butylphenol. MS trace shows 2,2′,6,6′-tetra-*tert*-butyl-4,4′-biphenol at m/z = 410.45 and m/z for $(-CH_3)^+$ = 395.41.

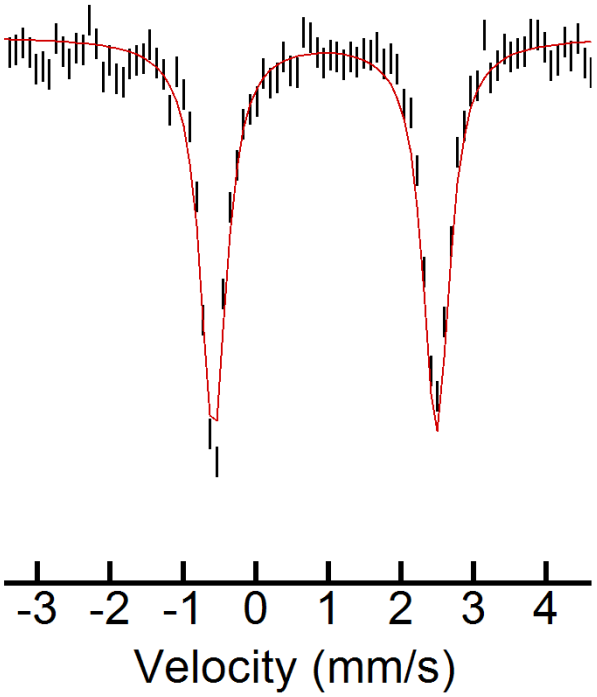

Figure B-2. Mössbauer spectrum of a 2 mM solution of [$^{57}Fe^{II}$bupa]$^-$ collected in EtCN at 4K with parameters δ = 0.95 mm/s and ΔE_Q = 3.06 mm/s. Red line is the least-square fit of the experimental data.

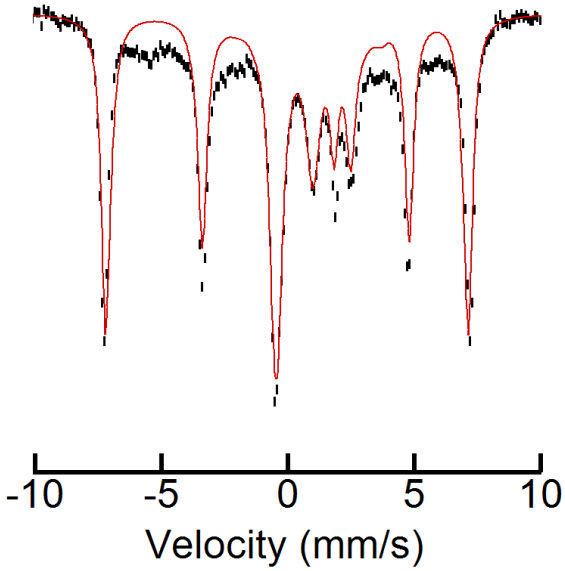

Figure B-3. Mössbauer spectrum of a 2 mM solution of [$^{57}Fe^{III}$bupa(O)(H)]$^-$ collected in EtCN at 4K with parameters δ = 0.74 mm/s and ΔE_Q = 2.31 mm/s. Red line is the least-square fit of the experimental data. Spectrum contains small amount of [Fe^{II}bupa]$^-$.

Materials for Chapter 5

The reactivity of $[Mn^{V}H_3buea(O)]$ and $[Mn^{IV}H_3buea(O)]^-$ with Sc^{III} ions was also examined at elevated temperatures. Addition of 30 equivalents of Sc^{III} ions to either the $[Mn^{V}H_3buea(O)]$ or $[Mn^{IV}H_3buea(O)]^-$ in 1:1 DMF:THF at –35 °C resulted in generation of new absorbance bands at λ_{max} = 380 and 500 nm in addition to a band for $[FeCp_2]^+$ at λ_{max} = ~620 nm (Figure B-4A and B). The new absorbance bands are only observed at elevated temperatures, not at –80 °C. The increase in the absorbance band at λ_{max} = ~620 nm suggests that the complexes have been reduced to the Mn^{III} oxidation state possibly by the coordination multiple Sc^{III} ions to a single Mn complex, raising the reduction potential, or from an unknown reaction.

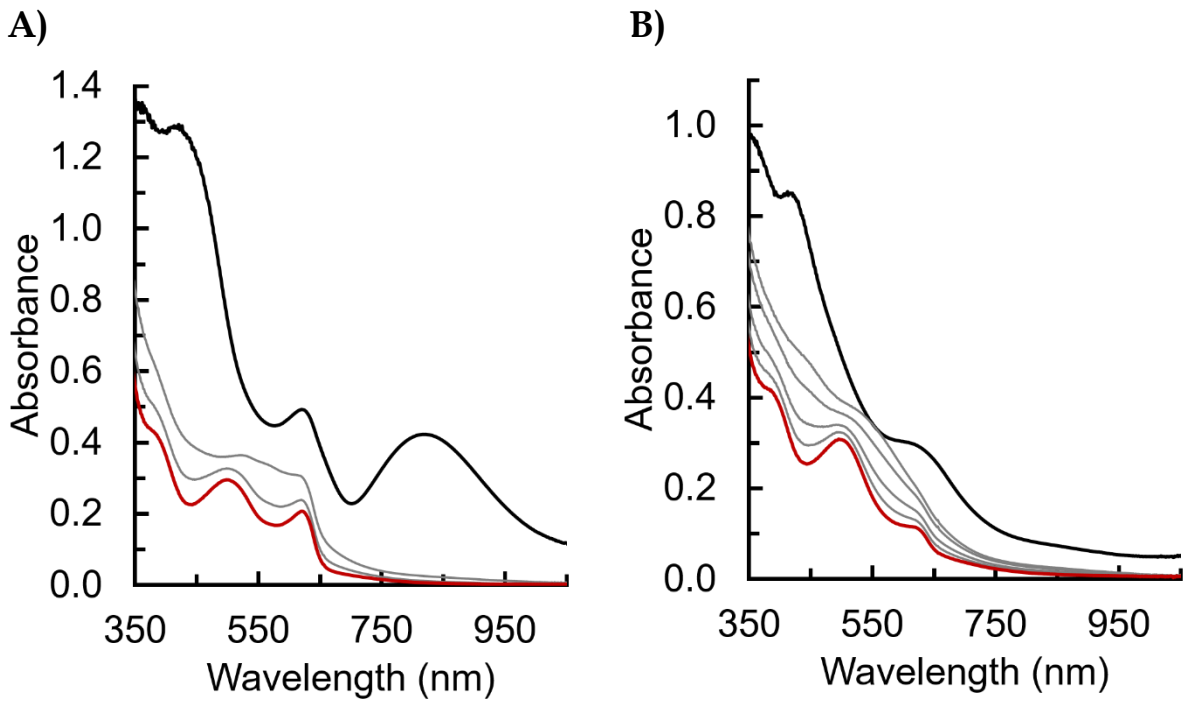

Figure B-4. UV-vis spectral changes upon addition of 30 equivalents of Sc^{III} ions to $[Mn^{V}H_3buea(O)]$ (A) and $[Mn^{IV}H_3buea(O)]^-$ (B) in 1:1 DMF:THF at –35 °C. Gray traces represent 30 s scans.

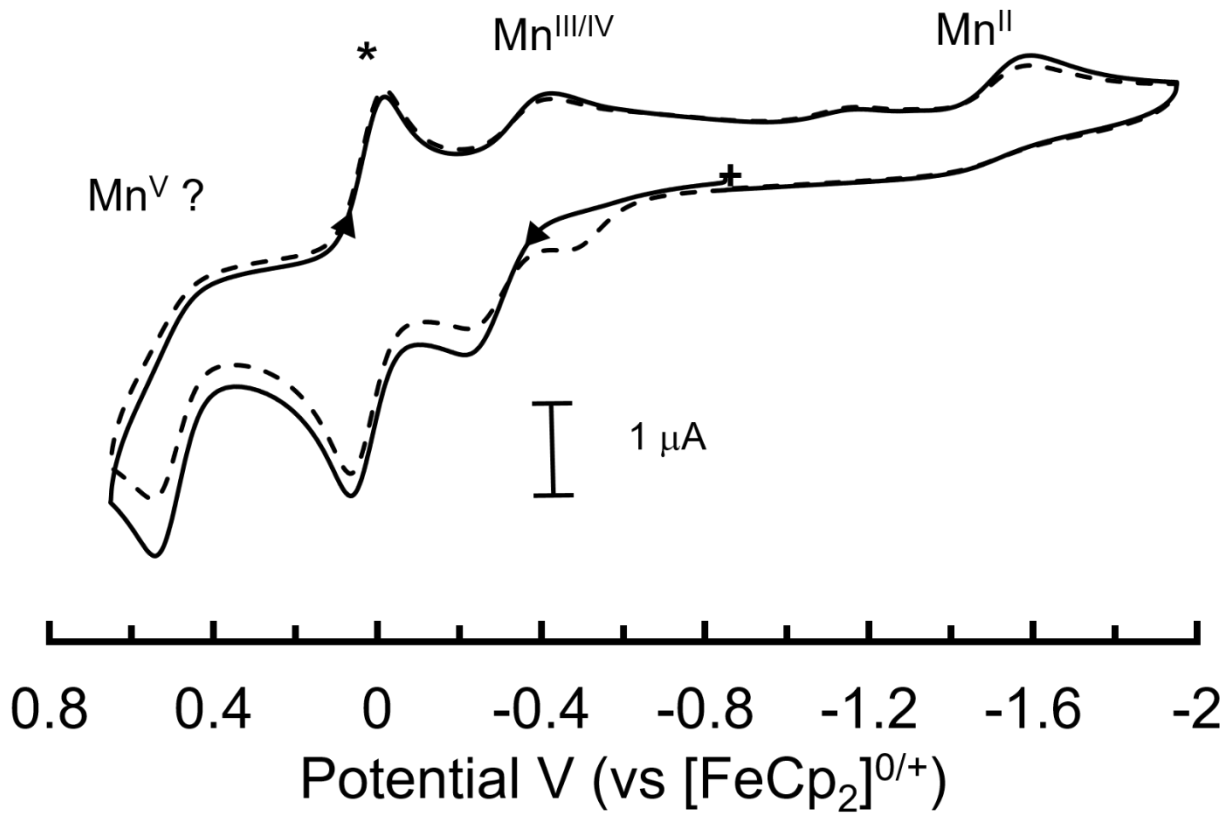

Figure B-5. Cyclic voltammogram for a 3 mM solution of $[Mn^{III}H_2bupa(O)(H)]^-$ in DMF collected at a 100 mV/s scan rate with 0.1 M supporting TBAP electrolyte. Asterisk indicates $[FeCp_2]$ internal standard. Plus sign indicates starting potential and arrows indicate direction of sweep. Potentials assigned to: Mn^{II} -1.55 V, $Mn^{III/IV}$ -0.33 V, and Mn^{V} 0.54 V.